

LUSAS

A nighttime photograph of a city skyline with a complex multi-level highway interchange in the foreground. The buildings are illuminated, and the traffic on the highway creates long, bright light trails. The sky is dark with some clouds.

Verification Manual

Verification Manual

LUSAS Version 24.0 : Issue 1

LUSAS
Forge House, 66 High Street, Kingston upon Thames,
Surrey, KT1 1HN, United Kingdom

Tel: +44 (0)20 8541 1999
Fax +44 (0)20 8549 9399
Email: info@lusas.com
<http://www.lusas.com>

Distributors Worldwide

Copyright ©1982-2026 LUSAS
All Rights Reserved.

Table of Contents

Example 1.1.1	1
Linear Static Analysis Of A Curved Cantilever (using 4 elements)	1
Example 1.1.2	4
Linear Analysis Of A Curved Cantilever (using 16 Elements)	4
Example 1.1.3	7
Linear Static Stress Analysis Of A Plane Frame Using Beam Elements	7
Example 1.1.4	12
Temperature Dependent Properties Constant Strain Cantilever	12
Example 1.2.1	15
Linear Elastic Static Fracture Analysis Of A Three-Point Bend Specimen..	15
Example 1.2.3	23
Connecting Incompatible Models Using Constraint Equations	23
Example 1.2.4	32
Plane Membrane Analysis - Perforated Sheet Under Pure Tension	32
Example 1.3.1	37
Orthotropic Plate Under Pressure Load.....	37
Example 1.3.2	41
Static Linear Analysis Of A Thick Circular Plate	41
Example 1.3.3	45
Eccentric Ribbed Plate	45
Example 1.4.1	47
Static Stress Analysis Of A Cantilever Subjected To Multiple Load Cases..	47
Example 1.5.1	51
Linear Elastic Stress Analysis Of A Compact Tension Fracture Specimen..	51
Example 1.6.1	55
A Simply Supported Twin Box Beam Under Concentrated Loads	55
Example 1.6.2	59
Static Stress Analysis Of A Shallow Spherical Shell	59
Example 1.6.3	63
Graphite/Epoxy Resin Laminated Orthotropic Square Plate.....	63
Example 1.7.1	67
Axisymmetric Analysis Of A Clamped Circular Plate.....	67
Example 1.7.2	70
Axisymmetric Thin-Walled Pressure Vessel.....	70
Example 1.7.3	75
Cooling Tower Subject To Wind Loading	75
Example 2.2.1	79

Groundwater Seepage Problem	79
Example 2.2.2	83
Steady State Thermal Analysis Of An Underground Tunnel	83
Example 2.2.3	91
Conductance Between A Plate And Half Cylinder	91
Example 2.3.1	96
Cylinder With Temperature Dependent Conductivity	96
Example 3.1.1	99
Frequency Analysis Of A Simply Supported Beam	99
Example 3.1.2	101
Frequency Analysis Of A Sprung Mass	101
Example 3.1.3	103
Linear Buckling Analysis Of A Simple Portal Frame	103
Example 3.1.4	106
Frequency Of Prestressed 3×3 Flat Cable Net	106
Example 3.3.1	109
Cantilevered Thin Square Plate	109
Example 3.4.1	115
Bifurcation Of A Double Arch	115
Example 3.5.1	118
Natural Frequency Analysis Of A Solid Cantilever	118
Example 3.6.1	121
Buckling Analysis Of A Rectangular Panel	121
Example 3.7.1	124
Eigen-Analysis Of A Cooling Tower	124
Example 4.1.1	128
Geometrically Nonlinear Analysis Of A Cantilevered Beam	128
Example 4.1.2	131
Bifurcation Of Simple Bar-Spring System	131
Example 4.1.3	134
Suspended Cable With Uniform And Concentrated Loading	134
Example 4.3.1	137
Free Vibration Analysis Of A Rotating Blade.	137
Example 4.3.2	141
Curved Cantilever Under Concentrated End Load	141
Example 4.5.1	144
Hinged Cylindrical Shell Under Central Point Load.	144
Example 4.5.2	147
Clamped Spherical Cap Subject To A Point Load	147
Example 4.5.3	151
Large Displacement Of A Hyperbolic Paraboloid	151

Example 4.5.4	155
Large Displacement Of A Hemispherical Shell	155
Example 4.5.5	160
Optimisation of cable forces in cable stayed bridge	160
Example 5.1.1	163
Elastoplastic Analysis Of A Cantilever Bar	163
Example 5.1.2	166
Uniaxial Tension/ Compression Cycling	166
Example 5.1.3	171
Uniaxial Cycling Elastic-Damage Analysis	171
Example 5.1.4	175
Uniaxial Cycling of a Piecewise Multi-Linear Elastic Material	175
Example 5.2.1	178
Buried Pipe With Soil-Pipe Interface Modelled Using 2d Interface Model ..	178
Example 5.2.2	181
Elasto-Plastic Analysis Of A Thick Cylinder Under Internal Pressure	181
Example 5.2.3	184
Nonlinear Stress Analysis Of A Two Span Reinforced Concrete Beam	184
Example 5.2.4	194
Uniaxial Cycling Elasto-Plastic Damage Analysis.....	194
Example 5.2.5	198
Thermally Induced Creep Of Internally Pressurised Hollow Sphere	198
Example 5.2.6	201
Combined Plasticity And Creep Of Bar	201
Example 5.2.7	205
Extension Of A Double Notched Specimen	205
Example 5.2.8	209
Plane Strain Limit Load Analysis of Granular Material	209
Example 5.2.9	217
Plane Strain Analysis Of Slope Stability Limit	217
Example 5.2.10	221
Four-point bending of a reinforced concrete beam.....	221
Example 5.2.11	226
Nonlinear Stress Analysis Of A Notched Fibre Reinforced Concrete Beam Under Three Point Bending	226
Example 5.2.12	238
Uniaxial Tension-Compression Cyclic Response Of Masonry Panel	238
Example 5.2.13	242
TU Eindhoven Shear-walls.....	242
Example 5.4.1	246
Buried Pipe With Soil-Pipe Interface Modelled Using 3d Interface Model ..	246

Example 5.4.2	250
Elasto-Plastic Analysis of a Thick Porous Cylinder Under Internal Pressure	250
Example 5.5.1	254
Cylindrical Shell Subject To Self Weight	254
Example 5.6.1	257
Axisymmetric analysis of sand under compression	257
Example 5.7.1	261
Single joint test for lateral earth pressure	261
Example 5.7.2	264
Plastic hinge with axial force dependent moment-curvature relation	264
Example 5.8.1	266
Definition of soil-structure interface material parameters from experimental data	266
Example 6.3.1	273
Materially And Geometrically Nonlinear Encastre Beam	273
Example 6.5.1	276
Elasto-Plastic Buckling Analysis Of A An Imperfect Rectangular Panel	276
Example 6.5.2	282
Elasto-Plastic Analysis Of A Clamped Spherical Cap	282
Example 6.5.3	286
Nonlinear Analysis Of A CHS Welded Tubular Joint	286
Example 6.5.4	290
Large Deflection Of Orthotropic Spherical Cap	290
Example 7.1.1	296
Transient Analysis With Radiation And Convection	296
Example 7.2.1	299
Transient Field Analysis Of Heat Conduction Problem	299
Example 7.2.2	302
2-D Solidification Of A Corner Region	302
Example 7.2.3	307
Heat Conducting Plate With Sudden Cooling	307
Example 8.1.1	310
Spectral Response Analysis Of A 2-D Frame Structure	310
Example 8.1.2	311
Linear Dynamic Analysis Of A Spring/Mass/ Damping System	311
Example 8.1.3	314
Beam Subject To A Harmonic, Periodic And Step Load	314
Example 8.1.4	320
Large Deformation Dynamics of Stiff and Elastic Pendulum	320
Example 8.1.5	329

Free-Free Nearly Rigid Beam Undergoing Large Overall Motion.....	329
Example 8.1.6	333
Static And Dynamic Responses Of Prestressed Cable Under Uniform Loading	333
Example 8.2.1	337
Linear Dynamic Analysis Of A Beam With Pressure Loading	337
Example 8.6.1	340
Nonlinear Dynamic Analysis Of A Clamped Spherical Shell	340
Example 9.1.1	343
Quenching Of An Infinite Plate.....	343
Example 9.1.2	346
Coupled Temperature Displacement Analysis	346
Example 9.2.1	350
Compression Of An Angle Into A Corner.....	350
Example 9.2.2	355
Upsetting Of A Cylindrical Billet	355
Example 10.1.1	359
Plastic Bar Impact Against A Rigid Wall.	359
Example 10.1.2	363
Cantilever Subject To Dynamic Loading.	363
Example 10.1.3	366
Interference Fit Test	366
Example 10.1.4	373
Cylinder Compression Between Platens.....	373
Example 10.2.1	376
Propped Cantilever With Joint Elements And Contact/Gap Model	376
Example 11.1.1	381
Eigenvalue Analysis Of Pinned Double Cross.....	381
Example 11.5.1	386
Tip Loaded Cantilever Analysed Using Superelements	386
Example 12.1.1	388
1-D Soil Consolidation	388
Example 12.1.2	392
Isothermal Drainage of Water from a Sand Column.....	392
Example 12.1.3	396
Volumetric deformation of unsaturated soils.....	396
Example 13.1.1	401
Coupled Hygro-Thermal-Mechanical Analysis	401
Index	412

Example 1.1.1

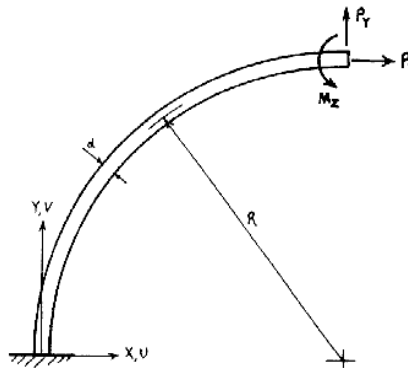
Linear Static Analysis Of A Curved Cantilever (using 4 elements)

Keywords

Curved Beam

Description

Determine the tip displacements for a quarter circle cantilever with the dimensions, properties and subject to the loading as given below. Neglect the effect of shear deformations but include the effect of axial deformations on the displacements.



Discretisation

Model with four equal length curved BM3 beam elements which, being thin beam elements, explicitly exclude the effects of shear deformations.

Geometric properties

Radius, mm	Cross-section breadth (b), mm	Cross-section depth (d), mm
200	10	10

Material properties

Young's modulus	200 x10 ³ N/mm ²
-----------------	--

Loading

Point load at tip in X direction (P _x), N	Point load at tip in Y direction (P _y), N	Concentrated moment at tip (M _z), Nm
200	200	20

Theory

The following equations for the tip displacements may be derived using the unit load method.

	Point load at tip in X direction, P _x	Point load at tip in Y direction, P _y	Concentrated moment at tip, M _z
u	$\frac{P_x R^3 (3-8)}{4EI} + \frac{P_x R}{4EA}$	$-\frac{P_y R^3}{2EI} + \frac{P_y R}{2EA}$	$-\frac{M_z R^2 (\pi-2)}{2EI}$
v	$-\frac{P_x R^3}{2EI} + \frac{P_x R}{2EA}$	$\pi \left(\frac{P_y R^3}{4EI} + \frac{P_y R}{4EA} \right)$	$\frac{M_z R^2}{EI}$
θ	$-\frac{P_x R^2 (\pi-2)}{2EI}$	$\frac{P_y R^2}{EI}$	$\pi \frac{M_z R}{2EI}$

Comparison

Load	Result source	u	v	θ
Point load at tip in X direction, P _x	LUSAS	3.42023	-4.79880	-0.0273976
	Theory	3.42104	-4.799	-0.0273982
Point load at tip in Y direction, P _y	LUSAS	-4.79880	7.54071	0.048
	Theory	-4.799	7.54139	0.048
Concentrated moment at tip, M _z	LUSAS	-2.73976	4.8	0.0376988
	Theory	-2.73982	4.8	0.0376991

References

1. Timoshenko, S.P., and Gere, J.W., Mechanics of materials, Van Nostrand Reinhold, 1972.

Input data

X01D11A.DAT

Example 1.1.2

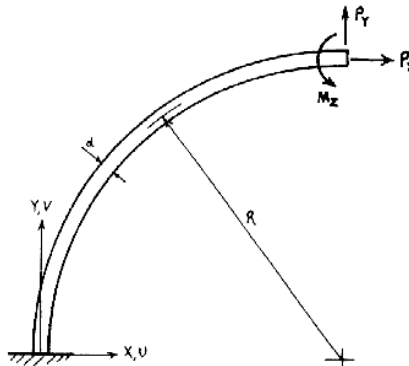
Linear Analysis Of A Curved Cantilever (using 16 Elements)

Keywords

Curved Beam

Problem Description

Determine the tip displacements for a quarter circle cantilever with the dimensions, properties and subject to the loading as given below. Neglect the effect of shear deformations but include the effect of axial deformations, on the displacements.



Discretisation

Model with 16 equal length curved BEAM elements. Use a large shear area to ensure negligible shear deformations.

Geometric properties

Radius, mm	Cross-section breadth (b), mm	Cross-section depth (d), mm
200	10	10

Material properties

Young's modulus	$200 \times 10^3 \text{ N/mm}^2$
-----------------	----------------------------------

Loading

Point load at tip in X direction (P_x), N	Point load at tip in Y direction (P_y), N	Concentrated moment at tip (M_z), Nm
200	200	20

Theory

The following equations for the tip displacements may be derived using the unit load method.

	Point load at tip in X direction, P_x	Point load at tip in Y direction, P_y	Concentrated moment at tip, M_z
u	$\frac{P_x R^3 (3-8)}{4EI} + \frac{P_x R}{4EA}$	$-\frac{P_y R^3}{2EI} + \frac{P_y R}{2EA}$	$-\frac{M_z R^2 (\pi-2)}{2EI}$
v	$-\frac{P_x R^3}{2EI} + \frac{P_x R}{2EA}$	$\pi \left(\frac{P_y R^3}{4EI} + \frac{P_y R}{4EA} \right)$	$\frac{M_z R^2}{EI}$
θ	$-\frac{P_x R^2 (\pi-2)}{2EI}$	$\frac{P_y R^2}{EI}$	$\pi \frac{M_z R}{2EI}$

Comparison

Load	Result source	u	v	θ
Point load at tip in X direction, P_x	LUSAS	3.42298	-4.79707	-0.0274258
	Theory	3.42104	-4.799	-0.0273982
Point load at tip in Y direction, P_y	LUSAS	-4.79707	7.52627	0.0479422
	Theory	-4.799	7.54139	0.048
Concentrated moment at tip, M_z	LUSAS	-2.74258	4.79422	0.0376840
	Theory	-2.73982	4.8	0.0376991

References

2. Timoshenko, S.P., and Gere, J.W., Mechanics of materials, Van Nostrand Reinhold, 1972.

Input data

X01D12A.DAT

Example 1.1.3

Linear Static Stress Analysis Of A Plane Frame Using Beam Elements

Keywords

Plane Frame

Problem Description

To determine the bending moments and shear forces when the plane frame shown in Figure 1 is subjected to the following load cases;

- Three horizontal point loads of 25 kN (Figure 2).
- Three vertical point loads of 50, 60 and 70 kN along with three udl loads of 10, 10 and 20 kN/m (Figure 3).
- A combination of load cases (1) and (2) with a scaling factor of 0.9 and 1.4 respectively (Figure 4).
- A combination of load cases (1) and (2) with a scaling factor of 1.4 (Figure 5).

Finite Element Model

The frame is made up of 11 BEAM elements with the element and nodal numbering detailed in Figure 6.

Geometric properties

Members	Area (m ²)	I (m ⁴)	Shear area (m ²)
1-6,10	0.1	0.00133	0.1
7,8	0.3	0.00399	0.3
9,11	0.2	0.00266	0.2

Material properties

Young's modulus	30×10^6 kN/m ²
Poisson's ratio	0.3

Boundary conditions

The left hand column (node 1) is fully restrained in both translation and rotation while the centre (node 2) and right hand columns (node 3) are only restrained in translation.

Theory

A number of methods exist for the solution of plane frames, e.g. moment distribution and slope deflection methods of analysis, which are described in [1].

Modelling Hints

The four load cases defined above may be specified in the LUSAS data file in the following way:

The horizontal and vertical load conditions (cases 1 and 2) are declared as two separate LOAD CASE's using CONCENTRATED LOAD (CL) and ELEMENT LOADS (ELDS) respectively. A number of combinations of the previously defined separate LOAD CASE's may be analysed by using the LOAD COMBINATION card. In addition the ENVELOPE facility may be used to compute the maximum loads of the combined load cases (i.e. worst conditions). The form in which the commands have been implemented is shown in the input data file listing.

References

1. Steel Designers' Manual (Constrado) Granada publishing 1983.

Input data

X01D13A.DAT

EXAMPLE 1.1.3

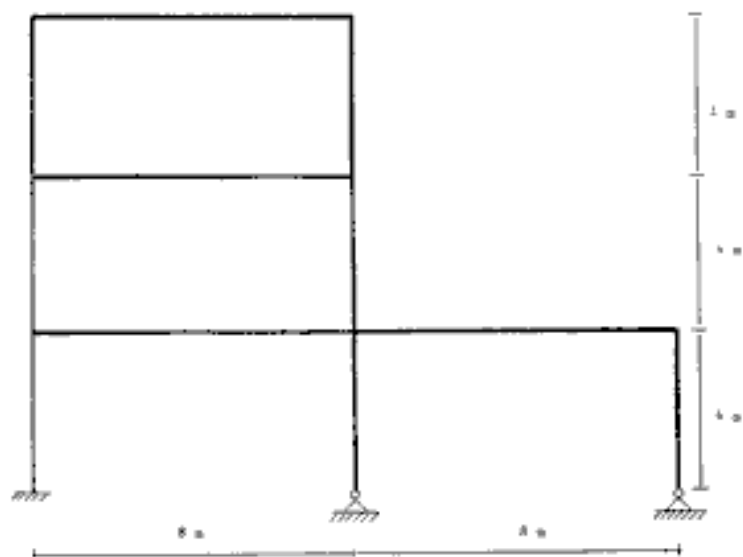
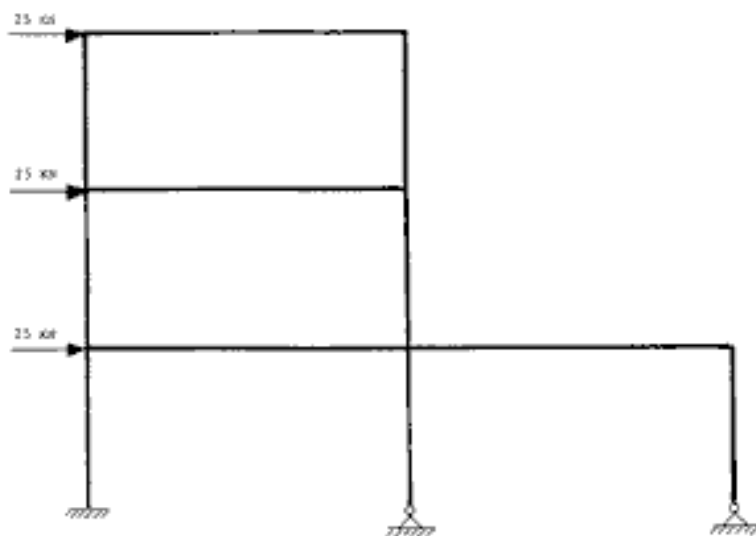


Figure 1. Dimensions of frame



EXAMPLE 1.1.3

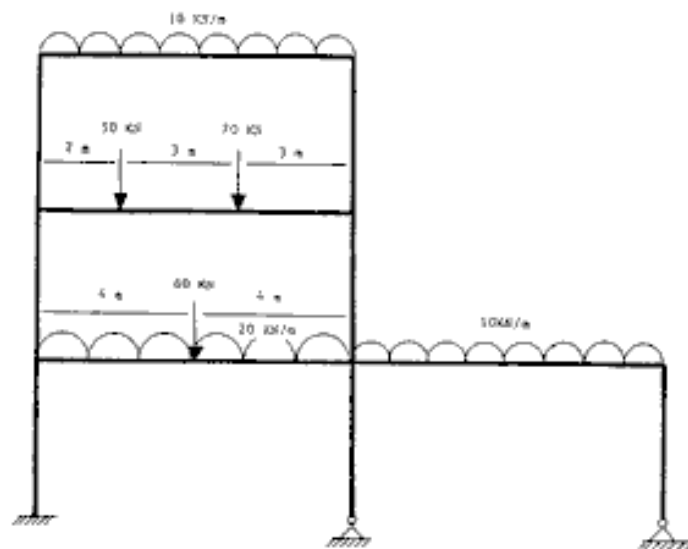


Figure 3. Load Case 2. Vertical loading condition

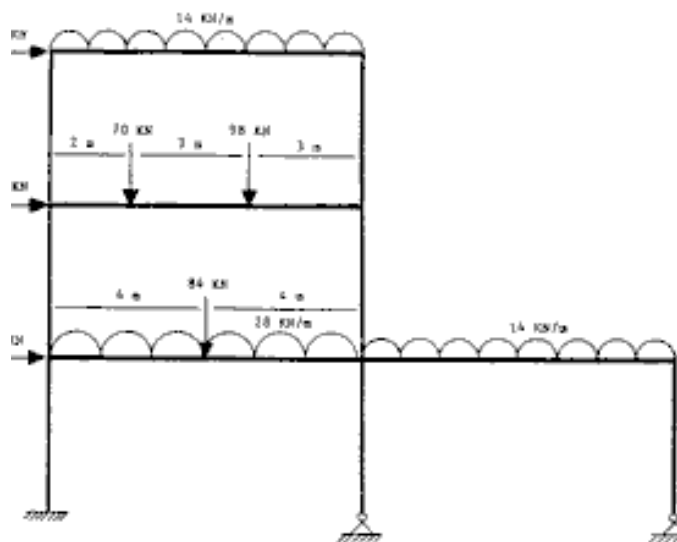


Figure 4. Load Case 3. A combination of Load Cases 1. and 2. with a scaling factor of 0.9 and 1.4 respectively

EXAMPLE 1.1.3

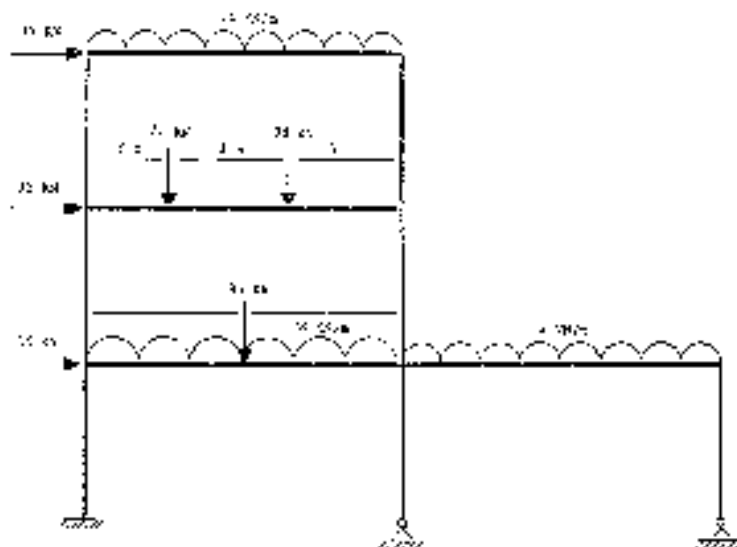


Figure 5. Load Case 4, a combination of Load Cases 1. and 2. with a scaling factor of 1.4

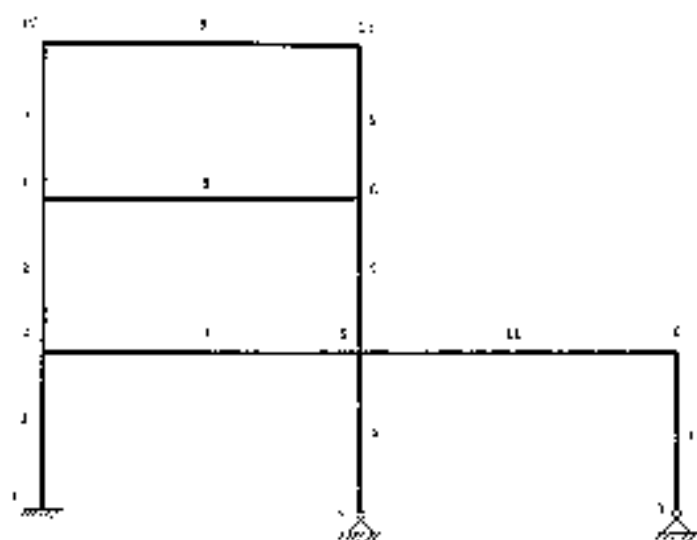


Figure 6. Finite element discretization of the structure

Example 1.1.4

Temperature Dependent Properties Constant Strain Cantilever

Keywords

Constant Strain, Temperature Dependent Properties, Beam 3D

Problem Description

A cantilever of length 10392mm, width 200mm and depth 100mm is subject to a variable temperature loading such that the product of the coefficient of thermal expansion and the temperature rise at any point is constant. Figures 1 and 2 show the geometry of the cantilever.

Discretisation

The cantilever beam is modelled using two meshes, each of three elements. The finite element discretisation is shown in figure 3.

Mesh 1 - three BS4 elements

Mesh 2 - three BSX4 elements

Material properties

The material properties assumed for the analysis are as follows:

Young's modulus = 200000 N/mm²

Poisson's ratio = 0.3

Thermal expansivity (variable) * Temperature

= Constant

= 2.4

Boundary conditions

One end of the beam is fully restrained while the other is free.

Theory

The structure is only restrained to prevent rigid body motions so that stress free, thermal expansion may occur. For load case 1, with constant temperature throughout the section, the strain at any point is constant and is the product of the coefficient of thermal expansion and the temperature at that point:-

$$\text{Strain} = \alpha * T = 2.4 \quad (0.0.1)$$

Where α is the coefficient of thermal expansion and T is the temperature rise.

For load cases 2 and 3, a linear variation is used such that the top and bottom fibre temperature strains are 120 and -120 respectively. Therefore the resulting strain will be pure bending with a value of:

$$\text{Strain} = \frac{(120) - (-120)}{100} = 2.4 \quad (0.0.2)$$

Comparison

A constant strain condition (of 2.4) is achieved for all the cases analysed.

References

1. Roark.R, Young.W 'Formulae for stress and strain: Fifth Edition', McGraw-Hill Publishing Company (1975).

Input Data

X01D14A.DAT

X01D14B.DAT

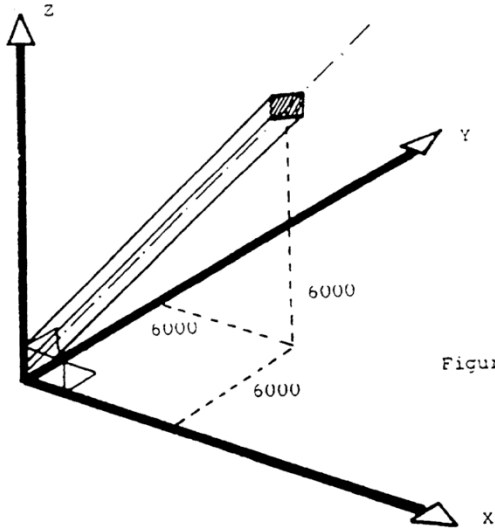


Figure 1.

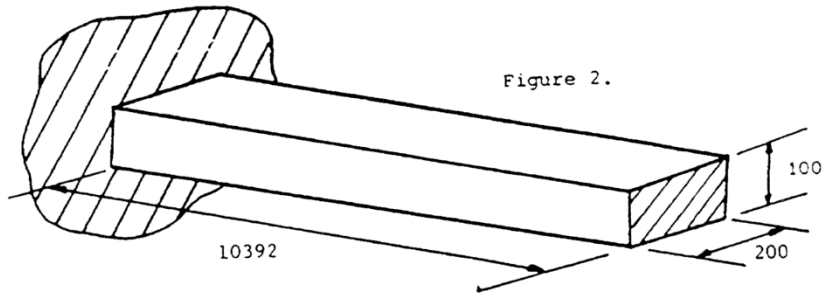


Figure 2.

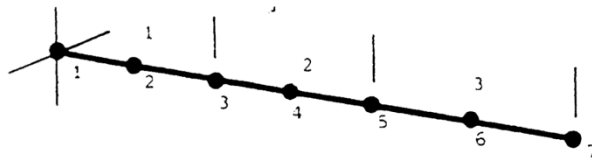


Figure 3.

Example 1.2.1

Linear Elastic Static Fracture Analysis Of A Three-Point Bend Specimen

Keywords

Fracture, Stress Intensity

Problem Description

In the specialised field of fracture mechanics a number of small scale tests are used extensively in determining the quality of a material. One such test is the three-point bend specimen. A typical arrangement is shown in Figure 1.

The test specimen is supported at positions A and B while a CONCENTRATED LOAD is applied at point C. The stress intensity factor may then be evaluated for the initial crack length a_0 .

Discretisation

As the test piece and loading conditions are symmetric, only half the specimen need be analysed. The finite element discretisation is shown in Figure 2, consisting of 126 eight-noded plane strain membrane elements (QPN8) and two crack tip elements (QNK8).

Material properties

Young's modulus, E	214x10 ⁶ Pa
Poisson's ratio, ν	0.3

Loading condition

A concentrated load (P) of 2000 N applied at position C.

Theory

$$\text{Griffith's criterion} \quad G = \frac{1}{t} \frac{\partial U}{\partial a} \quad (0.0.3)$$

Irwin's relation:
$$K_I^2 = \frac{GE}{(1-\nu^2)} \quad (0.0.4)$$

where

- a Crack length
- E Young's modulus
- G Energy release rate
- K_I Stress intensity factor (mode I)
- t Thickness
- U Strain energy
- ν Poisson's ratio

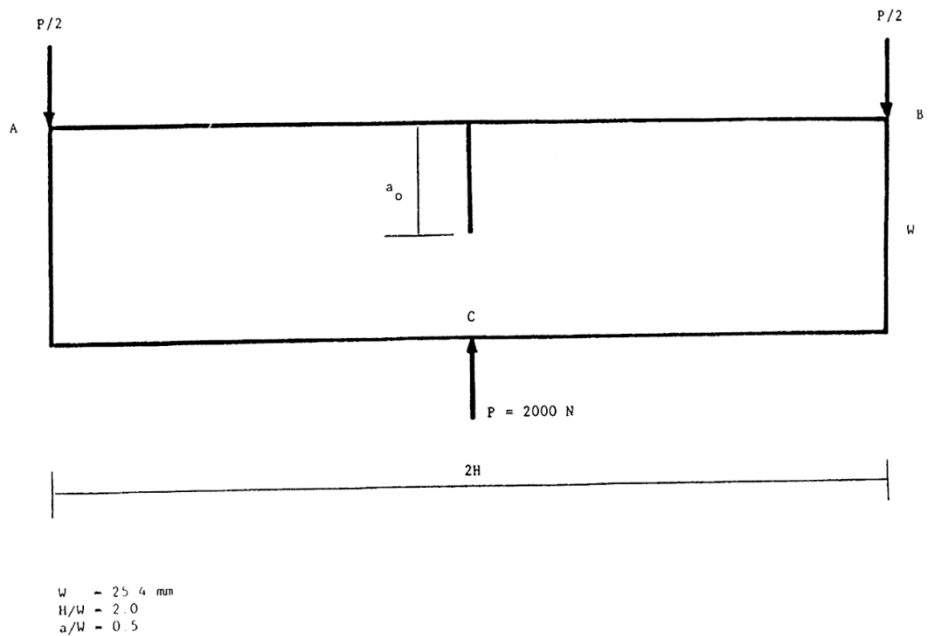


Figure 1. Three-point bend specimen.

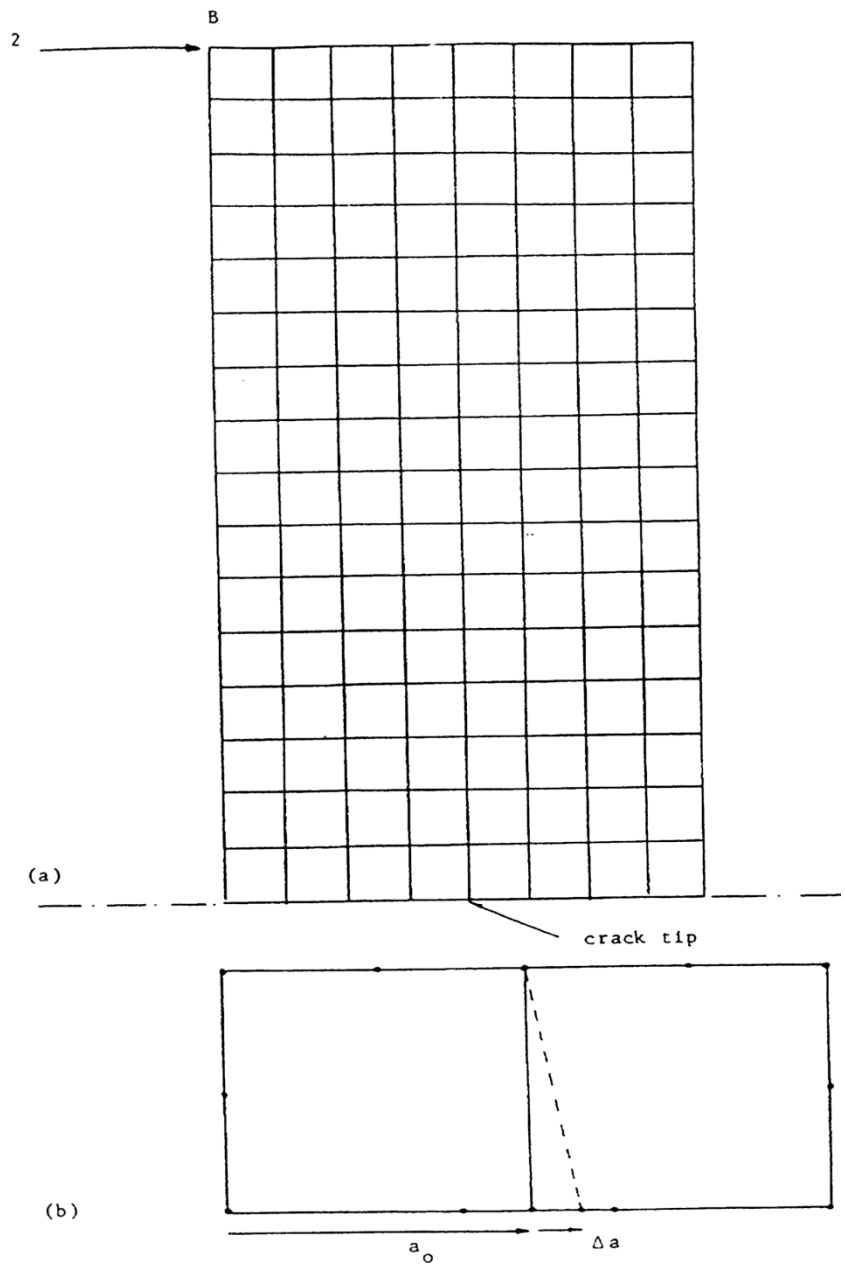


Figure 2. (a) Mesh discretisation (b) Effective crack extension.

Modelling Hints

In this example the load is applied at position A in the form of a reaction $P/2$. There exist a number of methods for determining the value of the stress intensity factor, the method adopted here is the energy balance approach.

The user conducts a linear elastic static analysis with an initial crack length a_0 . A second analysis may then be done after repositioning the crack tip to give a new crack length, $a_0 + a$. The change in energy may then be used to compute the value of K_I .

Solution Comparison

(1) Crack length a_0

Displacement at the point of application of the reaction

$$u_B = 0.513712 \text{ mm}$$

Strain energy

$$U_1 = P/2 * u_B = 0.513712 \text{ Nm}$$

(2) Crack length $a_0 + a$

Displacement at the point of application of the reaction

$$u_B = 0.553229 \text{ mm}$$

Strain energy

$$U_2 = P/2 * u_B = 0.553229 \text{ Nm}$$

Energy release rate

$$G = (0.553229 - 0.513712)/0.0005 = 79.036 \text{ Nm/m}^2$$

As symmetry has been considered this value of G must be multiplied by a factor of 2. Therefore:

$$G = 158.072 \text{ Nm/m}^2$$

This value of G , the energy release rate, may now be inserted into Irwin's relation (0.0.4) to give the stress intensity factor:

$$K_I^2 = 158.072 * 214 * 10^9 / 0.91 = 3.717 * 10^{13}$$

$$K_I = 6.097 \text{ MN/m}^{3/2}$$

An alternative method to the energy balance approach is the displacement extrapolation technique [1]. The analytical expressions for the displacement variations along radial lines emanating from the crack tip, in terms of the stress intensity factor are as follows:

$$KI [(2k-1)\cos\theta/2 - \cos3\theta/2] = 4\mu(2\Pi/r)1/2 \quad (u)$$

$$KI [(2k+1)\sin\theta/2 - \sin3\theta/2] = 4\mu(2\Pi/r)1/2 \quad (v)$$

where:

u	x displacement component
v	y displacement component
r	radial distance from nodal point to crack tip.
	shear modulus
k	$3-4\nu$ for plane strain
θ	angle between radial path chosen and the crack path ahead of the crack tip.

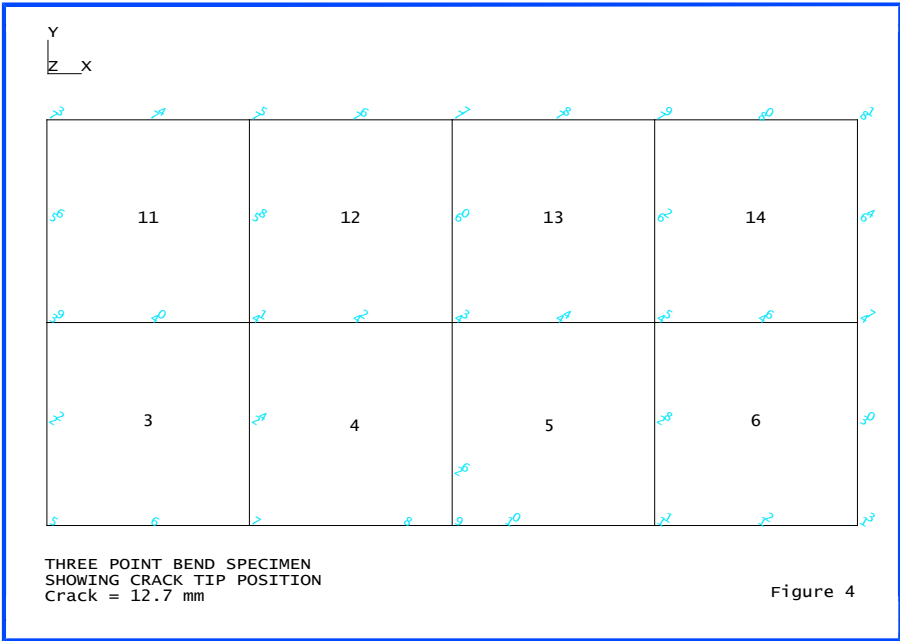
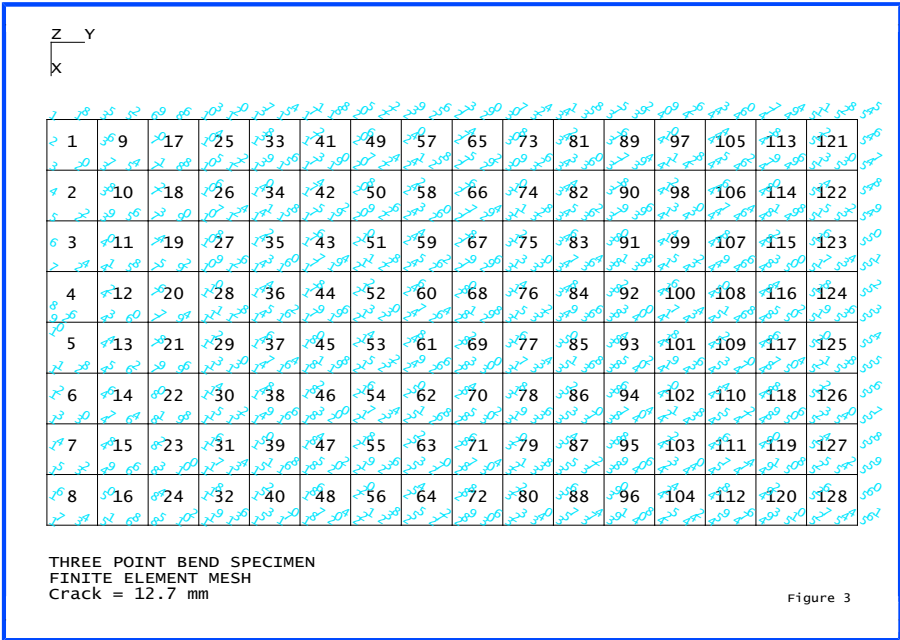
If we assume $\theta = 90$, then we are considering the radial path of nodes vertically from the crack tip i.e. nodes 9 to 553 (Figure 3). In this particular instant we shall only consider nodes 26, 43, 77, 11, 145, 179, 213, 247, 281, 315, 349, 383, 417, 451, 485, 519, and 553. The corresponding nodal displacements in the x-direction have been substituted into the above equation and the values of K computed. The results have been plotted and are shown in Figure 7. By discarding points close to the crack tip the solutions can be extrapolated to $r=0[1]$. In this case the result is approximately that obtained by the energy balance method.

References

1. Owen, D.R.J and Fawkes, A.J. Engineering Fracture Mechanics Numerical Methods and Applications. Pineridge Press Ltd. 1983. p43

Input Data

X01D21A.DAT



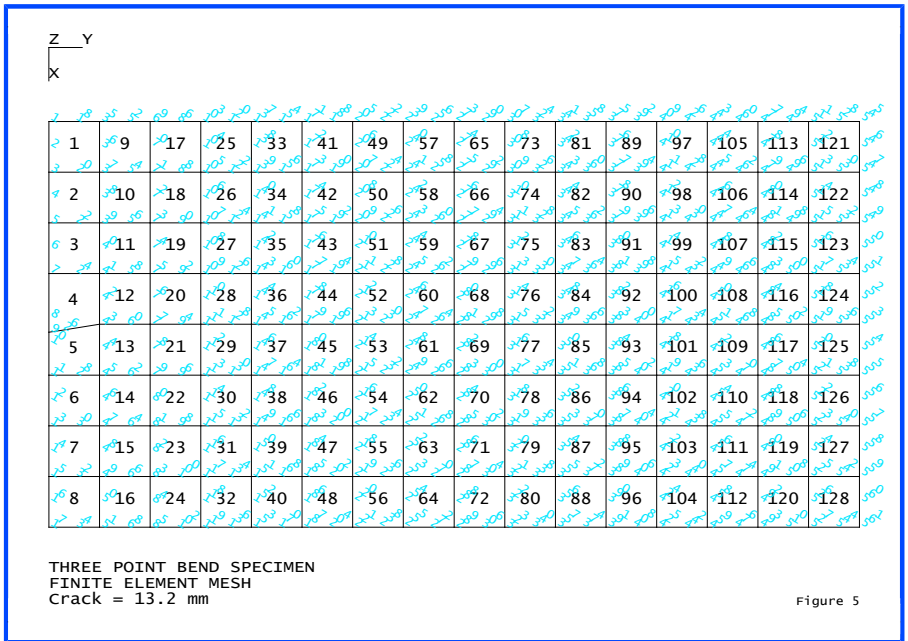


Figure 5

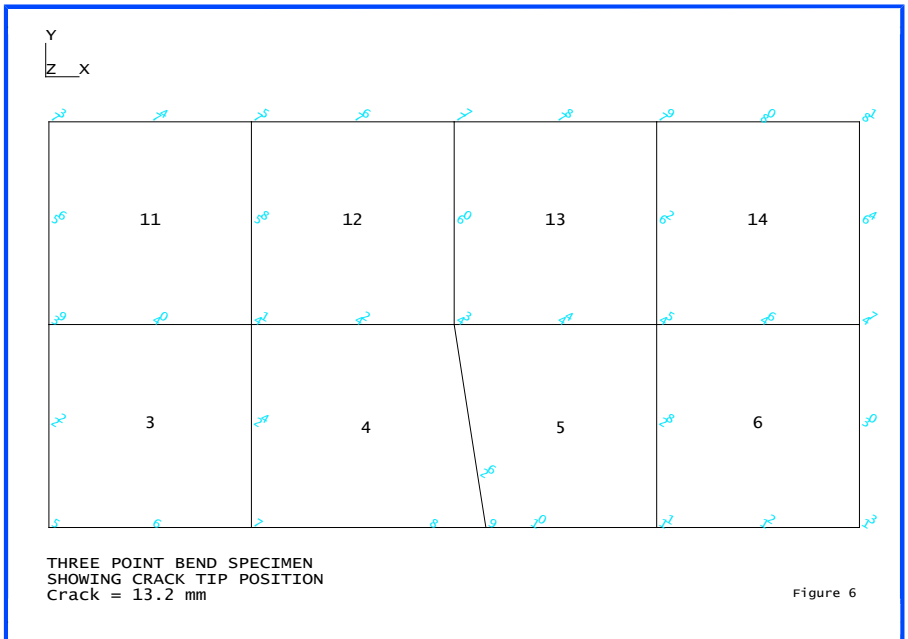
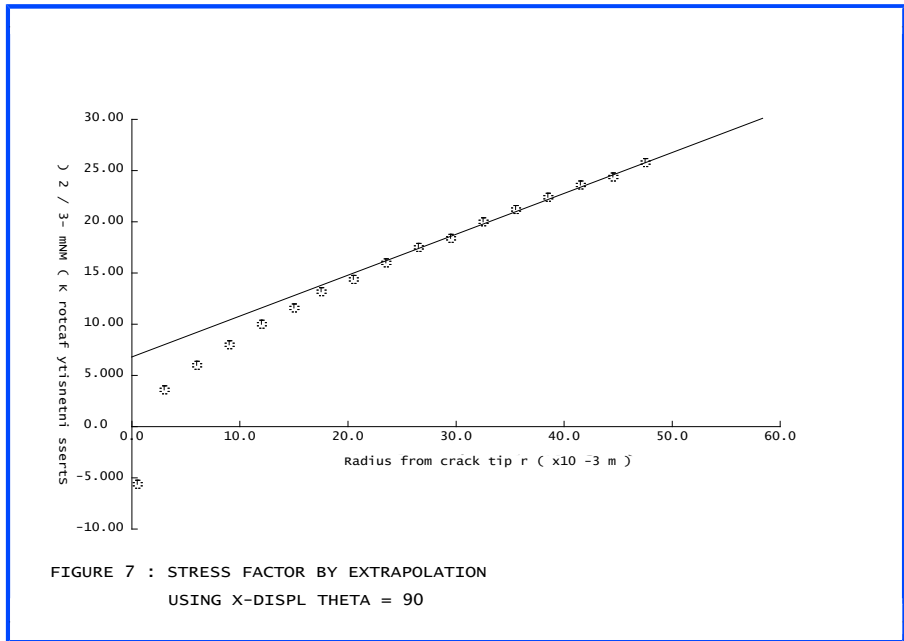


Figure 6



Example 1.2.3

Connecting Incompatible Models Using Constraint Equations

Keywords

Incompatible Models, Curvilinear Coordinates, Shape Functions

Problem Description

A study of the localised stresses at the root and tip of a cantilever beam, details of which are shown in Figure 1, is to be carried out. To save on computer resources, the central portion of the cantilever is to be modelled with a coarse mesh while finer meshes are to be used at the tip and the root. Derive the constraint equations relating the nodal variables at the interfaces between the fine meshes at the root and tip and the coarse mesh of the central portion. Analyse the cantilever when subject to a shear load of 135 MN at the tip. Compare the results for the tip displacements and the stress distributions for each Cartesian stress component with the results obtained using a fine mesh over the whole cantilever.

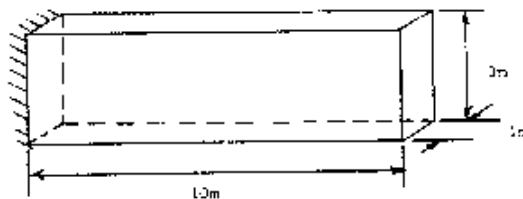


Figure 1 - Problem geometry and material properties

Discretisation

As the problem is essentially two dimensional, a finite element model using plane membrane elements is appropriate. The higher order, 8-noded plane membrane element, QPM8, is used and the mesh adopted for the analysis is shown in Figure 2. The full, fine mesh used for comparison purposes is shown in Figure 3.

Material properties

Young's modulus	200.0×10^9 Pa
-----------------	------------------------

Poisson's ratio	0.3
-----------------	-----

Theory

The variables at nodes 22, 39, 73, 90, 30, 47, 81 and 98 are required to be constrained to the edges of element 8, see Figure 1c. The displacement variation at any point in element 8 is given by:

$$u = \sum_{i=1}^m N_i u_i \quad (0.0.5)$$

where u is the displacement vector at any point, N_i are the shape or interpolation functions for nodal point i , u the displacement vector for nodal point i and m the total number of nodes for the element.

Using the plane membrane finite element QPM8, with $m = 8$, the interpolation functions are given by:

For corner nodes:-

$$N_i = \frac{1}{4}(1 + \xi_0)(1 + \eta_0)(\xi_0 + \eta_0 - 1) \quad (0.0.6)$$

For midside nodes:-

$$\text{when } \xi_i = 0, \quad N_i = \frac{1}{2}(1 - \xi^2)(1 + \eta_0) \quad (0.0.7)$$

$$\text{when } \eta_i = 0, \quad N_i = \frac{1}{2}(1 - \eta^2)(1 + \xi_0) \quad (0.0.8)$$

$$\xi_0 = \xi \xi_i, \quad \eta_0 = \eta \eta_i \quad (0.0.9)$$

The ξ, η curvilinear co-ordinate system for an 8-noded element is shown in Figure 4b. Comparing this with element 8, see Figure 4a, enables the co-ordinates of nodes 22, 39, 73, 90, 30, 47, 81 and 98 in the curvilinear co-ordinate system of element 8 to be determined. These are given in columns 2 and 3 of Table 1.

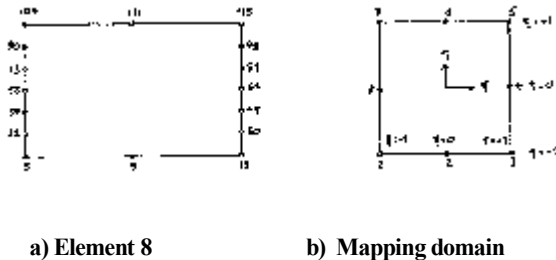


Figure 4

The required constraint equations are of the form:

$$u^8(\xi, \eta) = u_n \quad (0.0.10)$$

where the superscript 8 refers to element 8, the subscript n refers to the node (22, 39, 73, 90, 30, 47, 81 or 98) and ξ, η are the curvilinear co-ordinates of node η with respect to element 8. Using (0.0.5), equations (0.0.6) to (0.0.9) may be written as:

$$\sum_{i=1}^8 N_i u_i^8 - u_n = 0 \quad (0.0.11)$$

Substituting the ξ, η co-ordinates of each node in turn into equations (0.0.6)-(0.0.9) yields the N_i values, which are tabulated in cols 4 - 11 in Table 1.

Table 1: Interface node curvilinear co-ordinates and shape functions

Node	ξ	η	N_1	N_2	N_3	N_4	N_5	N_6	N_7	N_8
22	-1	-2/3	+5/9	0	0	0	0	0	-1/9	+5/9
39	-1	-1/3	+2/9	0	0	0	0	0	-1/9	+8/9
73	-1	+1/3	-1/9	0	0	0	0	0	+2/9	+8/9
90	-1	+2/3	-1/9	0	0	0	0	0	+5/9	+5/9
30	+1	-2/3	0	0	+5/9	+5/9	-1/9	0	0	0
47	+1	-1/3	0	0	+2/9	+8/9	-1/9	0	0	0
81	+1	+1/3	0	0	-1/9	+8/9	+2/9	0	0	0
98	+1	+2/3	0	0	-1/9	+5/9	+5/9	0	0	0

The displacement vector at any point for the plane membrane family of elements is given by:

$$\mathbf{u} = \begin{Bmatrix} U \\ V \end{Bmatrix} \quad (0.0.12)$$

where U and V are the displacement components in the global X and Y directions respectively. Using a subscript to denote the node number and noting the correspondence between the node numbering of the mapping domain, Figure 4b, and element 8, Figure 4a, the constraint conditions of (0.0.11) may be written explicitly as:

$$\begin{aligned}
 \frac{5}{9}U_5 - \frac{1}{9}U_{107} + \frac{5}{9}U_{56} - U_{22} &= 0 \\
 \frac{5}{9}V_5 - \frac{1}{9}V_{107} + \frac{5}{9}V_{56} - V_{22} &= 0 \\
 \frac{2}{9}U_5 - \frac{1}{9}U_{107} + \frac{8}{9}U_{56} - U_{39} &= 0 \\
 \frac{5}{9}V_5 - \frac{1}{9}V_{107} + \frac{8}{9}V_{56} - V_{39} &= 0 \\
 -\frac{1}{9}U_5 + \frac{2}{9}U_{107} + \frac{8}{9}U_{56} - U_{73} &= 0 \\
 -\frac{1}{9}V_5 + \frac{2}{9}V_{107} + \frac{8}{9}V_{56} - V_{73} &= 0 \\
 -\frac{1}{9}U_5 + \frac{5}{9}U_{107} + \frac{5}{9}U_{56} - U_{90} &= 0 \\
 -\frac{1}{9}V_5 + \frac{5}{9}V_{107} + \frac{5}{9}V_{56} - V_{90} &= 0 \\
 \frac{5}{9}U_{13} + \frac{5}{9}U_{64} - \frac{1}{9}U_{115} - U_{30} &= 0 \\
 \frac{5}{9}V_{13} + \frac{5}{9}V_{64} - \frac{1}{9}V_{115} - V_{30} &= 0 \\
 \frac{2}{9}U_{13} + \frac{8}{9}U_{64} - \frac{1}{9}U_{115} - U_{47} &= 0 \\
 \frac{2}{9}V_{13} + \frac{8}{9}V_{64} - \frac{1}{9}V_{115} - V_{47} &= 0 \\
 -\frac{1}{9}U_{13} + \frac{8}{9}U_{64} + \frac{2}{9}U_{115} - U_{81} &= 0 \\
 -\frac{1}{9}V_{13} + \frac{8}{9}V_{64} + \frac{2}{9}V_{115} - V_{81} &= 0 \\
 -\frac{1}{9}U_{13} + \frac{5}{9}U_{64} + \frac{5}{9}U_{115} - U_{98} &= 0 \\
 -\frac{1}{9}V_{13} + \frac{5}{9}V_{64} + \frac{5}{9}V_{115} - V_{98} &= 0
 \end{aligned} \tag{0.0.13}$$

Equations (0.0.13) are now in the form required for input to LUSAS.

Comparison

1. Tip displacements at node 17.

	Fine mesh	Coarse mesh with Constraint Equations
u	0.0228175	0.0228031
v	-0.107897	-0.107364

2. Stress distributions.

Figures 5 to 10 show the stress distributions as plotted with MYSTRO.

Note

The displacement field for the structure is relatively unaffected by the use of a single element to model the central half of the cantilever. Stress distributions at the tip and the root are also relatively unaffected by the use of a single element to model the central half of the cantilever.

Input data

X01D23A.DAT

X01D23B.DAT

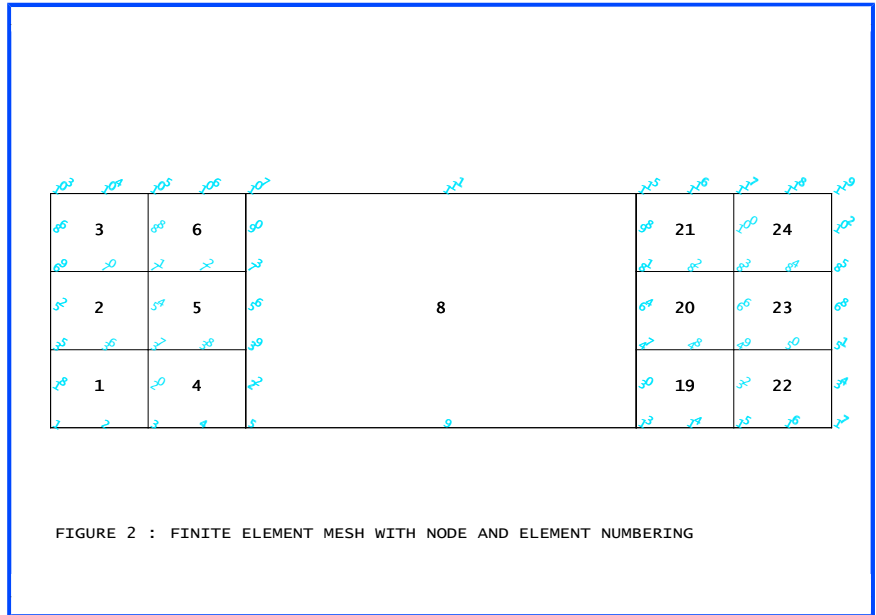
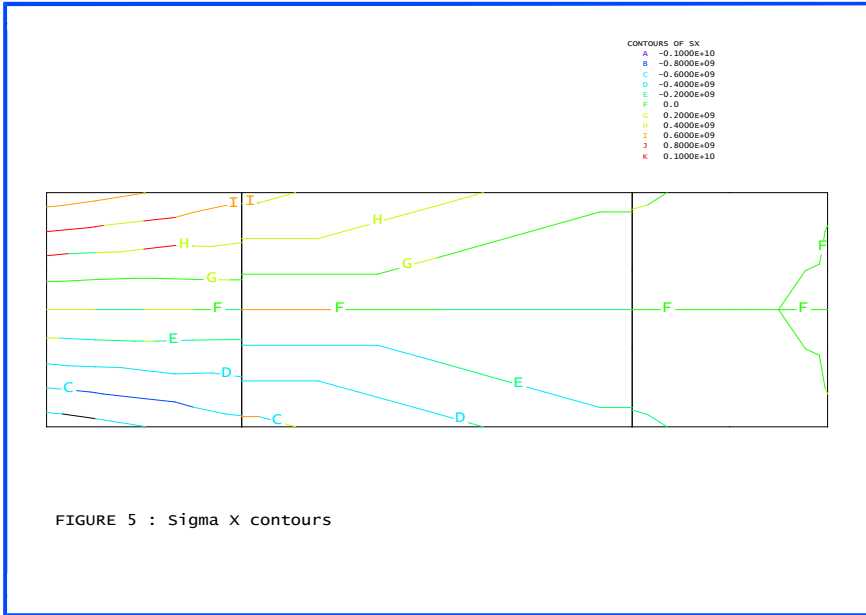
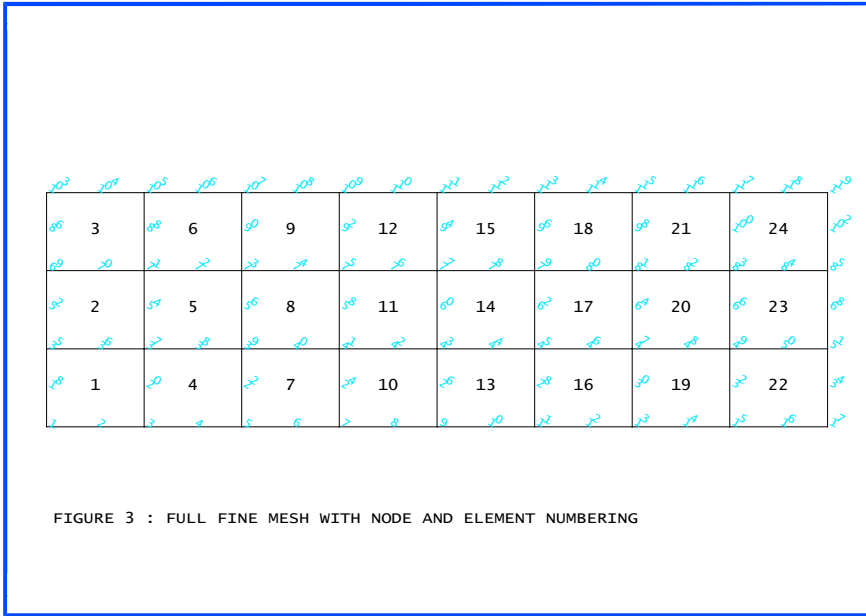


FIGURE 2 : FINITE ELEMENT MESH WITH NODE AND ELEMENT NUMBERING



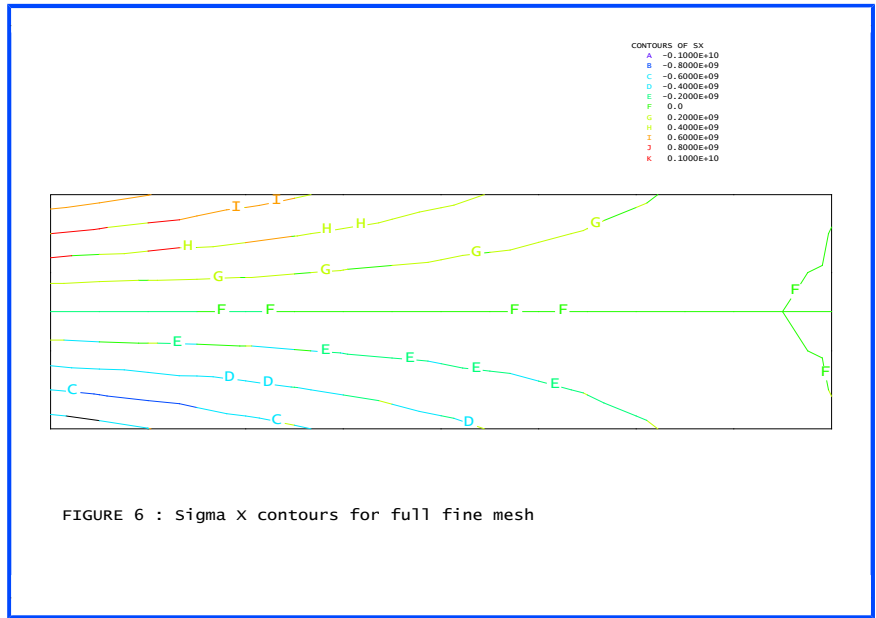


FIGURE 6 : Sigma X contours for full fine mesh

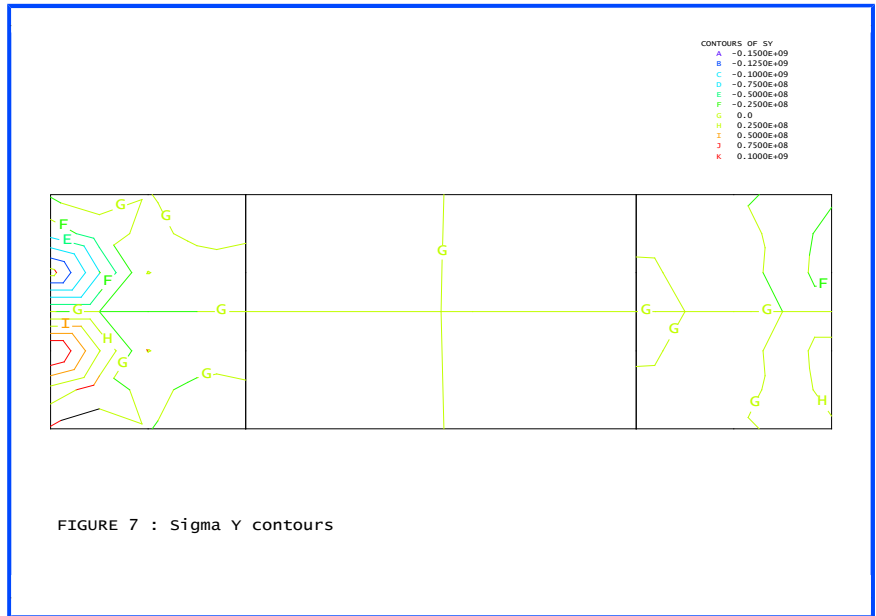
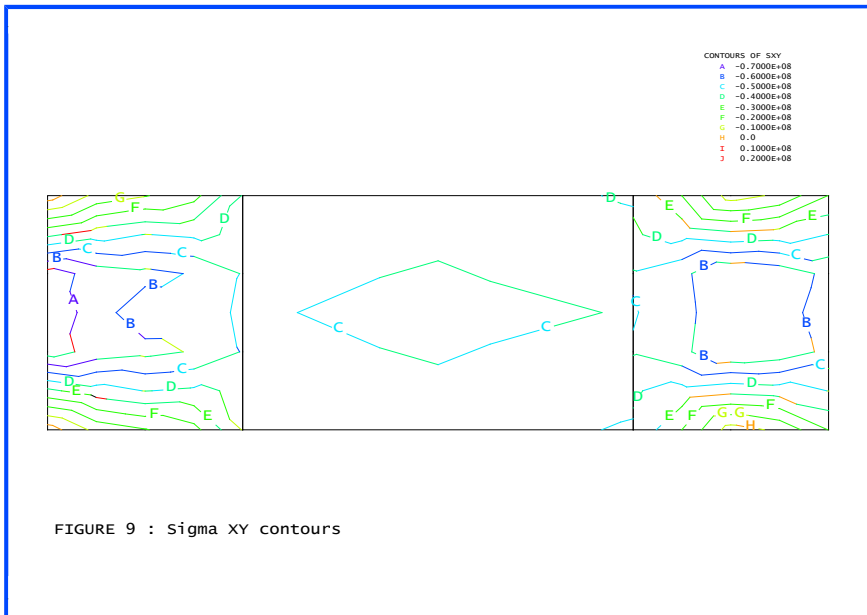
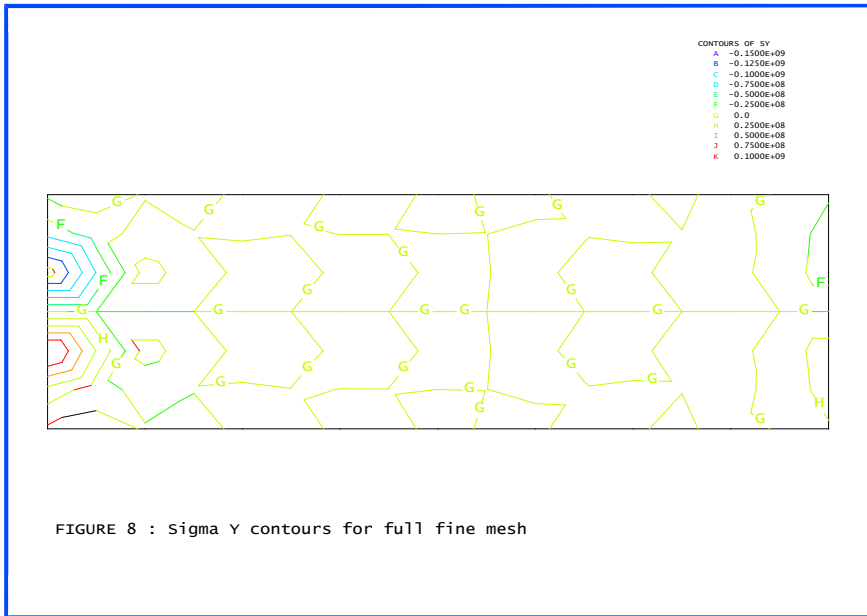
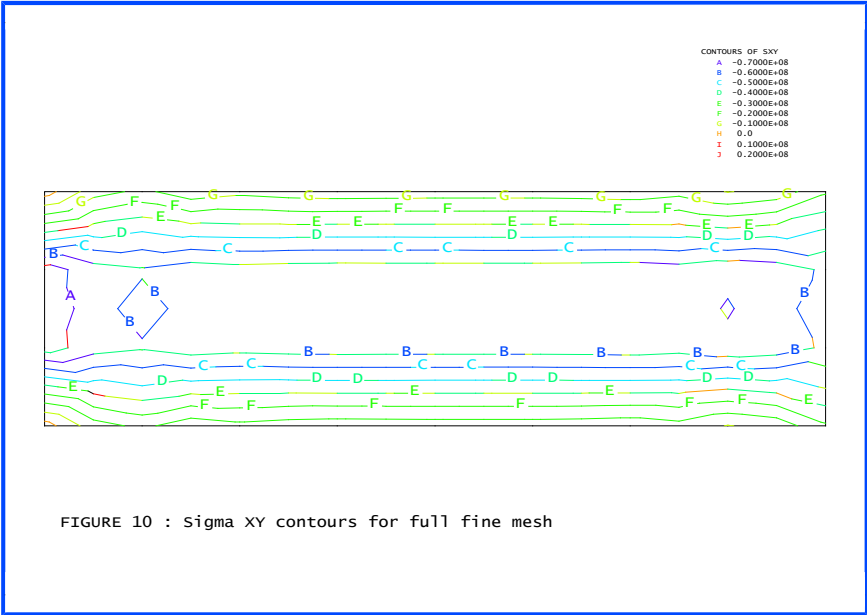


FIGURE 7 : Sigma Y contours





Example 1.2.4

Plane Membrane Analysis - Perforated Sheet Under Pure Tension

Keywords

Plane Stress, Stress Concentration Factor

Problem Description

A thin rectangular sheet with a central perforation is subjected to a tensile loading. The objective is to investigate the longitudinal stress distribution and to evaluate the stress intensity factor.

The geometry of the structure is as follows:

Length, l	240 mm
Width, w	180 mm
Thickness, t	5 mm
Radius of central opening, r	30 m

Discretisation

One quarter of the structure is discretised using 27 isoparametric plane stress elements (QPM8). The mesh is graded towards the central opening in order gain a better approximation to the stress concentration expected in this region of the structure. The internal boundaries of the mesh are restrained according to the double symmetry conditions assumed. The external boundaries of the mesh are unrestrained.

The uniform tensile load is modelled by the application of a series of nodal point loads acting in the Y direction along the bottom edge of the structure (note that in order to obtain a uniform distribution the nodal point loads are applied in the ratio 1:4:1 to the first corner, midside and second corner nodes of the element face respectively). The total load applied to the bottom edge of the structure is 36,000N.

Material properties

The material properties assumed in the analysis are as follows:

Young's modulus	$207 \times 10^3 \text{ N/mm}^2$
Poisson's ratio	0.3

Theory

The uniform stress distribution in the absence of the central opening may be calculated from elastic theory.

Total applied load	$F = 36,000 \text{ N}$
Total section area	$A_y = 5\text{mm} * 180\text{mm} = 900\text{mm}^2$
Stress	$S_y = F/A = (36,000/900) = 40 \text{ N/mm}^2 \quad (0.0.14)$

The presence of the central opening will change this uniform stress distribution to form a concentration of tensile stress in the proximity of the opening [1]. From Saint-Venant's principle it may be concluded that at distances which are large compared to the dimensions of the opening its effect on the stress distribution will be negligible. The expected distribution of longitudinal stress is therefore in the form of a decay from high tensile stresses at the opening towards the normal stress level at the edge of the plate. The concentration factor may be obtained from the mean stress (equation (0.0.14)) and the computed stress (at the opening) as

$$\text{stress concentration factor} = \text{computed stress} / \text{mean stress}$$

Comparison

The LUSAS results for the stress in the Y direction are given below. ((*) denotes the stress value is the average from the contributing nodes):

Node	LUSAS
13	143.431
26	111.922
39(*)	81.6375
52	69.7183
65(*)	57.2874
78	51.7408
91(*)	46.0919
104	38.1439
117	29.5542

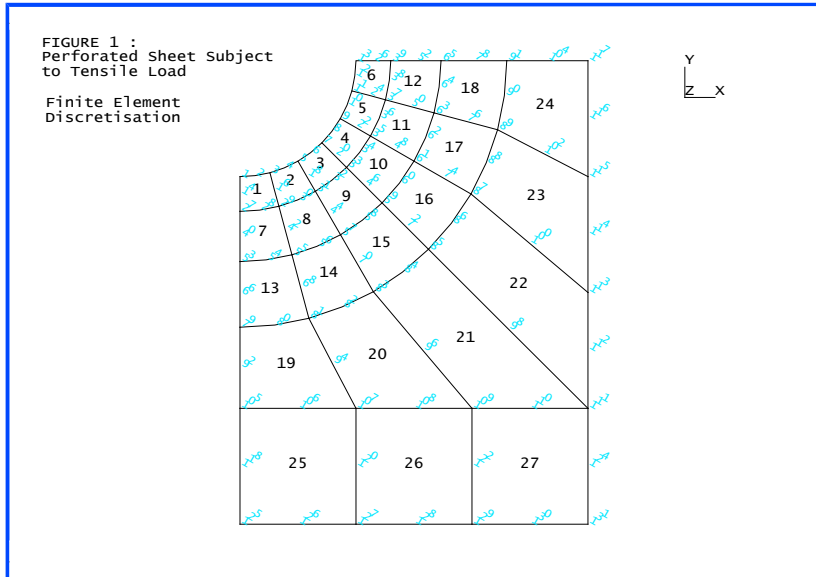
$$\text{Stress concentration factor} = 143.4/40.0 = 3.585$$

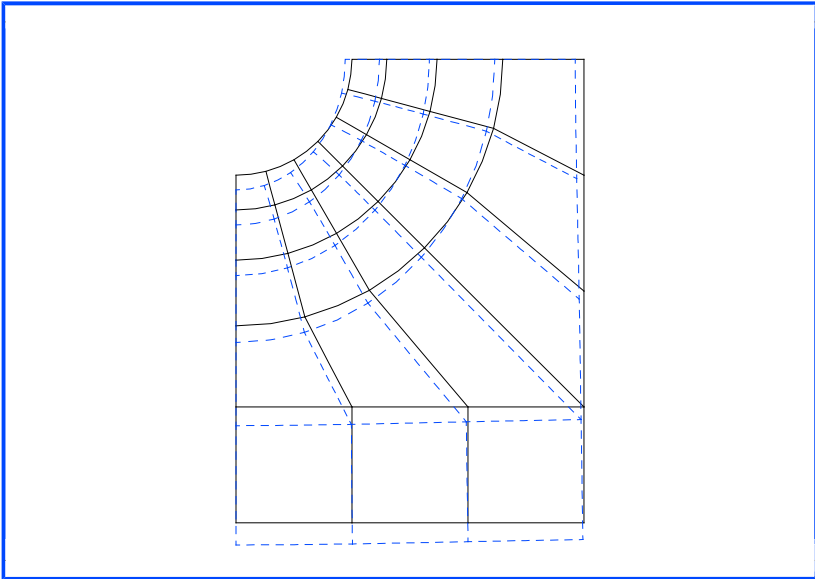
References

1. 'Theory of Elasticity', Second edition, S.Timoshenko, J.N.Goodier, Publisher. McGraw-Hill Book Co.Ltd. (1951)

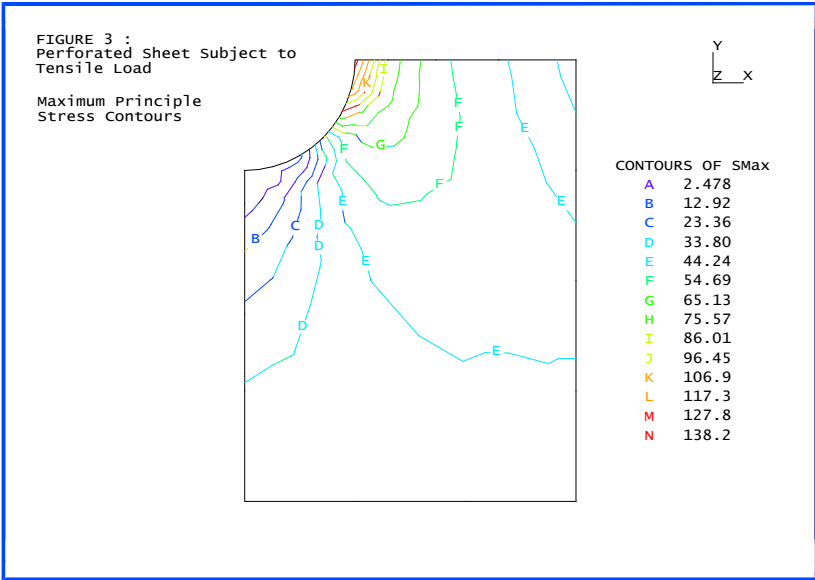
Input data

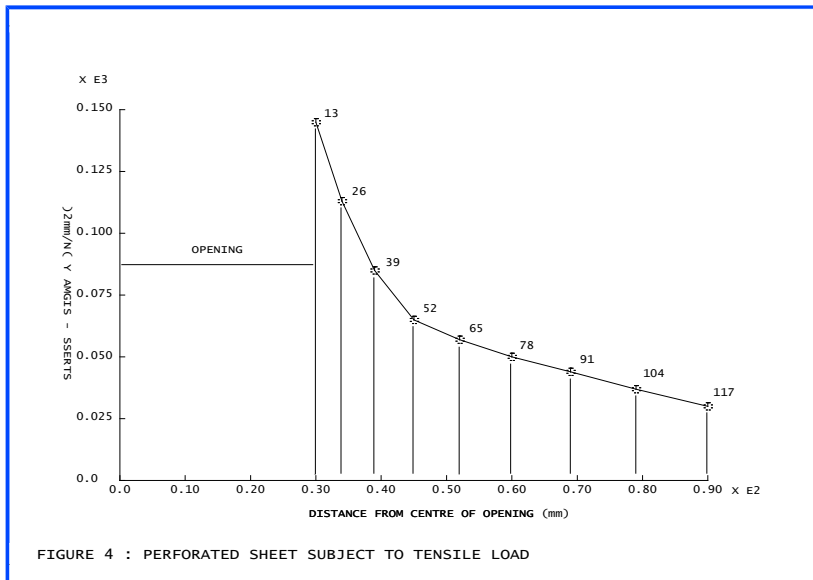
X01D24A.DAT





Perforated Sheet Subject to Tensile Load (Plane Membrane) Deformed Configuration





Example 1.3.1

Orthotropic Plate Under Pressure Load

Keywords

Plate, Orthotropic, Anisotropic

Problem Description

A simply supported square plate is analysed to verify the plate behaviour when the material is anisotropic and the plate is subjected to a uniform pressure load.

Finite Element Model

Allowing for symmetry only one quarter of the plate need be analysed. The model consists of a 4*4 element mesh with 8-noded elements.

The problem is solved using both data cards, MATERIAL PROPERTIES, ORTHOTROPIC and ANISOTROPIC.

Geometric Properties

Thickness	0.015 m
Length	0.3 m

Material properties

Anisotropic		Orthotropic		Isotropic	
E_{xx}	$1.38 \times 10^{10} \text{ N/m}^2$	E_x	$1.3555 \times 10^{10} \text{ N/m}^2$	E	$2.0 \times 10^{11} \text{ N/m}^2$
E_{xy}	$5.31 \times 10^8 \text{ N/m}^2$	E_y	$1.1290 \times 10^9 \text{ N/m}^2$	ν	0.3
E_{yy}	$1.15 \times 10^9 \text{ N/m}^2$	ν_{xy}	0.4619		
G_{xy}	$1.17 \times 10^9 \text{ N/m}^2$	ν_{yx}	0.03848		
		G_{xy}	$1.1700 \times 10^9 \text{ N/m}^2$		

Boundary Conditions

Simply supported around the plate edges.

Loading Conditions

A uniformly distributed pressure load $p = 1000 \text{ N/m}^2$

Theory

The expression for the deflection w in the z -direction takes the following form;

$$w = \sum_{m=1,3,5\dots} \sum_{n=1,3,5\dots} a_{mn} \sin\left(\frac{\pi mx}{a}\right) \sin\left(\frac{\pi ny}{b}\right) \quad (0.0.15)$$

where the coefficient a_{mn} and a full description of the theory is given in [1].

Solution Comparison

The solutions obtained from the LUSAS orthotropic and anisotropic analysis are presented below, and are shown in the following figures. A principal stress plot for the isotropic case is included for comparison.

Vertical Deflection w (m)

Location	Theory	LUSAS (Anisotropic)	LUSAS (Orthotropic)
C	3.543E-04	3.545E-04	3.545E-04
E	2.529E-04	2.531E-04	2.531E-04
F	1.925E-04	1.939E-04	1.937E-04

Bending Moments (Nm/m)

Location	Theory	LUSAS (Anisotropic)	LUSAS (Orthotropic)
C	$M_X=37.49$	$M_X=38.21$	$M_X=38.21$
	$M_Y=3.685$	$M_Y=3.710$	$M_Y=3.710$
E	$M_X=28.44$	$M_X=29.27$	$M_X=29.27$
	$M_Y=2.680$	$M_Y=2.690$	$M_Y=2.690$

References

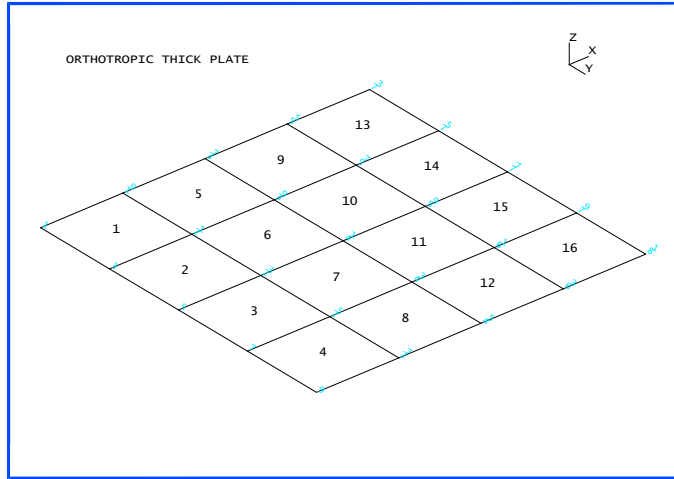
1. Timoshenko, S.P. and Woinowsky-Krieger, S., 'Theory of Plates and Shells, Second Edition, McGraw-Hill, 1959.

Input data

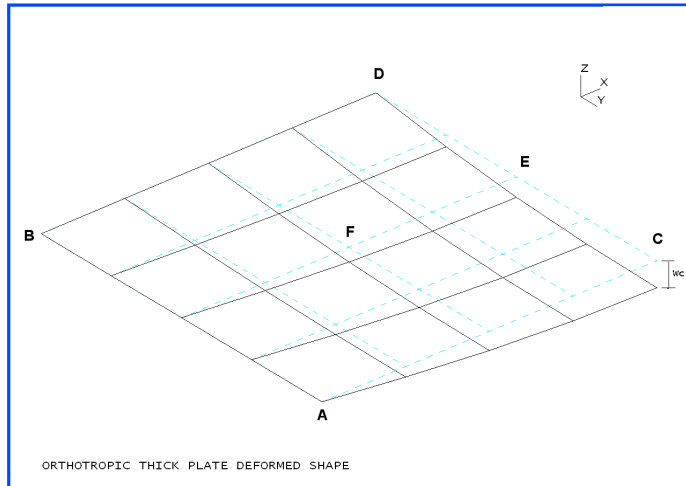
X01D31A.DAT

X01D31B.DAT

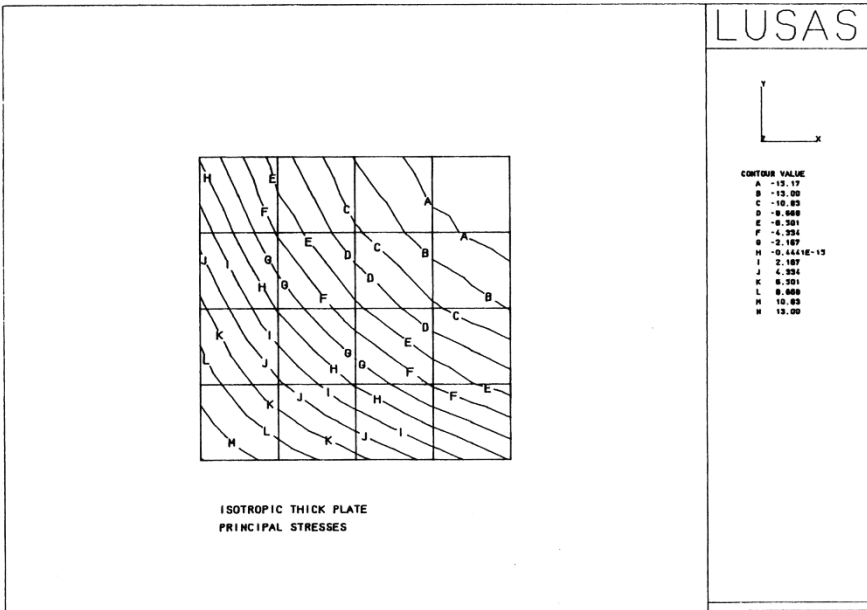
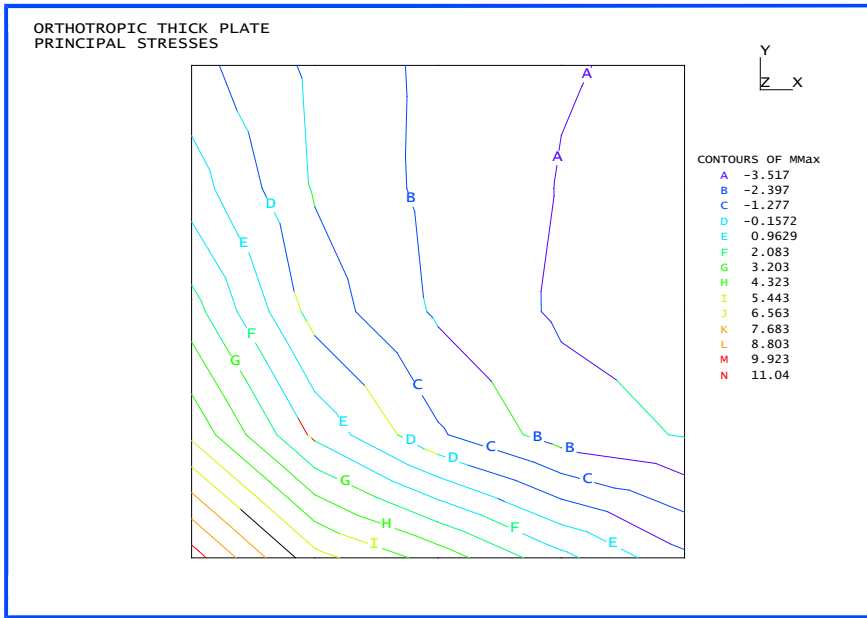
X01D31C.DAT



Quarter model of simply supported square plate



Vertical deflection under loading



Example 1.3.2

Static Linear Analysis Of A Thick Circular Plate

Keywords

Plate, Linear

Problem Description

A clamped circular plate is subjected to a transverse uniformly distributed load. The dimensions of the plate are as follows:

Radius, a	0.5 inches
Thickness, h	0.1 inches

Discretisation

The structure is idealised using the thick plate flexure elements QTF8 and TTF6. By using the CARTESIAN SETS and TRANSFORMED FREEDOM facilities it is only necessary to idealise a small segment of the total structure. In this example a 30 degree segment is analysed. The outer boundaries of the circular plate are assumed to be fully restrained.

The material properties are as follows

Young's modulus	10.92 lb/in ²
Poisson's ratio	0.3

Theory

The linear elastic thick plate solution may be obtained by combining the 'thin' plate solution with a correction for out of plane transverse shearing effects.

The thin plate solution is obtained by the solution of the biharmonic plate equation [1]

$$r \frac{d}{dr} \left(\frac{1}{r} \frac{d}{dr} \left(r \frac{dw}{dr} \right) \right) = \frac{1}{D} \int_0^r q r dr \quad (0.0.16)$$

Differentiating with respect to r and dividing by r yields

$$\frac{1}{r} \frac{d}{dr} \left(r \frac{d}{dr} \left(\frac{1}{r} \frac{d}{dr} \left(r \frac{dw}{dr} \right) \right) \right) = \frac{q}{D} \quad (0.0.17)$$

where

$$D = \frac{Eh^3}{12(1-\nu^2)} \quad (0.0.18)$$

Triple integration of (0.0.17) enables the deflection profile $w = f(r)$ to be obtained as:

$$w = \frac{qr^4}{64D} + \frac{Ar^2}{4} + B \log \frac{r}{a} + C \quad (0.0.19)$$

where A, B and C are the constants of integration. By applying the deflection and slope conditions associated with the clamped periphery of the plate, (0.0.19) may be simplified as:

$$w = \frac{q}{64D} (a^2 - r^2)^2 \quad (0.0.20)$$

The maximum displacement occurs at the centre of the plate ($r=0$) and is given by the expression

$$w_{\max} = \frac{qa^4}{64D} \quad (0.0.21)$$

The deflection profile defined by (0.0.20) was derived under the conditions of pure bending. The effects of transverse shear may be included by the addition of a shear correction term to yield the deflection profile [1]

$$w = \frac{q}{64D} \left((a^2 - r^2) + \frac{4h^2}{(1-\nu)} (a^2 - r^2) \right) \quad (0.0.22)$$

and the maximum deflection relationship (at $r=0$)

$$w = \frac{q}{64D} \left(a^4 + \frac{4h^2 a^2}{(1-\nu)} \right) \quad (0.0.23)$$

Comparison

The LUSAS results for the maximum deflection are compared to the thin and thick plate solutions below:

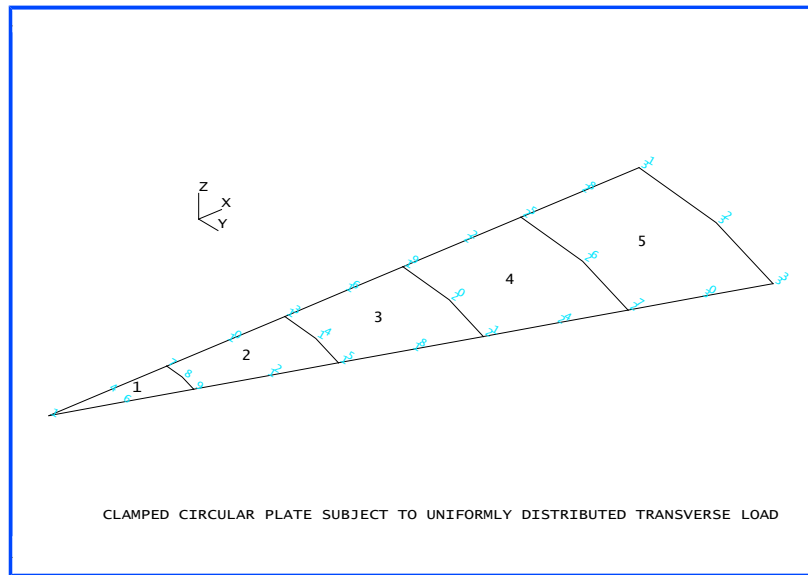
h	h/2a	Thin Plate Theory	Thick Plate Theory	LUSAS results
0.1	0.1	-0.97656	-1.19966	-1.15480

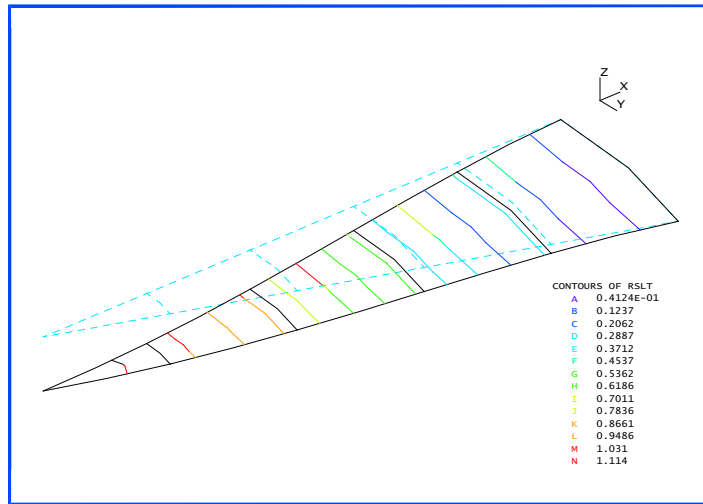
References

1. S.P.Timoshenko, S.Woinowsky-Kreiger, 'Theory of Plates and Shells', Second edition, Publisher. McGraw-Hill Book Co. Ltd (1959).

Input data

X01D32A.DAT





Clamped Circular Plate subject to uniform load deformed configuration and Displacement Contours

Example 1.3.3

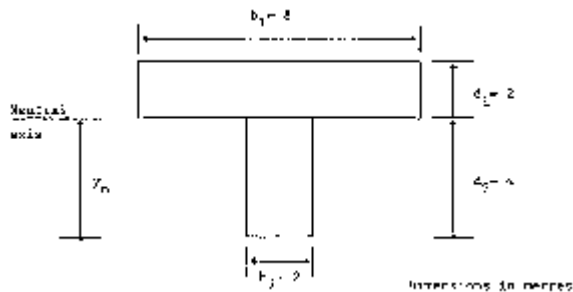
Eccentric Ribbed Plate

Keywords

Plate, Linear, Eccentric

Problem Description

A cantilevered eccentric ribbed plate is subjected to an end moment. The dimensions of the plate are as follows:



Discretisation

The structure is idealised using 4 thick shell elements QTS4 modelling the plate and 2 eccentric stiffeners BMS3 modelling the web. The plate is supported as a cantilever fully restrained at one end with a constant moment of 1000 kNm applied to the free end.

Material properties

Young's modulus	100.0×10^6 kN/m ²
Poisson's ratio	0.0

Theory

The position of the neutral axis from the bottom of the section is calculated as:

$$y_n = \frac{A_1 y_1 + A_2 y_2}{A_1 + A_2} = 4\text{m} \quad (0.0.24)$$

The moment of inertia about the neutral axis is:

$$I_{yy} = \frac{b_1 d_1^3}{12} + A_1 y_1^2 + \frac{b_2 d_2^3}{12} + A_2 y_2^2 = 64\text{m}^4 \quad (0.0.25)$$

Stress on the top surface:

$$\sigma_t = 2 \frac{M_y}{I_{yy}} = 31.25 \text{ KN/m}^2 \quad (0.0.26)$$

Stress on the bottom surface:

$$\sigma_b = 4 \frac{M_y}{I_{yy}} = 62.5 \text{ KN/m}^2 \quad (0.0.27)$$

Comparison

The LUSAS results for the stresses compared to theoretical results. Plate output for nodes at fixed end:

$$\text{Top stress} = 31.267 \text{ KN/m (average)}$$

Beam output for nodes at fixed end:

$$\text{Axial force} = 250.018 \text{ KN}$$

$$\text{Moment} = 167.424 \text{ KNm}$$

Moment of inertia for beam:

$$I_{yy} = \frac{bd^3}{12} = 10.667\text{m}^4 \quad (0.0.28)$$

Bottom Stress:

$$\sigma_b = \frac{F}{A} + \frac{M_y y}{I_{yy}} = 62.64 \text{ KN/m}^2 \quad (0.0.29)$$

Input Data

X01D33B.DAT

Example 1.4.1

Static Stress Analysis Of A Cantilever Subjected To Multiple Load Cases

Keywords

Three Dimensional Beam, Loading

Problem description

Determine the tip displacements, moments and flexural strains for a straight cantilever. The geometry of the cantilever is as follows:

Length, l	5.0
Breadth, b	0.25
Depth, d	1.0

Discretisation

The cantilever is modelled using one or two beam BMI21 (with Residual Bending Flexibility correction), BMI31 or BS4 elements. The material properties are as follows:

Young's modulus	30000.0
Poisson's ratio	0.3
Density	0.283
Coefficient of thermal expansion	0.0003

The fixed end of the cantilever is assumed to be fully restrained.

Theory

The cantilever is subjected to the following load cases:

Case	Loading	Description of load case
1	CL	End concentrated load -30 in Y direction
2	CL	End concentrated load 30 in X direction
3	CL	End anticlockwise moment (positive) 30
4	UDL	Uniformly distributed load 15 in local x direction
5	UDL	Uniformly distributed load -16 in local y direction
6	CBF	Constant body forces 15×4 in global X direction
7	CBF	Constant body forces -16×4 in global Y direction
8	CBF	Centrifugal forces 15 about global Y axis
9	CBF	Centrifugal forces 15 about global X axis
10	TEMP	Uniform temperature rise 50 at nodes
11	TEMP	Flexural temperature gradient $\partial T / \partial y = 10$ at nodes
12	BFP	Constant nodal body force 15*4 and -16*4 at nodes in global X and Y directions
13	SSI	Initial stress resultant 15 at nodes in local x direction
14	SSI	Initial strains -0.002 at nodes in local x direction
15	SSIG	Initial stress resultant 15 at Gauss points in local x direction
16	SSIG	Initial strains -0.002 at Gauss points in local x direction
17	BFP	Body force potential 15 in local x direction
18	BFP	Body force potential -16 in local y direction
19	COMB	Combination of 2 * case (1) + 2 * case (2)

Theory and Solution Comparison

Load case	Quantity	Theoretical solution	LUSAS
1	Displacement	$v = -PI^3/3EI = -2.00$	-2.0 (-2.062*)
	Moment	$M = P(x-1) = 150.0$	150.0
	Strain	$= M/EI = 0.24$	0.24 (0.12 [†])
2	Displacement	$u = PI/EA = 0.02$	0.02
	Axial Force	$F_x P = 30.0$	30.0
	Strain	$= P/EA = 0.004$	0.004
3	Displacement	$v = M1^2/2EI = 0.60$	0.60
	Moment	$M = M = -30.0$	-30.0
	Strain	$= M/EI = -0.048$	-0.048

Load case	Quantity	Theoretical solution	LUSAS	
4	Displacement	$d = Wl^2/2EA$	= 0.025	0.025
	Moment	$F_x = W(1-x)$	= 75.0	75.0
	Strain	= F_x/EA	= 0.01	0.01 (0.005 [†])
5	Displacement	$d = Wl^3/8EI$	= -2.0	-2.0 (-2.083 [*])
	Moment	$M = Wl^2/2$	= 200.0	191.67 (200 [†])
	Strain	= M/EI	= 0.32	0.3067 (0.1067 [†])
6		See load case (4)		
7		See load case (5)		
8	Displacement	$u = w^2l^3/3E$	= 0.08843	0.088437
	Axial force	$F_x = w^2Al^2/2$	= 198.98	207.3 (199.0 [†])
	Strain	$w^2l^2/2E$	= 0.02653	0.02764 (0.01769 [†])
9	Displacement	$v = Fyl^4/8EI$	= 0.99487	0.9949 (1.036 [*])
	Moment	$M = Fyl^2/2$	= -99.492	-95.347 (-99.492 [†])
	Strain	= M/EI	= 0.1592	-0.1526 (-0.0531 [†])
10	Displacement	$u = Tl$	= 0.075	0.075
	Strain	= u/l	= 0.015	0.015
11	Displacement	$v = (dT/dy) l^2/2$	= 0.0375	-0.0375
	Strain	= (dT/dy)	= 0.003	0.003
12		See load case (4) & (5) combined		
13	Displacement	$u = Fl / EA$	= -0.01	-0.01
	Strain	= u/l	= -0.002	-0.002
14	Displacement	$u = 1$	= -0.01	-0.01
	Strain	=	= -0.002	-0.002
15		See load case (13)		
16		See load case (14)		
17		See load case (4)		
18		See load case (5)		
19	Displacement	See load case (2) = 0.06		0.06
	Axial Force	See load case (2) = 90.0		90.0
	Strain	See load case (2) = -0.012		-0.012

* Displacements in brackets are results from thick beam elements BMI21/BMI31 if different from thin beam element BS4.

† Moments and strains in brackets are results from BMI21 if different from BMI31 and BS4.

References

1. Roark, R.J. Young, C.T. 'Formulas for stress and strain: Fifth edition', McGraw-Hill Publishing Company.

Input Data

X01D41A.DAT

X01D41B.DAT

X01D41C.DAT

Example 1.5.1

Linear Elastic Stress Analysis Of A Compact Tension Fracture Specimen

Keywords

Compact Tension Specimen, Three Dimensional Continuum, Solid

Problem Description

Determine the opening displacement and linear elastic stress distribution in a compact tension fracture specimen.

The compact tension test consists of a plane sheet loaded at either side of the crack by two loading pins (figure 1). The dimensions of the test specimen are as follows:

Height, h	120.0 mm
Width, w	100.0 mm
Thickness, t	3.0 mm

The loading pins are positioned at 55 mm centres and have a diameter of 25 mm. The stress concentration required for crack propagation is achieved by a pointed notch 50 mm long and 6 mm wide cut into the specimen. At the point of the notch a cut is made into the specimen to a further depth of 21.6mm.

The crack opening displacement is measured by a clip gauge mounted across the notch directly in line with the applied loading.

Discretisation

The full test specimen is modelled using three dimensional continuum (HX20 and PN15) elements.

The loading pins are included in the finite element model and assumed to behave as a rigid bodies compared to the test specimen. This is in an attempt to reduce localised effects around the loading pins and hence more accurately model the physical test conditions.

The following material properties are assumed in the analysis:

Young's modulus	210.915 kN/mm ²
Poisson's ratio	0.33

Theory and Loading

Previous experimental and numerical investigations of this specimen have established the stress concentration around the notch, and have indicated that localised plastification occurs around this point prior to the unstable propagation of the crack throughout the specimen [1-3]. The structure is known to behave linearly until a load of approximately 10 KN. In the finite element model the loading is applied to the structure via point loads acting at the centre of the rigid pins.

Solution

The results obtained from the LUSAS three-dimensional analysis are presented in figures 2-4.

References

1. Bleackley, M.H. Luxmoore, A.R. 'Comparison of finite element solutions with analytical and experimental data for elastic-plastic cracked problems'. International Journal of Fracture (in press)
2. Bleackley, M.H. 'A numerical study of energy criteria in fracture mechanics'. PhD. Thesis, University of Wales, (1981).
3. Owen, D.R.J., Fawkes, A.J., 'Engineering fracture mechanics: Numerical methods and applications'. Publisher. Pineridge Press Ltd, Swansea, U.K. (1983).

Input data

X01D51A.DAT

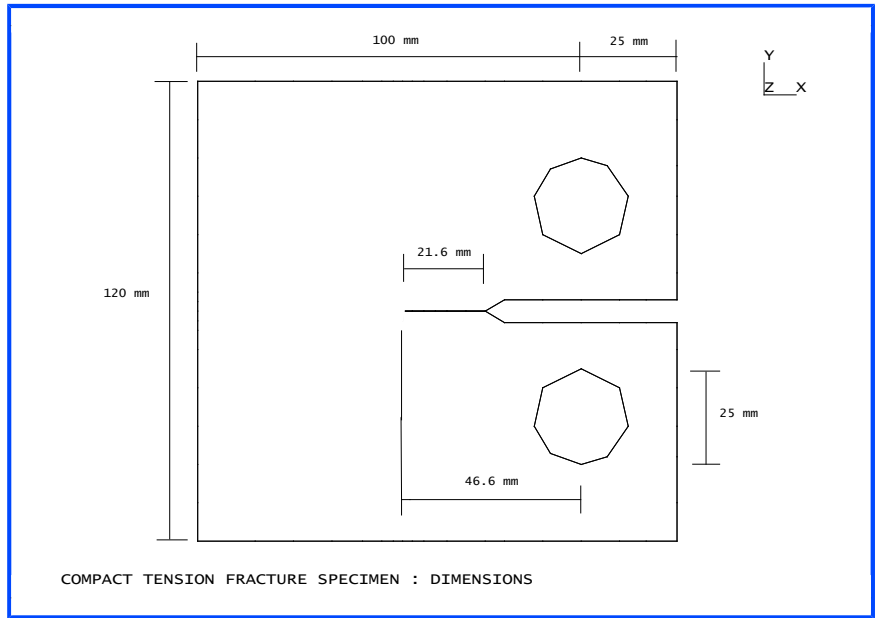


Figure 1: Dimensions of compact tension fracture specimen.

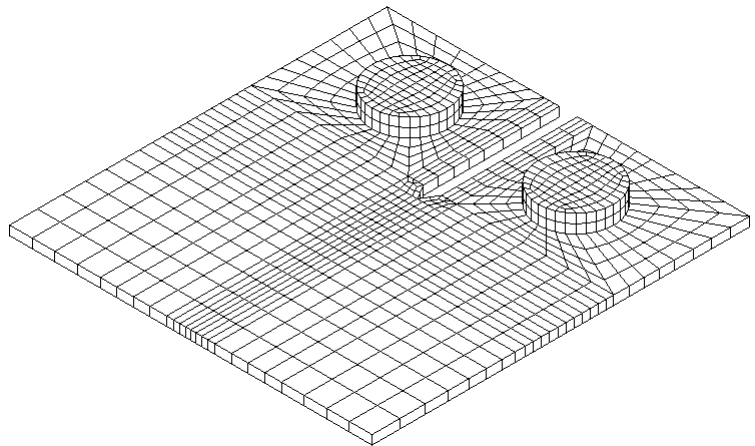


Figure 2: Finite element mesh for compact tension fracture specimen.

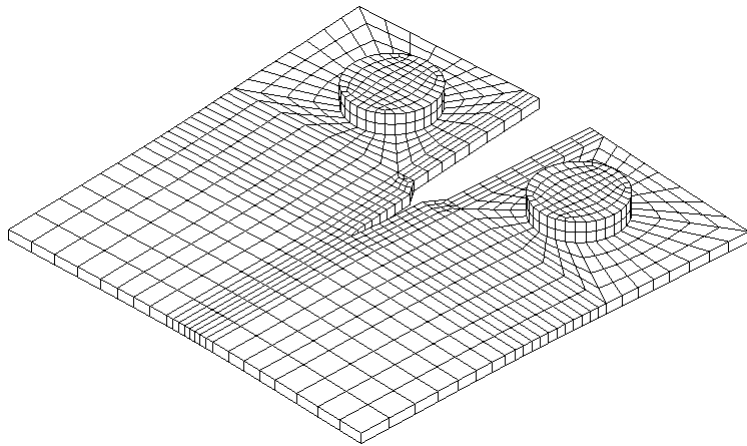


Figure 3: Deformed mesh under loading.

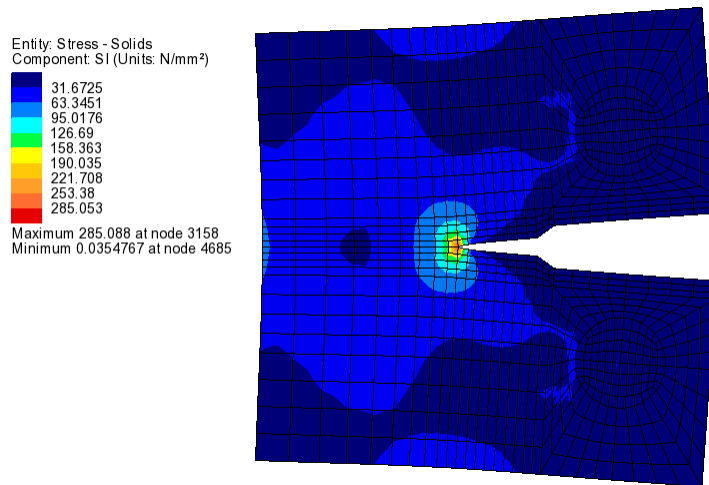


Figure 4: Contours of principal stress.

Example 1.6.1

A Simply Supported Twin Box Beam Under Concentrated Loads

Keywords

Box Beam

Problem description

A simply supported twin box beam with trapezoidal cross-section is subjected to two symmetrical point loads near the centre span (Figure 1). The beam is made of thin mild steel plates with the following thicknesses:

Top flange thickness	0.5 cm
Web thickness	0.3 cm
Bottom flange thickness	0.3 cm

Loading condition

Two point loads of 20KN are applied at a position $7/16$ of the span section over the inner webs (Figure 1).

Finite Element Model

The discretisation consists of 264 SHI4 elements. Due to the non-symmetric loading case the whole beam must be included in the discretisation.

Material properties

Young's modulus, E	19620 KN/cm ²
Poisson's ratio, ν	0.27

Boundary conditions

The beam is simply supported at each end along the bottom flange.

Theory

Structural design of spine-beam bridges presents many difficulties because of the complex nature of the interaction of individual elements. A number of analysis methods exist; however, the reader is referred to publications by Maisel and Roll [1,2] for further information.

Solution Comparison

The problem investigated in this example is one that was performed experimentally by Zhang [3] at The City University London. The experimental results obtained have been compared to those of LUSAS in Figures 3 and 4.

References

1. Maisel, B.I. Review of Literature Related to the Analysis and Design of Thin-Walled Beams, Technical Report TRA 440, Cement and Concrete Association London, July 1970.
2. Maisel, B.I. and Roll, F. Methods of Analysis and Design of Concrete Boxbeams with Side Cantilevers, Technical Report 42.494, Cement and Concrete Association London, November 1974.
3. Zhang, S.H. The Finite Element Analysis of Thin-Walled Box Spine Beam Bridges, PhD thesis, The City University, London February 1982.

Input data

X01D61A.DAT

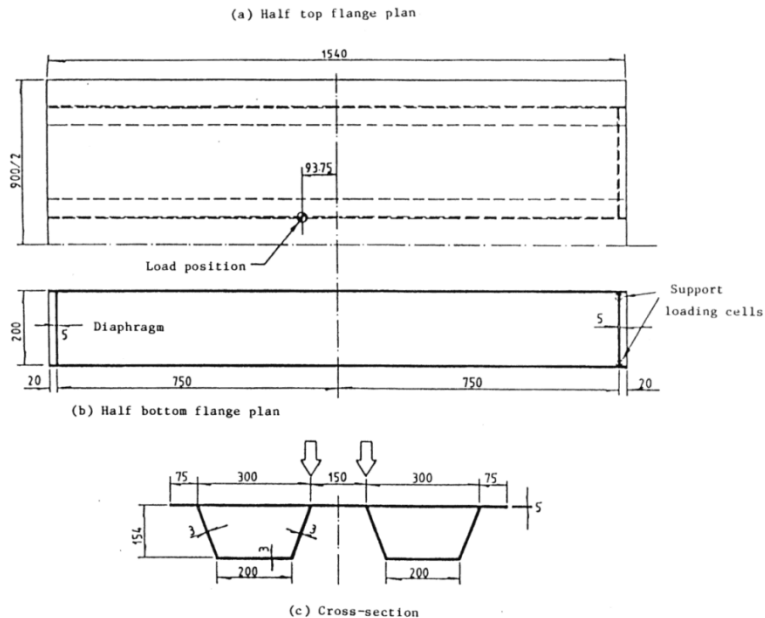
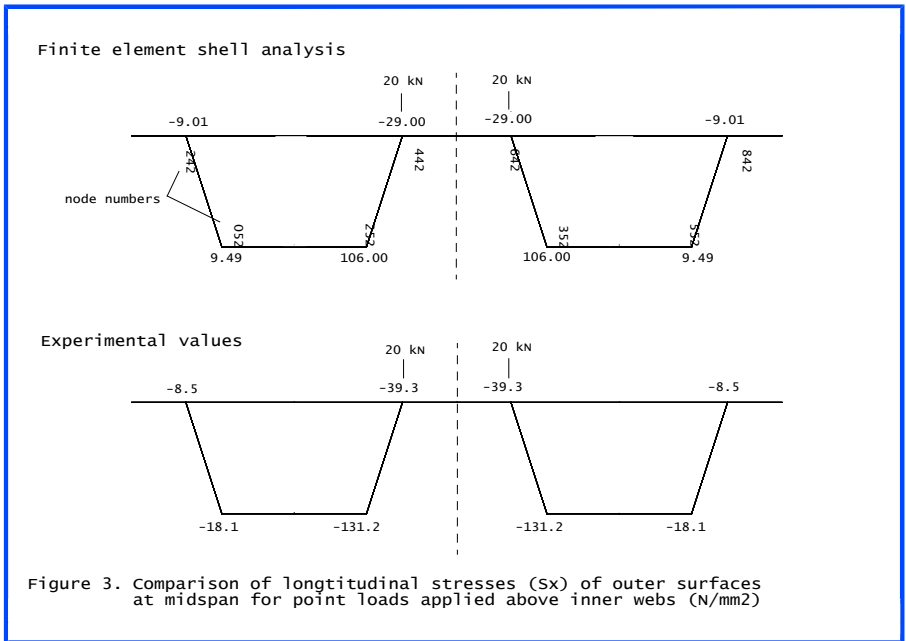
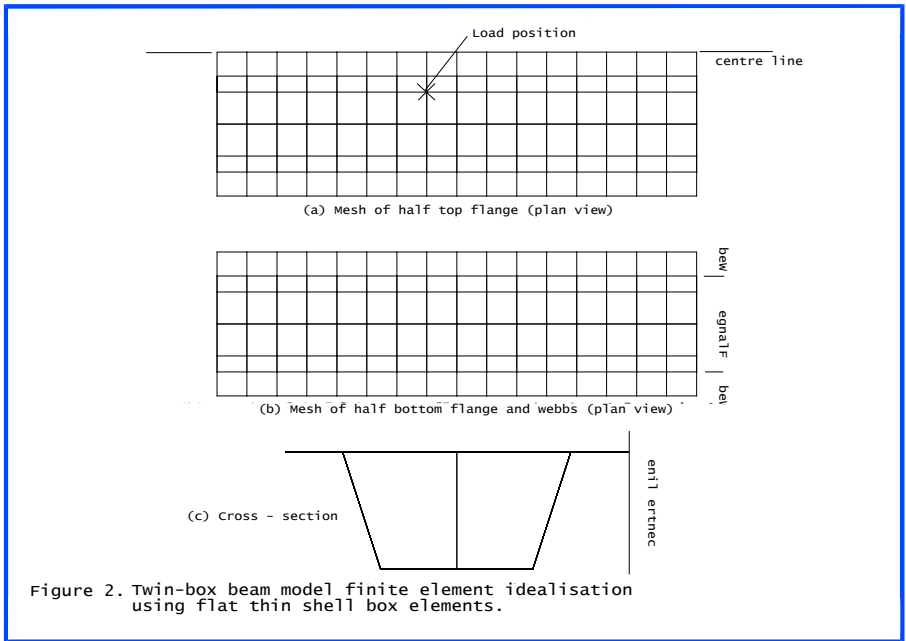
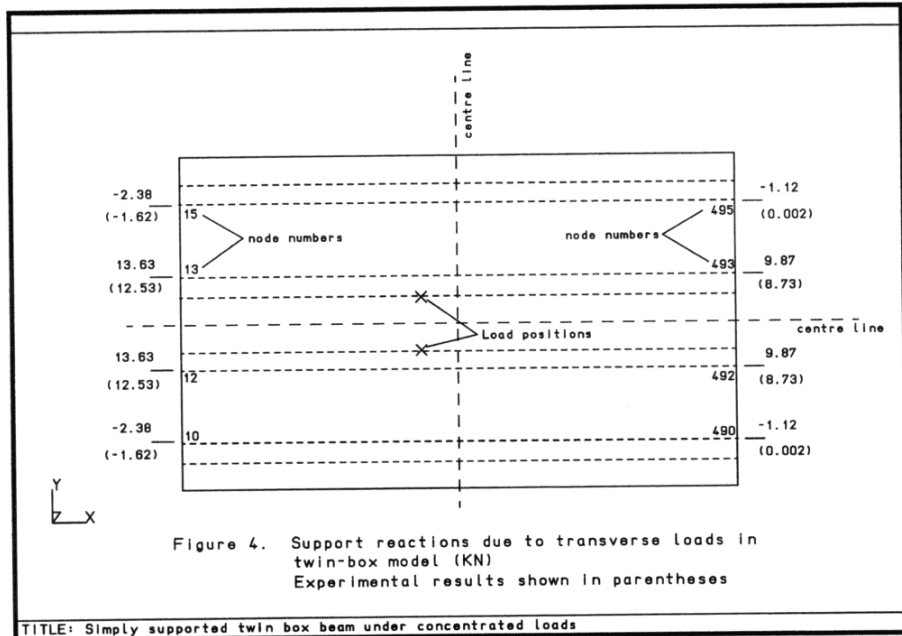


Figure 1. Simply supported twin-box beam model (in mm).





Example 1.6.2

Static Stress Analysis Of A Shallow Spherical Shell

Keywords

Shallow Spherical Shell

Problem Description

Determine the central deflection of a shallow spherical shell under a central point load and an eccentric patch load (see figure 1).

Discretisation

The analysis is performed with two different element meshes. The first model uses 6 BXS3 axisymmetric shell elements (see figure 2). This models one radian of the structure and consequently is only applicable to the central point load case. The second model uses 5 X 12 QSI4 and 1 X 12 TS3 incompatible flat shell elements (see figure 3). This models half of the structure and can therefore be applied to both load cases. It should be noted that a one radian section of 12 QSI4 and 1 TS3 flat shell elements would have been sufficient to model the central point load case.

Geometry

The geometry of the shallow spherical shell structure is shown in figure 1.

Material properties

Young's modulus	70000 N/mm ²
Poisson's ratio	0.3

Boundary conditions

The axisymmetric model is fully restrained at the base, node 1, and restrained from translation or rotation across the line of symmetry, node 13. The thin shell model is fully restrained at the base, nodes 7 to 91 in steps of 7, and restrained from translation or rotation across the line of symmetry, nodes 1 to 6 and nodes 86 to 90.

Theory

The fundamental theory for the central deflection of a shallow spherical shell under central point load is given in page 477 of [1].

Results

Table 1 gives the results for the central deflection due to a central point load for theory, axisymmetric model and thin shell model.

Analysis	Central deflection (mm)
Theory	-0.9514
BXS3	-0.8961
QSI4/TS3	-0.9495 (figure 4)

The central deflection due to the eccentric patch load is +0.0235 mm and the deflections at nodes 3 and 4 under the patch load are 0.473 mm and 0.458 mm (figure 5).

References

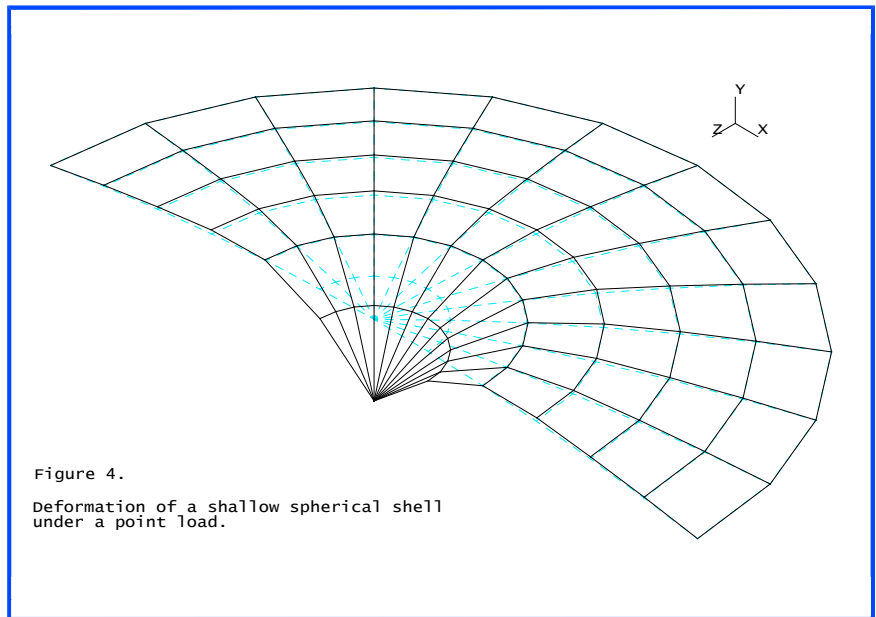
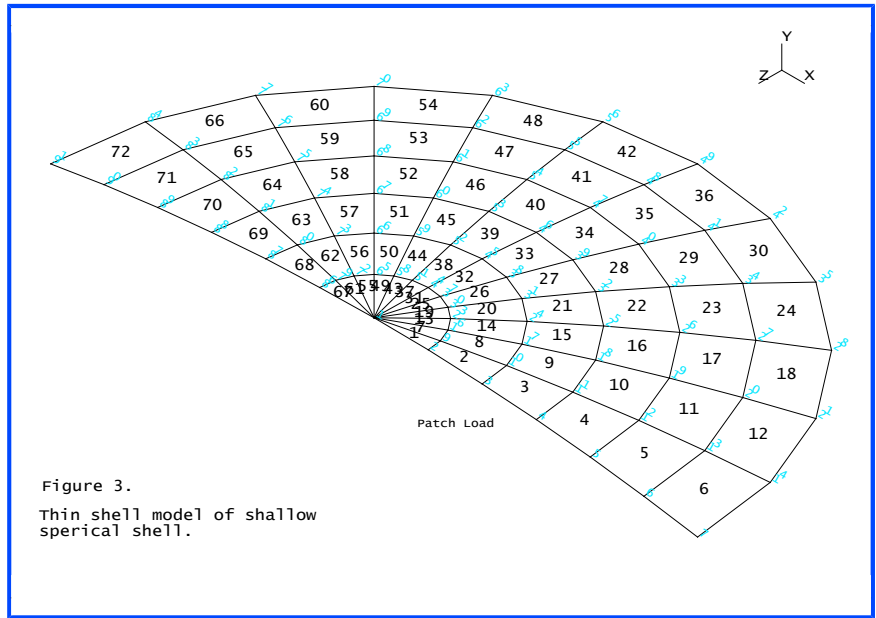
1. R. J. Roark and W. C. Young, "Formulas for Stress and Strain", Fifth edition. McGraw-Hill, 1975.

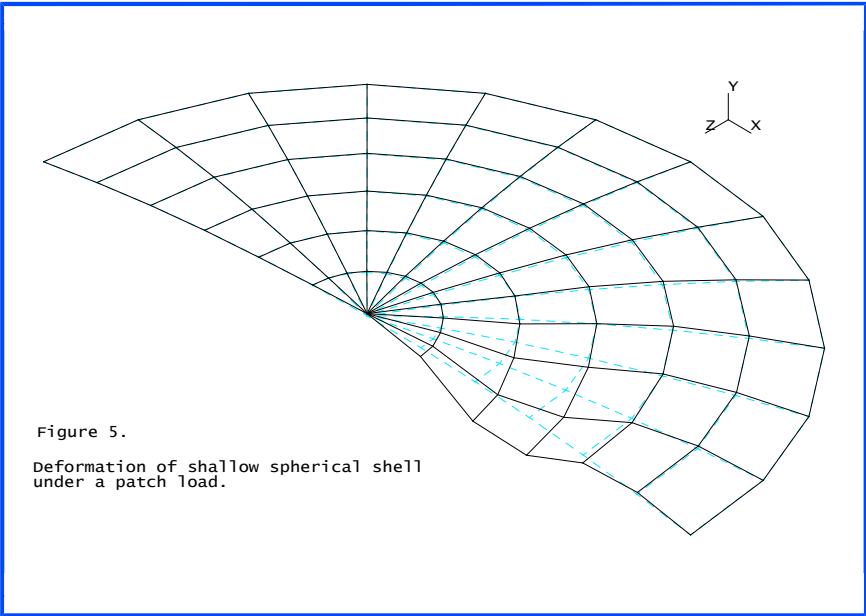
Input data

X01D62A.DAT

X01D62B.DAT

1. Axisymmetric shell analysis, central point load
2. Thin shell analysis, central point load and patch load





Example 1.6.3

Graphite/Epoxy Resin Laminated Orthotropic Square Plate

Keywords

Composite Analysis, Laminated Plate

Problem Description

The composite/laminated material comprises 9 graphite/epoxy resin material layers. Each layer is arranged so that its principal directions of orthotropy form a 0/90/0/90/0/90/0/90/0 sequence with respect to the global reference axes. The layup sequence is shown in figure 1. Owing to the different thicknesses of each of the layers in the parallel and perpendicular pairs, the plate is orthotropic with respect to both the material laminates and the resulting composite material. The plate is loaded with a udl and the central deflection of the plate is computed.

Discretisation

A symmetric quarter of the plate is modelled using a fine mesh of 6*6 Semiloof shell elements, figure 2. The composite construction of the material is modelled using 9 orthotropic material layers.

Geometry

The geometry of the plate is as follows:

Side length (a) = 10cm

Thickness (t) = 0.1cm

Span/Thickness = 100

Load Intensity (q) = 100 N/mm²

Material properties

The orthotropic material properties are as follows:

Young's modulus E_1 = 40E6 N/cm²

Young's modulus E_2 = 1E6 N/cm²

Poisson's ratio ν_{12} = 0.25

Shear Modulus $G_{12} = 0.6 E_6 \text{ N/cm}$

Orthotropy $E_1/E_2 = 40$

The material lay-up sequence for the laminated plate is as follows (note that the LUSAS convention is sequential from the bottom to the top of the material, and that the orientations are defined as that of the principal direction of orthotropy to the global x-axis:

Position	Layer	Thickness	Orientation
Bottom	1	0.01	0
	2	0.0125	90
	3	0.01	0
	4	0.0125	90
	5	0.01	0
	6	0.0125	90
	7	0.01	0
	8	0.0125	90
Top	9	0.01	0

Boundary Conditions

The external and internal plate boundary conditions are specified simply supported and symmetric respectively.

Theory

The non-dimensional central deflection of the plate may be obtained from the expression (see first reference):

$$\bar{w} = w \left(1000 \frac{E_2 t^3}{\text{Pa}^4} \right) \quad (0.0.30)$$

LUSAS results

Analysis method	Reference	Finite element mesh	Deflection w
Theory	(2)	N/A	-4.486
LUSAS		6*6 QSI8	-4.526
FE2000	(1)	Laminated solid 6*6*1	-4.480

LUSAS results for on-axis lamina stresses in layers 7, 8 & 9 are displayed in figure 3.

References

1. Razzaque, A. Mathers, M.D., 'Layered solid elements for non-linear analysis of composite structure', Quality assurance in Finite Element Technology (1988)
2. Noor, A.K., Mathers, M.D., 'Shear flexible models of laminated composite plates', NASA-TN D-8044 (1975)

Input data

X01D63A.DAT

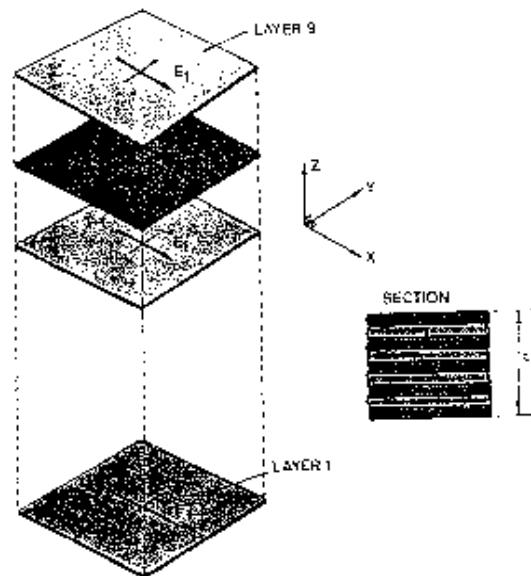
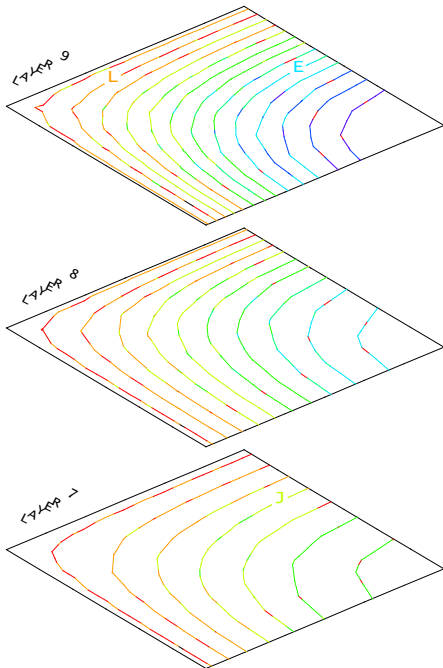
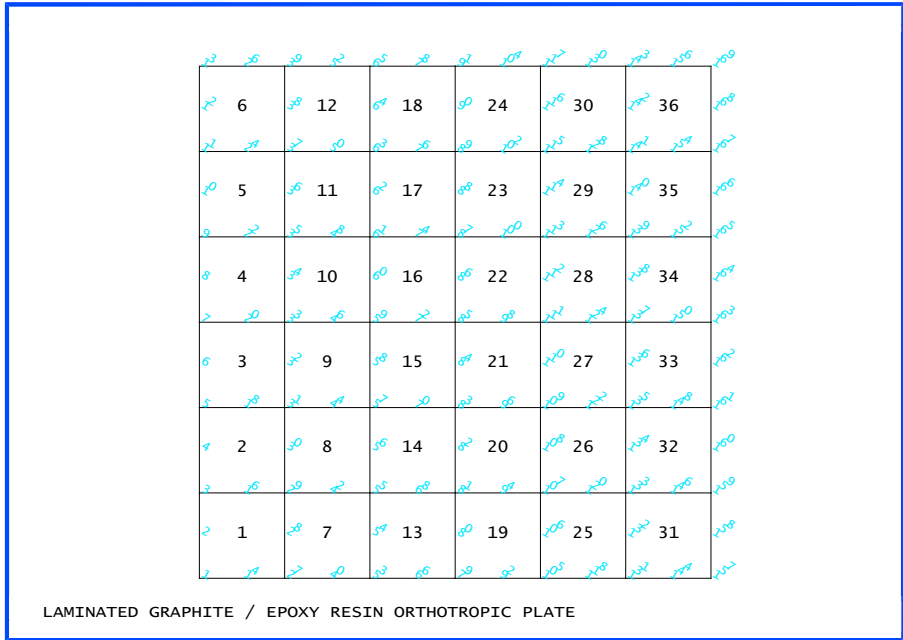


Figure 1 Layup Sequence for the Laminated Graphitic/Epoxy Resin Orthotropic Plate



- CONTOURS OF SX
- A -0.7000E+06
 - B -0.6434E+06
 - C -0.5868E+06
 - D -0.5303E+06
 - E -0.4737E+06
 - F -0.4171E+06
 - G -0.3605E+06
 - H -0.3040E+06
 - I -0.2474E+06
 - J -0.1908E+06
 - K -0.1342E+06
 - L -0.7764E+05
 - M -0.2106E+05
 - N 0.3552E+05

ON-AXIS LAMINA STRESSES FOR
(0.90.0.90.0)_s GRAPHITE/EPOXY PLATE

Example 1.7.1

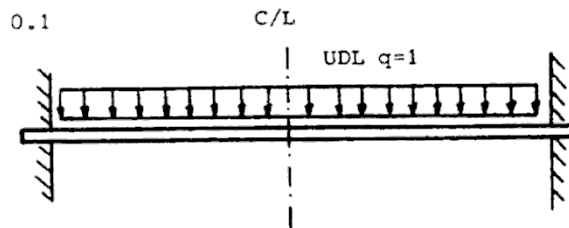
Axisymmetric Analysis Of A Clamped Circular Plate

Keywords

Circular Plate, Axisymmetric Solid, Axisymmetric Sheet

Problem Description

The problem considered in this example is a clamped circular plate subject to a uniform pressure load. Figure 1 shows the dimensions and material properties of the problem under consideration.



Discretisation

Four axisymmetric elements are used to model the circular plate. Figures 2 & 3 show the finite element mesh for QAX8 and BXS3 elements respectively.

Material properties

Young's modulus	$10.0 \times 10^6 \text{ N/m}^2$
Poisson's ratio, ν	0.3

Boundary conditions

The edge of the plate is fully fixed against translation or rotation.

Theory

$$D = \frac{Et^3}{12(1-\nu^2)} \quad (0.0.31)$$

$$w = \frac{qa^4(a^2 - r^2)^2}{64D} \quad (0.0.32)$$

where

w = downward deflection

q = uniform pressure

r = distance measured radially from centre of plate

a = radius of plate

D = flexural rigidity of plate

E = Young's Modulus

ν = Poisson's Ratio

t = thickness of plate

For further information see [2].

Solution comparison

Radius, m	Displacement Theory, m	Rotation Theory, radians	Displacement BXS3, m	Rotation BXS3, radians	Displacement QAX8, m
0	-0.17063	0	-0.17080	0	-0.16237
2.5	0.14996	0.01599	-0.15004	0.01597	-0.14212
5.0	-0.09598	0.02559	-0.09603	0.02558	-0.08970
7.5	-0.03266	0.02239	-0.03269	0.02239	-0.02891

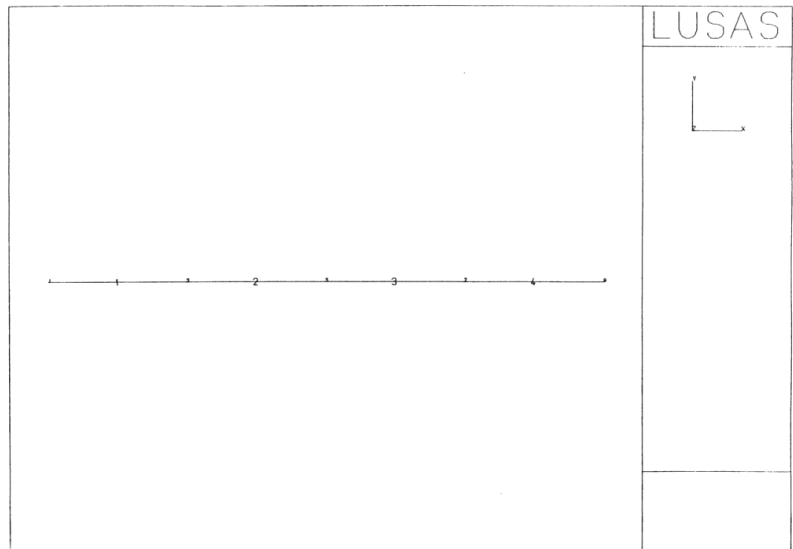
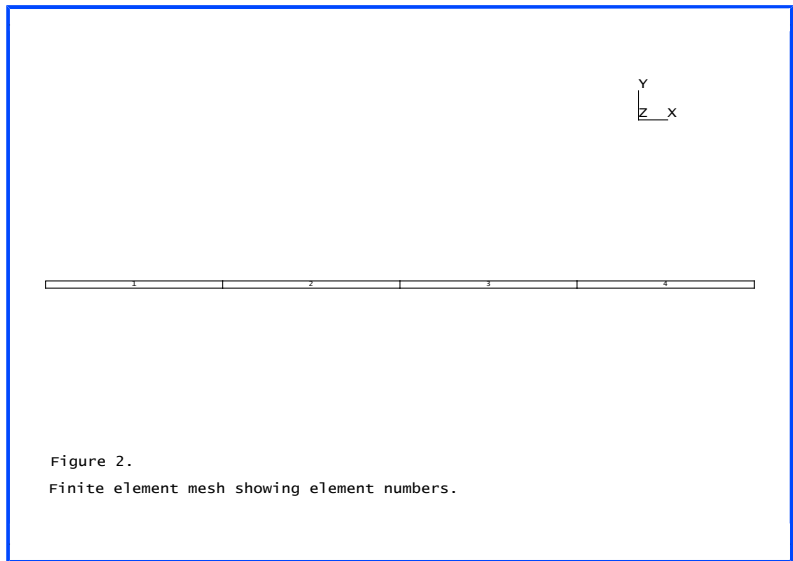
Although only one element is modelled through the thickness the LUSAS results compare favourably with the theory.

References

1. M.E. Honnor, 'Axisymmetric thin shell element', FEAL internal report FEAL503, 10th December 1985.
2. S.P. Timoshenko and S.Woinowsky-Krieger, 'Theory of plates and shells', pp. 55-56, McGraw-Hill, 1970.

Input data

X01D71A.DAT



Example 1.7.2

Axisymmetric Thin-Walled Pressure Vessel

Keywords

Pressure Vessel, Axisymmetric Solid, Axisymmetric Shell, Axisymmetric Sheet

Problem Description

The analysis of a thin-walled, cylindrical and hollow pressure vessel is considered in this example. Three different element types are utilised together with three different load cases. Axisymmetry about the X & Y axes is also considered for one set of the meshes. The element types are utilised as follows:-

- a) Axisymmetric eight-noded solid elements QAX8
- b) Axisymmetric thin shell element BXS3
- c) Axisymmetric sheet element BXM3

The three load cases considered are:

- Case 1) Uniform axial load per unit length of 6 N/m
- Case 2) Uniform radial pressure of 10 Pa
- Case 3) Linearly varying radial pressure from zero at the bottom to 100Pa at the top.

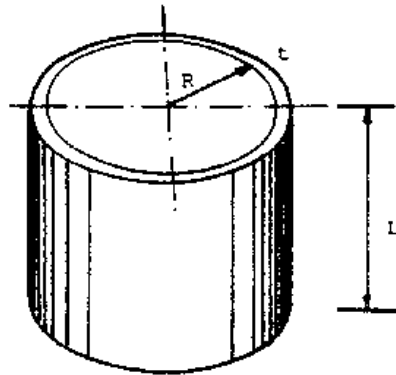
Figure 1 shows the dimensions and material properties of the problem under consideration.

Discretisation

Four elements are used along the length of the wall. The finite element mesh for QAX8 is shown in Figure 2. Figure 3 shows the mesh for BXS3 and BXM3.

Material properties

Young's modulus	200x10 ³ Pa
Poisson's ratio	0.3



$$L = 100\text{m}, R = 50\text{m}, t = 1.25\text{m}, E = 0.2\text{E}6 \text{ Pa } \nu = 0.3$$

Boundary Conditions

The bottom end of the cylinder is restrained against rotation and movement in the meridional direction but free to move radially.

Theory

Notation:

E	Young's Modulus
L	Length of cylinder
p	Axial load per unit length
q	Uniform pressure per unit area
r	Radial displacement at top end
R	Radius of cylinder
t	Thickness of cylinder
y	Meridional displacement at top end
ν	Poisson's Ratio
S_m	Meridional stress at top end
S_e	Circumferential stress top end
τ	Rotation of a meridian

	Case 1	Case 2	Case 3
σ_m	$\frac{P}{t}$	0	0
σ_e	0	$\frac{qR}{t}$	$\frac{qR}{t}$
r	$-\frac{pR}{Et}$	$\frac{qR^2}{Et}$	$\frac{qR^2}{Et}$
y	$\frac{pL}{Et}$	$-qR\frac{L}{Et}$	$-qR\frac{L}{2Et}$
τ	0	0	$\frac{qR^2}{EtL}$

For more information see [1].

LUSAS Results

Load case 1	Theory	QAX8	BXS3	BXM3
Meridional stress (Pa)	4.8	4.8	4.8	4.8
Circumferential stress (Pa)	0.0	0.0104	0.0	0.0
Radial displacement at end (m)	-3.5×10^{-4}	-3.6×10^{-4}	-3.6×10^{-4}	-3.6×10^{-4}
Meridional displacement at end (m)	2.4×10^{-3}	2.4×10^{-3}	2.4×10^{-3}	2.4×10^{-3}
Rotation (radians)	0.0	-	0.0	-

Load case 1	Theory	QAX8	BXS3	BXM3
Meridional stress (Pa)	0.0	0.0	0.0	0.0
Circumferential stress (Pa)	400.0	400.0	400.0	400.0
Radial displacement at end (m)	0.1	0.09998	0.1	0.1
Meridional displacement at end (m)	-0.06	-0.06	-0.06	-0.06
Rotation (radians)	0.0	-	0.0	-

Load case 1	Theory	QAX8	BXS3	BXM3
Meridional stress (Pa)	0.0	-0.0058	0.0	
Circumferential stress (Pa)	4000.0	4000.2	4000.0	4000.0

Load case 1	Theory	QAX8	BXS3	BXM3
Radial displacement at end (m)	1.0	0.9999	0.9999	1.0
Meridional displacement at end (m)	-0.3	-0.3	-0.3	-0.3
Rotation (radians)	-0.01	-	-0.0099	-

References

1. R.Roark and W.Young,'Formulas for stresses and strains', pp.448. LUSAS Results

Input data

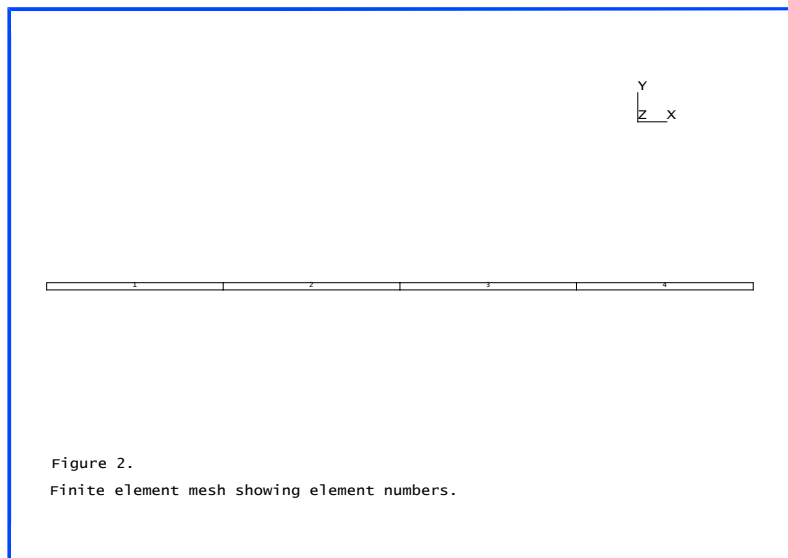
X01D72A.DAT

X01D72B.DAT

X01D72C.DAT

X01D72D.DAT

(axisymmetry about the Y-axis)



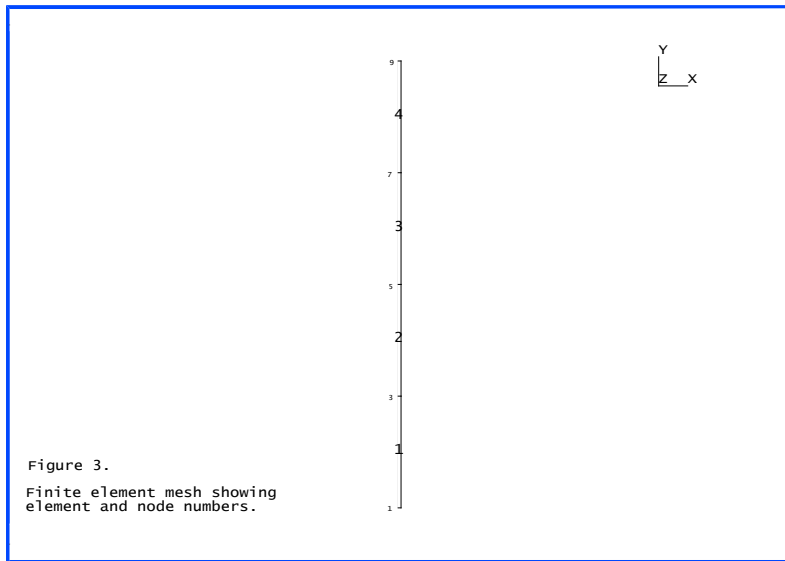


Figure 3.
Finite element mesh showing
element and node numbers.

Example 1.7.3

Cooling Tower Subject To Wind Loading

Keywords

Fourier, Semiloof Shell, Face Loading, Curve Definitions, Curve Assignment, Cartesian Set Cylindrical, Wind Loading

Problem Description

The effect of wind load on a cooling tower is modelled by a static analysis. For comparison, the analysis is performed using both the solid Fourier ring element QAX8F and the Semiloof shell element QSL8.

The pressure of the wind varies circumferentially, but is taken to be independent of the height above ground. The distribution of the load is symmetric about the diameter 0-180R. This simplifies the solution since only symmetric harmonics need be considered for the Fourier analysis, and only half the cooling tower need be meshed by the QSL8 elements. The load variation around the circumference is given in Figure 3.

Discretisation

The Fourier analysis utilises 10 elements to model the cooling tower length with 5 and then 10 harmonics taken to expand the variation of the load circumferentially. 10 QSL8 elements are also used to model the tower length, whilst 6 elements are used to model the circumferential section 0 to 180R.

Geometry

The shell mid-surface is defined by the parabolic equation:

$$\left[\frac{x}{84}\right]^2 - \left[\frac{y-270}{209.661}\right]^2 = 1 \quad (0.0.33)$$

The overall height of the cooling tower is 330ft (100.584m) and has a constant wall thickness of 0.5833ft (0.1778m). The outside radii at the bottom and top of the tower are 136.96ft (41.745m) and 87.4ft (26.64m) respectively.

Boundary Conditions

The cooling tower is encastre at the base. Symmetry boundary conditions are applied to the QSL8 mesh in cylindrical co-ordinates using transformed freedoms. Tangential displacements and loof rotations are restrained.

Material properties

Young's modulus	4.320x10 ⁸ psf, 20.68x10 ⁹ Pa
Poisson's ratio	0.15

Theory

The original problem was solved using a finite difference solution of the shell differential equations, with the circumferential variations modelled using a Fourier expansion. A fuller description is given in [1,2].

Note: the load was applied as a USER curve rather than using the Fourier coefficients given in [2] to allow a fairer comparison between the two analysis types.

LUSAS Results

Figures 1 & 2 show both the initial mesh and the final deformed shape from perspective and elevation views respectively. Figure 3 depicts the radial displacements for a node at the top of the tower; the crosses represent results from the Fourier analysis, the solid line corresponds to the shell analysis. The QSL8 radial displacements (Table 1) were obtained using option 115 to output displacements and reactions in transformed directions. Figure 3 also details the variation of wind load with circumference. Note that a positive face load acts in towards the surface.

Solution type	Radial displacement at the top edge
QAX8F (5 terms)	-0.2564 (Node 42, $\theta=0^\circ$)
QAX8F (10 terms)	-0.2565 (Node 42, $\theta=0^\circ$)
QSL8	-0.2493 (Node 21)

References

1. Program Verification and Qualification Library, ASME Pressure Vessel and Piping Division, Committee on Computer Technology, 1972.
2. Albasiny, E.L. and Martin, D.W., Bending and Membrane Equilibrium in Cooling Towers, Jour. Eng. Mech. Div., ASCE, EM3, 1967.

Input Data

X01D73A.DAT

X01D73B.DAT

X01D73C.DAT

Note: The different results for taking 5, 10 terms of the Fourier expansion can be obtained by changing the range of the harmonic series defined in the FOURIER CONTROL data chapter.

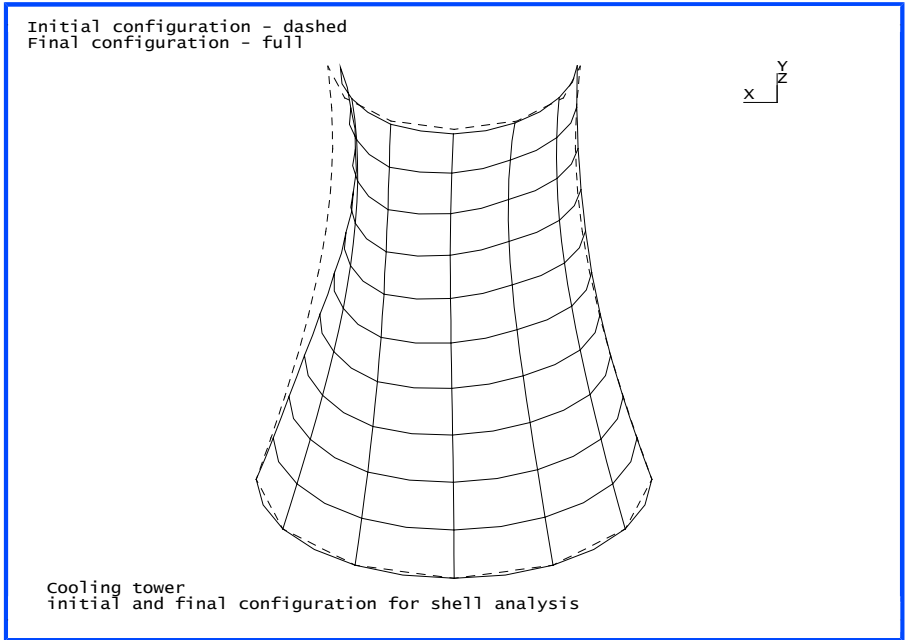


Figure 1

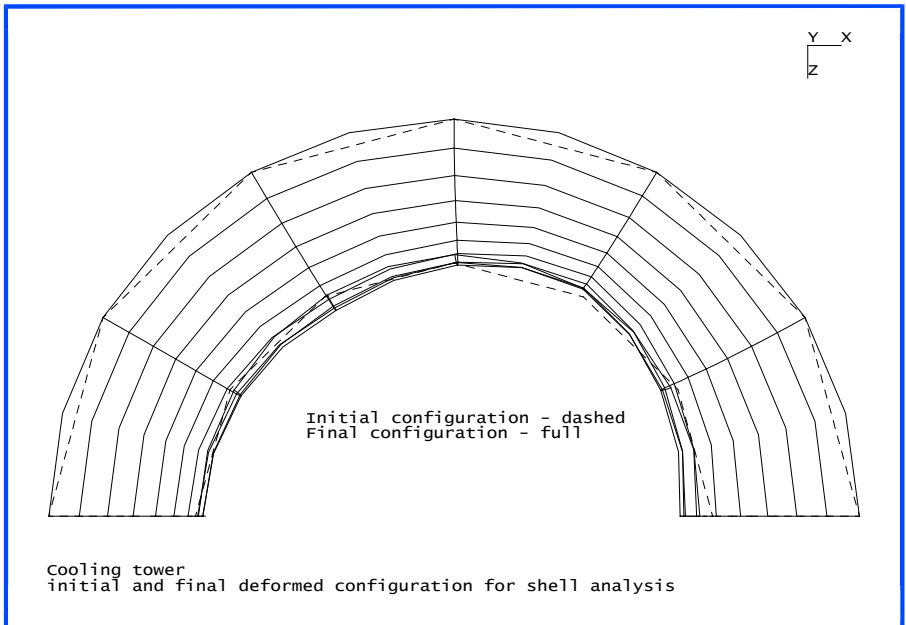
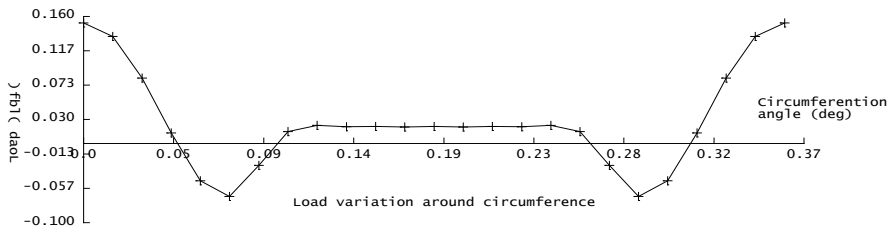
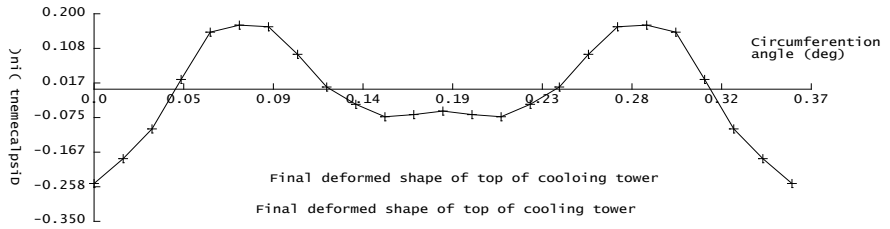


Figure 2



Cooling tower : Final deformed configuration and load variation

Figure 3

Example 2.2.1

Groundwater Seepage Problem

Keywords

Groundwater, Seepage, Cofferdam

Problem Description

The problem considered in this example is the flow of groundwater beneath a cofferdam using a potential formulation approach. Figure 1 shows the dimensions of the problem under consideration.

Finite Element Model

The finite element mesh is shown in Figure 2, where 180 regular quadrilateral elements are used. The thickness of the sheet pile wall has not been modelled as this is assumed negligible compared to the overall dimensions of the problem. The sheet pile wall is represented by a boundary where no flow occurs.

Material properties

Permeability $K_X = K_Y = 0.864$ m/day

Boundary conditions

It is assumed that the boundary ABC (see Figure 1) is impermeable as is the sheet pile wall EFG. The pressure head in this case is the difference in height between AG and DF which is 3.0 m. Arbitrarily setting $\phi = \text{zero}$ along DF, since the flow velocities depend only on the gradient of ϕ then $\phi = 3.0$ along AG. Along ABC and on either side of the sheet pile wall it is required that $\partial\phi/\partial n = 0$ (see theory section). Also symmetry conditions along CD require $\partial\phi/\partial n = 0$.

The total flow rate may be obtained by summing the nodal reactions across section AG or DF on which the value of ϕ is prescribed.

Theory

The steady state behaviour of many physical phenomena can be described in 2-dimensions by the following quasi-harmonic equation:

$$\frac{\partial}{\partial X} \left(K_X \frac{\partial \phi}{\partial X} \right) + \frac{\partial}{\partial Y} \left(K_Y \frac{\partial \phi}{\partial Y} \right) + Q = 0 \quad (0.0.34)$$

where ϕ is the unknown function and K_x , K_y and Q are material parameters which can be functions of x and y . A number of field problems are governed by (0.0.34) and the physical interpretations of K_x , K_y and Q are listed on page 2.31 of the LUSAS User Manual.

Two main types of boundary condition are of interest;

- (a) The value of the unknown to be specified at the nodal points on the boundary,

$$\phi = \phi_p \quad (0.0.35)$$

- (b) That a boundary loading exists of the form,

$$K_x \frac{\partial \phi}{\partial x} L_x + K_y \frac{\partial \phi}{\partial y} L_y + q + \alpha(\phi - \phi_a) = 0 \quad (0.0.36)$$

in which q , and f_a are constants and L_x , L_y are the direction cosines between the outward normal, n , and the x and y axes respectively.

Three different cases are now defined for boundary condition (b) assuming $K_x = K_y = K$.

Case 1. $q = \alpha = 0$
$$K \frac{\partial \phi}{\partial n} = 0 \quad (0.0.37)$$

which implies the temp (/flow etc) gradient in a direction normal to the surface is zero i.e. this portion of the surface is perfectly insulated (/impermeable).

Case 2. $\alpha = 0$
$$K \frac{\partial \phi}{\partial n} = -q \quad (0.0.38)$$

This states that a specified quantity of heat(/fluid), q , flows into the body per unit area of the surface. Also known as the 'flux' boundary condition.

Case 3. $q = 0$
$$K \frac{\partial \phi}{\partial n} = -a(\phi - \phi_a) \quad (0.0.39)$$

The flow of heat (/fluid) from any point on the surface is directly proportional to the difference in the temperature (/potential) and the ambient temperature (/potential) ϕ_a . Also known as the convection boundary condition.

Groundwater flow is given by:

$$\frac{\partial \phi}{\partial x} (K_x \frac{\partial \phi}{\partial x}) + \frac{\partial \phi}{\partial y} (K_y \frac{\partial \phi}{\partial y}) + S - \frac{dV}{dt} = 0 \quad (0.0.40)$$

where S is the rate fluid is injected into an element per unit volume and dV/dt is the rate of change in volume/unit volume in the element during flow. As stated previously (Case 1) the flow velocity in the direction normal to an impermeable boundary is equal to zero. From (0.0.34) and (0.0.40) we see a potential analysis problem reduces to a solution of the quasi-harmonic equation with:

$$Q = S - dV/dt \quad (0.0.41)$$

although S and dV/dt have no physical interpretation in ideal fluid flow.

Solution comparison

	Flow rate value qm^3/day
Theory	8.6
LUSAS	8.4

Figure 3 shows a contour plot of the pressure head variation, thus each contour line is a line of equal potential or equipotential line.

References

- Hinton, E. and Owen, D.R.J. 'An introduction to Finite Element Computations', Pineridge Press, 1981.

Input Data

X02D21A.DAT

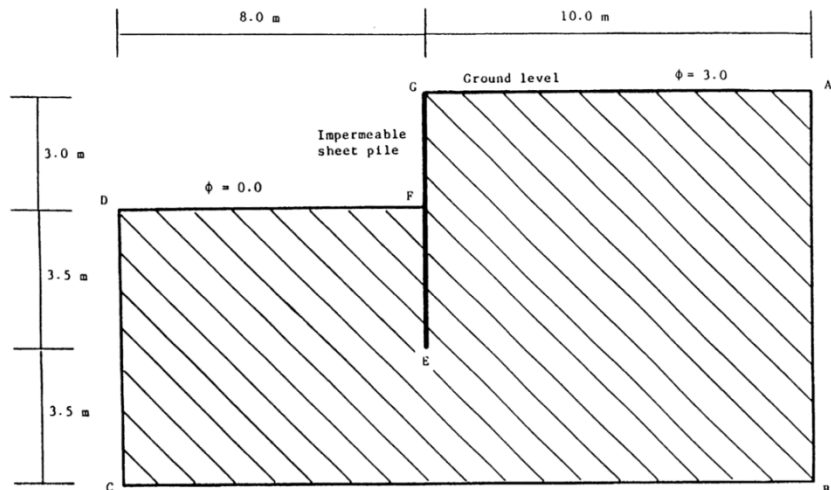


Figure 1. Groundwater flow beneath a coffer dam.

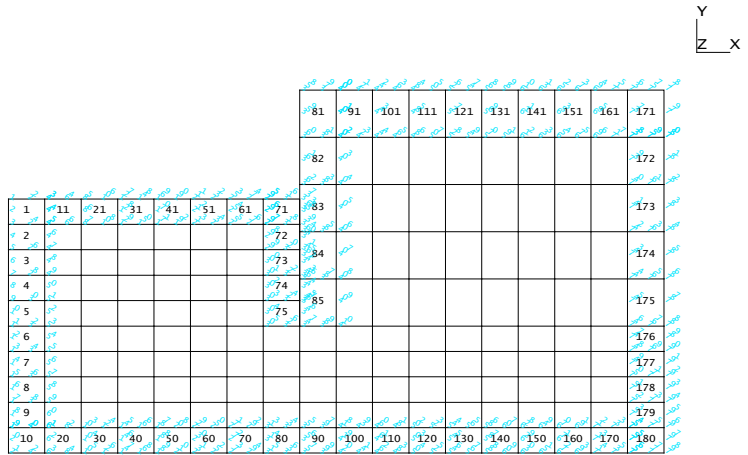


Figure 2.
 Finite element mesh with partial
 element and node numbering

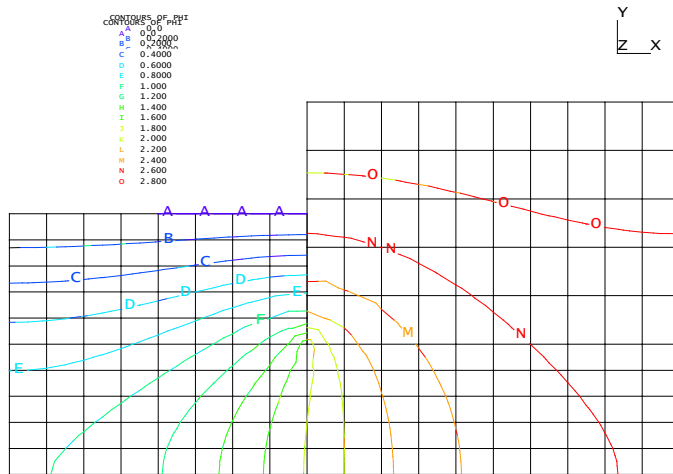


Figure 3.
 Finite element mesh with
 lines of equal potential.

Example 2.2.2

Steady State Thermal Analysis Of An Underground Tunnel

Keywords

Field, Steady State, Thermal Conduction, Tunnel

Problem Description

To determine the steady state temperature distribution in the rock strata surrounding an operational underground rail tunnel.

Figure (1) shows a section of the Channel Tunnel at a distance of 32 km from the Dover entrance. The surrounding rock mass consists of chalk, chalk/marl and clay, the tunnel itself being confined by the chalk/marl stratum.

The heat generated within the tunnel is assumed to act as a line heat source to the rock mass. The origins of this heat source are considered to be the result of turbulent frictional contact at the train/air and air/tunnel boundaries, increased air pressure within the tunnel, and the operating temperature of the train itself.

In addition it is assumed that the sea bed is environmentally controlled at a temperature of 10.1 degrees, and that a geothermal gradient of 0.036 degrees per metre exists at this latitude.

Discretisation

The section through the rock mass is discretised using quadrilateral field elements (QDF8). The finite element mesh is graded towards the tunnel opening in order to accurately model the local temperature gradient anticipated in this region. The boundaries of the mesh are considered to be sufficiently removed from the tunnel so as to be subject to environmental conditions only.

The material properties for the rock strata are as follows:

	K_x	K_y	C
Chalk	10.58	7.958	2178
Chalk/Marl	7.642	7.642	2267
Clay	7.988	7.988	2353

Boundary Conditions

Prescribed temperature conditions are imposed on the upper (sea bed) and lower mesh limits. Free conditions are imposed at the vertical mesh boundaries in order to impose a zero temperature gradient at these limits.

Theory

The heat flux input resulting from an operational tunnel is calculated on the basis of twelve trains per 24 hours [1]. The total heat generated per metre of tunnel in this time is 10,500 KJ.

Two heat flux input conditions are considered. The first (gross heat flux) assumes that all the heat generated within the tunnel is available to increase the temperature of the surrounding rock. The second (net heat flux) assumes that a percentage of the total heat generated will be responsible for an increase in the train operating temperature. The net heat flux condition is calculated as a function of the number, type, and mass of each carriage, and the initial train and tunnel lining temperatures [1].

Gross heat flux condition $q = 19.89$ KJ per hr, per sq.m.

Nett heat flux condition $q = 8.999$ KJ per hr, per sq.m.

The steady state temperature distribution is governed by the two dimensional quasi-harmonic equation [2]

$$0 = \frac{d}{dx} \left(K_x \frac{dT}{dx} \right) + \frac{d}{dy} \left(K_y \frac{dT}{dy} \right) + Q \quad (0.0.42)$$

where

K_x, K_y are the orthogonal thermal conductivities

C is the material heat capacity

T is the local temperature variable

A simplified analytical solution may be obtained by the 'mirror image method' [1]. The steady state temperature at a point P which is at distances R1 and R2 from the heat sink and source respectively may be calculated from the expression:

$$T_P = \frac{Q}{2\pi k} \left(\ln \left(\frac{R1}{R2} \right) \right) + T_O \quad (0.0.43)$$

where

T_P is the steady state temperature at point P

T_O is the steady state temperature at the boundary

Comparison

The temperature distributions (in degrees Celsius) obtained from the LUSAS steady state thermal analyses (gross and net heat flux input in the absence of a geothermal gradient) are compared to the analytical solution below.

Node	Distance(X)	Gross Heat Flux		Nett Heat Flux	
		Analytical temp	LUSAS temp	Analytical temp	LUSAS temp
42	20.0	24.118	24.997	16.487	17.791
44	60.0	15.606	17.179	12.592	14.252
46	160.0	11.401	13.231	10.688	12.465
48	280.0	10.556	12.313	10.310	12.050
50	400.0	10.334	12.074	10.206	11.942
52	700.0	10.177	11.956	10.131	11.888

Note: The analytical solution does not account for any stratification in the surrounding rock mass.

References

1. Kent, A.J. 'The English Channel Tunnel : An investigation of rock and lining temperatures', Internal thesis CP/838/83, Dept. Civil Engineering, University, College of Swansea, U.K. (1983).
2. Hinton, E. Owen, D.R.J. A simple guide to finite elements' Publisher. Pineridge press, Swansea, U.K.

Input Data

X02D22A.DAT

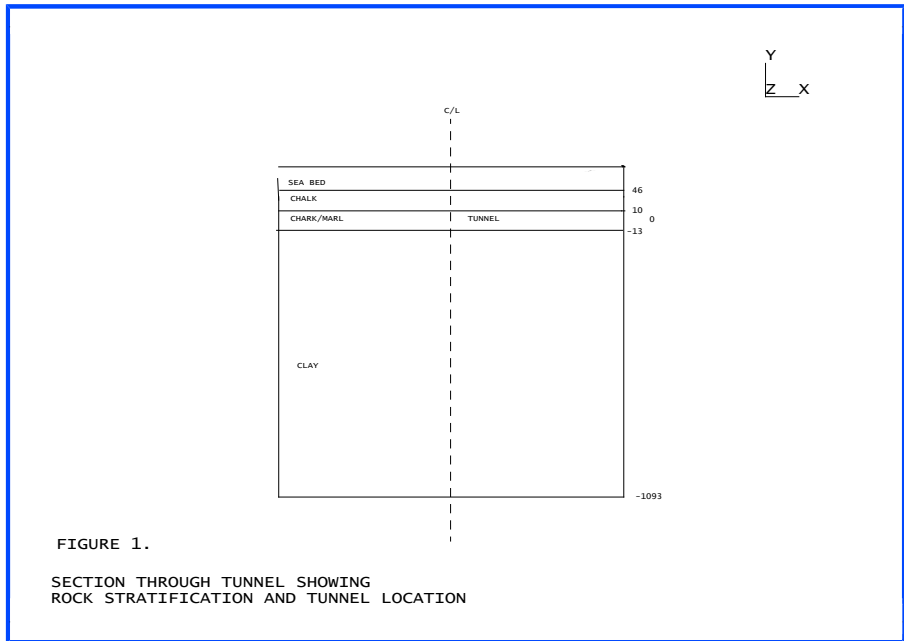


FIGURE 1.
SECTION THROUGH TUNNEL SHOWING
ROCK STRATIFICATION AND TUNNEL LOCATION

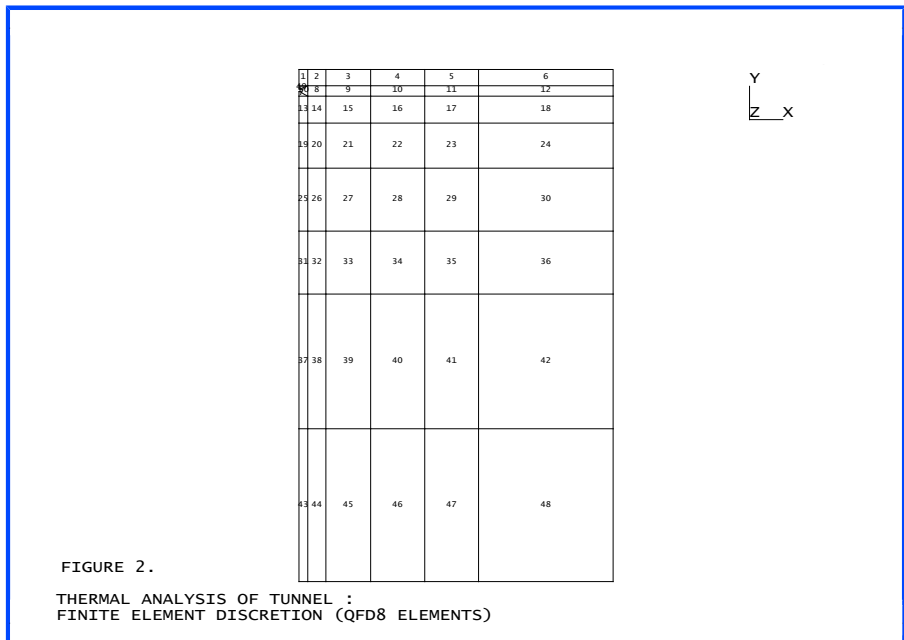
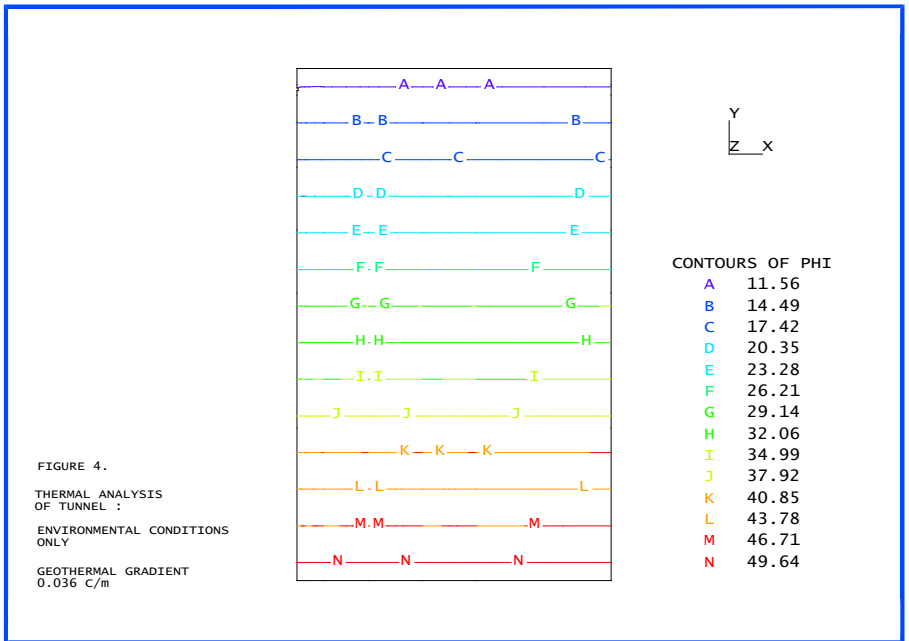
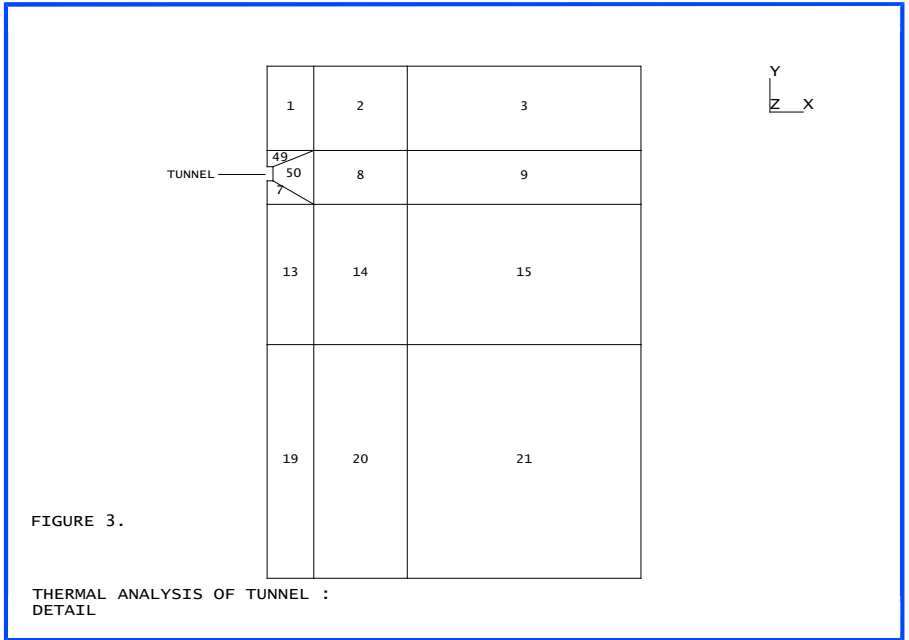
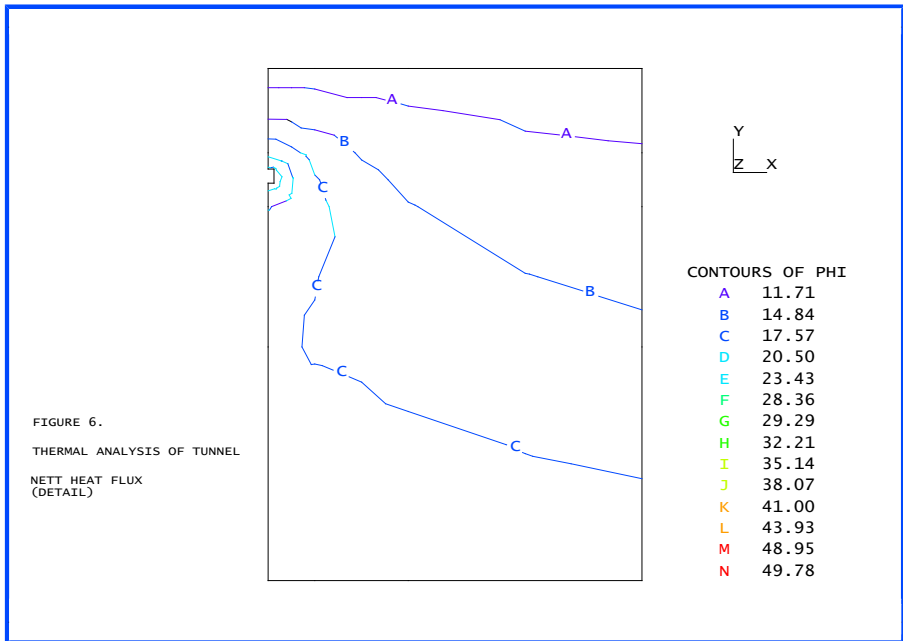
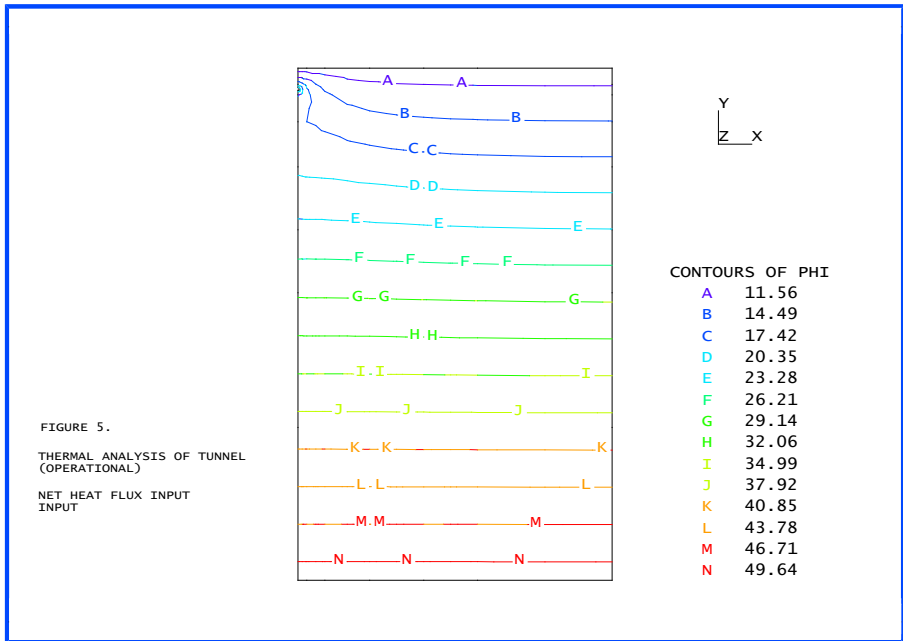
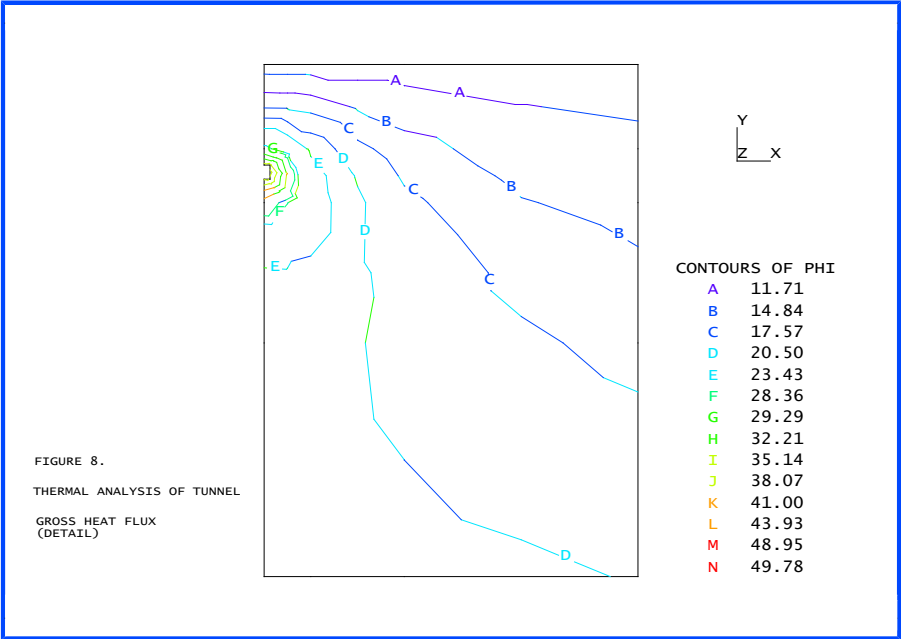
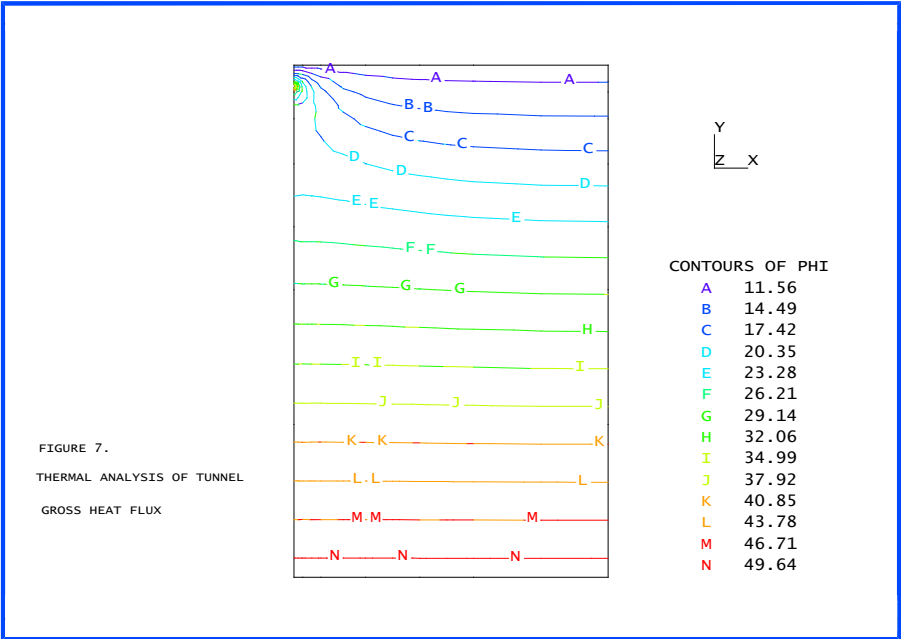
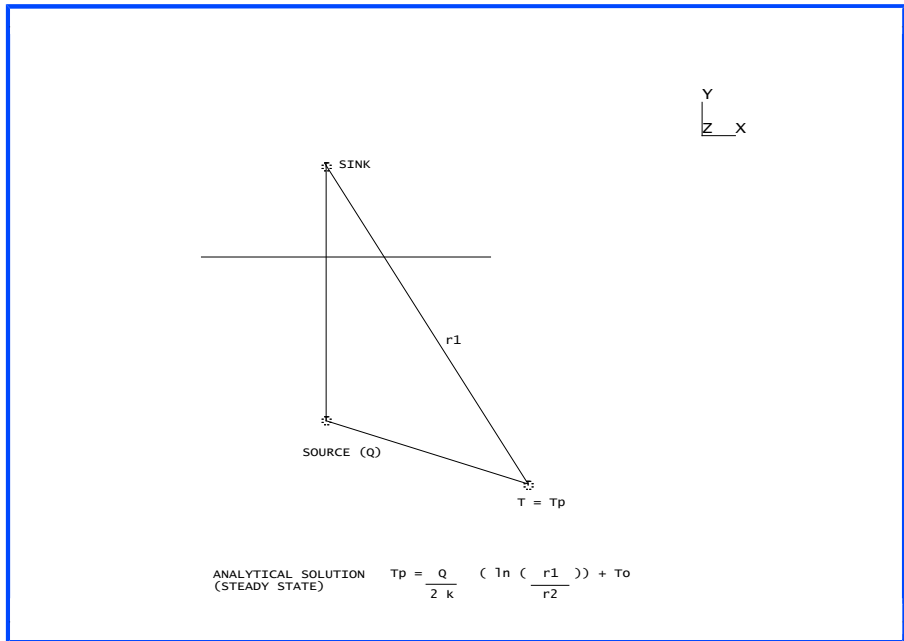


FIGURE 2.
THERMAL ANALYSIS OF TUNNEL :
FINITE ELEMENT DISCRETION (QFD8 ELEMENTS)









Example 2.2.3

Conductance Between A Plate And Half Cylinder

Keywords

Conductance, Thermal Surfaces, Environmental Nodes, Field

Description

Heat flows across the gap between a half cylinder and a plate, figure 1. The gap conductance is a linear function of gap opening and heat is allowed to flow to the environment. The problem is analysed with and without the use of environmental nodes for comparison. The first case corresponds to an infinite heat sink surrounding the structures and the second to an enclosure.

Discretisation

The plate and cylinder are modelled with QFD4 plane field elements and the element mesh is shown in figure 2.

Geometry

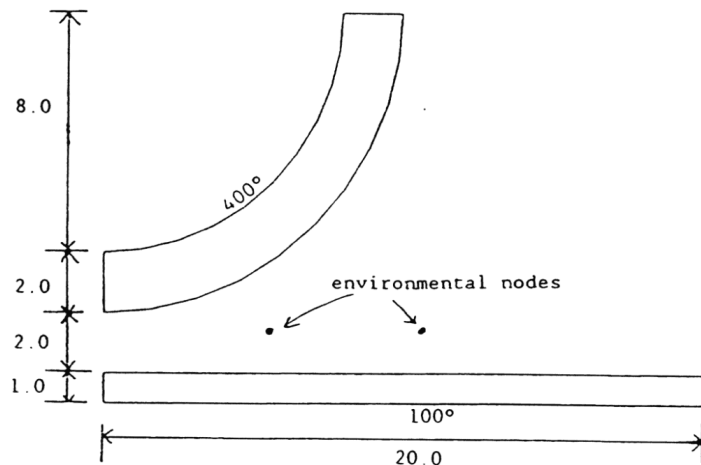


Figure 1 - Initial geometry

Boundary conditions

The internal surface of the cylinder is at 400 degrees and the bottom of the plate at 100 degrees.

Material properties

Solid conductivity = 80 W/m/degrees

Gap conductance

Conductance for closed gap $k_0 = 100$ W/m/degrees

Variation of conductance with gap opening, $dk/dL = -12.5$ W/m/m/degrees

Maximum limit for thermal link length, $L_{max} = 8$ m

Surface properties

Conductance to environment = 2.0 W/m/degrees

Environmental temperature = 0.0 degrees

LUSAS results

Smooth temperature profiles should result with hot spots occurring at the point of closest approach of the plate to the half cylinder.

Figures 3 and 4 show the temperature distribution of the analysis with and without the environmental nodes. It is noticeable that the point at which the links from the plate intersect with the cylinder results in a fluctuation in the isotherm.

Figure 5 illustrates the change in element connectivity when environmental nodes are included in the solution. Introducing these environmental nodes has the effect of increasing the surface area of the cylinder which is at the temperature of the inner surface. That is, they have the effect of insulating the surface. This is expected since heat cannot be lost from the solution, but must flow from the cylinder to the plate via the environmental nodes (the temperature distribution is seen to be slightly different in Figure 4 which shows that more of the cylinder remains at a higher temperature). The heat flows through the plate for the different analyses are:

Without environmental nodes = 39418 W

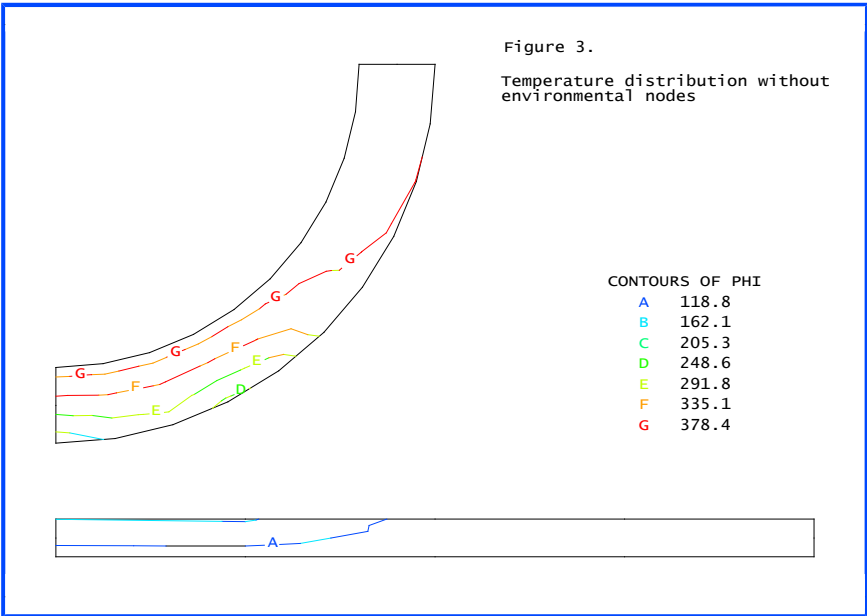
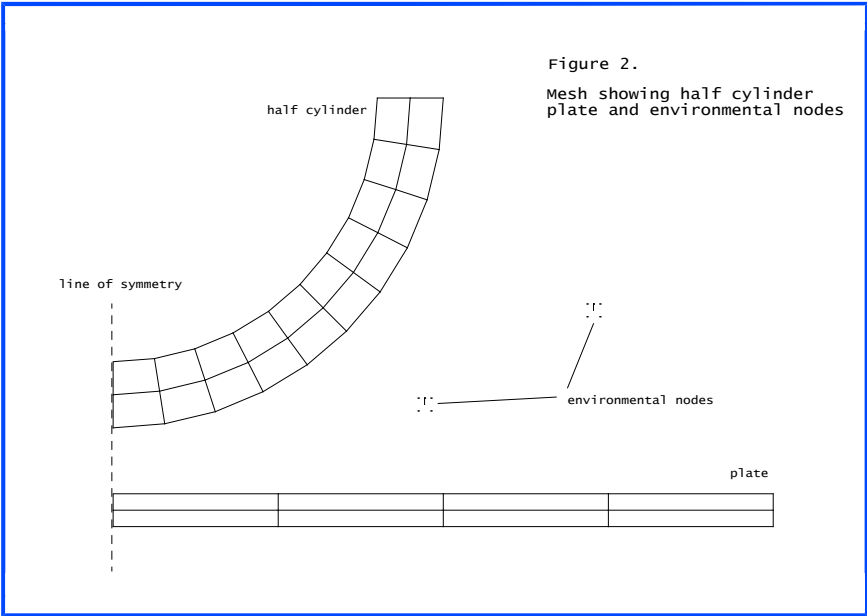
With environmental nodes = 43967 W

For this example, the introduction of environmental nodes increases the heat flow by approximately 10%

Input data

X02D23A.DAT

X02D23B.DAT



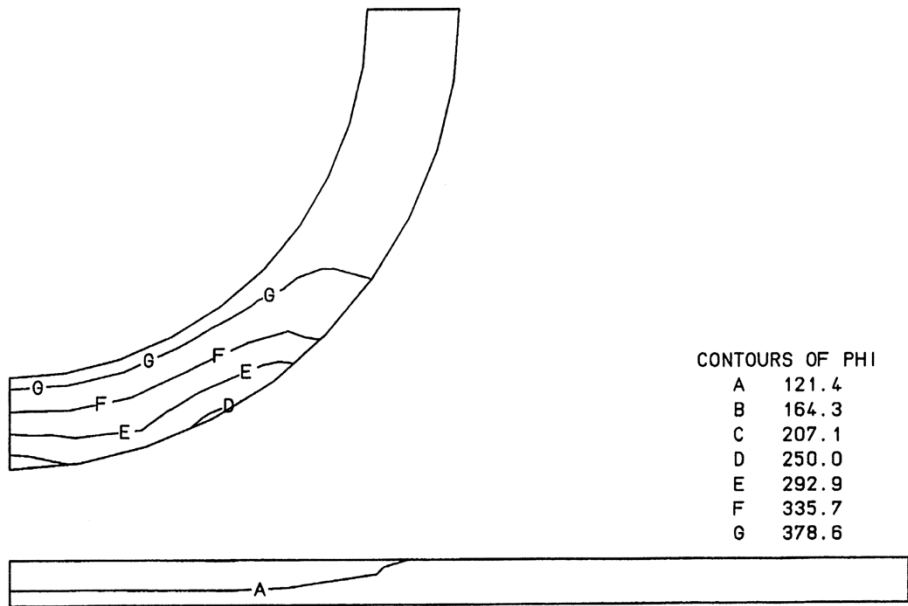
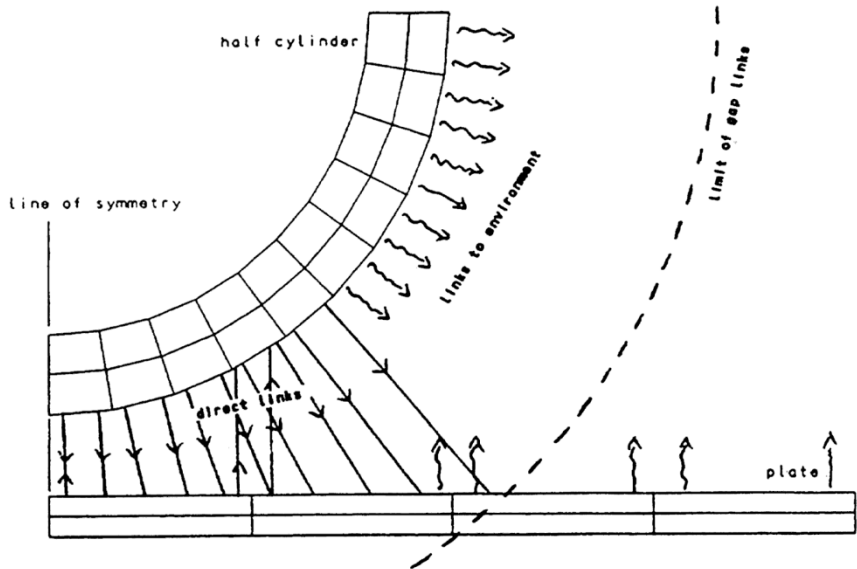


Figure 4 Temperature distribution with 2 environmental nodes



(a) links formed without environmental nodes

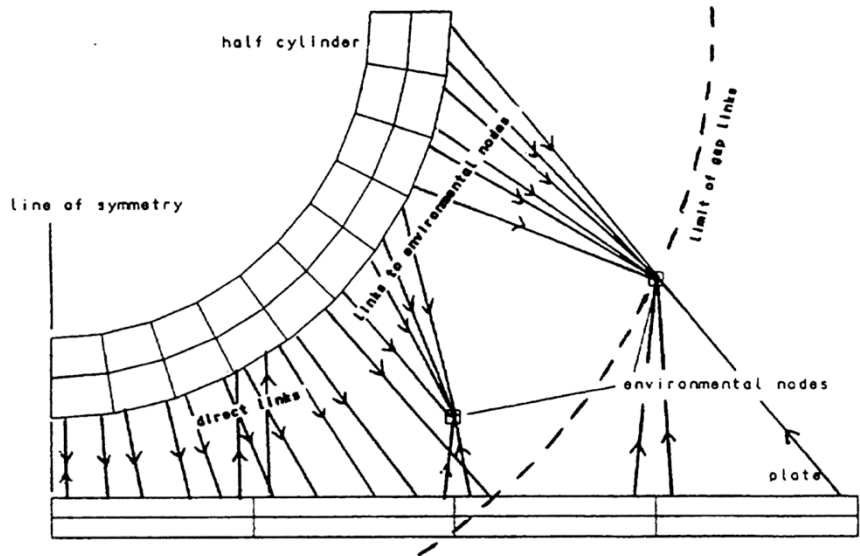


Figure 5 Thermal link formation

Example 2.3.1

Cylinder With Temperature Dependent Conductivity

Keywords

Steady State, Conductivity

Description

This problem involves a hollow cylinder with prescribed temperatures around the inner and outer circumferences. It is required to find the steady state temperatures at intervals of $1/5$ of the cylinder thickness. The convergence rate and CPU time for HF8 and QXF8 element discretisations using both MNR and NR solution procedures are also compared. This problem is an application of LUSAS to solve steady state heat conduction problems with temperature dependent materials.

Discretisation

15 Solid HF8 elements are used to model a 15R slice of the cylinder, figure 3. 5 QXF8 elements are used for the axisymmetric analysis, figure 2.

Geometry

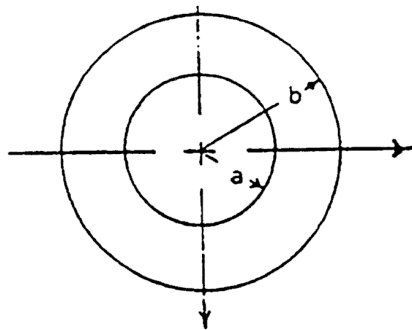


Figure 1

Inner radius, a	0.041666 ft
Outer radius, b	0.083333 ft

Material properties

C_0	50.0 BTU/hr.ft. F
C_1	0.5 BTU/hr.ft. F
$K(t)$	$C_0 + C_1 t$

Boundary conditions

Prescribed temperature $T=100RF$ around inner circumference $r=a$, and $T=0RF$, around outer circumference $r=b$.

Reference

1. Schneider, P. J., Conduction Heat Transfer, Addison-Wesley Publishing Co., Inc., Reading, Mass., USA, 2nd Printing, 1957.

LUSAS results

	Point 1	Point 2	Point 3	Point 4	Point 5	Point 6
REFERENCE	100.0	79.2	59.6	40.2	20.8	0.0
HF8	100.0	79.222	59.567	40.298	20.720	0.0
QXF8	100.0	79.190	59.490	40.206	20.665	0.0

Comparison of NR and MNR

	NR	CPU	MNR	CPU
HF8	4	67.46	10	88.02
QXF8	4	20.70		

The QFX8 element solution failed to converge using MNR after 20 iterations. At the time of ceasing computation the MNR solution appeared to be exhibiting a very slow rate of convergence.

Input Data

X02D31A.DAT

X02D31B.DAT

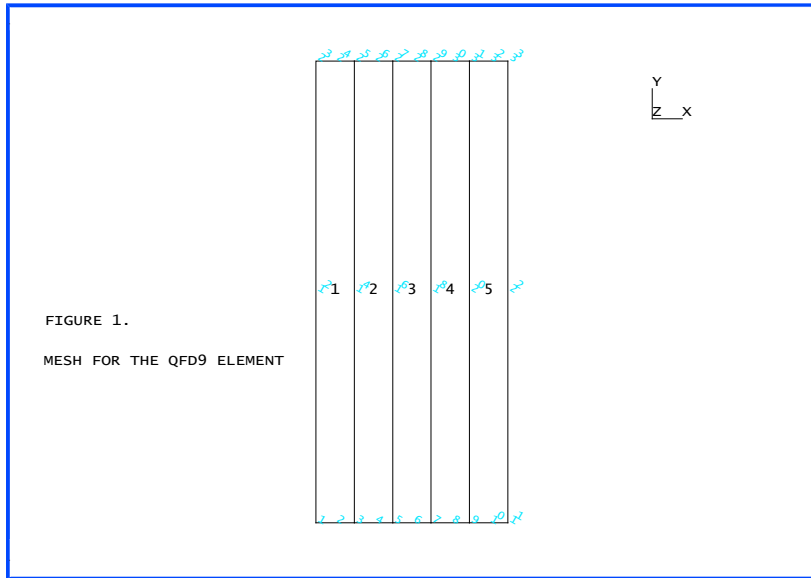


Figure 2

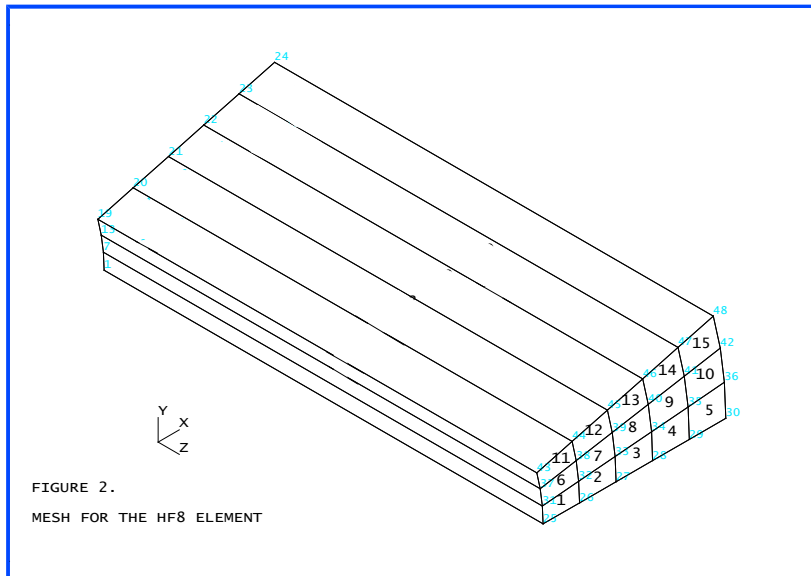


Figure 3

Example 3.1.1

Frequency Analysis Of A Simply Supported Beam

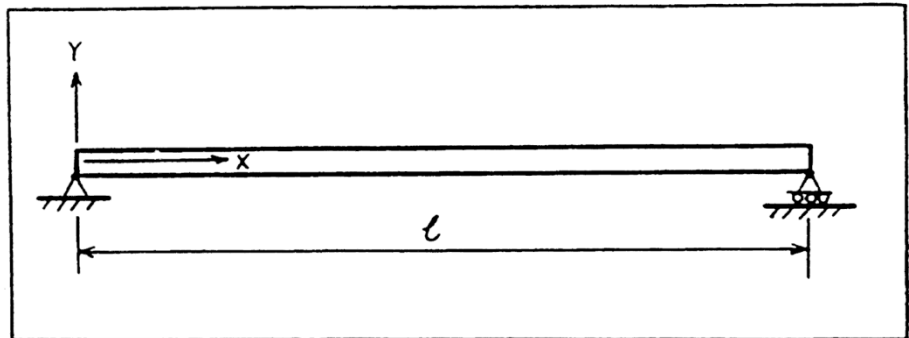
Keywords

Eigenvalue

Description

Determine the first three fundamental frequencies of the following simply supported beam.

Length, l	2.032 m
Area, A	$2.58 \times 10^{-3} \text{ m}^2$



Discretisation

Model the complete beam to include both symmetric and non-symmetric modes.

Geometric properties

Moment of inertia, I	$0.55497\text{E-}06 \text{ m}^4$
------------------------	----------------------------------

Material properties

Young's modulus, E	30 x10 ⁶ kN/m ²
Poisson's ratio, ν	0.3
Density, ρ	7780 kg/m ³

Theory

The fundamental frequencies may be determined from the following relationships;

$$\omega_n = (K_n)^2 \sqrt{(EI / ml^4)} \quad f_n = \frac{\omega_n}{2\pi} \quad (0.0.44)$$

$$l_n = w_n^2 = \text{eigenvalue}$$

$$K_n = np$$

$$m = \text{mass / unit length} = r A$$

Comparison

Mode	Exact	LUSAS
f ₁	28.763	28.7663
f ₂	115.05	115.400
f ₃	258.86	263.016

References

1. W.C. Hurty and M.F. Rubinstein, Dynamics of structures, Prentice-Hall, 1964. Chap. 5, p 203.

Input data

X03D11A.DAT

Example 3.1.2

Frequency Analysis Of A Sprung Mass

Keywords

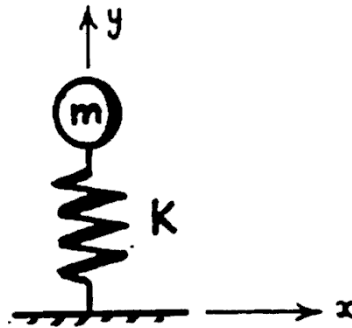
Eigenvalue

Description

Determine the natural frequency of vibration (f) of a mass, m , set on a rubber mount system with a stiffness K .

Mass (m) = 0.00647668 lb-sec² /in.

Stiffness of mount (K) = 48.0 lb/in.



Discretisation

Model with single joint element

Theory

The natural frequency may be determined from the following relationships;

$$\omega = \sqrt{\frac{K}{m}} \qquad \text{frequency} = \frac{\omega}{2\pi} \qquad (0.0.45)$$

$$I = \omega^2 = \text{eigenvalue}$$

Comparison

	Exact	LUSAS
Frequency (Hz)	13.7014	13.7014

References

1. W.C. Hurty and M.F. Rubinstein, Dynamics of structures, Prentice-Hall, 1964.

Input data

X03D12A.DAT

Example 3.1.3

Linear Buckling Analysis Of A Simple Portal Frame

Keywords

Linear Buckling

Problem Description

Determine the first two critical buckling loads for the rigid jointed portal frame shown in Figure 1. Compare the first in-plane critical load with a theoretical solution.

Discretisation

Model the rigid jointed portal frame using a coarse mesh of three BM3 beam elements and a finer mesh of nine BM3 or 18 BMI21 elements.

Geometry

The vertical members of the portal frame are 10m in length while the horizontal member is 8m in length (see Figure 1).

Geometric properties

All members have a 0.1m square, solid section.. The sections properties of the members are listed in the following table.

Cross-sectional area	0.01 m ²
Second moments of area (I_{yy} , I_{zz})	8.33333x10 ⁻⁶ m ⁴
Torsional constant	14.0833x10 ⁻⁶ m ⁴
Effective shear areas (A_{sy} , A_{sz})	8.33333x10 ⁻³ m ²

Material properties

All members have steel material properties (UK, BD2101), as listed below.

Young's modulus	20.0x10 ⁹ N/m ²
Poisson's ratio	0.3
Density	7.85x10 ³ Kg/m ³

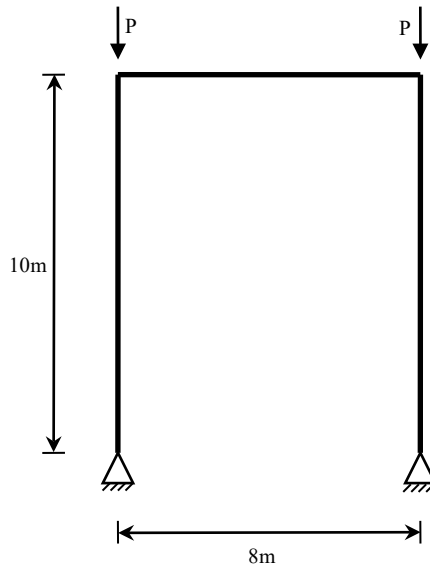


Figure 1: Rigid jointed portal frame used in linear buckling analysis. Loads P are unit loads.

Loading

The portal frame is subjected to unit loads applied to the ends of the vertical members in the vertical direction (Figure 1).

Boundary conditions

The portal frame is rigidly supported at the base nodes (Figure 1).

Theory

The theoretical solution for the in-plane critical buckling load, P_{cr} , is [1]

$$P_{cr} = k^2 EI_1 \quad (0.046)$$

where I_1 is the second moment of area of the horizontal member. The term k is found by solving the following equation.

$$\frac{k l}{\tan(k l)} = -6 \frac{I_1}{b I_2} \quad (0.047)$$

where l is the length of vertical member, b the length of horizontal member and I_2 the second moment of area of the vertical member.

With the material and geometric properties used in this example, the critical buckling load using equation (0.047) is

$$P_{cr} = 132.6 \times 10^3 \text{ N}$$

Comparison

The results from the theory, the coarse mesh and the fine meshes are listed in the table below

Analysis		$P_{cr}(N)$
Theory		132.6×10^3
Coarse mesh	BM3	147.9×10^3
Fine mesh	BM3	132.8×10^3
	BMI21	135.3×10^3

References

1. S.P. Timoshenko and J. M. Gere, "Theory of Elastic Stability."2nd ed. McGraw-Hill Kogakusha Ltd., 1961, pp 149-150

Input data

Coarse mesh (BM3) : X03D13A.DAT

Fine mesh (BM3) : X03D13B.DAT

Fine mesh (BMI21) : X03D13C.DAT

Example 3.1.4

Frequency Of Prestressed 3×3 Flat Cable Net

Keywords

Bar, Cable, Eigenvalue

Description

Determine the fundamental frequency of the prestressed 3 × 3 flat cable net shown in Figure 1.

Discretisation

Each cable is modelled by one three dimensional CTNS2 catenary or BRS2 bar element.

Geometry

Each cable has:

Cross-section area $A = 0.5 \text{ in}^2$

Chord length = 40 in

Material properties

Young's modulus $E = 20 \times 10^6 \text{ lb/in}^2$

Weight per unit volume $\rho g = 0.29 \text{ lb/in}^3$ or density $\rho = 7.51123 \times 10^{-4} \text{ lb/in}^3$

Loading

The initial prestress in each cable is $1.5 \times 10^5 \text{ lb/in}^2$; self-weight is considered as well.

Boundary conditions

The net outer perimeter is fixed (Figure 1).

Theory

Unstressed cables have zero stiffness; the frequency is determined by the mass and initial stress stiffness.

Comparison

The fundamental frequency obtained by LUSAS is presented in Table 1, agreeing well with the published results adopting lumped and consistent mass matrices, respectively.

Table 1: Comparison of the fundamental frequency of the 3×3 flat net (Figure 1) by various methods

Method	Frequency (Hz)	
	Lumped mass	Consistent mass
Soler and Afshari [7]: Galerkin		59.10
Shore and Chaudhari [6]:		
Lumped mass	56.40	
Membrane		58.80
Leonard [3], curved element:		
12 elements		61.59
24 elements		59.55
48 elements		59.05
Sangster and Batchelor [5]:		
Lumped mass	56.76	
Equiv. Membrane		60.43
Gambhir and Batchelor [1]: Curved element		60.06
Ozdemir [4], curved elements:		
2 node elements		61.64
3 node elements		58.97
4 node elements		58.93
Kwan [2]: 2-node elements	56.29	61.37
LUSAS		
CTNS2	56.4382	
BRS2		61.5944

References

1. Gambhir, M.L., Batchelor, BdeV. (1977) A finite element for 3-D prestressed cablenets. Int J Numer Meth Engng. 11: 1699-1718.
2. Kwan, A.S.K. (2000) A simple technique for calculating natural frequencies of geometrically nonlinear prestressed cable structures. Computers and Structures 74: 41-50.
3. Leonard, J.W. (1973) Non-linear dynamics of curved elements. ASCE J Engng Mech Div 99: 616-621.
4. Ozdemir, H. (1979) A finite element approach for cable problems. Int. J. Solids Structures 15: 427-437.
5. Sangster, K.G., Batchelor, BdeV. (1974) Non-linear dynamics analysis of 3-D cablenets. In: Proceedings of International Conference on Computational Methods in Non-linear Mechanics, University of Texas, 1974. p.301-310.
6. Shore, S., Chaudhari, B. (1972) Free vibration of cable networks utilizing analogous membranes. In: Proceedings of 9th International Congress of the Association of bridges and Structural Engineering, Amsterdam. 1972, p. 445-451.
7. Soler, A.I., Afshari, H. (1970) On the analysis of cable network vibrations using Galerkin's method. ASME J Appl Mech 37: 606-611.

Input data

X03D14A.DAT

X03D14B.DAT

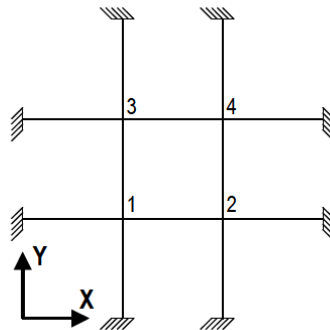


Figure 1: Prestressed cable net.

Example 3.3.1

Cantilevered Thin Square Plate

Keywords

Eigenvalue, Guyan Reduction

Description

A square plate with side length 10m and uniform thickness 0.05m is restrained against translation and rotation along the $X=0$ edge, figure 1. It is required to find the lowest 6 eigenmodes of the plate (shown in figures 2 to 7) using:

- i) Subspace iteration
- ii) Guyan reduction with 12 automatic master freedoms
- iii) Guyan reduction with 20 automatic master freedoms
- iv) Guyan reduction (with automatic masters) as a first approximation to the subspace iteration vectors
- v) Guyan reduction with 20 specified master freedoms
- vi) Guyan reduction (with specified masters) as a first approximation to the subspace iteration vectors

This example compares the convergence of Guyan reduced solutions with that of full subspace iteration analysis as master density is increased. Further, it illustrates the use of a Guyan reduced solution as a starting point for subspace iteration analyses.

Discretisation

The whole plate is discretised using a regular mesh of 16 ($4*4$) quadrilateral 8-noded Semiloof shell elements (QSL8).

Material properties

Young's modulus	$200.0 \times 10^6 \text{ N/m}^2$
Poisson's ratio, ν	0.3
Mass density, ρ	8000 Kg/m^3

Theory

Thin plate predictions of the natural frequencies of a cantilevered square plate of side length (a) and thickness (t) are given by the following relationship:

$$f_{ij} = \frac{\lambda_{ij}^2}{2\pi a^2} \left[\frac{Et^2}{12\rho(1-\nu^2)} \right]^{1/2} \quad (0.0.48)$$

For a Poisson's ratio of 0.3, the values tabulated below may be obtained:

Mode	λ_{ij}^2	f_{ij} (Hz)
1	3.494	0.421
2	8.546	1.029
3	21.440	2.582
4	27.460	3.306
5	31.169	3.753
6	54.440	6.555

Lusas results

The results obtained from the LUSAS analyses are presented below, and are compared with those given in [2]:

Mode Number	1	2	3	4	5	6
Reference solution	0.421	1.029	2.582	3.306	3.753	6.555
Subspace iteration eigenvalue evaluation	0.415	1.013	2.502	3.233	3.684	6.422
Guyan reduction 12 automatic masters	0.416	1.025	2.797	3.552	4.121	9.399
Guyan reduction 20 automatic masters	0.415	1.014	2.583	3.293	3.908	7.336
Guyan reduction with automatic master approximation	0.415	1.013	2.501	3.233	3.684	6.422
Guyan reduction 20 specified asters	0.415	1.014	2.519	3.274	3.746	6.762
Guyan reduction with specified master approximation	0.415	1.013	2.502	3.233	3.684	6.422

Note

1. The relatively poor solutions obtained using automatic master selection with Guyan reduction are due to the fact that the K/M ratios are constant for all internal nodes.
2. The subspace iteration procedure converges in less iterations when the eigenvectors of the Guyan reduction analysis are used as starting iteration vectors.

References

1. Abbassian,F., Dawswell,D.J., Knowles,N.C. "Free Vibration Benchmarks", Tests 73 and 74, NAFEMS Report FVB, EAD 6.11.87, (November 1987), Report prepared by W.S.Atkins Engineering Science for National Agency for Finite Element Methods and Standards.
2. Blevins, R.D., "Formulas for Natural Frequency and mode shape", Publishers Van- Nostrand, (1979).
3. LEISSA,A.W., "Vibration of plates", National Aeronautical and Space Administration, N.A.S.A Report SP-160, (1969)

Input Data

X03D31A.DAT

X03D31B.DAT

X03D31C.DAT

X03D31D.DAT

X03D31E.DAT

X03D31F.DAT

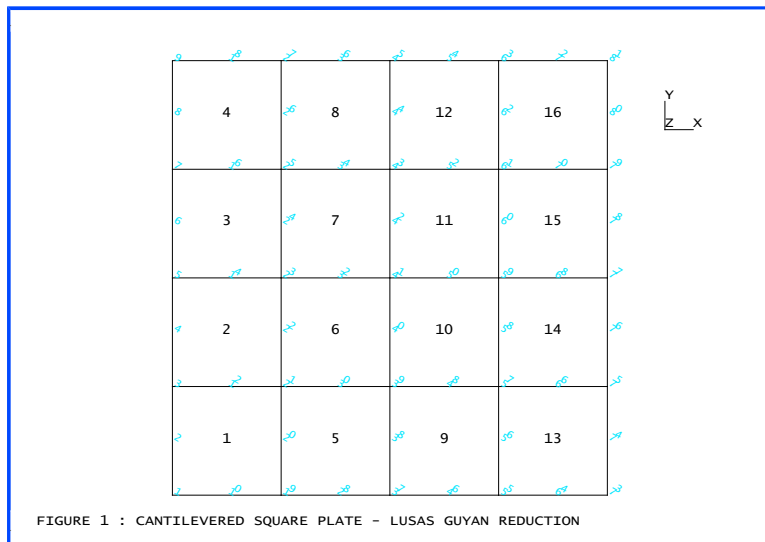


Figure 1

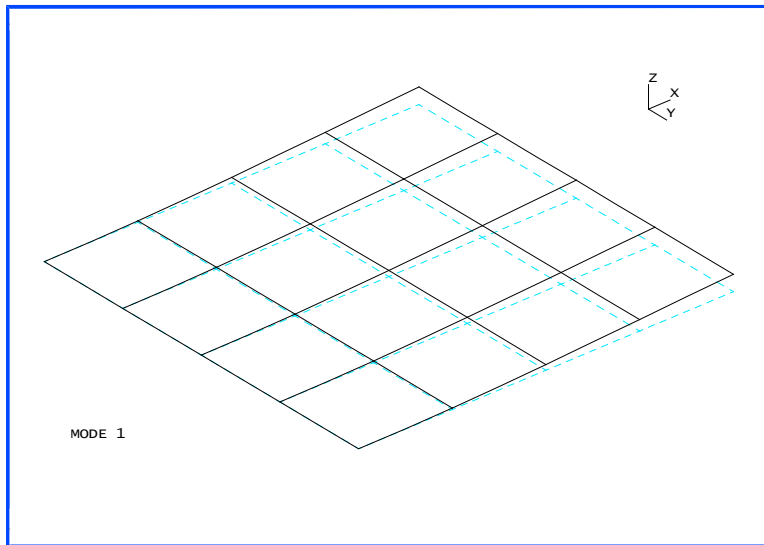


Figure 2

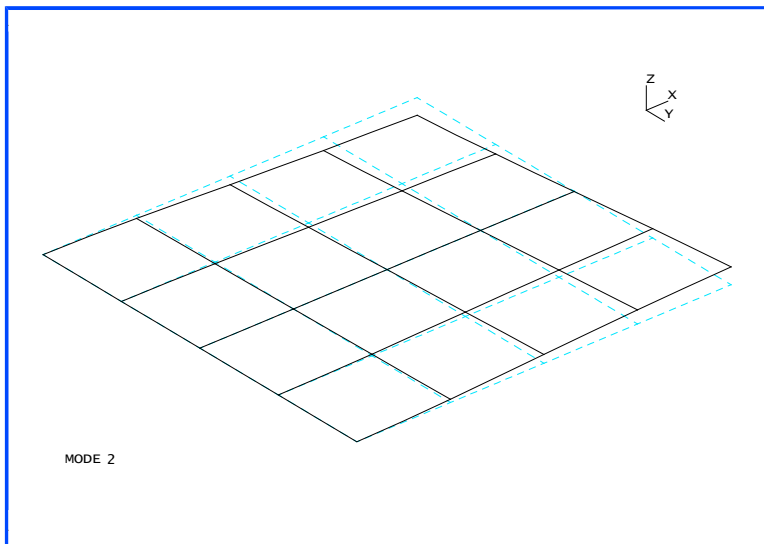


Figure 3

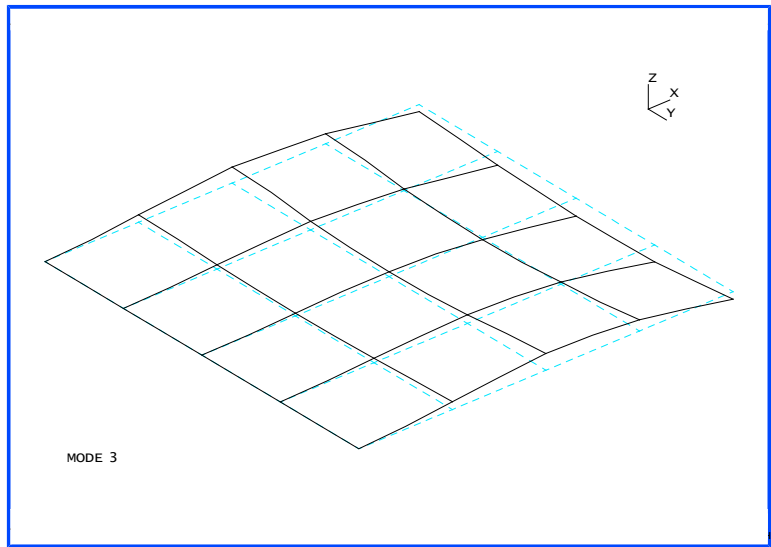


Figure 4

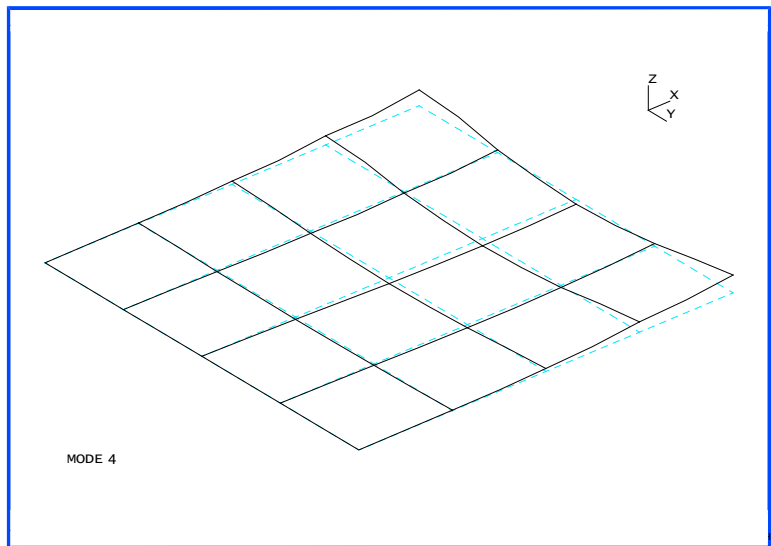


Figure 5

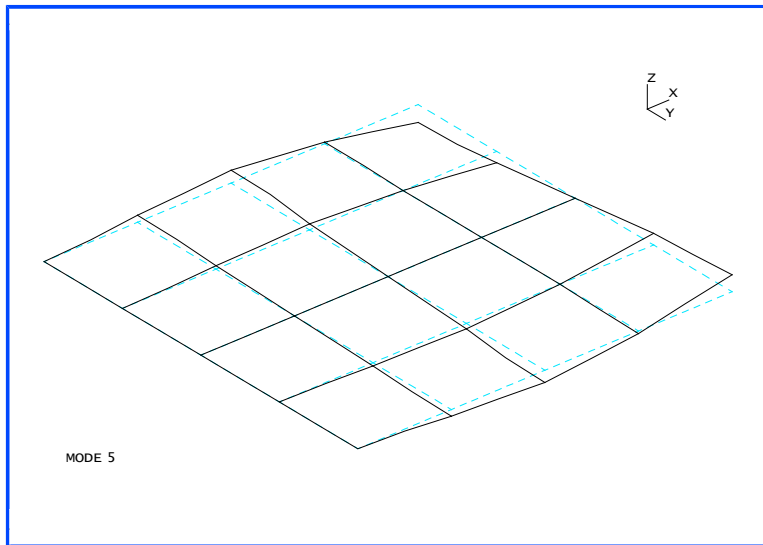


Figure 6

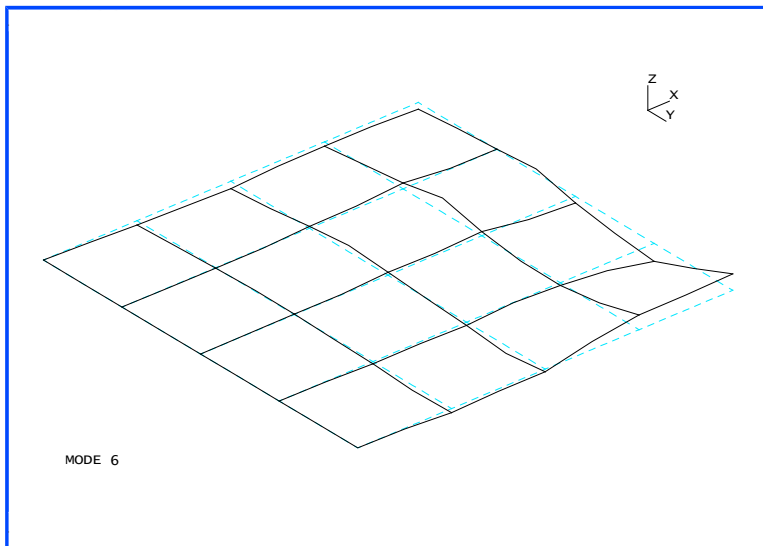


Figure 7

Example 3.4.1

Bifurcation Of A Double Arch

Keywords

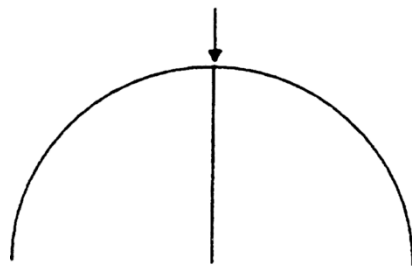
Total Lagrangian, Large Rotation, Eigenvectors Of Stiffness Matrix

Description

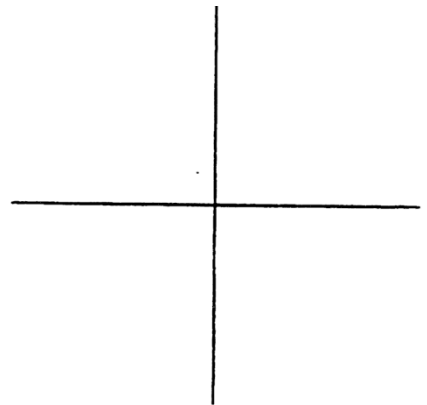
Two orthogonal arches, joined at their crowns, are subject to a point load applied in the vertical direction. The structure is loaded to close to its critical load and the eigenvectors corresponding to the buckling modes are evaluated.

Finite Element Model

The arches are modelled by 60 BTS3 beams, which are pinned at the supports.



Elevation



Plan

Geometry

Radius of the arch = 5

Angle subtended by arch = 180 degrees

Beam geometric properties

Area	= 0.1
2nd moment of area about y-axis I_{yy}	= 0.4E-5
2nd moment of area about z-axis I_{zz}	= 0.8E-5
Torsion stiffness K_T	= 0.1406x10 ⁻⁴
Shear area A_{s_y}	= 0.1
Neutral axis eccentricity e_z	= 0.0

Material properties

Young's modulus	210.0x10 ⁹
Poisson's ratio	0.0

Load

Load applied in (downwards) vertical direction at joint of arches in three

Steps

step 1 - 1.5*10⁵

step 2 - 3.0*10⁵

step 3 - 4.042*10⁵

Boundary Conditions

Beam ends are free to rotate but are restrained against translations in the x, y and z directions.

Solution Comparison

The eigenvalues extracted at near the critical load are:

Mode	Eigenvalue
1	-0.398217
2	-0.398217
3	1025.41
4	13100.2
5	13347.1
6	14828.8

At a critical load corresponding to a bifurcation or limit point, the determinant of the stiffness matrix is zero or equivalently one or more of the eigenvalues of the stiffness matrix are zero. The negative eigenvalues indicate that the load applied is slightly above the critical buckling load but these numbers are close enough to zero to assume that the buckling load is given by the load applied. The eigenvector corresponding to the lowest eigenvalue is the buckling mode. In this instance, the double symmetry of the combined arches leads to a compound bifurcation involving two buckling modes as shown in figure 1. Further higher modes are also presented in figure 1.

Input Data

X03D41A.DAT

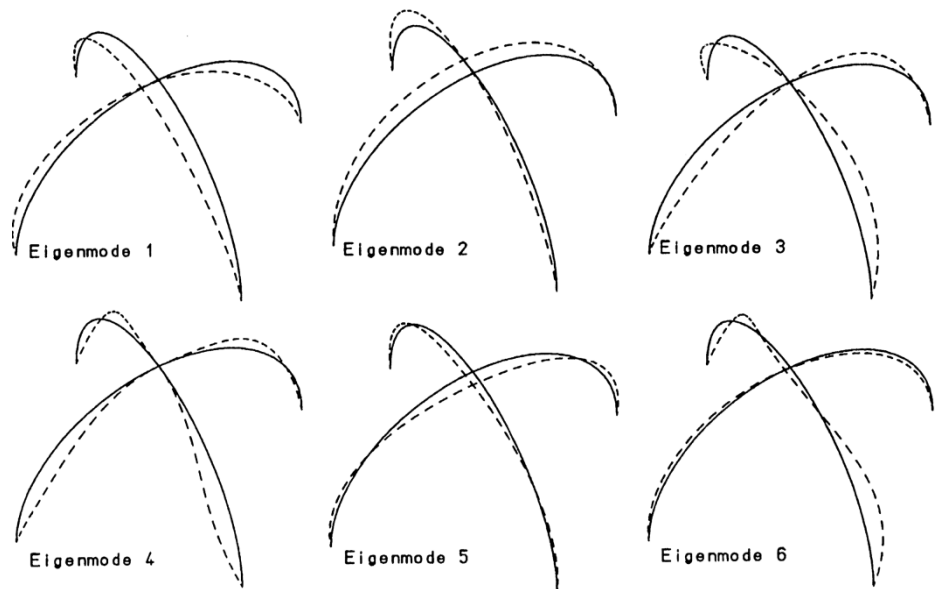


Figure 1 Eigenmodes of Double Arch

Example 3.5.1

Natural Frequency Analysis Of A Solid Cantilever

Keywords

Eigenvalue, Natural Frequency

Description

To determine the first four natural frequencies of the cantilevered beam shown in Figure 1.

Finite Element Model

The cantilevered beam consists of four HX20 3-D solid elements with the element and node numbering detailed in Figure 2.

Material properties

Young's modulus	30.0x10 ³ N/m
Mass density	5.0 kg/m

Boundary conditions

All nodes in the y-z plane at x=0 are fully restrained resulting in an encastre support condition.

Theory

The natural frequencies of beams with various end constraints can be found in [1]. The natural frequencies, w , of a cantilevered beam may be determined from the following equation:

$$w_n = (Bl)_n^2 \left(\frac{EI}{ml^4} \right) \quad (0.0.49)$$

where the Bl factors for the first four natural frequencies are given by

$$Bl_1 = 1.872$$

$$Bl_2 = 4.694$$

$$Bl_3 = 7.855$$

$$Bl_4 = 10.9955$$

The other terms appearing in the equation for the natural frequencies are, for this particular example

$$E = \text{Young's modulus} = 30,000 \text{ N/m}^2$$

$$I = \text{second moment of inertia} = 8.33333\text{E-}02 \text{ m}^4$$

$$m = \text{mass per unit length} = 5.00 \text{ Kg/m}$$

$$l = \text{beam length} = 10 \text{ m}$$

Modelling Hints

This simple example has been chosen for two main reasons. The first is to enable a comparison to be made with theoretical values, and the second is to highlight LOCAL CARTESIAN COORDINATES, COPY NODES and EIGENVALUE CONTROL facilities. Comments on the use of these commands have been included in the data file printout.

The first side of the beam is defined by using QUADRILATERAL SPACING and SIDE POINTS. The mid-height and full height nodes are described by defining a LOCAL CARTESIAN COORDINATE system about these heights and using COPY NODES to copy a repetitive pattern of nodes to a new position and orientation. In this case from the lower surface to the mid-height and full height. These coordinates are then transformed to the global system by using the command GLOBAL CARTESIAN COORDINATES.

It must be noted that because of the regular geometry, a more convenient method of generating the nodal coordinates, would be by using the INCREMENTAL line generation facility.

```
e.g.  NODE COORDINATES
      FIRST 1 0 0 0
      INC   1 0 0 0.5 3
      INC   3 0 0.5 (3)
      INC   9 0.125 (9)
```

Solution Comparison

Mode	1	2	3	4
Theory	0.6179	0.6179	24.27	24.27
LUSAS	0.6168	0.6168	24.00	24.00

Note:

The coefficients (Bl_1) and (Bl_2) defined in the theory section refer to modes in 2-D, and are repeated in the 3-D case. So modes 1 and 2 in 2-D correspond to modes 1, 2, 3 and 4 respectively in 3-D.

References

1. Hurty, W.C. and Rubinstein, M.F., 'Dynamics of Structures', Prentice-Hall Inc.

Input data

X03D51A.DAT

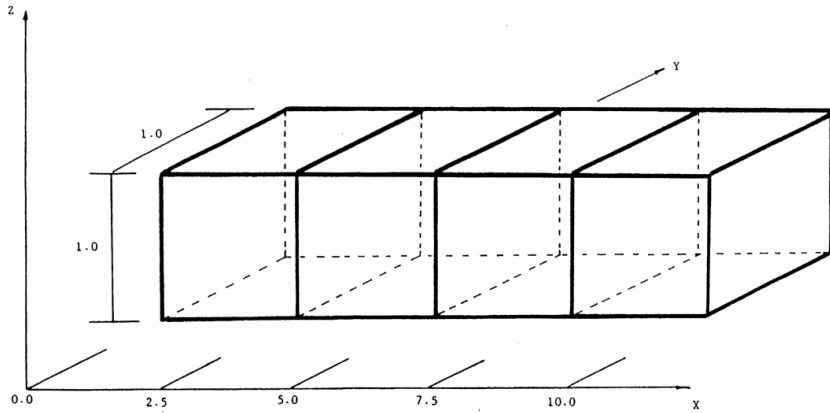
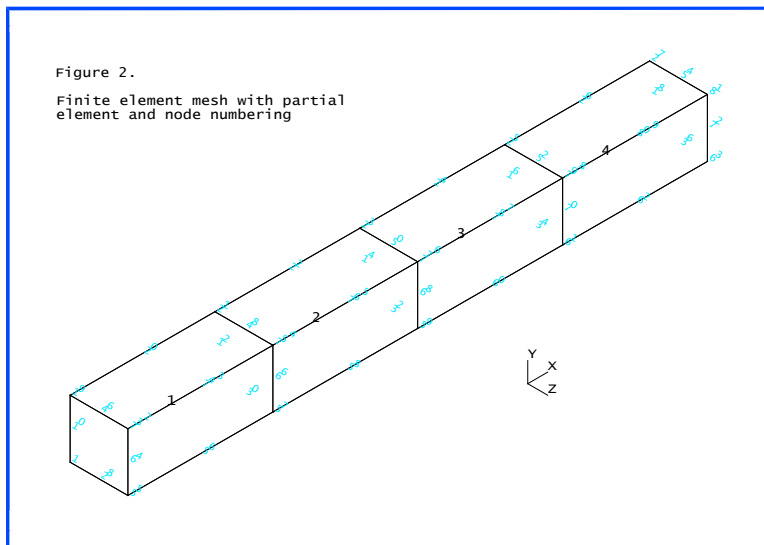


Figure 1. Cantilever beam made up of 4 HX20 type elements.



Example 3.6.1

Buckling Analysis Of A Rectangular Panel

Keywords

Buckling, Eigenvalue, Semiloof

Description

Determine the critical buckling load for a rectangular panel subject to in-plane compressive loading. The dimensions of the panel are as follows:

Length, a	2 m
Width, b	0.5 m
Thickness, t	0.001 m

The panel is subjected to an in-plane compressive load acting along the short edges.

Discretisation

The whole structure is discretised using 16 Semiloof shell elements (QSL8) and is simply supported on all sides. The in-plane compressive loading is applied as a series of concentrated loads acting in the plane of the structure parallel to its long sides. A total load of 24 N is applied to each loaded edge.

Material properties

Young's modulus	70×10^9
Poisson's ratio	0.3

Theory

For a given integer side length ratio (a/b) and number of half waves in the buckled configuration (m), the critical buckling load is given by the expression

$$N_{xcrit} = \frac{\pi^2 D}{b^2} \left(m \frac{b}{a} + \frac{1}{m} \frac{a}{b} \right)^2 \quad (0.0.50)$$

For 4 half waves and a side length ratio of 4, (0.0.50) therefore reduces to

$$N_{xcrit} = \frac{4^2 \pi^2 D}{b^2} \quad (0.0.51)$$

Where

$$D = \frac{Et^3}{12(1-\nu^2)} \quad (0.0.52)$$

The critical buckling stress is given by the expression

$$\sigma_{xcrit} = \frac{N_{xcrit}}{t} \quad (0.0.53)$$

or, combining (0.0.51)-(0.0.53) by

$$\sigma_{xcrit} = \frac{4\pi^2 Et^3}{12b^2(1-\nu^2)t} \quad (0.0.54)$$

Comparison

The results obtained from the LUSAS analysis are compared to the theoretical results. From (0.0.54) the theoretical critical buckling stress is given by the expression

$$\sigma_{xcrit} = 3.62 E \left(\frac{t}{b} \right)^2$$

or

$$s_{xcrit} = 1.013 \text{ MN} / \text{m}^2$$

Results from the LUSAS analysis were as follows:

Eigenvalues after 11 iterations

Mode	Eigenvalue	Load factor	Error norm
1	19.1316	19.1316	0.678980E-01

The critical buckling load and corresponding stress are

$$N_{x_{crit}} = 19.1316 * 24 = 459.184 \text{ N}$$

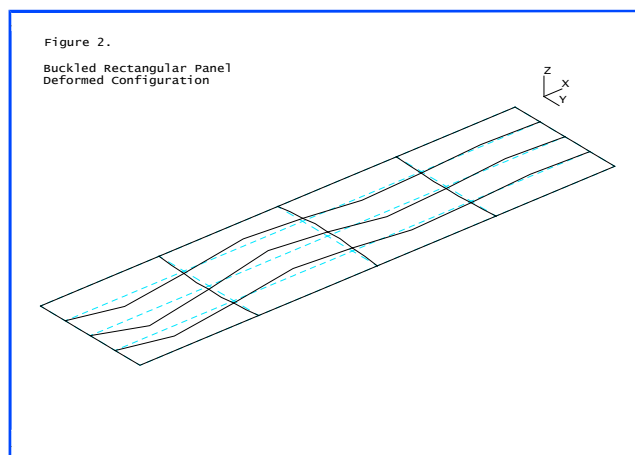
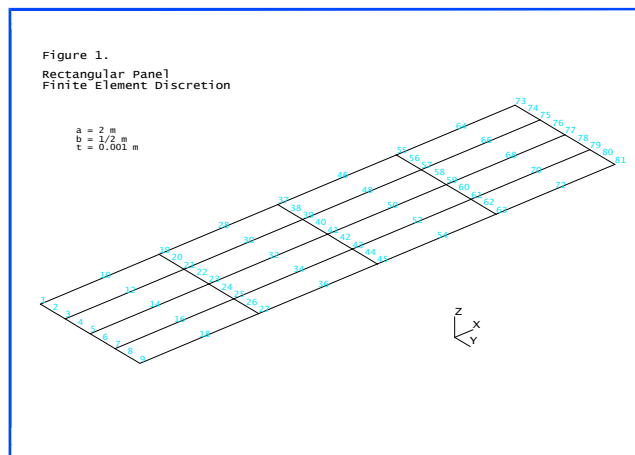
$$s_{x_{crit}} = 459.1584 / (\text{Area}) = 459.1584 / (0.5 * 0.001) = 0.918316 \text{ MN} / \text{m}^2$$

References

1. 'Formulas for stress and strain', Fourth Edition, R.J.Roark, Publisher. McGraw-Hill Book Co. Kogakusha Co. Ltd. Tokyo (1965).

Input data

X03D61A.DAT



Example 3.7.1

Eigen-Analysis Of A Cooling Tower

Keywords

Fourier, Semiloof Shell, Eigenvalue

Description

The first four modes of a cooling tower are extracted. Both Fourier and Semiloof elements are used and the results compared.

Discretisation

The cooling tower is modelled initially by 10 QAX8F Fourier elements. The circumferential number of harmonics is varied from 0 to 6 with an eigenvalue analysis performed for each harmonic.

The QSL8 elements are utilised with two meshes; 10 elements are used in both to model the length of the cooling tower, whilst 12 and 48 elements respectively are used to represent coarse and fine modelling of the circumference.

Geometry

The shell mid-surface is defined by the parabolic equation,

$$\left[\frac{x}{84} \right]^2 - \left[\frac{y - 270}{209.661} \right]^2 - 1 \quad (0.055)$$

The overall height of the cooling tower is 330ft (100.584m) and has a constant wall thickness of 0.5833ft (0.1778m). The outside radii at the bottom and top of the tower are 136.96ft (41.745m) and 87.4ft (26.64m) respectively.

Boundary Conditions

The cooling tower is assumed to be encastre at the base.

Material properties

Young's modulus	432.0 x10 ⁶ psf, 20.68x10 ⁹ Pa
Poisson's ratio	0.15

Mass density	8000 lb ft ⁻³ , 128,147.7 kg m ⁻³
--------------	---

Theory

The eigenvalues obtained from the two analysis types are compared.

LUSAS results

Figures 1 and 2 show the first four eigenvectors from the coarse and fine shell analyses respectively. The extracted frequencies from the Fourier analysis are detailed in Table 1 below.

Table 1: Fourier frequencies

Eigenvalue Number	Harmonic Number						
	0	1	2	3	4	5	6
1	0.1855	0.0788	0.0423	0.0332	0.0296	0.0283	0.0333
2	0.2805	0.1633	0.0889	0.0483	0.0360	0.0378	0.0387
3	0.2978	0.2544	0.1683	0.1052	0.0679	0.0514	0.0530

The eigenvalues obtained from the Fourier analyses indicate that the lowest four modes correspond to the n= 5,4,3,6 harmonics. However, the frequencies obtained from the coarse shell analysis (see Table 2) produce higher frequencies and ordered the harmonics as n=4,3,5,6. The inability of the structure to deform into its true eigenmodes is due to the coarse mesh discretisation and the resulting stiffer structural response. A refined QSL8 mesh produces answers that are in closer agreement with the Fourier analyses and predict a harmonic order of n= 5,4,3,6.

Table 2: Frequency comparison

Harmonic Number	Fourier	Course shell	Fine shell
n=3	0.03318	0.03423	0.03356
n=4	0.02958	0.03319	0.02994
n=5	0.02829	0.03637	0.02871
n=6	0.03333	0.03788	0.03394

Using the QSL8 elements, two repeated eigenvalues are obtained for each mode which are out-of-phase with each other (not always by 90 degrees). For a cylindrical structure there are an infinite number of eigenvectors for each harmonic, but all can be modelled by two out-of-phase eigenvectors. Relative solution times for the analyses are detailed in Table 3, from which it may be seen that the Fourier analysis compares favourably with the shell analyses.

Table 3: Solution times

Fourier (QAX8F)	QSL8(coarse)	QSL8(fine)
1	7	52

The mode number n can sometimes be very large for thin shell structures, and in these instances, the Fourier solution quickly provides a sweep of selected harmonics n . If the precise eigenvalues from a shell analysis are required, the knowledge provided from the Fourier analysis can be used to decide on the mesh discretisation for a complete model of the structure or on the selection of a segment of the shell to which symmetric and asymmetric boundary conditions can be applied in turn.

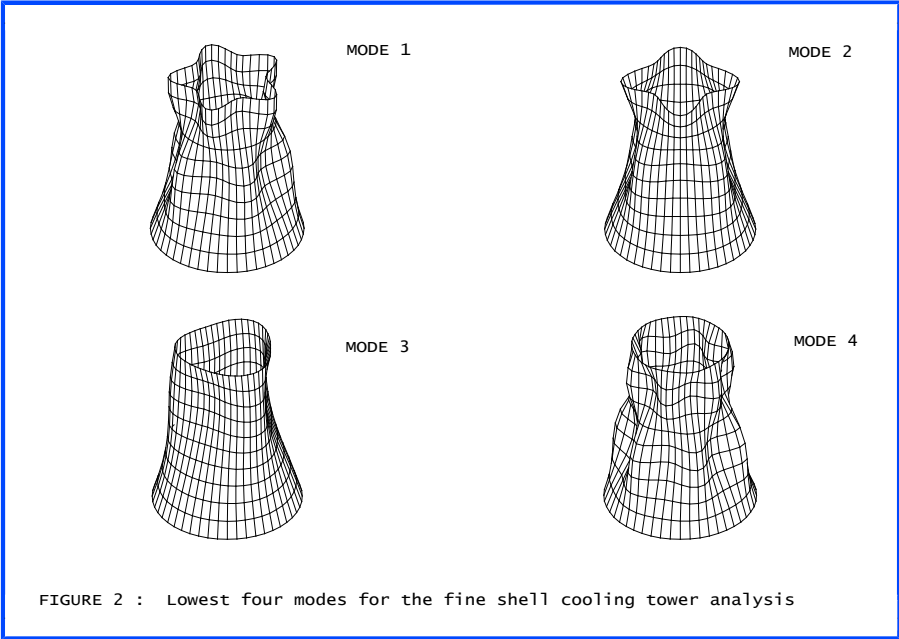
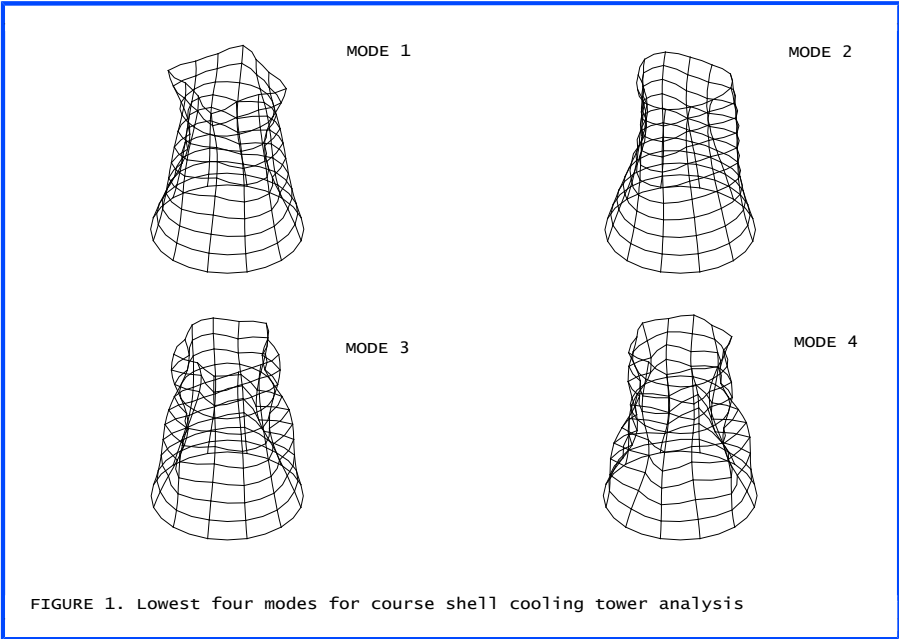
References

1. Program Verification and Qualification Library, ASME Pressure Vessel and Piping Division, Committee on Computer Technology, 1972.
2. Albasiny, E.L. and Martin, D.W., Bending and Membrane Equilibrium in Cooling Towers, Jour. Eng. Mech. Div., ASCE, EM3, 1967.

Input Data

X03D71A.DAT
X03D71B.DAT
X03D71C.DAT
X03D71D.DAT
X03D71E.DAT
X03D71F.DAT
X03D71G.DAT
X03D71H.DAT
X03D71I.DAT

Note: The different results for taking 0,1,2.. terms of the Fourier expansion can be obtained by changing the range of the harmonic series defined in the FOURIER CONTROL data chapter.



Example 4.1.1

Geometrically Nonlinear Analysis Of A Cantilevered Beam

Keywords

Updated Lagrangian, Geometric Nonlinearity

Description

Determine the large deformation response of the thin, cantilevered strip, shown in Figure 1, subject to a point load at the tip.

Discretisation

Model the cantilever using eight, equal length, two dimensional BM3 beam elements (see Figure 1).

Geometry

The cantilever has a width of 1 inch, a depth of 0.1 inches and the nodal line is assumed to coincide with the centroid of the cross section. Thus, each element has the following geometric properties;

Cross-sectional area	= 0.1 inch ²
Second moment of area about the local z axis	= 0.8333E-4 inch ⁴
First moment of area about the local z axis	= 0.0 inch ³

Material properties

Young's modulus	120.0x10 ⁶ lb/in ²
Poisson's ratio	0.3

Boundary conditions

The cantilever is rigidly supported at node 1 (see Figure 1).

Theory

This problem is one of the classical elastic problems which have analytical solutions based on elliptical integrals. Reference 1 gives further details on this method of solution and also presents a table of tip displacements and rotations for various load levels.

Comparison

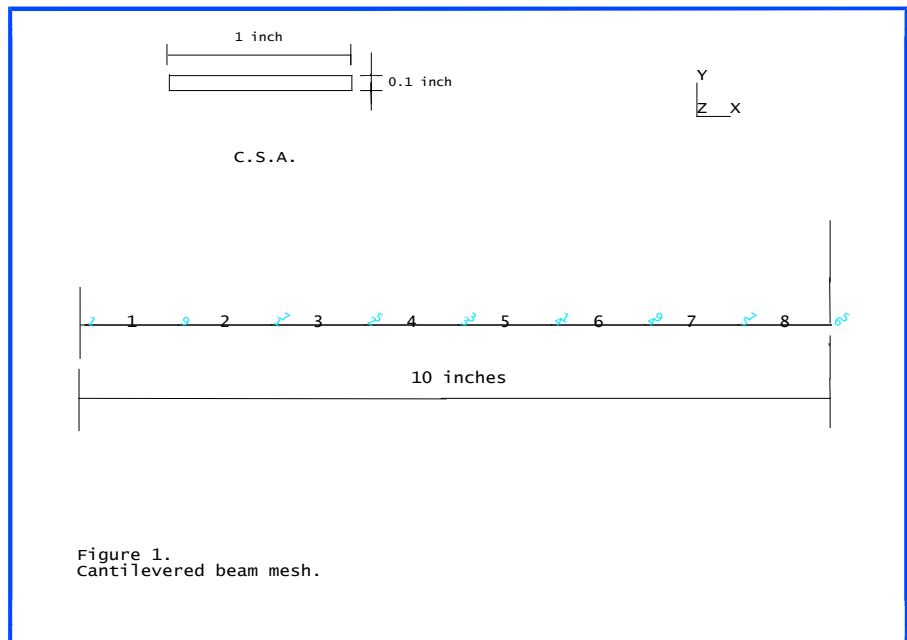
A comparison of the theoretical and LUSAS results is given in Figure 2. Theta is the rotation at the tip in radians. Figure 3 shows the deformed configurations for various PL^2/EI values.

References

1. TIMOSHENKO, S.P. and GERE, J.M. Mechanics of materials. Van Nostrand Reinhold Co., S.I. ed., 1973.

Input Data

X04D11A.DAT



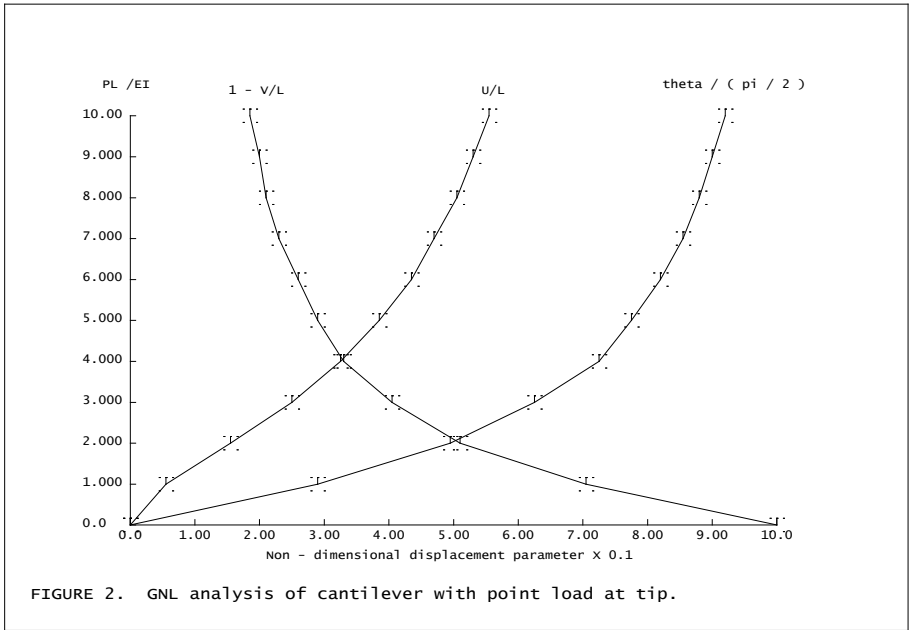


FIGURE 2. GNl analysis of cantilever with point load at tip.

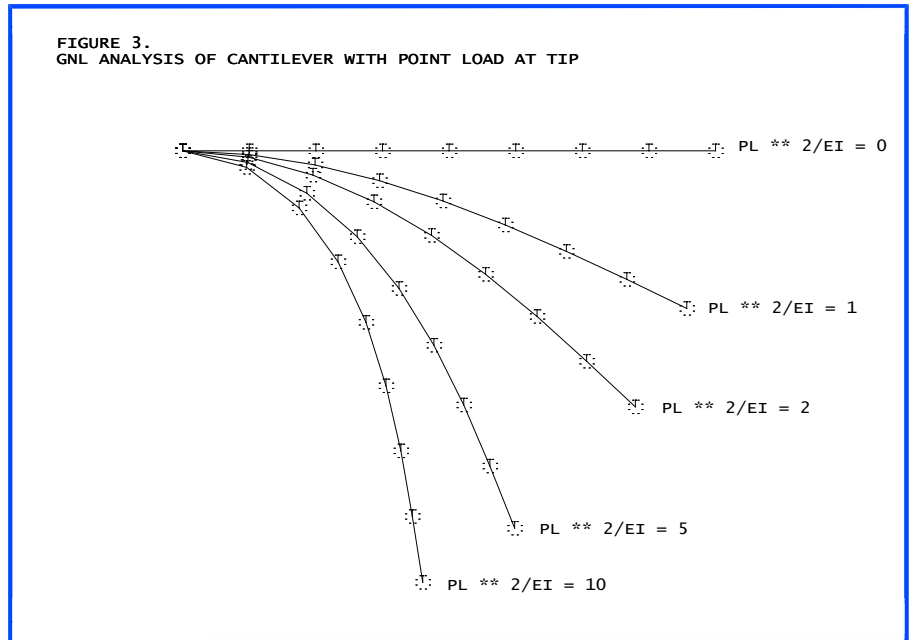


FIGURE 3. GNl analysis of cantilever with point load at tip

Example 4.1.2

Bifurcation Of Simple Bar-Spring System

Keywords

Bar, Spring, Bifurcation

Description

The bar-spring system shown in Figure 1 is subjected to an axial load. The system is stable until the horizontal load reaches the buckling load. At this point, the solution is forced to branch on to an unstable path and the end of the bar that is attached to the spring begins to move vertically. By continuing the solution further, the vertical displacement of the end of the bar reaches a peak and then reduces towards zero. The bifurcation path is followed until a second bifurcation point is encountered, Figure 2.

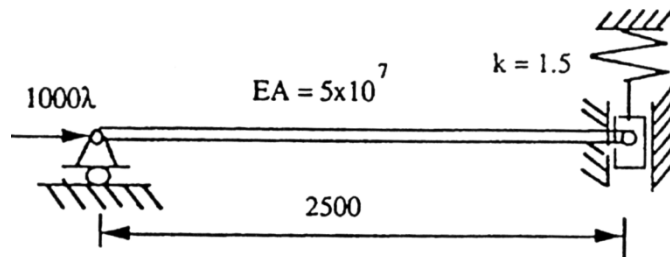


Figure 1: Bar-spring system

Discretisation

The system consists of a horizontal bar element BAR2 with area $A=1.0$ connected to a vertical spring element JNT3 at one end.

Material properties

BAR3: Young's Modulus	=	.5E8 KN/m ²
Poisson's ratio	=	0.0
JNT3: Spring stiffnesses	=	0.0 (x direction)
	=	1.5 (y direction)

Theory

The equilibrium equations for the system can be written as:

$$\begin{Bmatrix} F \\ 0 \end{Bmatrix} = \begin{bmatrix} EA/L & 0 \\ 0 & k + N/L \end{bmatrix} \begin{Bmatrix} \Delta u \\ \Delta w \end{Bmatrix} \quad (0.056)$$

where L is the length of the bar and N the axial force in the bar; the vertical spring stiffness is k . Δu and Δw are increments in the displacements shown in Figure 1. The bar-spring system is stable until the stiffness matrix becomes singular. This occurs when $N = -Lk$, which is equal to 3750 for the parameters used in this problem. As the axial force in the bar is given by $F=EA/L*u$, the axial displacement at the loaded end at the bifurcation point can be computed as $u=0.1875$.

Comparison

Figure 2 shows the stable primary solution path which was obtained by carrying out a nonlinear analysis with bracketing. It can be seen that the vertical displacement was zero along this path. The bifurcation point that was bracketed is shown to be at the point $F=3749.7$, $w=0$, $u=0.187506$ which agrees very closely with the theoretical values. The unstable secondary (or bifurcated) path is also shown in the figure and it can be seen that the vertical displacement peaks at a value of just under 2500 while the horizontal load varies between values of ± 3750 . This path was obtained after a restart analysis by utilising the branching option within the nonlinear control data section of the data file. The solution is continued along the unstable path until a second bifurcation point is encountered, Figure 2. It is only possible to bracket one bifurcation point therefore the solution along this unstable path cannot progress any further.

References

1. Non-linear Finite Element Analysis of Solids and Structures (volume 1), M.A. Crisfield. John Wiley & Sons Ltd., England (1991).

Input Data

X04D12A.DAT

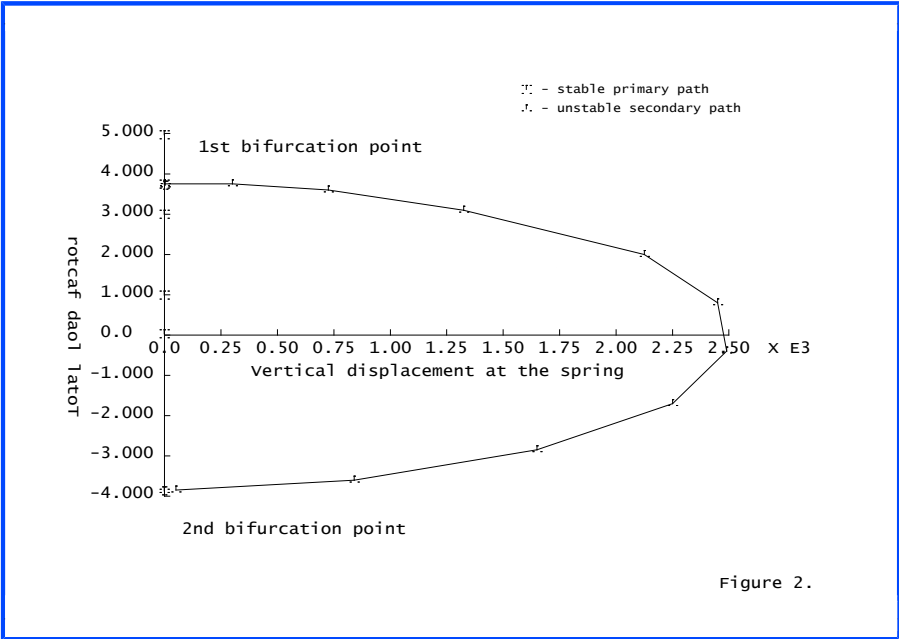


Figure 2.

Example 4.1.3

Suspended Cable With Uniform And Concentrated Loading

Keywords

Cable, Catenary, Shape Calculation, Geometric Nonlinearity

Description

Determine the response of a suspended cable subjected to uniform self-weight and concentrated loads (Figure 1).

Discretisation

Model cable segment 12 using one CTN2 catenary cable element, or four equal length BAR2 bar elements, or two equal length BAR3 curved bar elements; model cable segment 23 using one CTN2 element, or six equal length BAR2 elements, or three equal length BAR3 elements. Identical results will be obtained if using three dimensional counterpart elements.

Geometry

See Figure 1.

Material properties

See Figure 1.

Boundary conditions

End points 1 and 3 are simply supported (see Figure 1).

Theory

To analyse this problem correctly a nonlinear solution procedure is adopted to account for the large displacements.

Point 2 is set at an arbitrary Z coordinate. The self-weight load is applied first and the cable automatically assumes the correct catenary shape as a result of this analysis. Next the 8 kip load is applied continuing from the state at the end of the self-weight analysis (and including the loads from the self-weight case). Large displacement effects are intrinsic to the catenary cable element. The co-rotational formulation is adopted by BAR2; while BAR3 requires the use of a local Total Lagrangian formulation together with the global co-rotational formulation.

Comparison

The displacements at point 2 computed by LUSAS are compared with Tibert [1] in Table 1. CTN2 elements give results identical to Tibert. The results from BAR3 agree very well with the catenary element; BAR2 element is slightly stiffer, a discretisation of finer elements will lead to improvement.

Table 1: Displacements at point 2 due to the point load only

Displacement, ft	Tibert [1] 2 CTNS2	LUSAS		
		2 or 10 CTN2/CTNS2	10 BAR2/BRS2	5 BAR3/BRS3
x-Displacement	-2.819	-2.819	-2.770	-2.819
z-Displacement	-18.457	-18.457	-17.945	-18.455

References

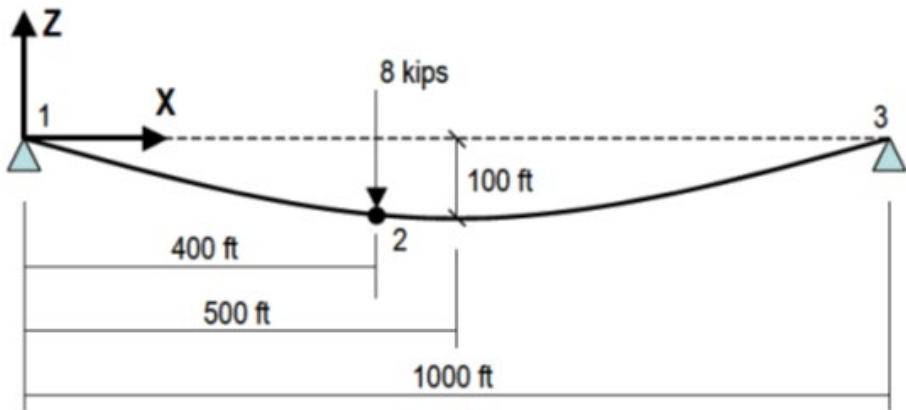
1. Tibert, G. (1999) Numerical analyses of cable roof structures Licentiate thesis, Royal Institute of Technology, Stockholm, Sweden.

Input Data

X04D13A.DAT

X04D13B.DAT

X04D13C.DAT



Cable Properties

Cable cross-sectional area = 0.85 in^2

Equivalent modulus of elasticity = 19000 kips/in^2

Cable self weight = 3.16 lb/ft

Undeformed length of cable segment 1-2 = 412.8837 ft

Undeformed length of cable segment 2-3 = 613.0422 ft

Figure 1: Geometry and properties for suspended cable with uniform and concentrated loading.

Example 4.3.1

Free Vibration Analysis Of A Rotating Blade.

Keywords

Centripetal Stiffening, Rotating Machinery, Total Lagrangian, Geometric Nonlinearity

Description

Determine the free vibration response of a cantilevered plate rotating at 20000 rpm. The dimensions and details of the blade are shown in Figure 1.

Discretisation

Model the blade structure using four BSL4 Semiloof beam elements (see Figure 2).

Geometry

The blade structure has the following geometric properties for each element

Cross-sectional area	= 6.4516E-5 m ²
Second moment of area about the local y axis	= 3.46859E-11 m ⁴
Second moment of area about the local z axis	= 3.46859E-9 m ⁴
Torsional constant	= 3.50327E-9 m ⁴
First moment of area about the local y axis	= 0.0 m ³
First moment of area about the local z axis	= 0.0 m ³
Product moment of area	= 0.0 m ⁴

Material properties

Young's modulus	72.4072x10 ⁹ N/m ²
Poisson's ratio	0.3
Density	2726.0 kg/m ³

Boundary conditions

The blade is rigidly supported at the root, node 1 (see Figure 2).

Theory

To analyse this problem correctly a nonlinear solution procedure is adopted to account for the large displacements [1]. These geometric nonlinearities are handled via the Total Lagrangian formulation. In addition to the usual large displacement and initial stress stiffness matrices a further contribution to the tangential stiffness due to centripetal acceleration is included. This additional stiffness matrix is called a load correction stiffness matrix.

Comparison

Table 1 compares the natural frequencies of the fundamental mode for various element meshes for an angular velocity of zero, 20000 rpm and 20000 rpm with the load correction stiffness matrix due to centripetal acceleration neglected (Lusas Solver option 102). As can be seen from Table 1, the effect of neglecting the load correction stiffness matrix due to centripetal acceleration results in errors of approximately 20% in the calculation of the natural frequency of the fundamental mode of vibration.

Table 1: Natural Frequencies of vibration

				Frequency, Hz		
Element		Integration rule			Load correction stiffness included	Load correction stiffness neglected
Mesh	Type	Mass matrix	Stiffness matrix	$\omega=0$	$\omega=20,000$ rpm	$\omega=20,000$ rpm
4 x 1	HX16	2 x 2 x 2	2 x 2 x 2	225	380	458
4 x 1	QSL8	5 point	5 point	208	358	440
5 x 2	HX20	3 x 3 x 3	3 x 3 x 3	216	345	454
5 x 2	QSL8	5 point	5 point	211	366	447
5 x 2	HX20	2 x 2 x 2	2 x 2 x 2	216	375	454
4	BSL4	3	3	209	367	448
10	BSL4	3	3	209	367	448
5 x 2	HX20	3 x 3 x 3	3 x 3 x 3	219	347	456

References

1. M. E. Honnor and P. Lyons, "Free Vibrations in Rotating Machinery.", Finite Element Analysis Ltd Internal Report No. FEAL401, 1984.

Input data

X04D31.DAT

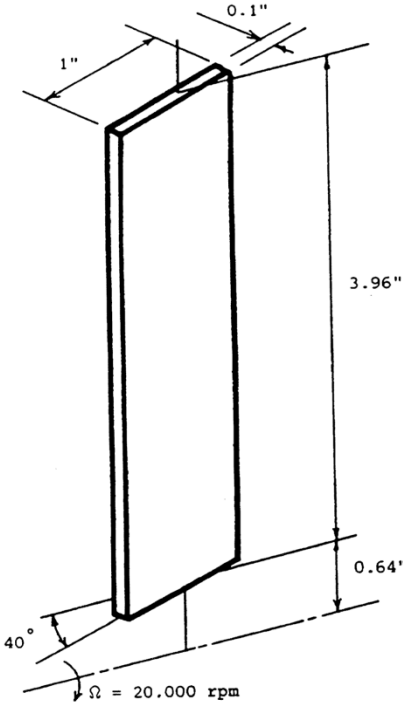


Figure 1 Problem Geometry and Material properties

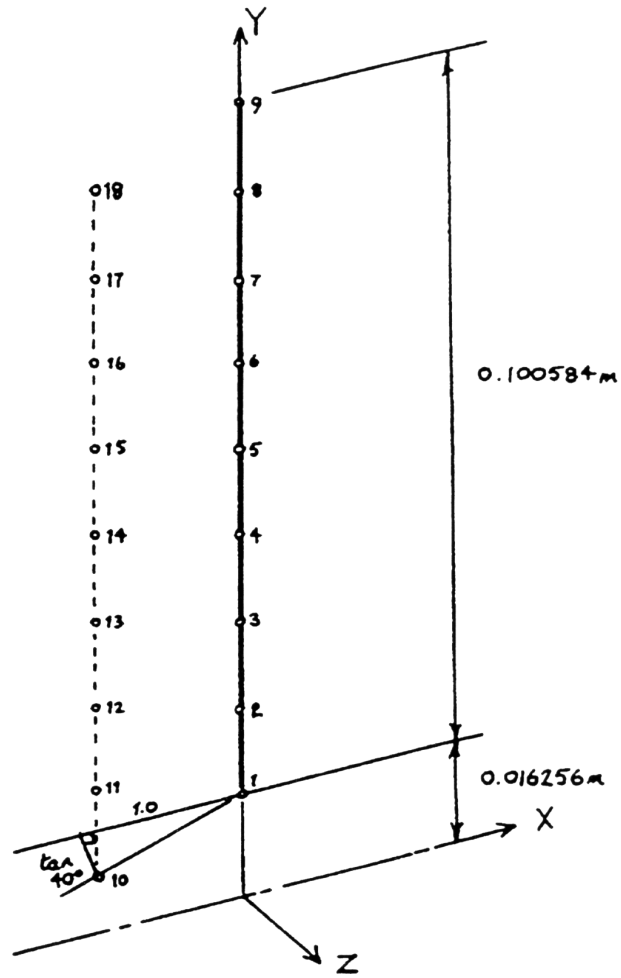


Figure 2 Finite Element Mesh

Example 4.3.2

Curved Cantilever Under Concentrated End Load

Keywords

Nonlinear, Co-Rotational, Total Lagrangian

Description

A curved cantilever is subjected to a transverse concentrated load applied at the free end. This problem involves a three dimensional response to a geometrically nonlinear problem. Large displacements and rotations occur in this example and the beam element used, BTS3, is based on a co-rotational formulation. The beam is also modelled with continuum elements where a Total Lagrangian formulation is used. Linear material properties are assumed.

Discretisation

The curved cantilever is modelled with:

- i) 8 straight linear BTS3 elements of equal length.
- ii) 16 HX8M solid elements of equal length and unit square cross section.

Geometry

Figure 1 shows the initial geometry of the beam $P=0.0$

Radius of curvature = 100.0

Co-ordinates for centre of curvature = (0.0, 0.0, 100.0)

The co-ordinates at the ends of the beam centre line are:

Fixed end= (0.0, 0.0, 0.0)

Free end = (70.71, 0.0, 29.29)

Sectional properties for beam elements:

$A_{xx} = 1.0$

$A_{yy} = 1.0$

$A_{zz} = 1.0$

$$I_{yy} = 8.3333E-2$$

$$I_{zz} = 8.3333E-2$$

$$K_t = 14.06E-2$$

The cantilever is of unit square cross section and K_t is evaluated from:

$$K_t = 0.1406a^4$$

where a is the length of the sides of the cross section.

Boundary conditions

Fully fixed at one end.

Material properties

Young's modulus	10×10^6
Poisson's ratio	0.0

Loading

For the beam elements, total concentrated loads of 300, 450 and 600 are applied incrementally at the free end. For the solid elements, the total load of 600 is applied in 12 equal steps. The loads are applied in the vertical (Y) direction.

Lusas Results

Figure 1 shows the deformation of the beam elements for the loading considered. A table of tip displacements is given below including a comparison with the reference solutions. For the HX8M elements the average of the 4 end node displacements is quoted.

Tip displacement (u,v,w) for curved cantilever

	Load level		
	300	450	600
Simo and Vu-Quoc	-11.87,40.08,-6.96	-18.39,48.39,-10.67	-23.48,53.37,-13.50
Cardona and Geradin	-12.07,40.35,-7.15	-18.60,48.59,-10.91	-23.67,53.50,-13.74
BTS3	-12.16,40.47,-7.16	-18.78,48.76,-10.93	-23.91,53.71,-13.77
HX8M	-11.83,40.05,-7.06	-18.29,48.29,-10.79	-23.30,53.20,-13.60

Comparison

The results obtained for this example are very sensitive to the value taken for the torsional constant K_t . The actual value used for executing this test is seldom given in published results.

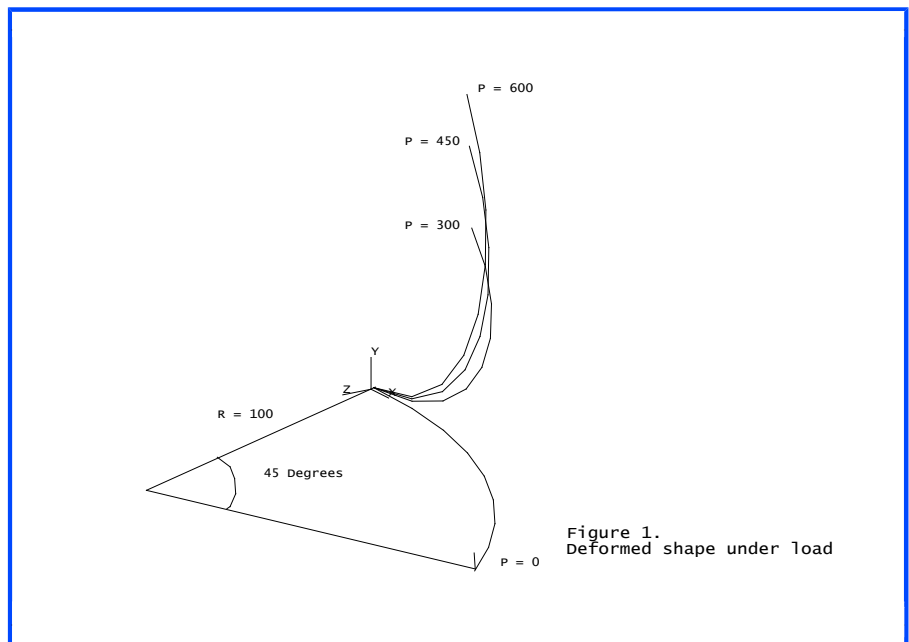
The effective value of K_t for the solid elements is slightly higher than that used for the beam elements; this results in a stiffer response when using HX8M elements. For the analysis involving BTS3 elements, large load steps were taken to demonstrate the robustness of the consistent co-rotational formulation. Load steps of this size can cause negative pivots to occur during the iterative solution procedure. However, these negative pivots are not present when a solution has converged. In practise, smaller load steps should be used to ensure a more stable sequence of iterations.

References

1. SIMO, J.C. and VU-QUOC, L., A Three Dimensional Finite Strain Rod Model. Part II: Computational Aspects, *Comp. Meth. in Appl. Mech. and Engineering*, Vol 58, pp 79-116, 1986.
2. CARDONA, A., GERADIN, M. A Beam Finite Element Non-Linear Theory with Finite Rotations. *Int. Journ. for Num. Meth. in Eng.*, Vol 26, pp 2403-2438, 1988.

Input data

X04D32A.DAT



Example 4.5.1

Hinged Cylindrical Shell Under Central Point Load.

Keywords

Total Lagrangian, Geometric Nonlinearity, Snap Through

Description

Determine the nonlinear load/displacement response of a cylindrical shell of the form shown in Figure 1, when it is subjected to a point load acting vertically downwards at its centre.

Discretisation

As the loading and boundary conditions are symmetric, only 1/4 of the shell is analysed, using a 4x4 mesh of QSL8 Semiloof shell elements (see Figure 1).

Geometry

The geometry of the hinged cylindrical shell is shown in Figure 1.

Material properties

Young's modulus	3103 N/mm ²
Poisson's ratio	0.3

Boundary conditions

The shell structure is hinged along the left-hand side, nodes 1 to 9, restrained from crossing and rotating about the yz plane, nodes 73 to 80, restrained from crossing and rotating about the xz plane, nodes 18, 27, 36, 45, 54, 63 and 72, and totally restrained at its centre, node 81. The z direction is restrained to permit the application of prescribed displacements.

Theory

This example is commonly referred to as a snap through problem which has been studied by Sabir and Lock [1]. Due to the large displacements and this snap through effect the problem must be analysed nonlinearly using the Total Lagrangian geometric nonlinearity formulation.

Comparison

A Comparison of the results obtained by LUSAS with those of [1] are shown in Figure 2.

References

1. Sabir, A.B., Lock, A.C.'The Application of Finite Elements to the Large Deflection Geometrically Nonlinear Behaviour of Cylindrical Shells'. Variational Methods in Engineering. Ed. Brebbia et al. Pub. Soton. Univ. Press. 1972.

Input data

X04D51A.DAT

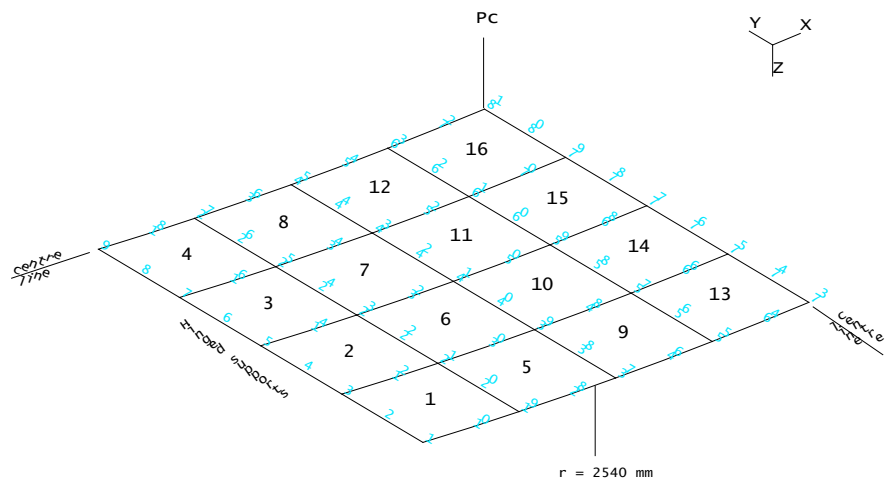
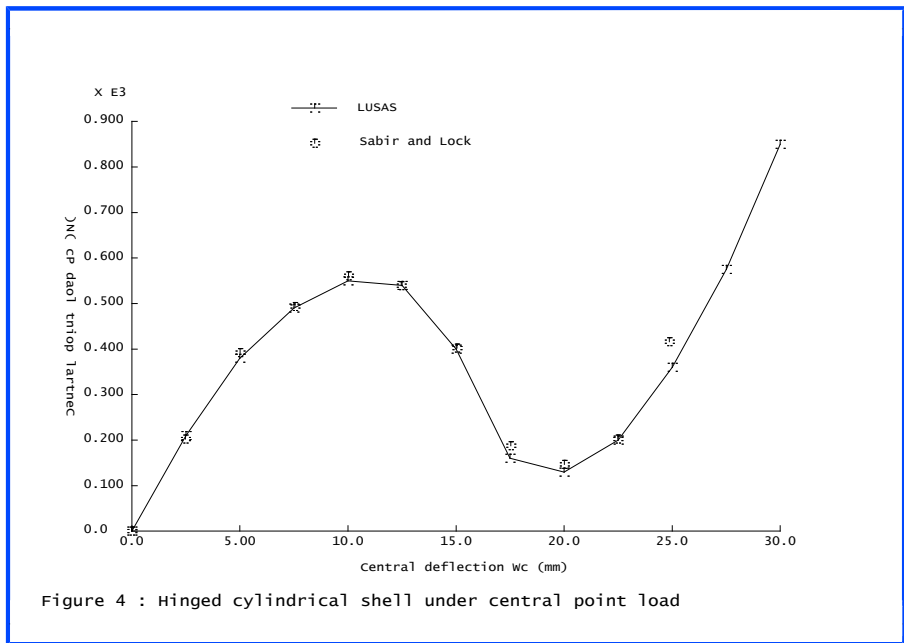


Figure 1.
Finite element mesh for
cylindrical shell problem



Example 4.5.2

Clamped Spherical Cap Subject To A Point Load

Keywords

Total And Updated Lagrangian, Axisymmetric Solid, Axisymmetric Shell

Description

This geometrically non-linear example consists of a clamped spherical cap subject to a point load at the apex. Figure 1 shows the geometry and loading of the problem under consideration. For each mesh the analysis is performed using a total Lagrangian formulation and an updated Lagrangian formulation.

Internal Radius	R	22.27 inches
Thickness of shell	t	0.41 inches
Semi-angle	θ	26.67 degrees

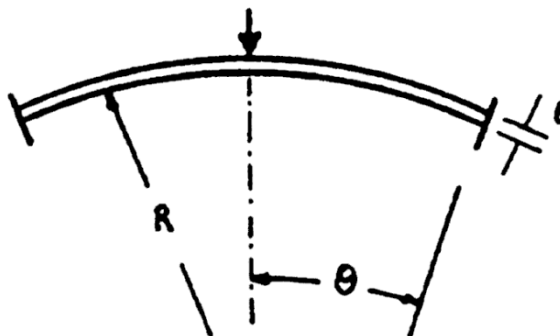


Figure 1.

Discretisation

The spherical cap is modelled with five QAX8 elements for the first mesh and twelve BXS3 elements for the second mesh. Figures 2 and 3 show the mesh for QAX8 and BXS3 elements respectively.

Material properties

Young's modulus	10.0x10 ⁶ N/m ²
Poisson's ratio	0.3

Boundary conditions

The edge of the cap is fully fixed against translation and rotation.

Theory

See [2].

Solution comparison

Apex Deflection	Load P QAX8 Updated Lagrangian (N)	Load P BXS3 Total Lagrangian (N)
0.01	9.576	9.689
0.02	14.00	14.28
0.03	16.75	17.06
0.04	19.29	19.53
0.05	22.02	22.17
0.06	25.01	25.09
0.07	28.18	28.20
0.08	31.34	31.37
0.09	34.28	34.42
0.10	36.83	37.16
0.11	38.94	39.46
0.12	40.81	41.32
0.13	43.30	43.21
0.14	48.40	46.56
0.15	59.18	54.13
0.16	78.58	69.32

References

1. M.E. Honnor, 'Axisymmetric thin shell element', FEAL internal report FEAL503.
2. W.E. Haisler, J.A. Stricklin and F.J. Stebbins, 'Development and evaluation of solution procedures for geometrically nonlinear structural analysis by the direct stiffness method',

AIAA/ASME 12th Structures Struct. Dynamics and Materials Conference, Anaheim, California.

Input Data

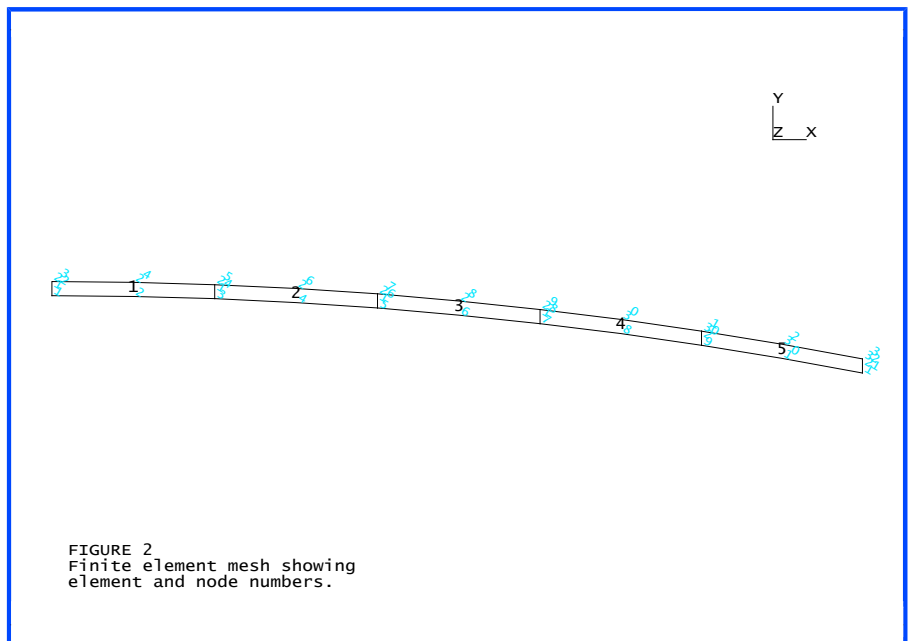
X04D52A.DAT

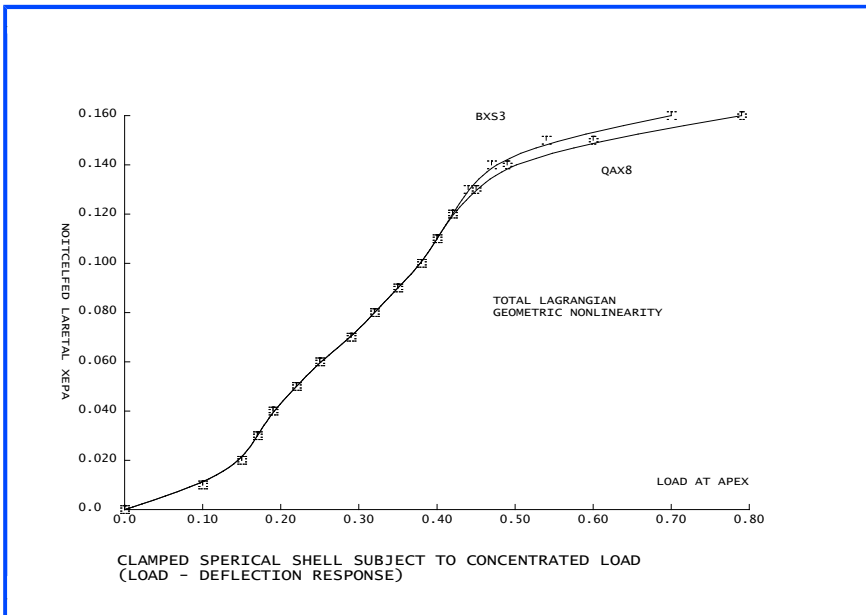
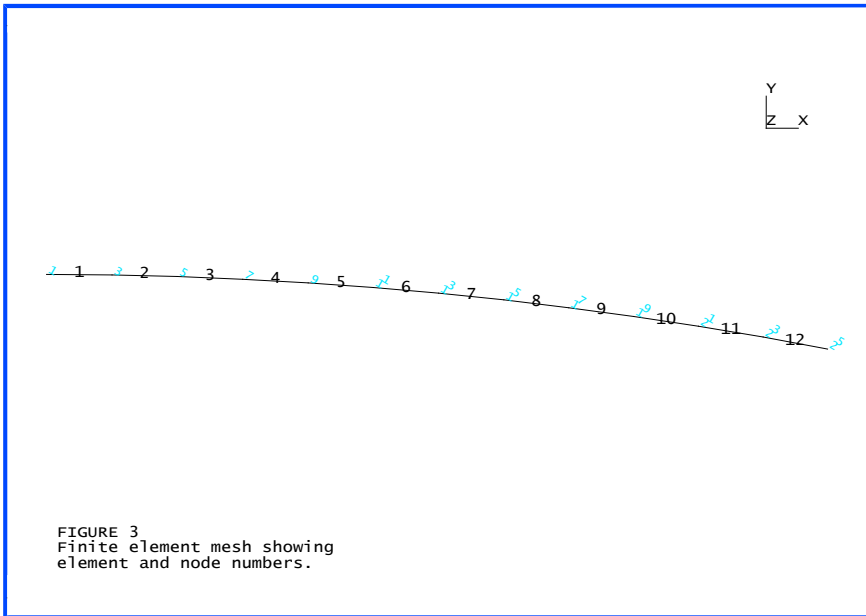
X04D52B.DAT

Input data for axisymmetry about the Y-axis:

Note: Include OPTION 47 for axisymmetry about the X-axis.

Note: Include OPTION 47 for axisymmetry about the X-axis





Example 4.5.3

Large Displacement Of A Hyperbolic Paraboloid

Keywords

Total Lagrangian, Large Rotation, Warped Elements

Description

The hyperbolic paraboloid tests the large rotational and translational behaviour of a structure with an initial mesh of distorted and warped elements. The paraboloid is supported on two inwardly sloping rollers about which concentrated moments are applied. The sloping supports provide membrane restraint only, but allow large rigid body motion under the moment loading.

Finite Element Model

Taking advantage of symmetry only one quarter of the paraboloid is modelled. Symmetry conditions are imposed along two of the edges while the third edge is free. The paraboloid is supported on inwardly sloping hinged rollers as shown below. A 12x4 graded mesh (see Figure 1) comprising QTS4 elements compares directly with the results presented in [1].

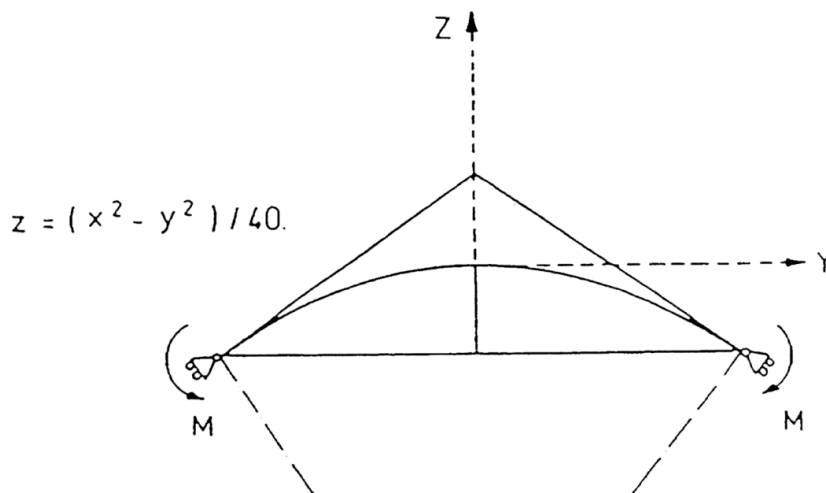
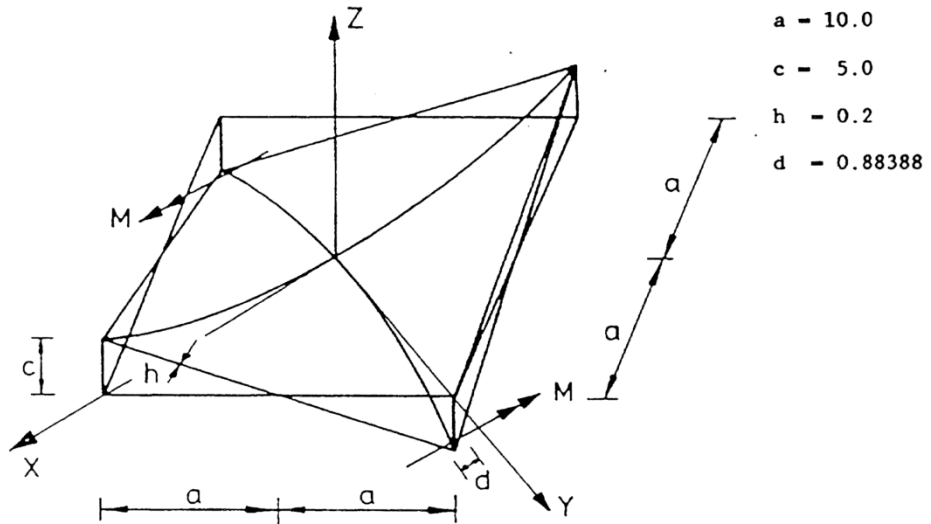


Figure 1

Geometry

The full problem geometry is:



Material properties

Young's modulus	10.0×10^3
Poisson's ratio	0.0

Boundary Conditions

Roller supports allowing rotation about and translation along the transformed axes.

Solution Comparison

LUSAS results are detailed for node 13. The deformed shape is shown in Figure 2.

Support displacement along transformed freedom

Load	0.5	1.0	1.5	2.0	2.5	3.0	3.5	4.0
Ref.	1.8567	5.1118	9.0081	12.8471	15.9420	17.8904	19.4014	20.2423
LUSAS	1.8574	5.1081	8.9973	12.8238	15.9011	17.8400	19.3280	20.1348

Support rotation

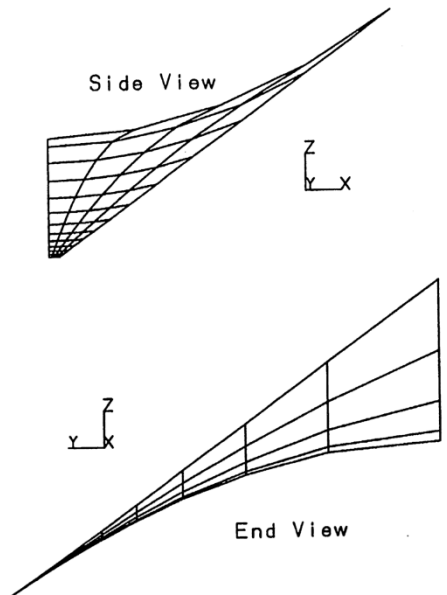
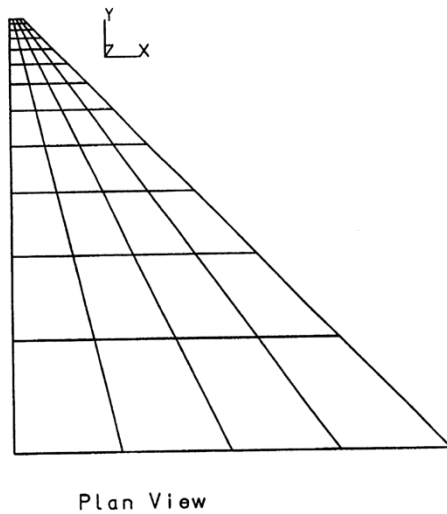
Load	0.5	1.0	1.5	2.0	2.5	3.0	3.5	4.0
Ref.	34.32	74.49	116.85	160	207.55	244.00	292.43	352.79
LUSAS	34.36	74.54	116.43	160.83	207.23	243.54	291.02	346.95

References

1. Stander N, Matzenmiller A, and Ramm E. An assessment of assumed strain methods in finite rotation shell analysis. Engineering Computations, Vol. 6, pp58-66, 1989.

Input Data

X04D53A.DAT



Grading of Mesh for Hyperbolic Paraboloid

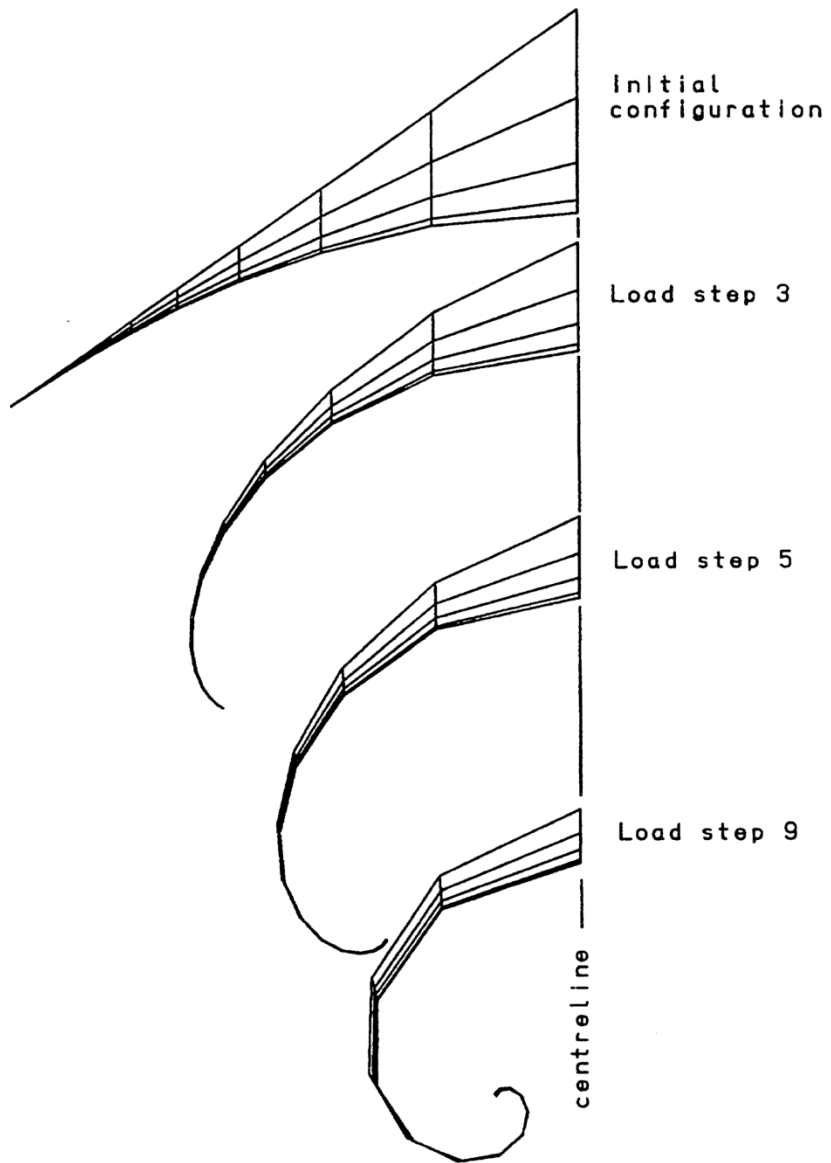


Figure 2 Deformation of hyperbolic paraboloid

Example 4.5.4

Large Displacement Of A Hemispherical Shell

Keywords

Co-Rotational Geometric Nonlinearity, Large Rotations

Description

A hemispherical shell is subjected to point loads as shown in Figures 1 and 2. In addition to rigid body rotations, both membrane and bending strains contribute significantly to the radial displacement at the loading points.

Finite Element Model

Taking advantage of symmetry only one quarter of the hemisphere is modelled. Symmetry conditions are imposed along two of the edges while the other edges are free. The hemisphere is discretised with TSR6 facet shell elements as shown in Figure 1.

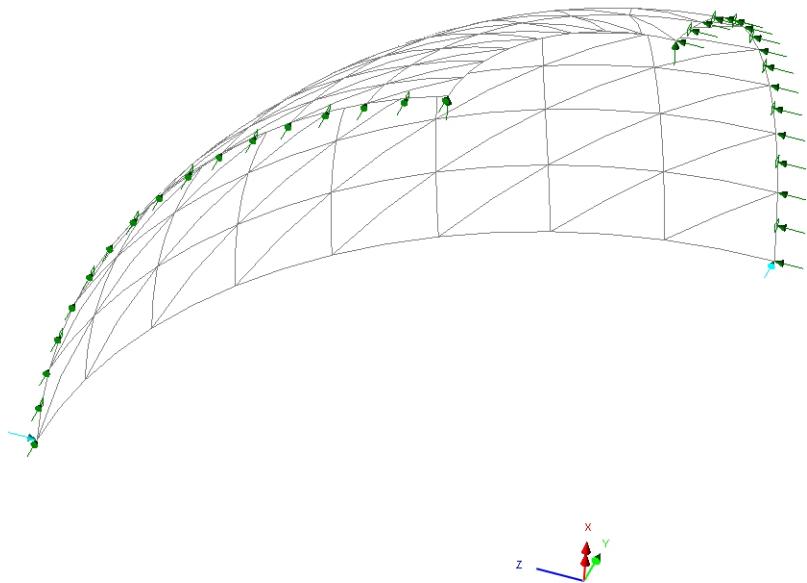


Figure 1

Geometry

The full problem geometry is:

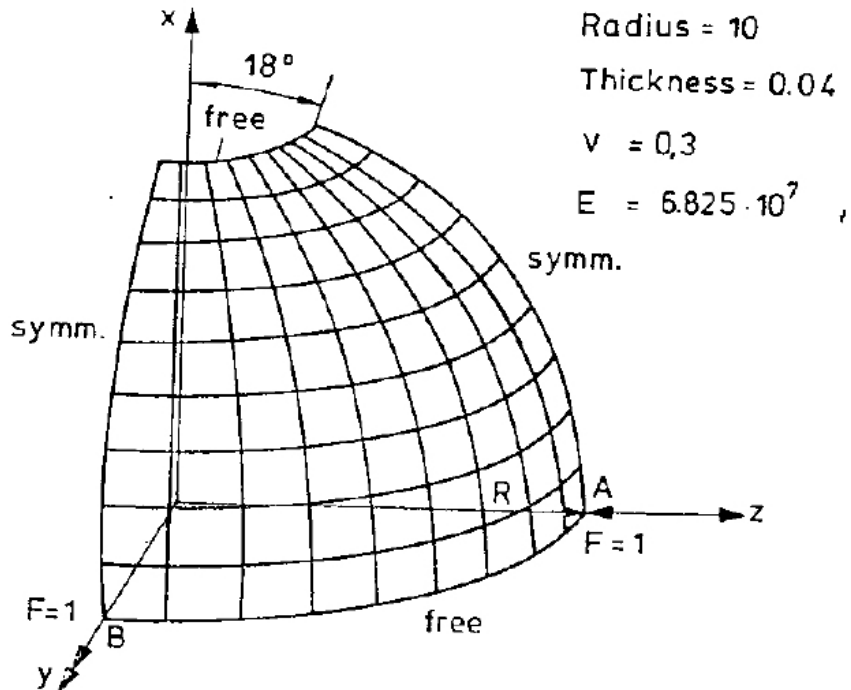


Figure 2

Material properties

Young's modulus, E	68.25x10 ⁶
Poisson's ratio, ν	0.3

Boundary Conditions

Due to the symmetry of the problem only $\frac{1}{4}$ of the hemisphere is modelled. Two of the edges are free while symmetry is imposed at the other two edges.

Solution Comparison

LUSAS results are compared with [1] in the following figures; the final deformed mesh is shown in Figure 6.

References

1. Stander N, Matzenmiller A, and Ramm E. An assessment of assumed strain methods in finite rotation shell analysis. Engineering Computations, Vol. 6, pp58-66, 1989.

Input Data

X04D54.DAT

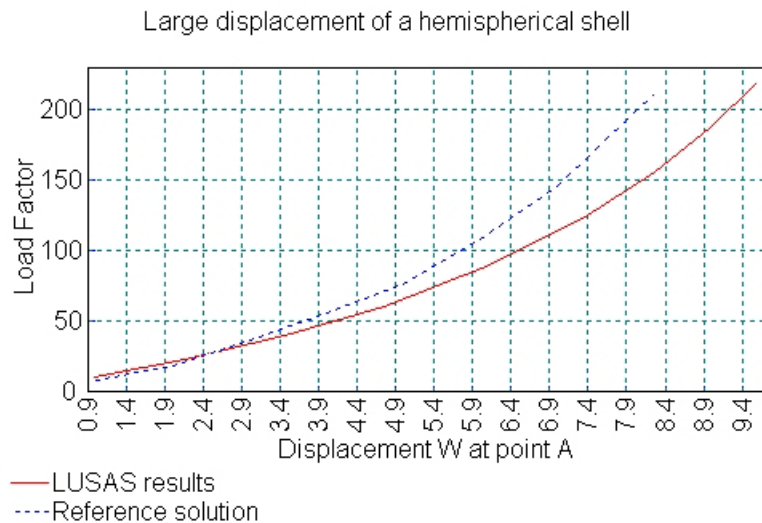


Figure 3

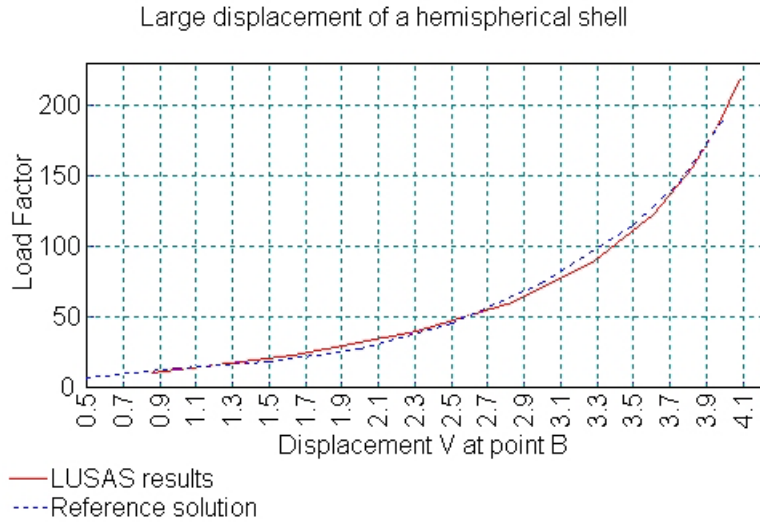


Figure 4

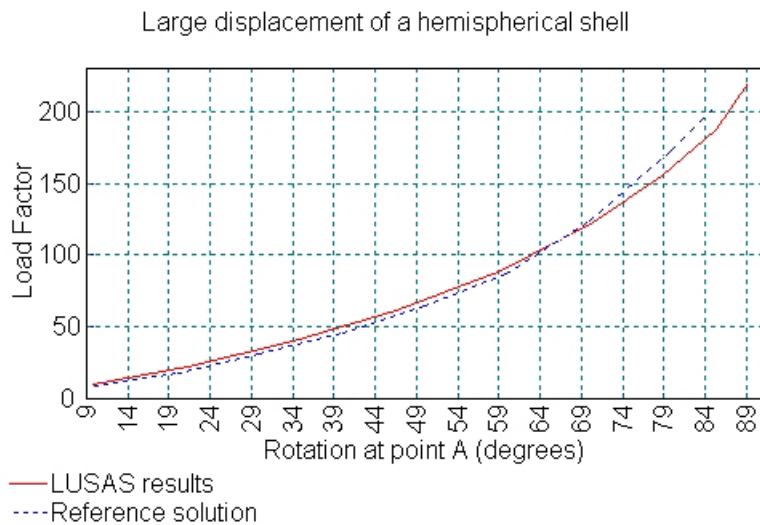


Figure 5

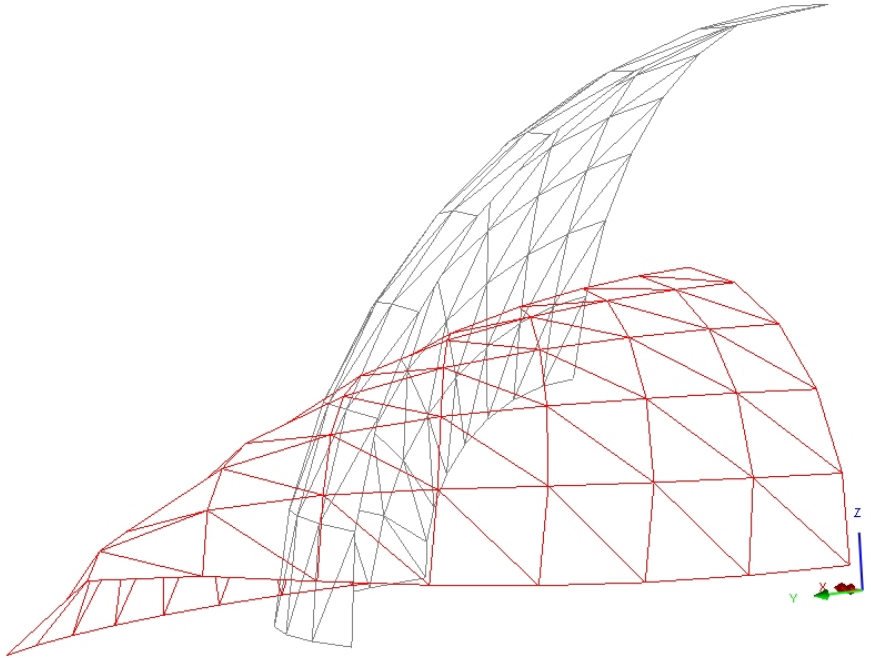


Figure 6

Example 4.5.5

Optimisation of cable forces in cable stayed bridge

Keywords

Geometric Nonlinearity, Optimisation, Target value

Description

A geometrically nonlinear cable stayed bridge is optimised to minimise the cable forces subject to limits in the tower sway and deck displacement under self weight loading. Additionally, The force in a pair of cables is specified using the target value loading type.

The horizontal movement at the top of the tower U_A is limited to a displacement of 1cm whilst the vertical displacements at W_B and W_C must be greater than or equal to zero. Finally, the cable forces in the pair of cables labelled T_1 is set to 38,000kN.

Finite Element Model

The simple cable stayed bridge is shown in figure 1.

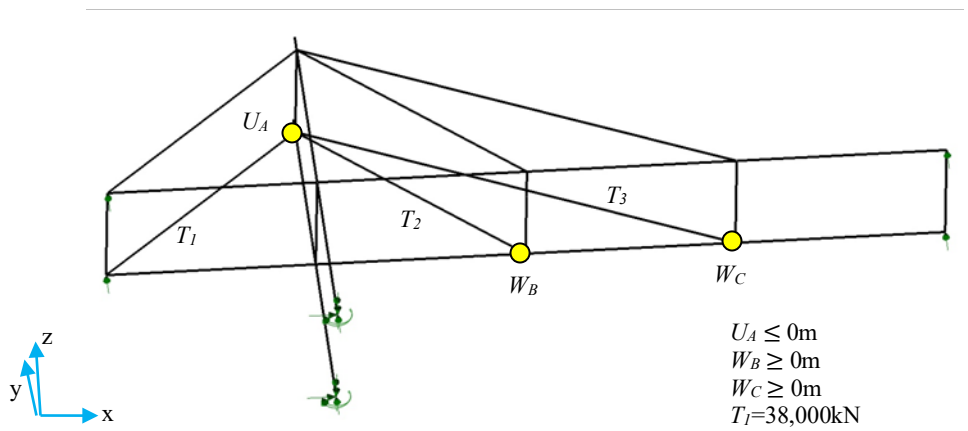


Figure 1

Geometry

The problem geometry is:

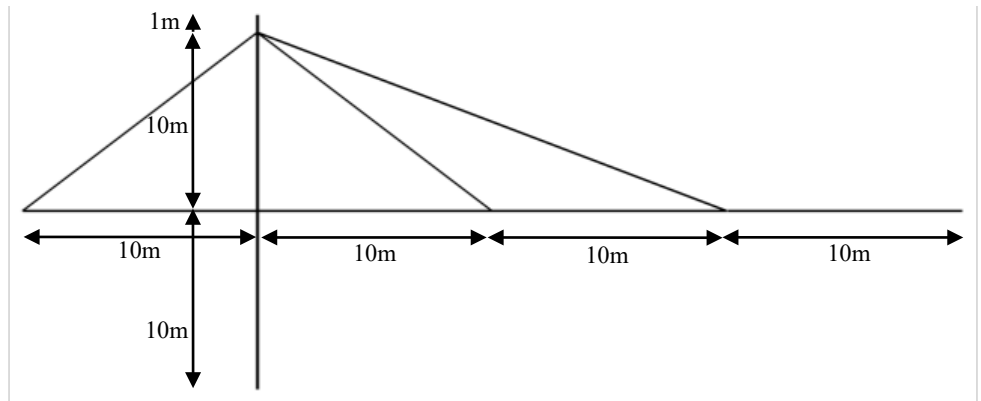


Figure 2

Material properties

Young's modulus, E	210×10^6 kN
Poisson's ratio, ν	0.3
Density, ρ	7850 kg/m ³

Boundary Conditions

The base of the towers are fully restrained and the ends of the spans are supported in the vertical direction.

Solution Comparison

Value	Target	LUSAS
U_A	≤ 0	-0.0013
W_B	≥ 0	0.0041
W_C	≥ 0	-0.66×10^{-18}
T_I	38,000	38,000

References

Input Data

X04D55.DAT

Example 5.1.1

Elastoplastic Analysis Of A Cantilever Bar

Keywords

Elastoplasticity, Strain Hardening, Load Cycling

Description

The cantilever bar shown in Figure 1a is subjected to a uniaxial load which alternates from tension to compression. The nonlinear behaviour of the material is given in Figure 1b as the stress/strain relationship with strain hardening. The required output is the load/displacement history.

Finite element model

A single BAR2 element is used to model the complete cantilever. The bar is assumed to be perfectly straight and is not subject to buckling or any other geometrically nonlinear effects.

Geometric properties

Length	10 mm
Cross-sectional area	1 mm ²

Material properties

Young's modulus, E	1.0x10 ⁵ N/mm ²
Plasticity modulus, E _p	2.0x10 ⁴ N/mm ²
Yield stress	400 N/mm ²

Loading condition

A displacement condition at end 2 of u_2 (Figure 1a) is prescribed using load type PDSP. This displacement varies from + 0.14 mm to -0.08 mm.

Solution Comparison

The results in the form of the load/displacement curve are given in figure 2, where R_{x_1} is the reaction at node 1 and the positions marked on the graph are the displacement increments with the corresponding values of R_{x_1} and u given in Table 1. This example of a uniaxial load shows

how the solution converges to the exact value instantaneously. It should also be noted how if the loading/ unloading procedure were continued within the limits stated above, the model would converge to its linear elastic form, represented by the line 9-13 of the graph in Figure 2, as further strain hardening occurs.

Input Data

X05D11A.DAT

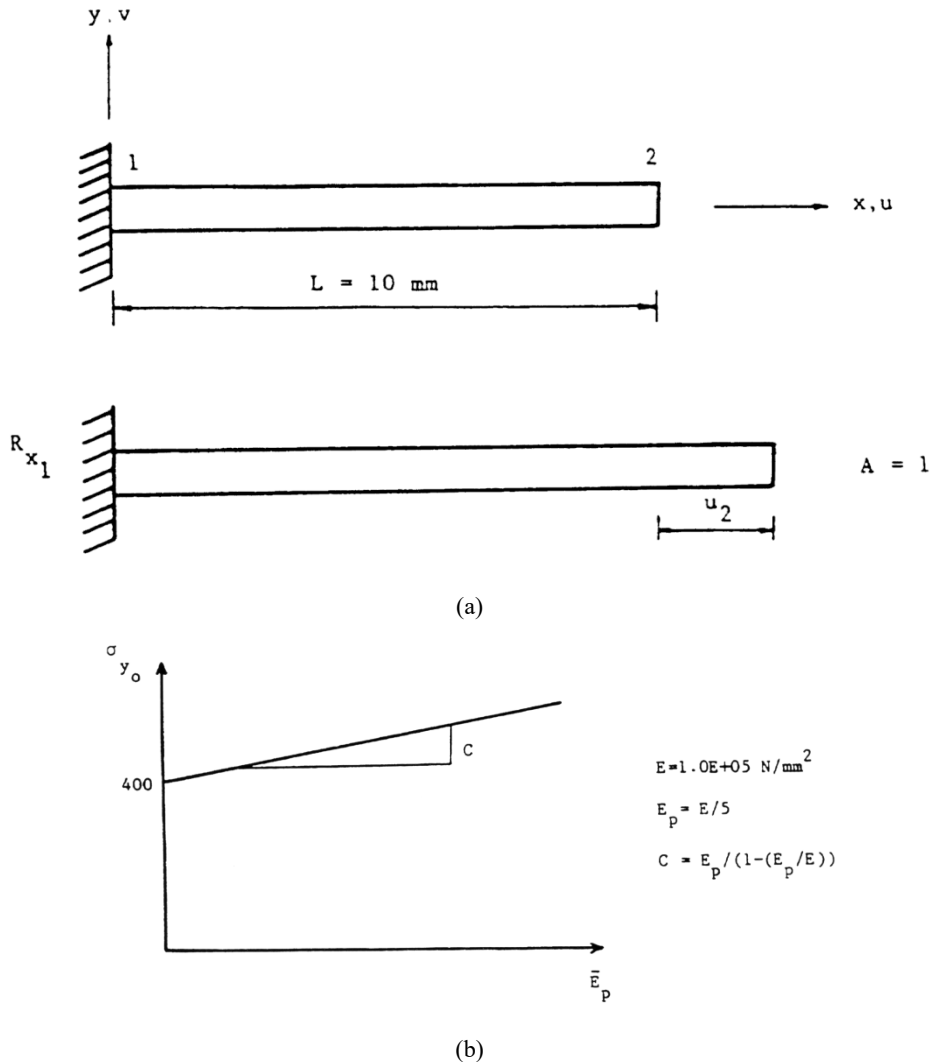


Figure 1. (a) Cantilever beam subjected to an extension (b) Nonlinear stress/strain relation for material model.

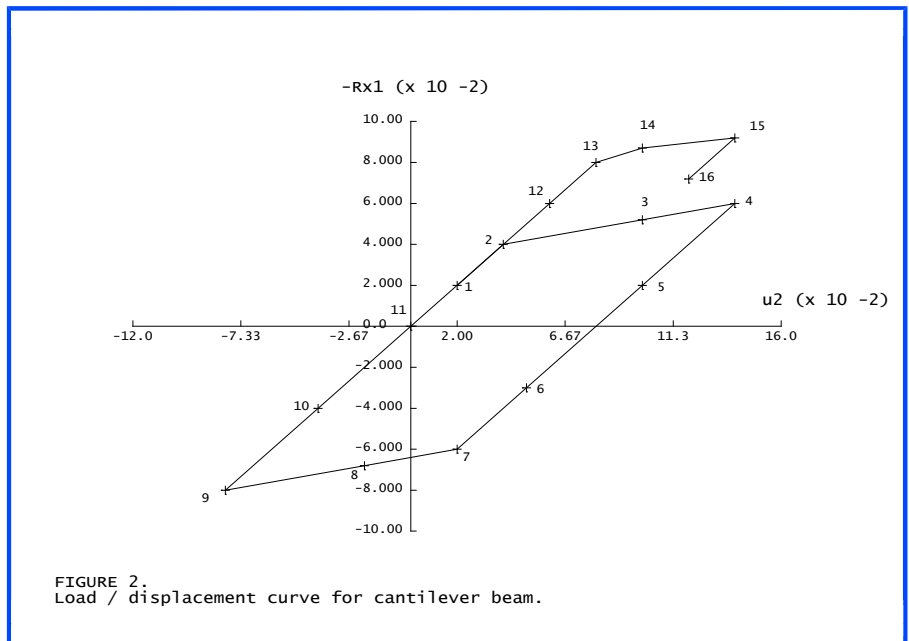


FIGURE 2:
Load / displacement curve for cantilever beam.

Figure 2. Load/displacement curve for cantilever beam.

Example 5.1.2

Uniaxial Tension/ Compression Cycling

Keywords

Modified Von Mises

Description

A bar is subjected to cycling under uniaxial stress conditions, which causes yield in both tension and compression. The material is modelled by a Modified von Mises yield criterion which allows for different yield properties in tension and compression. Additionally, both the compressive and tensile strain hardening characteristics may be different.

Finite Element Model

One plane stress element.

Geometry



Length = 10

Width = 1

Depth = 1

P

Material properties

Young's modulus = 2000

Poisson's ratio = 0.0

Yield stress $\sigma_{y,0}^c = 30$, $\sigma_{y,0}^t = 20$

Hardening $H^c = 150$ $H^t = 100$

Boundary Conditions

Free to pull-in at laterally supported end

Solution Comparison

The load/displacement relationship is calculated by prescribing the load which uniquely determines the plastic strain developed to sustain it. As the plastic strain is accumulated, the yield stress in both tension and compression is changed according to the hardening characteristics of the material in each sector.

The plastic stress multiplier, λ , is given by:

$$\lambda = \frac{\Delta \bar{\varepsilon}^P}{\left\{ \left[\underline{\underline{\mathbf{P}\sigma}} + \gamma \underline{\underline{\hat{\mathbf{p}}}} \right]^T \underline{\underline{\mathbf{M}}} \left[\underline{\underline{\mathbf{P}\sigma}} + \gamma \underline{\underline{\hat{\mathbf{p}}}} \right] \right\}^{1/2}} \quad (0.0.57)$$

where:

$\Delta \bar{\varepsilon}^P$ effective plastic strain = $(\mathbf{s}_{y,t}^a - \mathbf{s}_{y,0}^a) / H^a$, where H^a is the hardening gradient and $\mathbf{s}_{y,t}^a$ the current yield stress and α may be the tension or compression value.

$\underline{\underline{\mathbf{P}}}$ deviatoric components of the yield function

$$\underline{\underline{\mathbf{P}}} = \begin{bmatrix} \frac{2}{3} & -\frac{1}{3} & -\frac{1}{3} & 0 & 0 & 0 \\ -\frac{1}{3} & \frac{2}{3} & -\frac{1}{3} & 0 & 0 & 0 \\ -\frac{1}{3} & -\frac{1}{3} & \frac{2}{3} & 0 & 0 & 0 \\ 0 & 0 & 0 & 0 & 0 & 0 \\ 0 & 0 & 0 & 0 & 0 & 0 \\ 0 & 0 & 0 & 0 & 0 & 0 \end{bmatrix} \quad (0.0.58)$$

$\underline{\underline{\hat{\mathbf{p}}}}$ pressure dependent components of the yield function

$$\underline{\underline{\hat{\mathbf{p}}}} = \begin{bmatrix} \frac{1}{3} \\ \frac{1}{3} \\ \frac{1}{3} \\ 0 \\ 0 \\ 0 \end{bmatrix} \quad (0.0.59)$$

$\underline{\underline{\sigma}}$ current stress vector

and

$$\gamma = \sigma_{y,t}^c - \sigma_{y,t}^t, \quad \underline{\underline{\mathbf{M}}} = \begin{bmatrix} 1 & & & & & \\ & 1 & & & & \\ & & 1 & & & \\ & & & \frac{1}{2} & & \\ & & & & \frac{1}{2} & \\ & & & & & \frac{1}{2} \end{bmatrix} \quad (0.0.60)$$

When considering the S_{xx} component of the stress vector to be the only non-zero value, the denominator of (0.0.57) reduces to:

$$\left[\underline{\underline{\mathbf{P}\boldsymbol{\sigma}}} + \gamma \underline{\underline{\hat{\mathbf{p}}}} \right]^T \underline{\underline{\mathbf{M}}} \left[\underline{\underline{\mathbf{P}\boldsymbol{\sigma}}} + \gamma \underline{\underline{\hat{\mathbf{p}}}} \right] = \frac{2}{3} \sigma_{xx}^2 + \frac{1}{3} \left(\sigma_{y,t}^c - \sigma_{y,t}^t \right)^2 \quad (0.0.61)$$

The incremental plastic strain vector is then computed from:

$$\Delta \underline{\underline{\boldsymbol{\varepsilon}}}^P = \lambda \left[\underline{\underline{\mathbf{P}\boldsymbol{\sigma}}} + \gamma \underline{\underline{\hat{\mathbf{p}}}} \right] \quad (0.0.62)$$

Using equations (0.0.57), (0.0.61) and (0.0.62) the computation of the $\Delta \varepsilon_{xx}$ component of $\Delta \underline{\underline{\boldsymbol{\varepsilon}}}$ reduces to:

$$\Delta \varepsilon_{xx}^P = \frac{\Delta \varepsilon^{-P} \left(\sigma_{xx} + \frac{1}{2} \left(\sigma_{y,t}^c - \sigma_{y,t}^t \right) \right)}{\left[\sigma_{xx}^2 + \frac{1}{2} \left(\sigma_{y,t}^c - \sigma_{y,t}^t \right)^2 \right]^{1/2}} \quad (0.0.63)$$

The compressive and tensile yield stresses are a function of the plastic strain, which may be calculated for one dimensional problems from

$$\bar{\varepsilon}^P = \frac{|\sigma_{xx}| - \sigma_{y,0}^t}{H^t} \quad \text{if} \quad \sigma_{xx} \text{ is tensile} \quad (0.0.64)$$

$$\bar{\varepsilon}^P = \frac{|\sigma_{xx}| - \sigma_{y,0}^t}{H^t} \quad \text{if} \quad \sigma_{xx} \text{ is tensile} \quad (0.0.65)$$

The yield stresses are then computed from:

$$\sigma_{y,t}^c = \sigma_{y,0}^c + H^c \bar{\varepsilon}^P \quad (0.0.66)$$

$$\sigma_{y,t}^t = \sigma_{y,0}^t + H^t \bar{\varepsilon}^P \quad (0.0.67)$$

Summing the elastic and plastic strain components, the total axial strain is,

$$\epsilon_{xx}^T = \epsilon_{xx}^e + \sum_{i=1}^n \Delta \epsilon_{xx,i}^p = \frac{\sigma_{xx}}{E} + \sum_{i=1}^n \Delta \epsilon_{xx,i}^p \quad (0.0.68)$$

The results can be calculated by using (0.0.64) or (0.0.65) to calculate the total plastic strain. Once the plastic strain is known, the yield stresses are defined using (0.0.66) and (0.0.67). The axial plastic strain is then given by (0.0.63) and the total strain by (0.0.68).

Load σ_{xx}	$\bar{\epsilon}^p$	$\Delta \bar{\epsilon}^p$	$\sigma_{y,t}^c$	$\sigma_{y,t}^t$	$\Delta \epsilon_{xx}^p$	$\Sigma \epsilon_{xx}^p$	ϵ_{xx}^T
20.000	0.0000	0.0000	30.000	20.000	0.0000	0.0000	0.0100
25.000	0.0500	0.0500	37.500	25.000	0.0589	0.0589	0.0714
30.000	0.1000	0.0500	45.000	30.000	0.0589	0.1178	0.1329
29.000	0.1000	0.0000	45.000	30.000	0.0000	0.1178	0.1324
-45.000	0.1000	0.0000	45.000	30.000	0.0000	0.1178	0.0954
-65.000	0.2333	0.1333	65.000	43.333	-0.1081	0.0097	-0.0228
-64.000	0.2333	0.0000	65.000	43.333	0.0000	0.0097	-0.0223
43.333	0.2333	0.0000	65.000	43.333	0.0000	0.0097	0.0314
50.000	0.3000	0.0667	75.000	50.000	0.0786	0.0883	0.1133

Exact agreement is obtained from LUSAS. The load/displacement history is shown on figure 1. To prevent convergence difficulties, the stress is relaxed from the yield surface prior to applying a large stress reversal.

Input Data

X05D12A.DAT

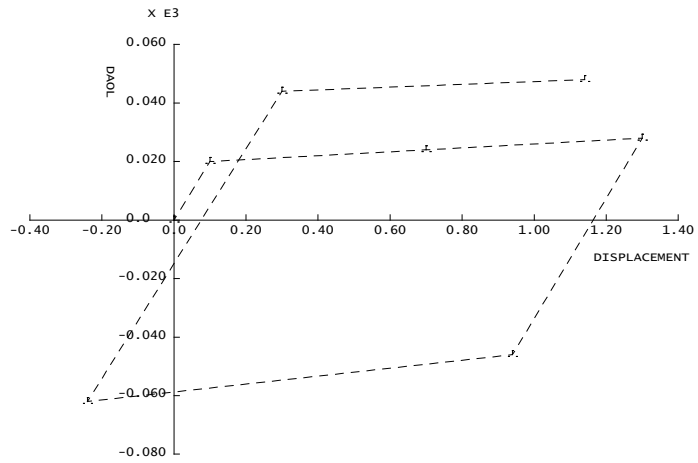


FIGURE 4. Cyclic Behaviour of Modified von Mises Material

Example 5.1.3

Uniaxial Cycling Elastic-Damage Analysis

Keywords

Damage, Cyclic Loading

Description

A bar of elastic material is subjected to uniaxial compressive load cycling with an increasing stress level. A damage criterion for the material is specified so that progressive degradation of the elastic Young's modulus takes place as the analysis proceeds. As an elastic material is defined, zero strains are produced when the bar is stress free. Under this stress free state the stress/strain curve returns to the origin.

Discretisation

A single BAR2 element of length 10mm and unit cross section is used to represent the bar.

Material properties

Young's modulus = 2E3 N/mm²

Poisson's ratio = 0.0

Damage property data (Simo [1,2]):

Initial damage threshold, r_0 = 0.44

Constants, A = B = 1.0

Boundary conditions

Fully fixed at one end, lateral displacements restrained at the other.

Loading

Cyclic vertical compressive load at the free end.

Theory

The damage parameter, d , for the Simo [1,2] model is given by:

$$d = 1 - \frac{r_0(1-A)}{r_t} - A e^{B(r_0-r_t)} \quad (0.0.69)$$

Using the specified damage properties this reduces to:

$$d = 1 - e^{(0.44-r_t)} \quad (0.0.70)$$

For the uniaxial case, the complementary energy norm, r_t , reduces to:

$$r_t = \left[\frac{\sigma^2}{E} \right]^{1/2} \quad (0.0.71)$$

The axial strain is then given by:

$$\varepsilon = \frac{\sigma}{E'} \quad \text{where} \quad E' = (1-d)E \quad (0.0.72)$$

More information on the damage models available in LUSAS can be found in the LUSAS Theory Manual.

Solution comparison

Using the above equations strains can be computed for each step of the analysis:

	Load	σ	r_t	d	ε
Loading	20	20	0.447214	0.007188	0.010072
	30	30	0.670820	0.206118	0.018894
	40	40	0.894427	0.365189	0.031505
Unloading	30	30	0.894427	0.365189	0.023629
	20	20	0.894427	0.365189	0.015753
	0	0	0.894427	0.365189	0.000000
Loading	40	40	0.894427	0.365189	0.031505
	60	60	1.341641	0.594097	0.073909
Unloading	50	50	1.341641	0.594097	0.061591
	0	0	1.341641	0.594097	0.000000
Loading	60	60	1.341641	0.594097	0.073909
	80	80	1.788854	0.740463	0.154120
	85	85	1.900658	0.767916	0.183124
	90	90	2.012461	0.792466	0.216832
Unloading	85	85	2.012461	0.792466	0.204786
	0	0	2.012461	0.792466	0.000000

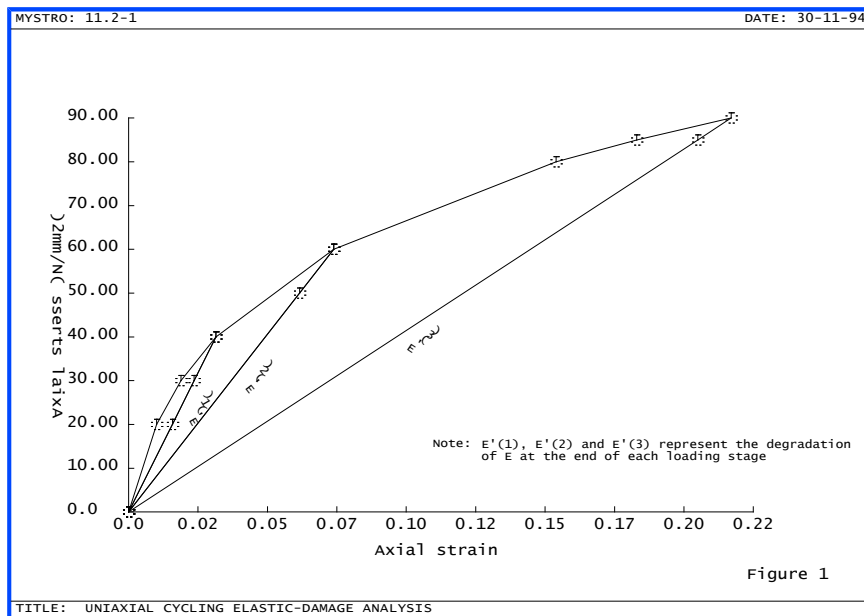
The theoretical assumptions for this damage model are such that, after the onset of damage, no further damage can occur until the maximum stress previously attained is exceeded. Hence the table shows that the damage parameter remains constant during unloading and reloading until a stress higher than the previous maximum is attained. The results for the LUSAS analysis reproduce these values exactly and are plotted in Figures 1 and 2.

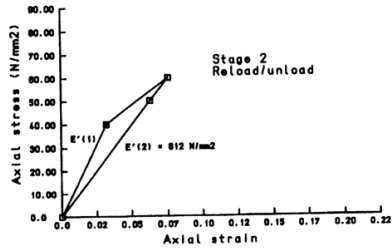
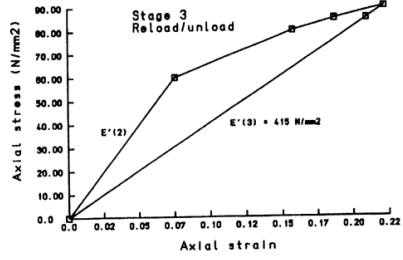
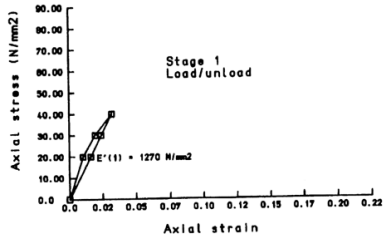
References

1. Simo, J.C. and JU, J.W. Strain- and stress-based continuum damage models - I. Formulations. Int. Journ. Solids and Structures, Vol. 23, No. 7, pp821-840, 1987.
2. Simo, J.C. and JU, J.W. Strain- and stress-based continuum damage models - II. Computational aspects. Int. Journ. Solids and Structures, Vol. 23, No. 7, pp841-869, 1987.

Input Data

X05D13A.DAT





Note:
 $E'(1)$, $E'(2)$ and $E'(3)$ represent the degradation of E at the end of each loading stage

Figure 2. Loading/unloading stages plotted separately.

Example 5.1.4

Uniaxial Cycling of a Piecewise Multi-Linear Elastic Material

Keywords

Multi-linear Material, Cyclic Loading

Description

A bar comprising a multi-linear elastic material is subjected to three different loading sequences:

1. Increasing monotonic
2. Decreasing monotonic
3. Random cyclic sequence

The material model is such that stress/strain behaviour is completely recoverable.

Discretisation

A single BAR2 element of length 100 and unit cross section is used to represent the bar.

Material properties

The piecewise linear material properties are defined by a series of stress/strain points which results in a segmental curve defining a series of Young's moduli, Table 1.

Strain	-0.01	0.00	0.02	0.025	0.065
Stress	-15.00	-10.00	10.00	20.00	30.00

Table 1 Stress/strain input data defining piecewise E values

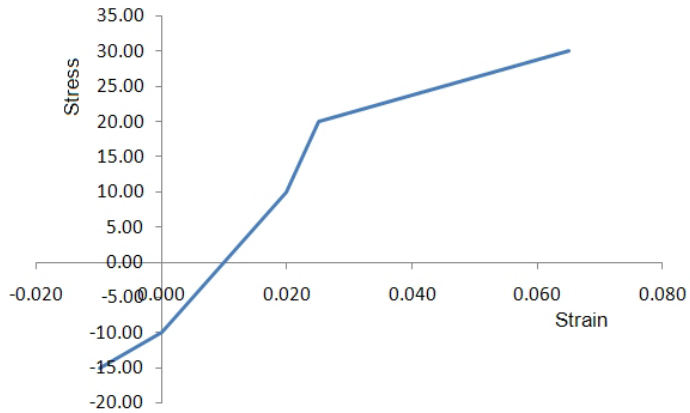


Figure 1 Stress/strain input data defining piecewise E values

Boundary conditions

Fully fixed at one end, lateral displacements restrained at the other.

Loading

The three loading sequences described above are applied via an axial concentrated load at the free end as shown in Table 2:

	Increment number						
Loading sequence	1	2	3	4	5	6	7
1	-17.50	-15.00	-12.50	-10.00	-6.25	-1.25	0.00
2	35.00	30.00	25.00	20.00	15.00	10.00	5.00
3	35.00	-10.00	30.00	25.00	-15.00	20.00	15.00

	Increment number (cont'd)						
Loading sequence	8	9	10	11	12	13	14
1	5.00	10.00	15.00	20.00	25.00	30.00	35.00
2	0.00	-1.25	-6.25	-10.00	-12.50	-15.00	-17.50
3	-17.50	-6.25	5.00	-12.50	-1.25	10.00	0.00

Table 2 Load sequences for applied concentrated load

Results

Load ascending order							
Results	1	2	3	4	5	6	7
Stress	-17.50	-15.00	-12.50	-10.00	-6.25	-1.25	0.00
Strain	-0.01500	-0.01000	-0.00500	0.00000	0.00375	0.00875	0.01000

Load ascending order (cont'd)							
Results	8	9	10	11	12	13	14
Stress	5.00	10.00	15.00	20.00	25.00	30.00	35.00
Strain	0.01500	0.02000	0.02250	0.02500	0.04500	0.06500	0.08500

Table 3 Stress/strain results for all tests

Each test yielded identical results for stress/strain, convergence was achieved in 1 or 2 iterations, results are displayed in Table 3 and have been verified via hand calculations.

Input Data

X05D14A.DAT

X05D14B.DAT

X05D14C.DAT

Example 5.2.1

Buried Pipe With Soil-Pipe Interface Modelled Using 2d Interface Model

Keywords

Elasto-Plastic, Friction

Description

This example (figure 1) consists of an elastic pipe buried in a homogeneous and elastic soil. The interface between the pipe and soil is modelled using an elasto-plastic interface material. Three cases of interface friction are considered:-

- (i) frictionless slip ($\tan\phi = 0.001$),
- (ii) stick ($\tan\phi = 2$),
- (iii) frictional slip ($\tan\phi = 0.25$).

Discretisation

The discretisation (figure 2) is similar to that used in [1]. QPM8 elements are used to discretise the pipe, soil and interface.

Theory

The interaction between the soil and pipe is governed by a frictional type law i.e. bond between the pipe and soil is maintained by a frictional force and once this is overcome debonding and slip will occur. This friction/slip behaviour is modelled using an elasto-plastic interface model, with yielding (slip) defined using the Mohr-Coulomb criterion [2] defined as

$$\tau = c + \sigma \tan \phi \quad (0.0.73)$$

where

τ	maximum shear stress,
σ	stress normal to the soil/pipe interface,
c	cohesion,
ϕ	friction angle.

Comparison

Figure 3 is the deformed mesh for the frictionless slip analysis. A large amount of sliding is visible in the interface. Figure 4 shows the shear stress distribution along the pipe-soil interface.

References

1. DESAI, C.S., ZAMAN, M.M., LIGHTNER, J.G. and SIRIWARDANE, H.J. Thin-layer element for interfaces and joints. *Int. J. Num. Anal. Meth. Geomech.*, Vol.8, 19-43, 1984.
2. OWEN, D.R.J. and HINTON, E. *Finite elements in plasticity: theory and practice*. Pineridge Press, Swansea, UK, 1980.
3. KATONA, M.G. A simple contact-friction interface element with applications to buried culverts. *Int. J. Num. Anal. Meth. Geomech.*, Vol.7, 371-384, 1983.

Input data

X05D21A.DAT

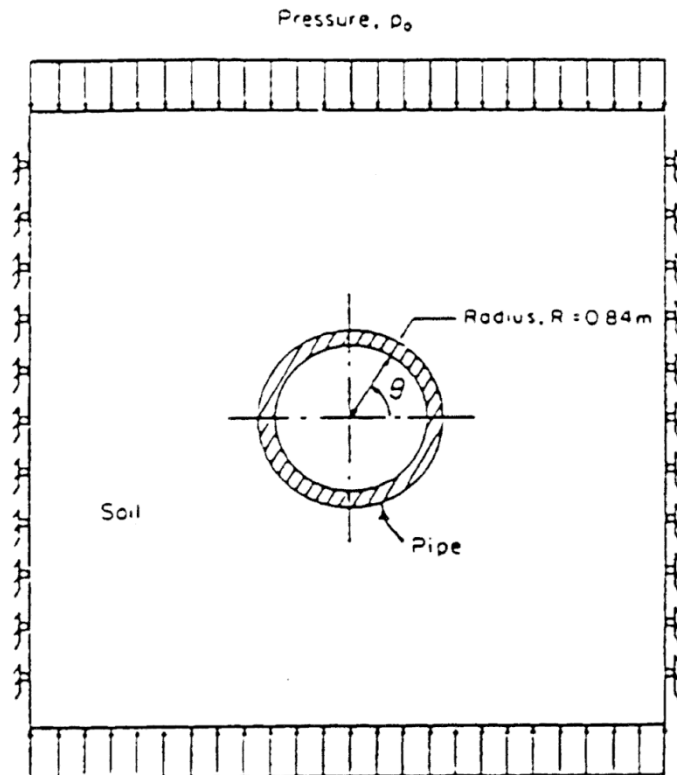


Figure 1 Buried Pipe Example

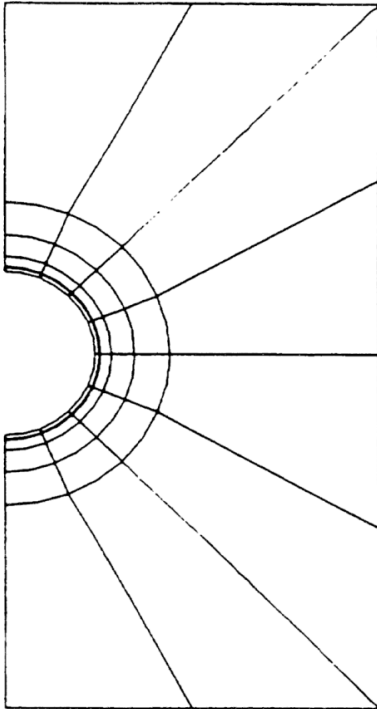


Figure 2 Finite Element Mesh

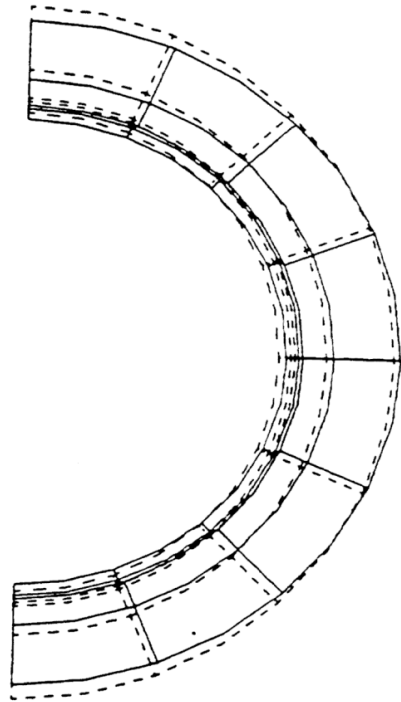
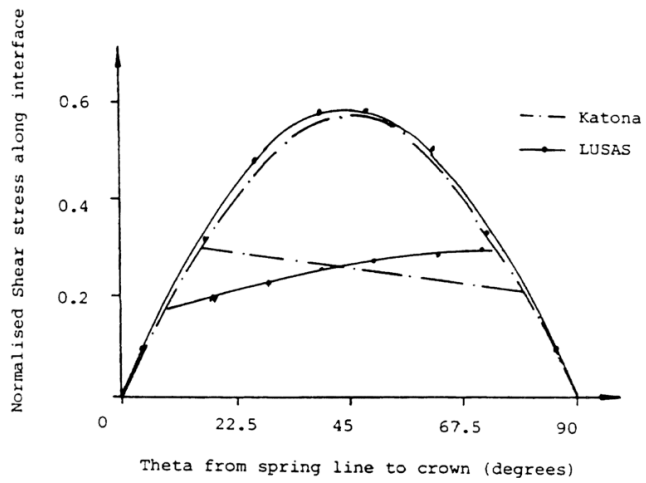


Figure 3 Deformed Mesh Showing Sliding on Interface



Example 5.2.2

Elasto-Plastic Analysis Of A Thick Cylinder Under Internal Pressure

Keywords

Plane Strain, Cylinder, Elasto-Plastic, Pressure

Description

An infinitely long thick cylinder of internal and external radii 100 mm and 200 mm respectively subject to an increasing internal pressure

Discretisation

Plane strain conditions are idealised, the global Z axis being coincident with the axis of the cylinder. One symmetric quarter of the structure is idealised using 30 quadrilateral plane strain (QPN8) elements. Symmetric conditions are specified on the straight line boundaries, and the curved internal and external surfaces are unrestrained. The finite element discretisation is shown in Figure (1).

The nonlinear material behaviour is modelled using a Von-Mises yield criterion and a perfectly plastic post-yield response. The material properties are as follows:

$$\text{Young's Modulus} = 21000 \text{dN/mm}^2$$

$$\text{Poisson's ratio} = 0.25$$

$$\text{Yield stress} = 24 \text{ dN/mm}^2$$

Theory

An increasing internal pressure is applied to the structure. The cylinder deforms elastically until an internal pressure of approximately 12dN/mm^2 is reached. Beyond this pressure level the cylinder behaves elasto-plastically. The spread of plastic deformation through the thickness of the cylinder can be seen from the distribution of the hoop stress component with increasing load.

LUSAS Results

The progressive deformation of the cylinder is shown in Figure (2). Figure (3) shows the von Mises stress distribution obtained from LUSAS as the internal pressure is increased.

References

1. Owen, D.R.J., Hinton, E. Finite Elements in Plasticity: Theory and Practice Publisher. Pineridge Press Ltd. Swansea, U.K. 1980. ISBN 0-906674-05-2
2. Hinton, E., Owen, D.R.J. An Introduction to Finite Element Computations. Publisher. Pineridge Press Ltd. Swansea, U.K. 1979. ISBN 0-906674-06-9
3. Zienkiewicz, O.C.Z. The Finite Element Method, 3rd Edition. Publisher. McGraw Hill Ltd, London, U.K. 1977. ISBN 0-07-084072-5
4. FEAL internal Report 'Plane Strain', FEAL708, Finite Element Analysis Ltd. Forge House, 66 High Street, Kingston Upon Thames, Surrey KT1 1HN. 1986.
5. Hodge, P.G., White, G.N. A quantitative comparison of flow and deformation theories of plasticity. J.Applied Engineering Mechanics, Vol.17, 180-184, 1950.

Input Data

X05D22A.DAT

Note: The load incrementation may alternatively be defined automatically using the following NONLINEAR CONTROL INCREMENTATION and TERMINATION cards:

C	Ref.factor	Max.Factor change	Iterative variation
---	------------	-------------------	---------------------

INCREMENTATION	1	0.25	0
----------------	---	------	---

C	Max.Factor	Max.No.Increments
---	------------	-------------------

TERMINATION	0	5
-------------	---	---

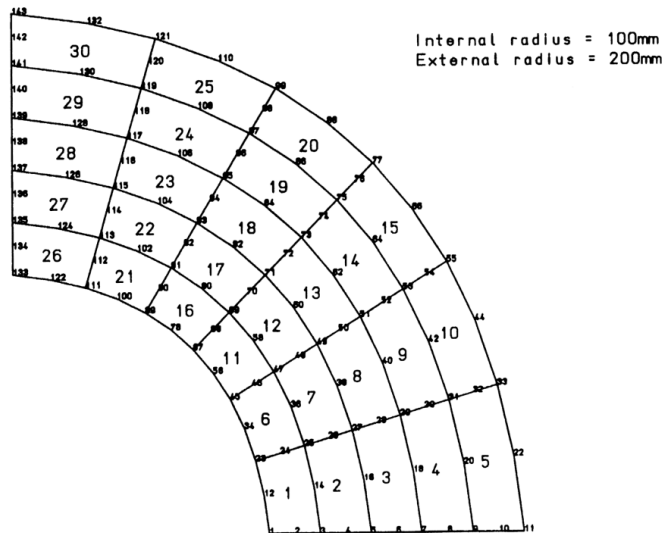


Figure 1

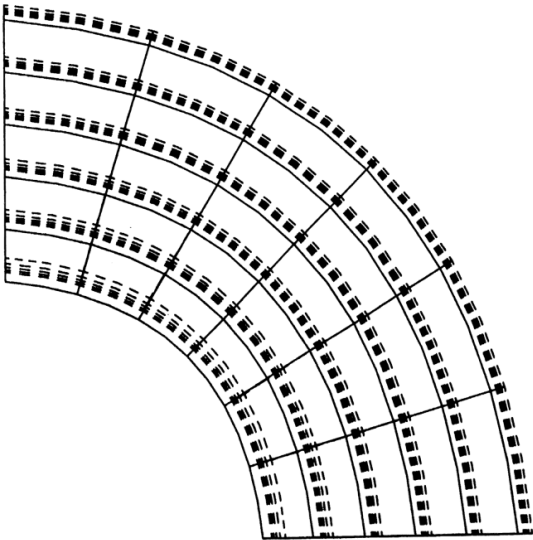


Figure 2

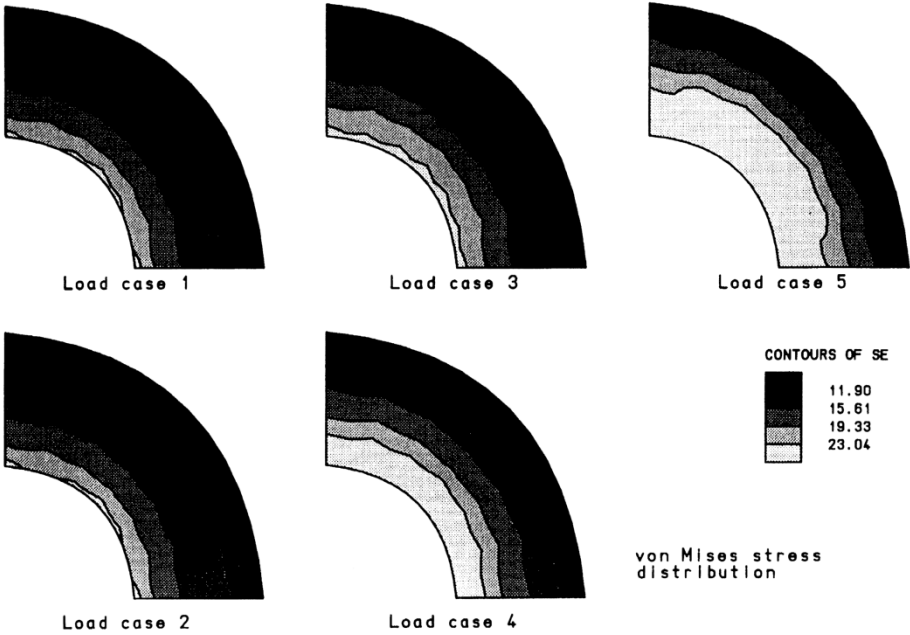


Figure 3

Example 5.2.3

Nonlinear Stress Analysis Of A Two Span Reinforced Concrete Beam

Keywords

Plane Stress, Concrete, Reinforcement, Cracking, Fibres

Description

Nonlinear plane stress analysis of a reinforced concrete beam. The beam dimensions are as follows:

Total Length	1800 mm
Effective Length	1680 mm
Span	840 mm
Depth	80 mm
Effective depth	72.5 mm
Breadth	60 mm

Longitudinal reinforcement is provided continuously at the upper and lower faces of the beam with an average cover of 3 mm. The average effective depth to the tensile reinforcement in either hogging or sagging section is 72.5 mm. Both the upper and lower reinforcement arrangements consist of 4 bars with diameter of 4 mm each, and a total cross-sectional area of 50.4 mm².

The beam is simply supported at its ends and centre, and a concentrated vertical load is applied at each midspan point.

Details of the geometry and steel arrangement are shown in Figures (1) and (2).

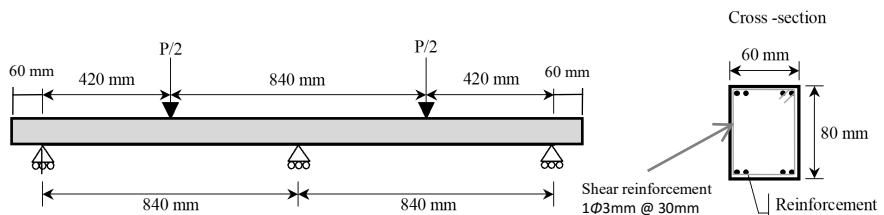


Figure 1: Geometry of reinforced concrete two span beam, also showing beam cross-section.

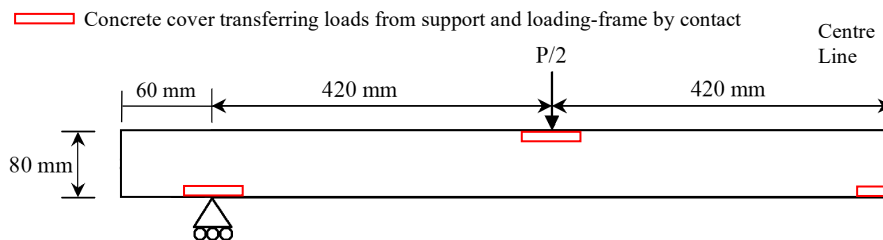


Figure 2: Dimensions of left-hand span of reinforced concrete beam. Symmetry means that only one span of the beam needs to be analysed.

Discretisation

Owing to its symmetrical nature only one span of the beam is discretised. The finite element mesh reproduces closely the structural components, and the load-transfer mechanisms as reported in [1,2,3] and consists of 621 elements. The mesh uses 310 plane stress (QPM4) elements for the concrete. Transverse steel reinforcement and the two layers of longitudinal steel reinforcement are considered using 308 bar (BAR2) elements. The mesh includes 3 joint (JNT3) elements (one joint in between either of the supports and the lower face of the beam, and one joint in between the loading device and the upper face of the beam). The plane stress elements are integrated using a 4-point Gaussian integration scheme.

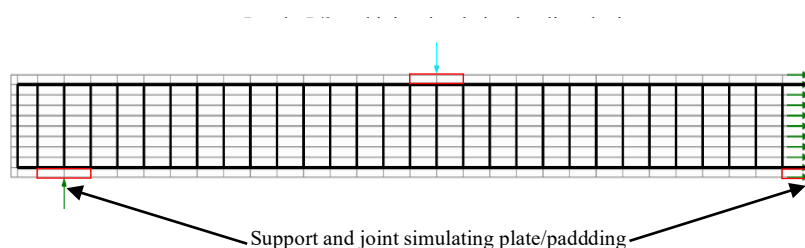


Figure 3: Mesh configuration of the two-span reinforced concrete beam by Duddeck et al [2].

Material properties

The constitutive behaviour of the reinforced concrete beam is modelled using the following material models:

- i. Concrete¹: a handful of the LUSAS nonlinear concrete models as shown in Table 1.

¹ Note that the QPM4 elements highlighted in the mesh in Figure 3, within the concrete cover zone and right in contact with joints, were assigned with elastic concrete properties only. This structural idealisation enables a more realistic redistribution of point loads from the joints.

- ii. Steel reinforcement: LUSAS nonlinear von-Mises material model (model 72), combined with a hardening curve. Material properties are shown in Table 2.
- iii. Compressible paddings and plates used in the experimental setup to transfer loads: LUSAS elastic-spring joint material model (model 2). Joint material properties are shown in Table 3.

Table 1: List of LUSAS concrete material models.

Concrete material no.	Table of material properties	LUSAS model	Material model name and reference
1	Table 4	82	Multi-crack concrete [4, 5]
2	Table 5	84	Multi-crack concrete with crushing [4 ,5]
3	Table 6	109	Smoothed Multi-crack concrete [6,7,8,9,10]
4	Table 7	119	Fibre Multi-crack concrete [11,12]

Table 2: Reinforcement material properties - Nonlinear von-Mises model (model 72) with piecewise hardening curve²

Young's modulus	196.0 kN/mm ²	Hardening gradient 1	100.0 kN/mm ²
Poisson's ratio	0.3	Plastic strain limit 1	5.0E-4
Density	0.0	Hardening gradient 2	40.0 kN/mm ²
Thermal Expansion	0.0	Plastic strain limit 2	1.5E-3
Mass damping	0.0	Hardening gradient 3	12.0 kN/mm ²
Stiffness damping	0.0	Plastic strain limit 3	5.0E-3
Heat fraction	0.0	Hardening gradient 4	2.0 kN/mm ²
Reference temperature	0.0	Plastic strain limit 4	2.5E-2
Yield stress	470.0 N/mm ²		

Table 3: Joint material properties - Joint material model (model 2).

Local horizontal elastic spring stiffness	0.20 kN/mm	Local vertical elastic spring stiffness	20.0 kN/mm
---	------------	---	------------

² Steel reinforcement material properties were calibrated to closely match uniaxial stress-strain experimental curves [1,2,3].

Table 4: Concrete material 1 - Nonlinear multi-crack concrete material model (model 82).

Young's modulus	16.68 kN/mm ²	Tensile strength	1.67 N/mm ²
Poisson's ratio	0.0	End of tensile softening curve	0.0035
Density	0.0	Fracture energy	0.0
Thermal Expansion	0.0	Post fracture friction coefficient	1.5
Mass damping	0.0	Post fracture dilatancy coefficient	0.0
Stiffness damping	0.0	Shear/tensile strength ratio	2.5
Heat fraction	0.0	Reduction factor for shear plastic strain	0.5
Reference temperature	0.0		

Table 5: Concrete material 2 - Nonlinear multi-crack concrete with crushing material model (model 84).

Young's modulus	16.68 kN/mm ²	Compressive strength	32.0 N/mm ²
Poisson's ratio	0.0	Tensile strength	1.67 N/mm ²
Density	0.0	Peak compressive strain	0.0027
Thermal Expansion	0.0	End of compressive softening curve	0.0035
Mass damping	0.0	End of tensile softening curve	0.0035
Stiffness damping	0.0	Fracture energy	0.0
Heat fraction	0.0	Yield/peak compressive stress ratio	1.0
Reference temperature	0.0		

Table 6: Concrete material 3 - Smoothed multi-crack concrete material model1 (model 109).

Young's modulus	16.68 kN/mm ²	Constant in interlock state function	0.425
Poisson's ratio	0.2	Contact multiplier on ϵ_0	0.5
Mass density	0.0	Final contact multiplier on ϵ_0	5.0
Coefficient of thermal expansion	0.0	Shear intercept to tensile strength	1.25
Mass Rayleigh damping constant	0.0	Slope of friction asymptote for damage	0.8
Stiffness Rayleigh damping constant	0.0	Crack fixity strain	0.05
Reference temperature	0.0	Fracture process zone width	60.0 mm
Uniaxial compressive strength	32.0 N/mm ²	Number iterations	2.0
Uniaxial tensile strength	1.67 N/mm ²	Maximum iterations	2.0
Strain at peak uniaxial compression	0.0027	Residual softening factor	0.01
Strain at end of softening curve	0.0	Material constant A_p	0.60
Fracture energy per unit area	0.07 N/mm	Material constant A_n	0.75
Biaxial to uniaxial stress ratio	1.15	Contact sharpness Z1	8.0
Initial relative position of yield surface	0.6	Contact sharpness Z2	8.0
Dilatancy factor	-0.1	Limit of contact transition	3.0

Table 7: Concrete material 4 - Fibre multi-crack concrete material model (model 119).

Young's modulus	16.68 kN/mm ²	Final contact multiplier on e0	5.0
Poisson's ratio	0.2	Shear intercept to tensile strength	1.25
Mass density	0.0	Limiting friction ratio	0.8
Coefficient of thermal expansion	0.0	Crack fixity strain	0.05
Mass Rayleigh damping constant	0.0	Fracture process zone width	60.0 mm
Stiffness Rayleigh damping constant	0.0	Number iterations	2.0
Reference temperature	0.0	Maximum iterations	2.0
Uniaxial compressive strength	32.0 N/mm ²	Residual softening factor	0.01
Uniaxial tensile strength	1.67 N/mm ²	Material constant Ap	0.60
Strain at peak uniaxial compression	0.0027	Material constant An	0.75
Strain at end of softening curve	0.0	Contact sharpness Z1	8.0
Fracture energy per unit area	0.07 N/mm	Contact sharpness Z2	8.0
Fibre Young's modulus	210.0 kN/mm ²	Limit of contact transition	3.0
Fibre volume fraction	1.0E-9	Fibre-matrix interface hardening parameter	0.0
Fibre length	60.0 mm	Fibre-matrix interface hardening ratio	1.0
Fibre diameter	0.90 mm	Fibre frictional sliding stress	1.0 N/mm ²
Biaxial to uniaxial stress ratio	1.15	Fibre snubbing parameter	0.7
Initial relative position of yield surface	0.6	Fibre SUR parameter 1	0.1
Dilatancy factor	-0.1	Fibre SUR parameter 2	0.2
Constant interlock state function	0.425	Effective pull-out displacement parameter	0.8
Contact multiplier on e0	0.5	Limiting COD parameter	0.8

Support Conditions

Node	Support Type	Prescribed Boundary Conditions
356	Roller	FR
357	Restrained	RR
329-335 349-352	Symmetric (C/L)	RF

Notes:

The flexural steel reinforcement is represented by bar elements of equivalent cross-sectional areas. It should be noted that the superposition of the nodal degrees of freedom at the steel/concrete interface assumes that a perfect bond exists between the two components.

Any deformation resulting from the self-weight of the beam is neglected as being small compared to that resulting from the applied load.

The Fibre multi-crack concrete material model (model 119) has been used considering standard steel fibre properties and a negligible dosage of fibres, such that its response matches with that of the smoothed multi-crack concrete material model (model 109).

Theory

The reinforced concrete beam analysed here formed part of an experimental investigation undertaken by Duddeck et al [2]. Under load the beam exhibits both flexural and shearing deformation, and progresses from a well distributed cracking pattern to a local material failure under the loads and at the middle support. The beam has been used as a benchmark test by many research workers in the field of nonlinear concrete analysis [1,2,3].

LUSAS results

1. Figure 4 shows the load-deflection responses obtained from nonlinear analyses of the beam, which compared well against experimental recordings and a theoretical yield-line analysis.
2. Analyses with concrete models 109 and 119 show a stable numerical performance under a tight convergence tolerance (residual norm RDNORM = 0.1 %). This is an improvement over earlier concrete models (models 82 and 84) that needed looser convergence tolerances, and which took a larger number of iterations in stages approaching structural failure.
3. Figure 5 shows contours of the major principal stress at the initial loading stage and clearly demonstrates the areas of tensile stress.
4. Figure 6 onwards show the progression of the cracks through the section of the beam as the load is increased.

References

1. Mueller, G. (1977). 'Numerical Problems in Nonlinear Analysis of Reinforced Concrete', Report to National Science Foundation NSF Grant ENG 77-00146, Structures and Materials Research – Department of Civil Eng., University of California, Berkeley, California.
2. Duddeck, H., Griebenow, Schaper, G. (1978). 'Material and time dependent nonlinear behaviour of cracked reinforced concrete slabs' IASS symposium, Nonlinear behaviour of reinforced spatial structures, Vol.1, 103-133.
3. Abdel-Rahman, H.H. (1982). 'Computational models for the nonlinear analysis of reinforced concrete flexural slab systems'. Ph.D. thesis, University of Wales, Department of Civil Engineering, Swansea.
4. The LUSAS User's Manual Finite Element Analysis Ltd. Forge House, 66 High Street, Kingston Upon Thames, London, U.K.
5. LUSAS Internal Report, 'Nonlinear Concrete Model 24', FEAL703, Finite Element Analysis Ltd. Forge House, 66 High Street, Kingston Upon Thames, London, U.K.
6. Jefferson A.D. (2003). Craft – a plastic-damage-contact model for concrete. I. Model theory and thermodynamic considerations. *International Journal of Solids and Structures* **40**: 5973-5999.
7. Jefferson A.D. (2003). Craft – a plastic-damage-contact model for concrete. II. Model implementation with implicit return-mapping algorithm and consistent tangent matrix. *International Journal of Solids and Structures* **40**: 6001-6022.
8. Jefferson A.D. and Mihai I.C. (2015). The simulation of crack opening-closing and aggregate interlock behaviour in finite element concrete models. *International Journal for Numerical Methods in Engineering* **104**(1): 48-78.
9. Jefferson A.D., Mihai I.C., Tenchev R., Alnaas W.F., Cole G., Lyons P. (2016). A plastic-damage-contact constitutive model for concrete with smoothed evolution functions. *Computers and Structures* **169**: 40-56.
10. LUSAS Internal Report, 'SDR/LUSAS/484h concrete model, CraftS – Solver', Finite Element Analysis Ltd. Forge House, 66 High Street, Kingston Upon Thames, London, U.K.
11. Mihai I.C., Jefferson A.D., Lyons P. (2016). A plastic-damage constitutive model for the finite element analysis of fibre reinforced concrete. *Engineering Fracture Mechanics* **159**: 35-62.
12. LUSAS Internal Report, 'SDR/LUSAS/484n Fibre reinforced concrete model, CraftH – Solver', Finite Element Analysis Ltd. Forge House, 66 High Street, Kingston Upon Thames, London, U.K.

Input data

X05D23B.DAT

X05D23C.DAT

X05D23D.DAT

X05D23E.DAT

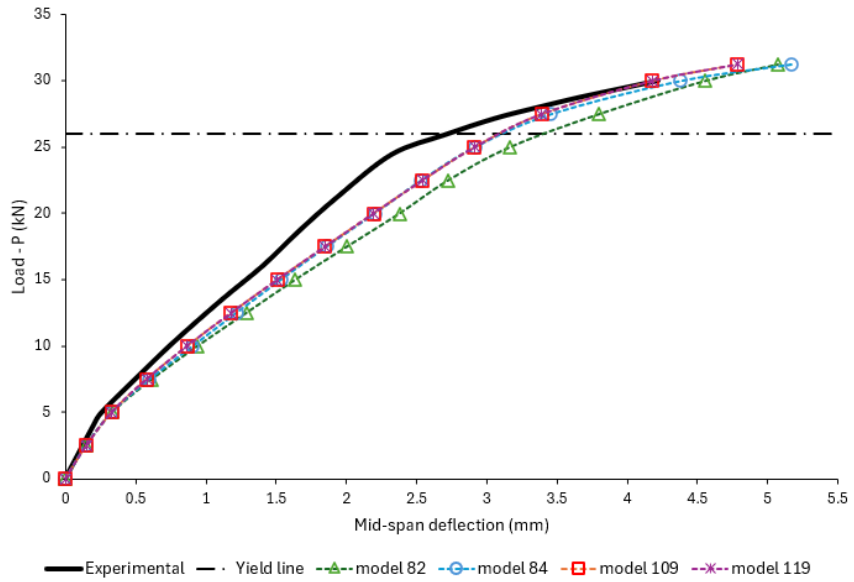
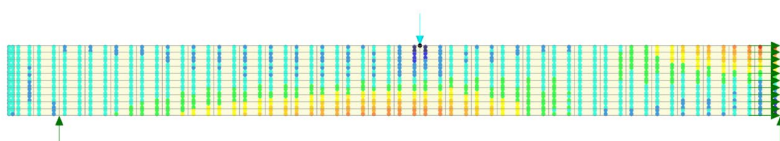
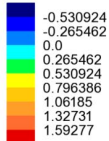


Figure 4: Load (P) vs. mid-span deflection curve for Duddeck's reinforced concrete beam.

Analysis: Analysis 1
 Loadcase: 1:Loadcase 1, 2:Increment 2 Load Factor = 1.00000
 Results file: x05d23d-Analysis 1.mys
 Entity: Stress - Plane Stress
 Component (Gauss point): SMax (Units: N/mm²)



Maximum 1.59989 at Gauss point 3 of element 618
 Minimum -0.789265 at Gauss point 2 of element 600

Figure 5: Duddeck's reinforced concrete two-span beam. Load P=2.5 kN. Major principal stress contour from smoothed multi-crack concrete material model 109.

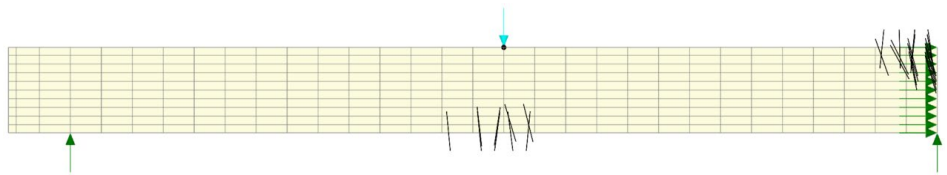


Figure 6: Crack pattern across one span of reinforced concrete beam. Load $P=10.0$ kN. Crack pattern from multi-crack concrete material model 109.

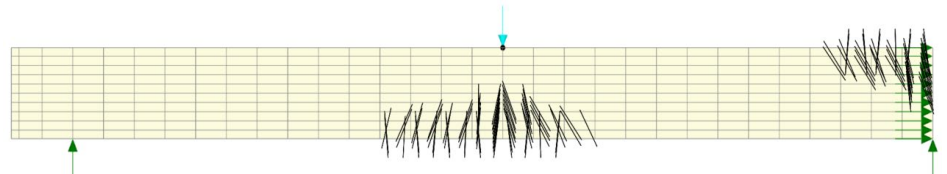


Figure 7: Crack pattern across one span of reinforced concrete beam. Load $P=12.5$ kN. Crack pattern from multi-crack concrete material model 109.

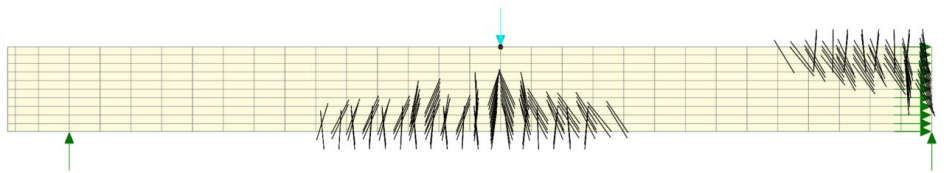


Figure 8: Crack pattern across one span of reinforced concrete beam. Load $P=15.0$ kN. Crack pattern from multi-crack concrete material model 109.

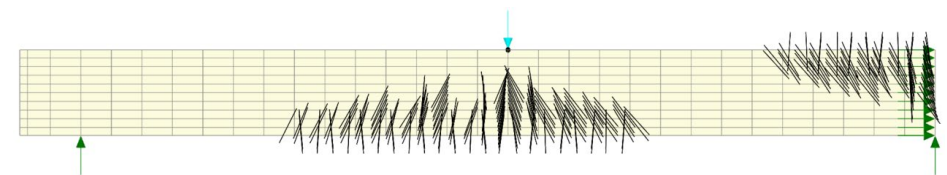


Figure 9: Crack pattern across one span of reinforced concrete beam. Load $P=17.5$ kN. Crack pattern from multi-crack concrete material model 109.

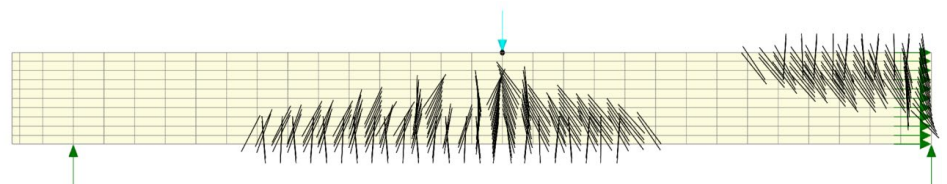


Figure 10: Crack pattern across one span of reinforced concrete beam. Load $P=20.0$ kN. Crack pattern from multi-crack concrete material model 109.

Example 5.2.4

Uniaxial Cycling Elasto-Plastic Damage Analysis

Keywords

Damage, Cyclic Loading, Plasticity

Description

A bar of elasto-plastic material is subjected to uniaxial compressive/ tensile load cycling with an increasing stress level. A damage criterion for the material is specified so that progressive degradation of the elastic Young's modulus takes place as the analysis proceeds. The damage model due to Oliver [1] is invoked which allows different damage thresholds to be specified for tension and compression.

Discretisation

A single QPM4 element of length 10mm and unit width and depth is used to represent the bar.

Material properties

Young's modulus, $E = 2E3 \text{ N/mm}^2$

Poisson's ratio, $\nu = 0.0$

Initial yield stress, $\sigma_{yo} = 22 \text{ N/mm}^2$

Hardening gradient, $h = 100 \text{ N/mm}^2$

Damage property data (Oliver):

Initial damage threshold, $r_0 = 0.44$

Constant, $A = 0.44$

$$\text{Ratio of initial stresses that cause damage in compression/tension} = \frac{S_d^c}{S_d^t} = n = 2$$

Boundary conditions

The boundary conditions are such that lateral displacements are unrestrained while longitudinal displacements are fixed at one end, Figure 1.

Loading

Cyclic vertical compressive/tensile load at the free end, Figure 1.

Theory

The damage parameter, d , for the Oliver [1] model is given by:

$$d = 1 - \frac{r_0}{r_t} \exp \left[A \left(1 - \frac{r_t}{r_0} \right) \right] \quad (0.0.74)$$

Using the specified damage properties this equation becomes:

$$d = 1 - \frac{0.44}{r_t} \exp \left[0.44 \left(1 - \frac{r_t}{0.44} \right) \right] \quad (0.0.75)$$

For this example, the complementary energy norm, r_t , reduces to:

$$r_t = \beta \left[\frac{\sigma_{yy}^2}{E} \right]^{1/2} \quad (0.0.76)$$

The parameter, β , is defined as:

$$\beta = \left(\theta \frac{1-\theta}{n} \right) \quad (0.0.77)$$

where for this example:

$$\theta = \frac{\langle \sigma_{yy} \rangle}{|\sigma_{yy}|} \quad \text{with} \quad \langle \sigma_{yy} \rangle = \begin{cases} \sigma_{yy} & (\sigma_{yy} \geq 0) \\ 0 & (\sigma_{yy} < 0) \end{cases} \quad (0.0.78)$$

The plastic strain, ε_{yy}^p , is computed using:

$$\sigma_{yy} = \sigma_{y0} + \varepsilon_{yy}^p h \quad (0.0.79)$$

The axial strain, ε_{yy} , is then given by:

$$\varepsilon_{yy} = \frac{\sigma_{yy}}{E'} + \varepsilon_{yy}^p \quad \text{where} \quad E' = (1-d)E \quad (0.0.80)$$

More information on the damage models available in LUSAS can be found in the LUSAS Theory Manual.

Solution comparison

Using the above equations strains can be computed for each step of the analysis:

Load	σ_{yy}	β	r_t	d	ε_y^p	ε_{yy}
20	20	1.0	0.447213	0.023202	0.000	0.010238
22.5	22.5	1.0	0.503115	0.178941	0.005	0.018702
25	25	1.0	0.559017	0.301322	0.030	0.047888
27.5	27.5	1.0	0.614919	0.399285	0.055	0.077889
30	30	1.0	0.670820	0.479282	0.080	0.108806
32.5	32.5	1.0	0.726722	0.545470	0.105	0.140751
35	35	1.0	0.782624	0.600883	0.130	0.173847
37.5	37.5	1.0	0.838525	0.647744	0.155	0.208228
40	40	1.0	0.894427	0.687714	0.180	0.244044
42.5	42.5	1.0	0.950329	0.722063	0.205	0.281456
45	45	1.0	1.006230	0.751776	0.230	0.320644
44.9999	49.9999	1.0	1.006230	0.751776	0.230	0.320644
0	0	1.0	1.006230	0.751776	0.230	0.230000
-20	-20	0.5	1.006230	0.751776	0.230	0.189714
-50	-50	0.5	1.006230	0.751776	0.180	0.079285
-60	-60	0.5	1.006230	0.751776	0.080	-0.040859
-70	-70	0.5	1.006230	0.751776	-0.020	-0.161001
-80	-80	0.5	1.006230	0.751776	-0.120	-0.281145
-90	-90	0.5	1.006230	0.751776	-0.220	-0.401288
-100	-100	0.5	1.118030	0.800230	-0.320	-0.570288
-99.9999	-99.999	0.5	1.118030	0.800230	-0.320	-0.570288
0	0	1.0	1.118030	0.800230	-0.320	-0.320000

The theoretical assumptions for this damage model are such that after the onset of damage, no further damage can occur until the maximum stress previously attained is exceeded. The Oliver damage model also allows some control over the damage threshold (by specification of the n parameter), depending on whether the material is in tension or compression. For this example, it can be seen from the table that the damage parameter remains constant between loads of -20 and -90 as a result of specifying $n=2$. The results for the LUSAS analysis reproduce these values exactly and are plotted in Figure 2.

References

1. Oliver, J., Cervera, M., Oller, S. and Lubliner, J. Isotropic damage models and smeared crack analysis of concrete. Computer Aided Analysis and Design of Concrete Structures, Edited by, Bicanic, N. and Mang, H., Vol. 2, 4th-6th April 1990.

Input Data

X05D24A.DAT

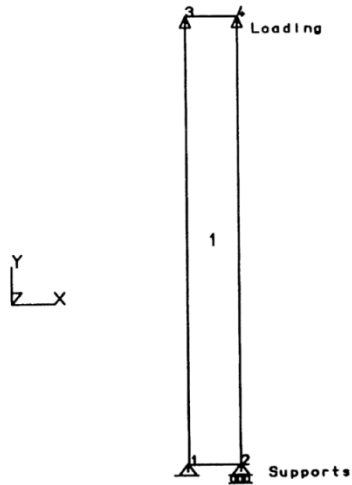


Figure 1. Supports and Loading condition

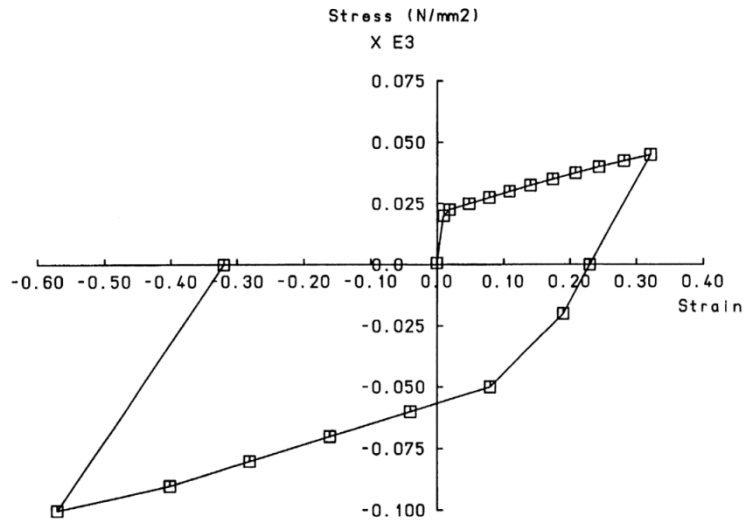


Figure 2. Stress v total strain - Sky components.

Example 5.2.5

Thermally Induced Creep Of Internally Pressurised Hollow Sphere

Keywords

Implicit, Creep, Viscous

Description

An internally pressurised sphere with a linear variation of temperature through its thickness is allowed to creep over a period of 10^{10} . The creep is defined using a variant of the eighth parameter law.

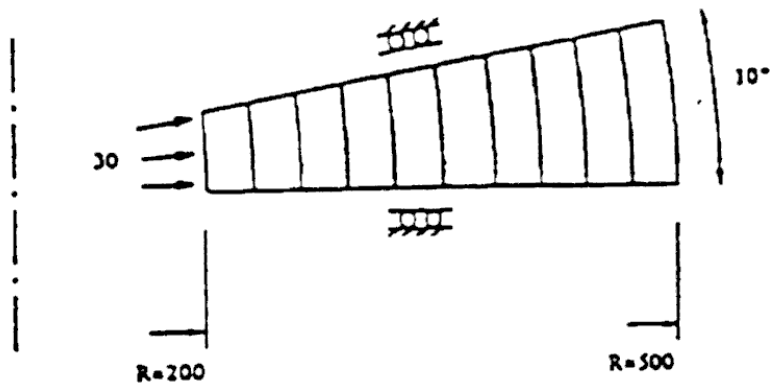
Finite Element Model

10 axisymmetric elements are used to model the through thickness variation.

Geometry and loads

Internal radius 200

External radius 500



Face load of 30

Temperature gradient along sphere radius of $T=333(1+100/R)$

Material properties

Young's modulus = 10000

Poisson's ratio = 0.25

Eight parameter law (specialised form of)

$$\varepsilon = Aq^n t^m e^{(-h/T)}$$

where A=3E-6, n=5.5, m=1, h=12500, T=temperature

Boundary conditions

Free to displace along radius of centre of sphere

Solution Comparison

The effective stresses at time 10^{10} at various radii are compared below with the NAFEMS target solution. The solution is fully automatic with the initial step size evaluated from the first (static) stress solution. Further time steps are calculated using criterion which limit the change in creep strain across an increment. Figure 1 shows the variation of stresses with respect to time.

Radius	NAFEMS	LUSAS
205	11.47	11.54
350	17.61	17.81
495	21.10	21.07

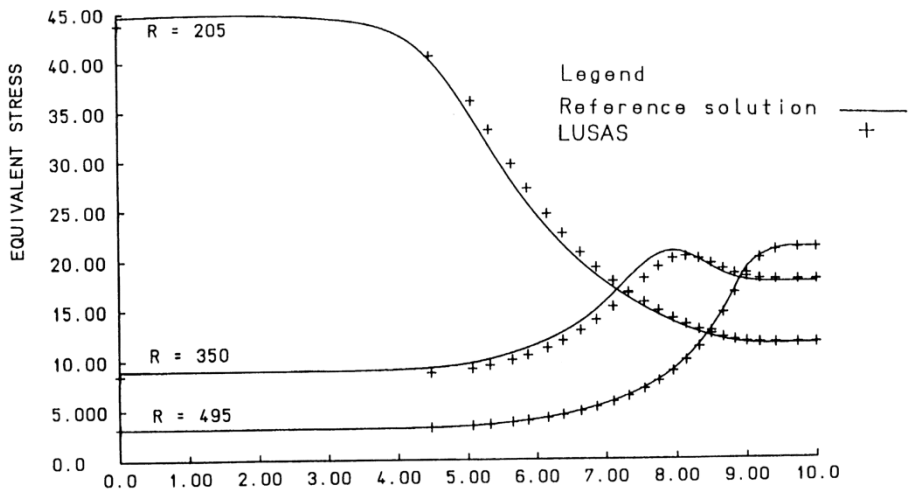
References

1. NAFEMS selected benchmarks for material non-linearity (to be published)

Input Data

X05D25A.DAT

Variation of effective stress with time



Example 5.2.6

Combined Plasticity And Creep Of Bar

Keywords

Implicit, Creep, Viscous, Plastic

Description

A bar is loaded from yield to a value of twice the initial yield stress and then unloaded back to the original yield stress. The unloading takes place in the elastic regime so that there is no additional plastic flow. However, the bar continues to creep since it is subject to stress.

Finite Element Model

A single plane stress element

Geometry

Bar length = 10

cross sectional area = 1



P

Material properties

Young's modulus = 2×10^5

Poisson's ratio = 0.3

Hardening = 100

Power hardening law - time dependent form $\epsilon = A \sigma^N t^m$

where $A=1E-7$, $n=5$, $m=0.5$

Boundary Conditions

The element is restrained at one end in the axial direction, but it is allowed to pull-in to relieve stress in the orthogonal direction.

Solution Comparison

Since the area of the bar is unity, the uniaxial stress s is equivalent to the applied load P . The stress varies linearly, initially increasing to twice the yield stress over a period of 1 second and then reducing back to the yield stress in 0.5 seconds.

$$P(t) = 20(t + 1) \quad 0 < t < 1$$

(0.0.81)

$$P(t) = 40 - 40(t - 1) \quad 1 < t < 1.5$$

and the stress history is therefore,

$$\sigma(t) = \sigma_o + \dot{\sigma}_1 t \quad 0 < t < 1$$

(0.0.82)

$$\sigma(t) = \sigma_1 + \dot{\sigma}_2 t \quad 1 < t < 1.5 \quad (0.0.83)$$

Where $\sigma_1 = \sigma_o + \dot{\sigma}_1$ since $t = 1$ and assuming $\dot{\sigma}_1$ is constant.

Considering the period for $0 < t < 1$, the rate of creep strain is

$$\dot{\epsilon}^c = Am(\sigma_o + \dot{\sigma}_1 t)^n t^{m-1} \quad (0.0.84)$$

and integrating with respect to time, gives the creep strain as,

$$\epsilon^c = Am \int_0^t (\sigma_o + \dot{\sigma}_1 t)^n t^{m-1} dt \quad (0.0.85)$$

The plastic strain is evaluated from the strain hardening definition as,

$$\epsilon^p = \frac{\dot{\sigma}_1 t}{h} \quad (0.0.86)$$

and the elastic strain is

$$\epsilon^e = \frac{\sigma_o + \dot{\sigma}_1 t}{E} \quad (0.0.87)$$

Summing the components, the total strain over the period $0 < t < 1$ is then,

$$\begin{aligned}\varepsilon^T &= \varepsilon^e + \varepsilon^p + \varepsilon^c \\ &= \frac{\sigma_0 + \dot{\sigma}_1 t}{E} + \frac{\dot{\sigma}_1 t}{h} + At^{1/2} \left[\sigma_0^5 + \frac{5}{3} \sigma_0^4 \dot{\sigma}_1 t + 2\sigma_0^3 \dot{\sigma}_1^2 t^2 + \frac{5}{9} \sigma_0^2 \dot{\sigma}_1^3 t^3 + \frac{1}{11} \dot{\sigma}_1^4 t^4 + \frac{1}{11} \dot{\sigma}_1^5 t^5 \right]\end{aligned}\quad (0.0.88)$$

For the period $1 < t < 1.5$ the prescribed stresses decrease. The new creep strain rate is then

$$\varepsilon^c = A \left[\sigma_1 + \dot{\sigma}_2 (t-1) \right]^5 t^{-1/2} \quad (0.0.89)$$

For simplicity the rate of decrease of stress $\dot{\sigma}_2$ has been set to the minus of the maximum attained stress σ_1 . Integrating the creep strain over the period $1 < t < 1.5$ yields,

$$\varepsilon_c^c = A \sigma_1^5 t^{1/2} \left[32 - \frac{80}{3} t + 16t^2 - \frac{40}{7} t^3 + \frac{10}{9} t^4 - \frac{1}{11} t^5 \right] - \frac{11531}{693} A \sigma_1^5 \quad (0.0.90)$$

and the total strain for the period $1 < t < 1.5$ is,

$$\varepsilon^T = \frac{\sigma_1 + \dot{\sigma}_2 (t-1)}{E} + \frac{\dot{\sigma}_1}{h} + \frac{4672}{693} A \sigma_0^2 + \varepsilon_c^c \quad (0.0.91)$$

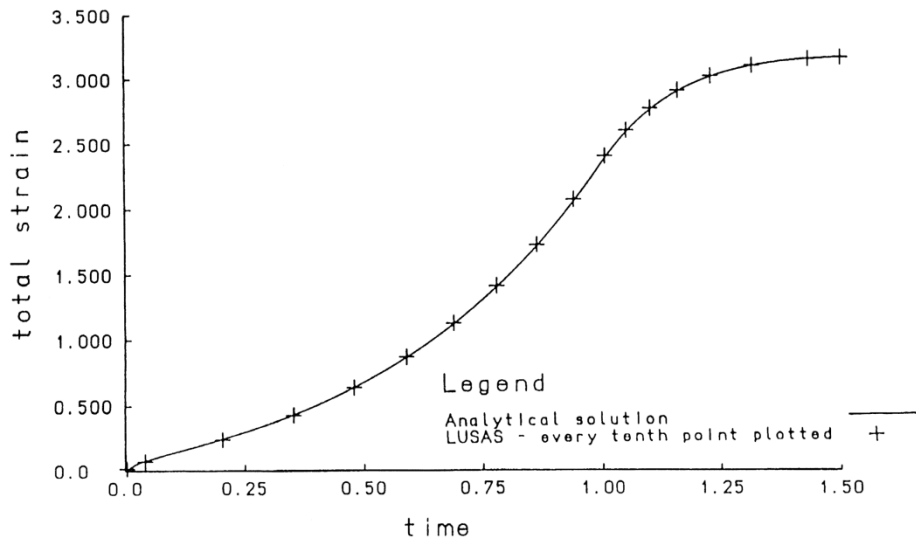
Note: the solution produces strains of over 3 which are invalid in the context of linear deformations. However, the purpose of the example is simply to demonstrate the integration of combined creep and plastic material behaviour and to compare with an analytical solution derived from the same assumptions as the implemented theory.

The LUSAS results are shown in Figure 1 and compare exactly with those computed by equations (0.0.88) and (0.0.91).

Input Data

X05D26A.DAT

Elasto-plastic creep with cyclic load



Example 5.2.7

Extension Of A Double Notched Specimen

Keywords

Incompatible Elements, Plasticity

Description

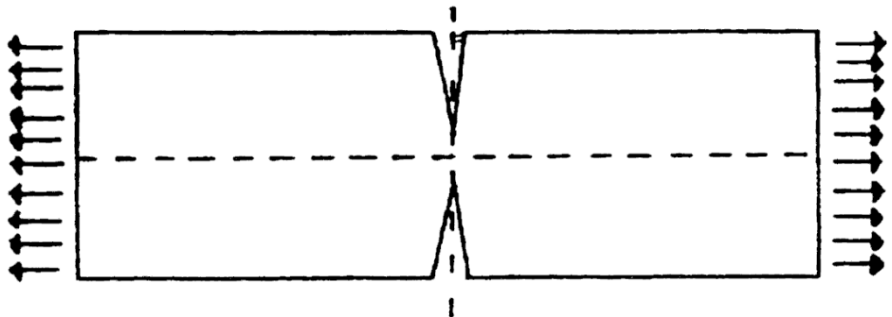
A notched bar is stretched until the limiting load, following yield, is attained. Standard (compatible) displacement based elements produce a load- deflection curve which increases monotonically beyond the limit load, whilst the incompatible elements are able to capture the true behaviour.

Finite Element Model

A rectangular mesh of 15*5 elements models one quarter of the structure. The bar is considered to be in a state of plane strain.

Geometry

Length	30.0
Width	10.0



Material properties

Young's modulus	70.0
Poisson's ratio	0.3
Yield stress	0.243
Hardening	0.0

Boundary Conditions

Symmetry boundary conditions are applied along the edges. The notch is modelled by freeing the displacements along its length.

Solution Comparison

The theoretical limit load is $5.94 \times \text{yield stress} = 1.4434$. Two solutions are illustrated, one for the standard displacement elements and the other for the incompatible elements. The applied load is calculated by the summation of the reactions along the extended edge. From symmetry, the expected load is half that calculated for the full plate.

The initial mesh and support conditions are shown in the top diagram of figure 1. The two other diagrams of figure 1 shown the distribution of yield and the equivalent von Mises stress at the end of the final loadstep, for the incompatible elements. Figure 2 displays the corresponding yield and equivalent stress plots for the standard displacement elements. The yield zone for the standard elements is less localised than that of the incompatible elements and is capable of sustaining a larger load as is shown in figure 3.

References

1. Simo J.C., Rifai, M.S., A class of mixed assume strain methods and the method of incompatible modes, Int. J. Num. Meth. Eng., 31, 385-405, 1991.

Input Data

X05D27A.DAT

The data file for the standard elements is obtained by substituting the element type QPN4 for QPN4M in the above data file.

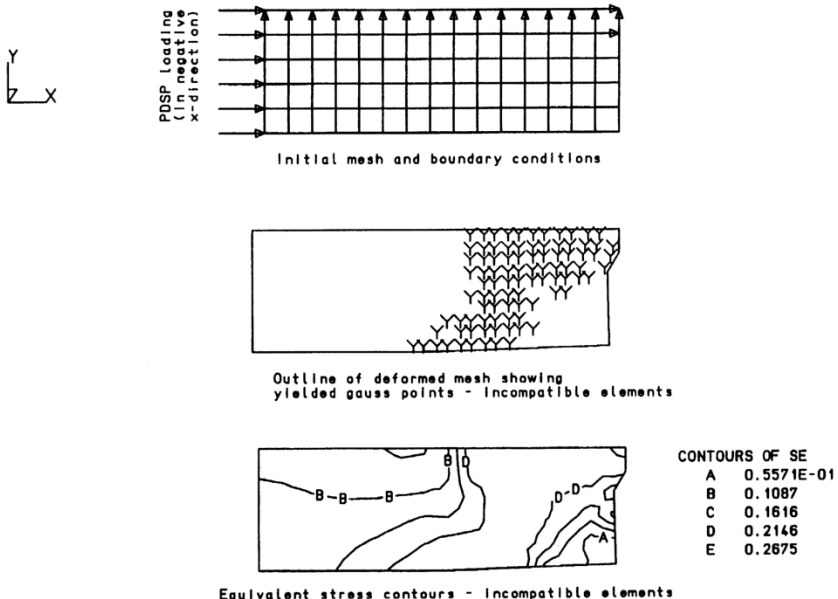


Figure 1 Failure of Notched Bar (1)

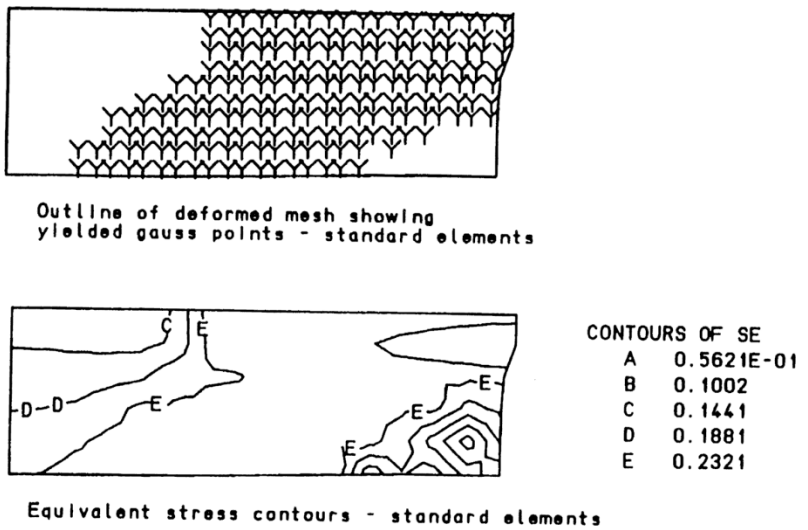


Figure 2 Failure of Notched Bar (2)

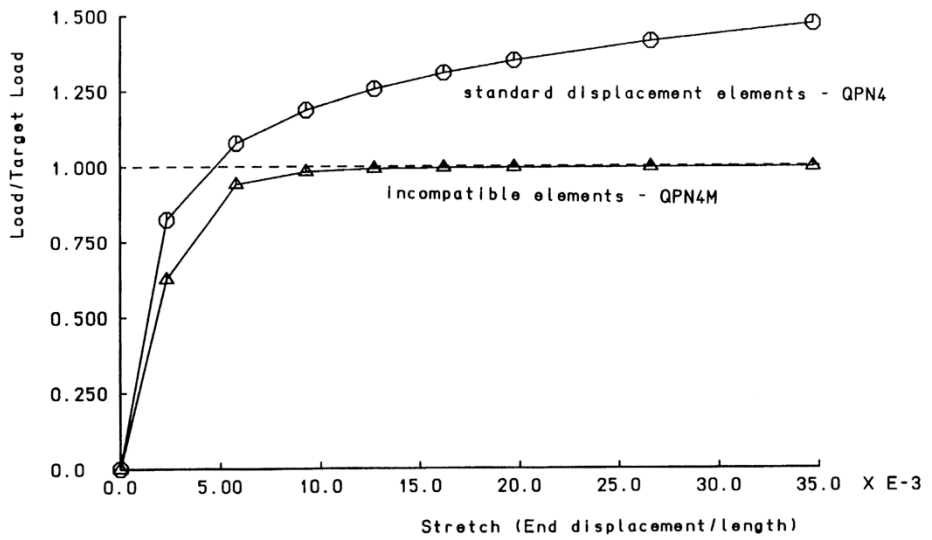


Figure 3 Load/Displacement Behaviour of Notched Bar

Example 5.2.8

Plane Strain Limit Load Analysis of Granular Material

Keywords

Elasto-Plastic, Volumetric Crushing, Drucker-Prager, Mohr-Coulomb

Description

A strip of granular material compressed by a rigid footing is analysed to determine its limit load. Details of the problem can be found in Figure 9.

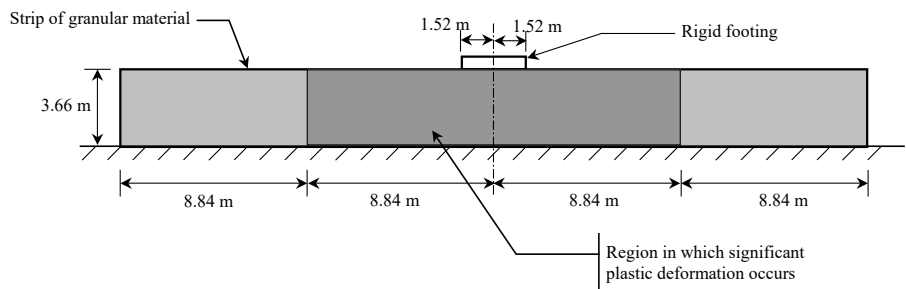


Figure 11: Dimensions of the granular material for which the limit load analysis is carried out. The dark shaded area is considered the region where significant plastic deformation takes place.

The strip of granular material is in fact considered to be infinitely long, so the vertical boundaries at the edge of the specimen have been positioned such that their presence has a minimal effect on the results.

The performance of three material models is examined – the Drucker-Prager material model, the Mohr-Coulomb material model and the Volumetric Crushing material model.

Discretisation

Utilising symmetry about the centre plane, only one half of the problem in Figure 9 is meshed. The strip itself is modelled using quadratic plane strain elements, QPN8. The finite element mesh can be found in Figure 10.

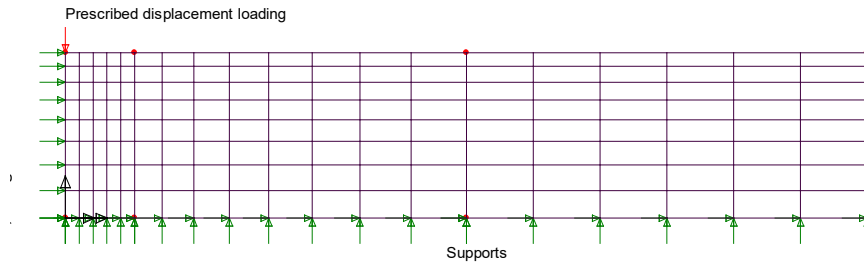


Figure 12: Finite element mesh for the granular material limit load analysis, showing supports and loading.

Material properties

The material properties of the strip are defined using the Drucker-Prager material model in one test, the Mohr-Coulomb material model in a second test and the Volumetric Crushing material model in a third. Table 1 gives the Mohr-Coulomb material properties for this test.

Table 8: Mohr-Coulomb material properties for granular material limit load verification test.

Young's modulus, E	Poisson's ratio, ν	Angle of friction, ϕ	Cohesion, c
206.8 MPa	0.3	20°	68.94 KPa

Mohr-Coulomb material properties

The Mohr-Coulomb material properties can be found in Table 1.

Drucker-Prager material properties

In order to determine the appropriate Drucker-Prager parameters to use in this test it is useful at this stage to probe the relationship between the Drucker-Prager and Mohr-Coulomb material models.

The general form of the Drucker-Prager yield function is given by

$$F(\underline{\sigma}, \kappa) = \alpha I_1 + \sqrt{J_2} - k \quad (0.092)$$

where I_1 is the first stress invariant, J_2 is the second stress invariant and α and k are constants that define the yield surface.

$$I_1 = \sigma_{xx} + \sigma_{yy} + \sigma_{zz} \quad (0.093)$$

$$J_2 = \frac{1}{2} \left[(\sigma_{xx} - \sigma_m)^2 + (\sigma_{yy} - \sigma_m)^2 + (\sigma_{zz} - \sigma_m)^2 \right] + \tau_{xy} + \tau_{yz} + \tau_{zx} \quad (0.094)$$

where $\sigma_m = \frac{1}{3}I_1$
(0.0.95)

The LUSAS Drucker-Prager material model has its yield criteria coincide with the outer apices of the Mohr-Coulomb material model (see Figure 11). In this case, the yield function is given by

$$F(\underline{\sigma}, \kappa) = \frac{2 \sin \phi}{\sqrt{3}(3 - \sin \phi)} I_1 + \sqrt{J_2} - \frac{6 \cos \phi}{\sqrt{3}(3 - \sin \phi)} c \quad (0.0.96)$$

where ϕ is the angle of friction and c is the cohesion.

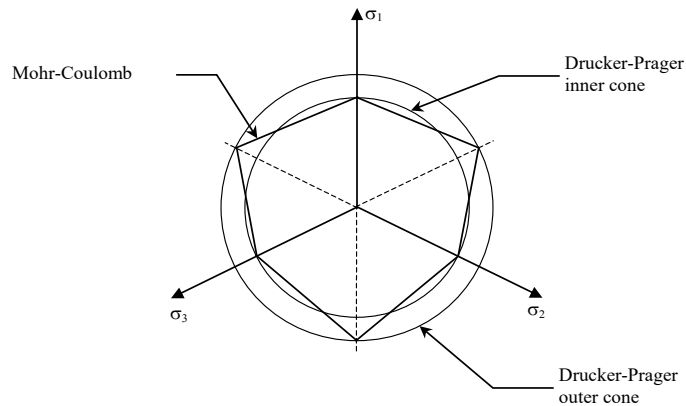


Figure 13: The two forms of the Drucker-Prager material model. The outer cone coincides with the outer apices of the Mohr-Coulomb model while the inner cone coincides with the inner apices of the Mohr-Coulomb model.

There is another form of the Drucker-Prager material model that coincides with the inner apices of the Mohr-Coulomb model (Figure 11). This given by

$$F(\underline{\sigma}, \kappa) = \frac{2 \sin \phi}{\sqrt{3}(3 + \sin \phi)} I_1 + \sqrt{J_2} - \frac{6 \cos \phi}{\sqrt{3}(3 + \sin \phi)} c \quad (0.0.97)$$

It is possible to modify the outer Drucker-Prager cone in Figure 11 so that it coincides with the inner apices of the Mohr-Coulomb model. This is achieved by modifying the angle of friction and the cohesion used in (5) so that yield function for the outer cone form simulates the inner form.

The first step is to compute values for α and k that represent the inner cone. Comparing the inner cone formulation in (6) with the more general form in (1), leads to

$$\alpha_{\text{int}} = \frac{2 \sin \phi}{\sqrt{3}(3 + \sin \phi)} \quad \text{and} \quad k_{\text{int}} = \frac{6 \cos \phi}{\sqrt{3}(3 + \sin \phi)} c \quad (0.0.98)$$

Next, by comparing the outer cone formulation in (5) with (1), α_{int} and k_{int} can then be used to derive an angle of friction and a cohesion that simulates the inner cone. They are given by

$$\sin\phi = \frac{3\alpha_{\text{int}}\sqrt{3}}{2 + \alpha_{\text{int}}\sqrt{3}} \quad (0.0.99)$$

$$c = \frac{k_{\text{int}}\sqrt{3}(3 - \sin\phi)}{6\cos\phi} \quad (0.0.100)$$

In the computation of the cohesion in (9) the value of ϕ computed from (8) is used.

Applying this technique to the problem being investigated here, the angle of friction and the cohesion that will simulate the inner cone form of the Drucker-Prager material model, using the data in Table 1, are

$$\phi = 16.2 \quad \text{and} \quad c = 54\,927 \text{ Pa} \quad (0.0.101)$$

It can be seen that the difference between the material properties in Table 1 and those in equation (10) is quite significant.

Having shown how the LUSAS Drucker-Prager yield function can be adjusted to take different forms, we can proceed to make a further adjustment for plane strain. A proposed modification, corresponding to an adjustment of failure loads, is based on the following.

$$\alpha = \sin\frac{\phi}{3} \quad \text{and} \quad k = c \cos\phi \quad (0.0.102)$$

Using (1), (5) and (11), the angle of friction and cohesion that should be used in the LUSAS Drucker-Prager model for plane strain are

$$\phi = 15.9^\circ \quad \text{and} \quad c = 53\,007 \text{ Pa} \quad (0.0.103)$$

A summary of material properties to use with the Drucker-Prager material model is given in Table 2.

Table 9: Material properties to be used with the LUSAS Drucker-Prager material model.

	Young's modulus, E	Poisson's ratio, ν	Angle of friction, ϕ	Cohesion, c
Outer cone form	206.8 MPa	0.3	20o	68 940 Pa
Inner cone form	206.8 MPa	0.3	16.2o	54 927 Pa
Proposed plane strain	206.8 MPa	0.3	15.9o	53 007 Pa

Volumetric crushing material properties

The Volumetric Crushing material properties are computed to match the Drucker-Prager properties. The yield function for the Volumetric Crushing material model is given by

$$\Phi = \frac{1}{2} \underline{\underline{\mathbf{S}}}^T \underline{\underline{\mathbf{L}}} \underline{\underline{\mathbf{S}}} - (a_0 + a_1 p + a_2 p^2) \quad (0.0.104)$$

where $\underline{\underline{\mathbf{S}}}$ is the deviatoric stress vector, $\underline{\underline{\mathbf{L}}}$ is given by

$$\underline{\underline{\mathbf{L}}} = \begin{bmatrix} 1 & 0 & 0 & 0 & 0 & 0 \\ 0 & 1 & 0 & 0 & 0 & 0 \\ 0 & 0 & 1 & 0 & 0 & 0 \\ 0 & 0 & 0 & 2 & 0 & 0 \\ 0 & 0 & 0 & 0 & 2 & 0 \\ 0 & 0 & 0 & 0 & 0 & 2 \end{bmatrix} \quad (0.0.105)$$

$\underline{\underline{\mathbf{P}}}$ is the volumetric pressure and a_0 , a_1 , a_2 are user defined constants. If the following applies

$$a_0 + a_1 p + a_2 p^2 = \sigma_o \quad (0.0.106)$$

then the yield function in (13) resembles the basic von Mises yield criterion, where σ_o is the uniaxial yield stress. If we also assume infinitesimal strains then the volumetric pressure, $\underline{\underline{\mathbf{P}}}$, is defined as

$$p = -\frac{1}{3} (\sigma_{xx} + \sigma_{yy} + \sigma_{zz}) \quad (0.0.107)$$

When both (15) and (16) apply the Volumetric Crushing yield criteria can be re-expressed as

$$J_2 - \frac{1}{9} (3a_0 - a_1 I_1 + a_2 I_1^2) = 0 \quad (0.0.108)$$

Taking the square of (1) we have for the Drucker-Prager yield function

$$J_2 - (k^2 - 2\alpha k I_1 + \alpha^2 I_1^2) = 0 \quad (0.0.109)$$

By equating the Volumetric Crushing yield function in (17) with the squared Drucker-Prager yield function in (18) the constants for the Volumetric Crushing model are given by

$$a_0 = k^2, \quad a_1 = 6\alpha k, \quad a_2 = 9\alpha^2 \quad (0.0.110)$$

If the inner cone form of the Drucker-Prager model is to be matched, then (6) should be used to compute α and k while if the plane strain form is to be matched then (11) should be used.

The Volumetric Crushing constants can then be computed from (19) using these values of α and k .

The remaining material properties for the Volumetric Crushing model are

$$\text{Bulk modulus} \quad : K = \frac{E}{3(1-2\nu)} = 1.725 \times 10^8 \text{ Pa}$$

$$\text{Shear modulus} \quad : G = \frac{E}{2(1+\nu)} = 7.962 \times 10^7 \text{ Pa}$$

The tension cut off, p_c , is defined as a large number, $1 \times 10^9 \text{ Pa}$.

A summary of the material properties for the Volumetric Crushing material model can be found in Table 3. To enable a comparison with the Drucker-Prager material model, the pressure-logarithm of relative volume curve is defined as linear, see Table 3: Material properties for the Volumetric Crushing material model that simulate the plane strain adjusted Drucker-Prager material model.

Table 10: Material properties for the Volumetric Crushing material model that simulate the plane strain adjusted Drucker-Prager material model.

Drucker-Prager match	Bulk Modulus, K	Shear Modulus, G	Constant a_0	Constant a_1	Constant a_2	Tension cut off, p_c
Inner cone	172.5 MPa	79.62 MPa	4.509 GPa	47.61 KPa	0.1257	1.0 GPa
Plane strain	172.5 MPa	79.62 MPa	4.192 GPa	45.10 KPa	0.1213	1.0 GPa

Table 11: Data for the pressure-logarithm of relative volume curve.

	$\ln(V/V_0)$	p
Start point	0	0
End point	-1×10^{-4}	17.25 KPa

Loading

A compressive prescribed displacement is applied to the node at the centre of the rigid footing in the vertical direction. This is shown on the mesh in Figure 10. This vertical displacement is then linked to remainder of the nodes underneath the footing via constraint equations. In this way perfect roughness is ensured. A total prescribed displacement of 1.25m is applied.

LUSAS Results

Figure 12 shows results that are obtained from the Mohr-Coulomb, the Drucker-Prager and the Volumetric Crushing material models. On the same graph are limit analysis solutions from Terzaghi and Prandtl. The graph shows that all three material models have produced limit loads that lie within or are close to the boundaries of the two analytical solutions. The models have therefore returned acceptable limit loads.

In this test the outer cone form of the Drucker-Prager model produced a limit load of approximately 2.5 MPa. Both the inner cone form and the plane strain adjusted form produce results that are much closer to the analytical solutions. Since the outer cone form represents triaxial compression this illustrates that care is needed in identifying the dominant stress state and adjusting the Drucker-Prager material parameters accordingly.

Comparing the adjusted LUSAS Drucker-Prager results with those from the LUSAS Mohr-Coulomb model shows that the plane strain adjustment has brought the results closer to the Mohr-Coulomb results, but indicates that adjustment could be refined further for this particular problem. However, since the stress combination in this test is not simple, further refinement may not be feasible or straightforward.

Considering the Volumetric Crushing material model, results from both the inner cone and the plane strain matched models lie closer to the Mohr-Coulomb results than the Drucker-Prager results do. However, the Volumetric Crushing model produces results that are softer than both models. The latter is due to the non-associative flow rule that the Volumetric Crushing model uses.

Input Data

Drucker-Prager	: X05D28E.DAT, X05D28F.DAT, X05D28G.DAT
Mohr-Coulomb	: X05D28H.DAT
Volumetric crushing	: X05D28I.DAT, X05D28J.DAT

References

1. A. Mouazen, M. Nemenyi. 'Tillage tool design by the finite element method: Part1. Finite element modelling of soil plastic behaviour'. J. Agric. Engng. Res, Volume 72, pp.37-51 (1999).
2. D.R.J. Owen, E. Hinton . 'Finite elements in plasticity: Theory and Practice'. Pineridge Press Limited, Swansea, UK. (1980).
3. G. Duffett, G. Jelinc, P. Lyons. 'A study of the material models in LUSAS for the analysis of geotechnical materials'. In Computational Plasticity: Fundamentals and Applications, Barcelona 1995, Editors D.R.J. Owen, E. Onate. Pineridge Press Limited, Swansea, UK. (1995).
4. Theory Manual, LUSAS v13. LUSAS, Kingston-upon-Thames, UK (2001).
5. LUSAS internal report SDR/LUSAS/061. 'Crushable foam material model', LUSAS, Kingston-upon-Thames, UK (1994).
6. LUSAS internal report SDR/LUSAS/255a. 'Verification of the LUSAS Drucker-Prager material model', LUSAS, Kingston-upon-Thames, UK (2001).

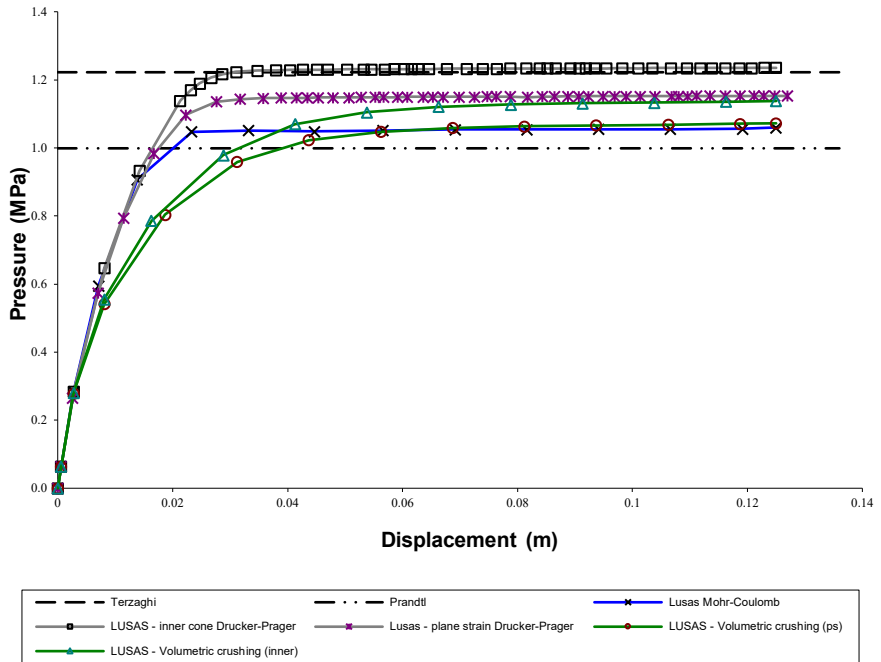


Figure 14: Variation of pressure underneath the footing against applied displacement. Volumetric crushing key: ps – matched with plane strain Drucker-Prager, inner – matched with Drucker-Prager inner cone.

Example 5.2.9

Plane Strain Analysis Of Slope Stability Limit

Keywords

Elasto-Plastic, Mohr-Coulomb, Associative/non-associative Flow

Description

In this analysis gravity is increased in value until the slope collapses. The larger the final value above the actual value of gravity the safer the slope. The problem is modelled using plane strain elements. The analysis is run twice, once using associative plastic flow properties and then for non-associative plastic flow. The non-symmetric solver is used for the non-associative flow solution.

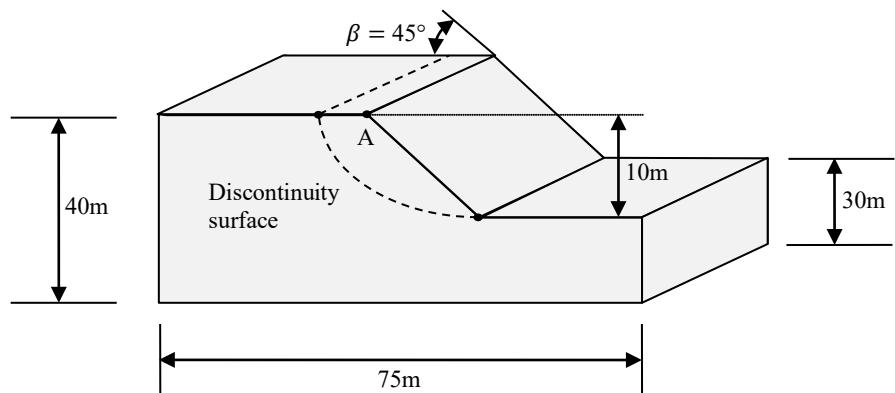


Figure 13: Dimensions of slope.

The strip of granular material is in fact considered to be infinitely long, so the vertical boundaries at the edge of the specimen have been positioned such that their presence has a minimal effect on the results.

Discretisation

The strip itself is modelled using quadratic plane strain elements, QP8. The finite element mesh can be found in Figure 14.

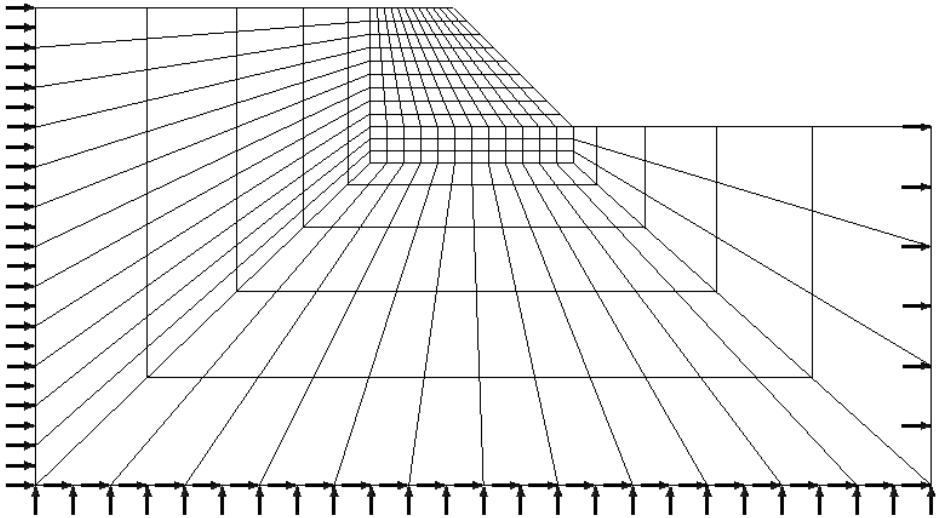


Figure 15: Finite element mesh showing supports.

Material properties

The material properties of the strip are defined using the Modified Mohr-Coulomb material model. Table 1 gives the material properties for this test.

Table 12: Modified Mohr-Coulomb material properties for granular material limit load verification test.

Young's modulus, E	Poisson's ratio, ν	Angle of friction, ϕ	Cohesion, c
2×10^4 KPa	0.49	20°	50 KPa
Angle of dilation ψ	Density ρ		
Test 1. 20°	2039 Kg/m ³		
Test 2. 10°			

Loading

The soil weight due to gravity is increased using the arclength method until the soil fails.

LUSAS Results

If the slope angle β is greater than the angle of internal friction ϕ the slope will collapse when the ratio N reaches a critical value

$$N = h \frac{\gamma}{c} \quad (5.2.39)$$

where h is the slope height and γ the specific weight of the soil

$$\gamma = \rho g \tag{5.2.40}$$

and ρ is the soil density, g the gravitational acceleration. The critical value of N , for the present geometry is tabulated [1] as

$$N_s \approx 16.18 \tag{5.2.41}$$

The load factor α_c applied to gravitational acceleration at collapse is therefore

$$\alpha_c = \frac{N_s}{N} = \frac{N_s c}{h \rho g} = 4.045 \tag{5.2.42}$$

Figure 15 shows the increase in the gravity load factor until failure. The displacement plotted is for the total displacement at point A as shown on figure 13.

Both the associative and non-associative material models slightly overpredict the ultimate failure load.

The contours of effective stress at failure are shown in figure 16.

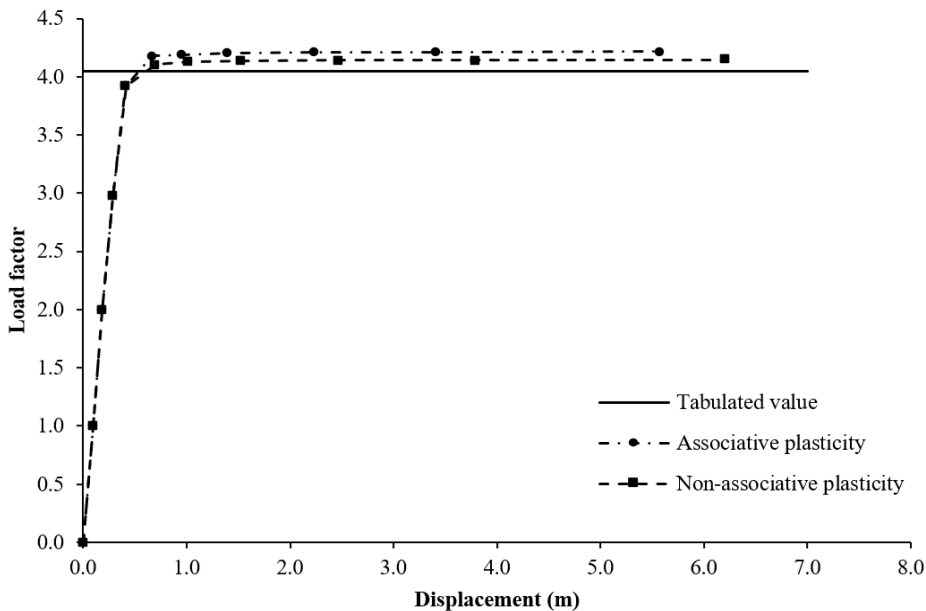


Figure 15 Load v. total displacement at point A

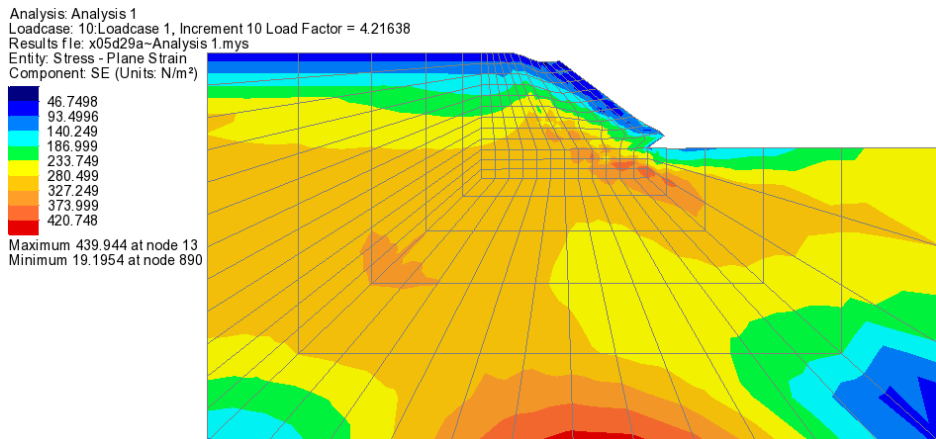


Figure 16 Contours of effective stress at failure (Associative flow)

Input Data

Associative flow : X05D29A.DAT
Non-associative flow : X05D29B.DAT

References

- 1 de Souza Neto EA, Peric D. and Owen DRJ, Computational Methods for Plasticity, John Wiley and Sons Ltd, 2008.

Example 5.2.10

Four-point bending of a reinforced concrete beam

Keywords

Concrete, Reinforcement, Cracking, Creep, Shrinkage, Parasitic bars

Description

This example concerns a reinforced concrete beam that is loaded in four-point bending. A schematic depicting the beam geometry and test set-up can be seen in Figure 1.

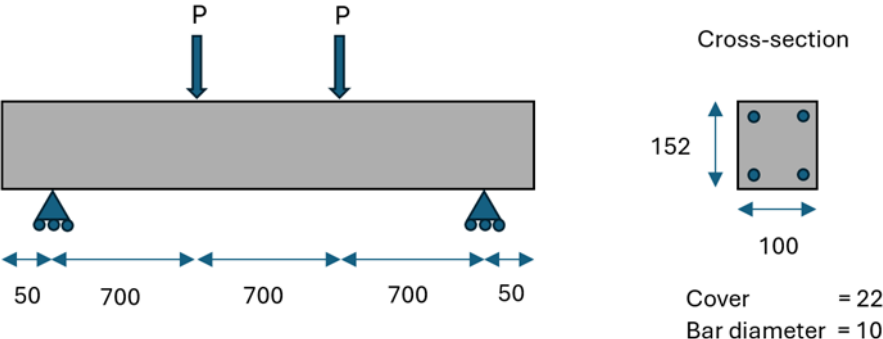


Figure 1: Geometry of reinforced concrete beam, including beam cross-section (all dimensions given in mm)

Discretisation

Owing to the symmetrical nature one half of the beam is discretised. The finite element mesh consists of 616 HX8 elements representing the concrete beam and steel loading and support plates, and 148 parasitic BRS2 elements representing the reinforcing bars. A depiction of the finite element mesh can be seen in Figure 2.

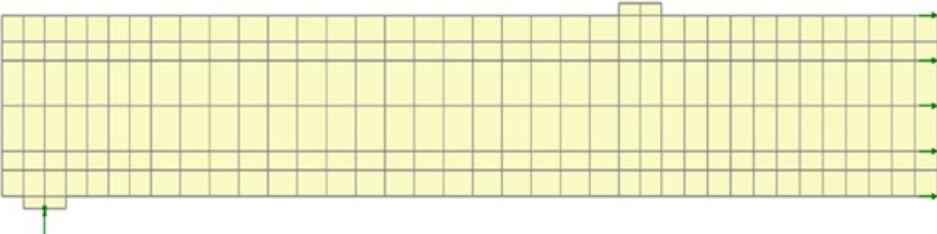


Figure 2: Finite element mesh employed

Material Properties

The constitutive behaviour of the concrete beam is modelled using the LUSAS smoothed Multi-crack concrete material model (model 109) combined with creep and shrinkage according to both the Australian and New Zealand codes of practice, AS5100.5-2017 [5] and NZS3101-2006 [3]. The reinforcing bars were modelled using an elastic-perfectly plastic material model, whilst the steel loading and support plates were modelled using linear elasticity. A depiction of the arrangement of the concrete and steel platens can be seen in Figure 3.



Figure 3: Assignment of constitutive models

The material properties employed in each of the constitutive models can be found in the following Tables:

Concrete material properties

Young's modulus (MPa)	Poisson's ratio (-)	Compressive strength (MPa)	Tensile strength (MPa)	Strain at peak uniaxial compression (-)	Fracture energy (N/mm)
22,000	0.2	32.4	2.0	0.0022	0.11

Advanced concrete material properties (a full description of the advanced concrete material properties can be found in [6])

β_x	Z_0	ψ	m_g	m_{hi}	m_{ful}	r_σ	μ	m_{cf}	f_{pz}	it_{cf}	it_{mx}	R_s	A_p	A_n	C_{z1}	C_{z2}	C_{LM}
1.15	0.6	-0.1	0.3	0.5	5	1.25	0.8	0.05	60	2	2	0.001	0.6	0.75	8	8	3

Reinforcement material properties

Young's modulus (MPa)	Yield stress (MPa)	Area (mm ²)
200,000	345	314.2 (2D10+2D10)

Creep and shrinkage material properties

Environment factor (-)	Notional size ratio (-)	Aggregate factor (-)	Basic drying shrinkage strain (-)	Final drying basic shrinkage strain (-)	Reinforcement ratio (-)
0.7	0.6	1.0	0.0007408	0.001	0

Steel loading and support plate material properties

Young's modulus (MPa)	Poisson's ratio (-)
200,000	0.3

Element ages

Element age (days)
28

Theory

The reinforced concrete beam analysed here was tested in [1] and was used as a benchmark test by [2]. Under the load the beam exhibits cracking and a significant degree of creep and shrinkage. In the simulations the bond slip was assumed to be negligible. In addition, the value of the basic drying shrinkage strain ($\epsilon_{csd,b}$) was calibrated to match the data and does not correspond directly to those recommended in NZS3101 [3] (though the value is within the range of those recommended in [3]).

The model theory for each of the constitutive models can be found in [4].

Loading

Two point loads of 5kN were applied to the beam at an age of 28 days and held constant for 200 days. In the model, this was applied as a face load of 1MPa to the steel loading plate. Fixed supports were applied to the bottom of the steel support plate, whilst a symmetry condition was applied to the center of the beam.

LUSAS Results

The comparison of the displacement vs response time with the experimental data can be seen in Figure 4. It can be seen from Figure 4 that the model response is in good agreement with the experimentally observed data. The predicted crack pattern can be seen in Figure 5. The predicted crack pattern is in reasonably good agreement with alternative numerical results presented in [2].

It is noted that the results presented correspond to the model that uses the NZS3101-2006 creep and shrinkage material but that the results corresponding to the model that uses the AS5100.5-2017 creep and shrinkage material are identical.

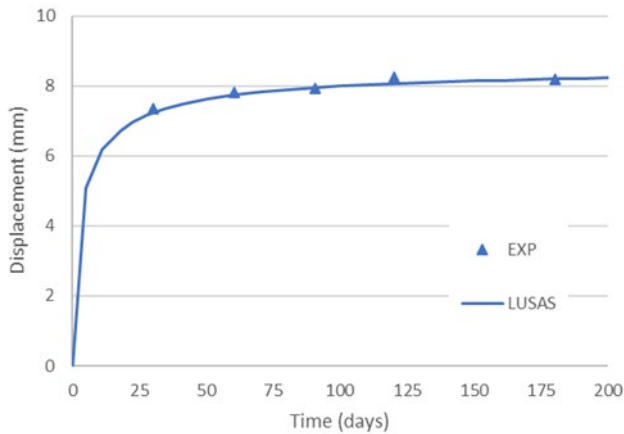
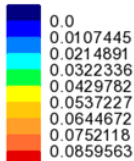


Figure 4: Comparison of predicted displacement with experimental data

Analysis: Analysis 1
 Loadcase: 1:Loadcase 1, 24:Time Step 23 Time = 200.000
 Results file: e01u152-Analysis 1.mys
 Response time: 200.0
 Entity: Concrete Results - Solids
 Component (Gauss point): CWMMax (Units: mm)



Maximum 0.0967009 at Gauss point 1 of element 433
 Minimum 0.0 at Gauss point 1 of element 5

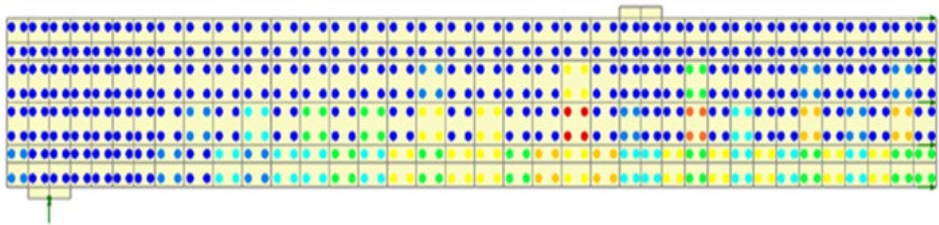


Figure 5: Predicted crack pattern

References

1. Clark, G.S. Long-term deflection of reinforced concrete flexural elements (1987) M.Sc. thesis, Graduate Program in Civil and Environmental Engineering, Univ. of the Witwatersrand
2. Ren X., Wang Q., Ballarini R., Gao X. Coupled creep-damage-plasticity model for concrete under long-term loading (2020) J. Eng. Mech. 146(5):04020027

3. NZS 3101:2006 – New Zealand Standard – Concrete Structures Standard. Part 1: The design of concrete structures Part 2: Commentary on the design of concrete structures Incorporating Amendment No. 1, 2, and 3 Paerewa Aotearoa (Standards New Zealand)
4. The LUSAS Theory manual. Finite Element Analysis Ltd. Forge House, 66 High Street, Kingston upon Thames, London UK
5. AS5100.5-2017 Bridge design, Part 5: Concrete Standards Australia, Sydney, 2017
6. The LUSAS Solver reference manual. Finite Element Analysis Ltd. Forge House, 66 High Street, Kingston upon Thames, London UK

Input Data

X05D210a.DAT

X05D210b.DAT

Example 5.2.11

Nonlinear Stress Analysis Of A Notched Fibre Reinforced Concrete Beam Under Three Point Bending

Keywords

Plane Stress, Concrete, Cracking, Fibres

Description

In this analysis a notched Fibre Reinforced Concrete (FRC) beam is subjected to three-point bending under plane stress. The beam dimensions are as follows:

Total Length	600 mm
Effective Length	500 mm
Depth	150 mm
Notch depth	25 mm
Breadth	150 mm

The beam is simply supported at its ends. An actuator prescribes vertical displacement incrementally at the midspan axis. At this mid-span location, a load-cell and linear-displacement sensing devices monitor the vertical force reaction (P) and the vertical deflection of the beam (δ) at each of the faces, respectively.

The beam geometry and loading conditions are illustrated in Figure 1.

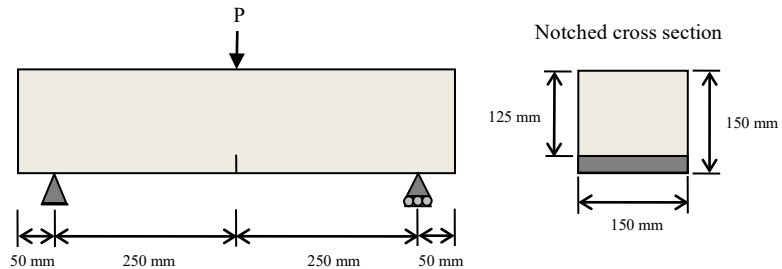


Figure 1: Geometry of notched concrete beam, also showing beam cross-section.

Three concrete mixes are considered – one for Plain Concrete (PC) and two for Steel Fibre Reinforced Concrete (SFRC) with varying fibre content as indicated in Table 1.

Table 1: Brief description of concrete mixes of PC and SFRC.

Mix no.	Concrete type	Fibre volume fraction	Fibre material (type)	Fibre anchorage type	Fibre diameter (mm)	Fibre length to diameter ratio
1	PC	-	-	-	-	-
2	SFRC	1 %	Steel (Dramix)	Hooked end	50	80
3	SFRC	2 %	Steel (Dramix)	Hooked end	50	80

Discretisation

The finite element mesh consists of 836 elements and closely reproduces the structural element and the load-transfer mechanisms as reported in [1]. The mesh uses plane stress (QPM4) elements for the concrete prism, where a notch is discretised explicitly as shown in Figure 2. The plane stress elements are integrated using a 4-point Gaussian integration scheme.

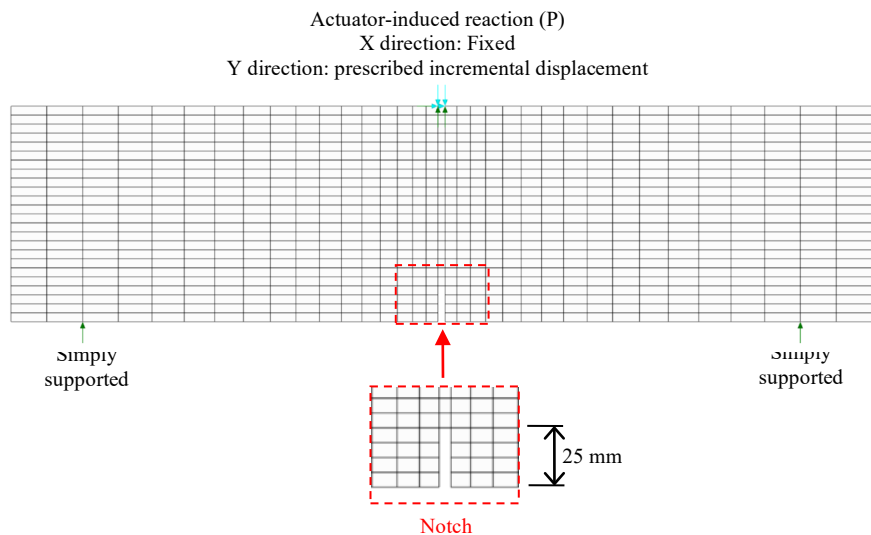


Figure 2: Mesh configuration of the notched PC and SFRC beams by Bencardino et al [1].

Material properties

The constitutive behaviour of the PC and SFRC beams are modelled using the concrete material models listed in Table 2. These concrete material models were calibrated to each of the concrete mixes in Table 1 as shown in Table 3.

Table 2: List of LUSAS concrete material models.

Material model name	LUSAS model	References
Smoothed Multi-crack concrete	109	[2, 3, 4, 6]
Fibre Multi-crack concrete	119	[7, 8]

Table 3: Concrete material models calibrated to mixes in Table 1.

Concrete mix (see Table 1)	Concrete type	Fibre volume fraction	Concrete material no.	Table of material properties	LUSAS model
1	PC	-	1a	Table 4	109
			1b	Table 5	119
2	SFRC	1 %	2	Table 6	119
3	SFRC	2 %	3	Table 7	119

Notes:

- The Fibre Multi-crack concrete material model (model 119) uses 12 fibre-based properties in addition to the (base) concrete properties in the Smoothed Multi-crack concrete material model (model 109).
- The material properties of the PC material (1a) based on the Smoothed Multi-crack concrete material model (model 109) are preserved when the FRC materials (concrete materials 1b, 2 and 3) are modelled using the Fibre Multi-crack concrete material model (model 119).
- The Fibre Multi-crack concrete material model (model 119) was used to analyse the PC beam by setting the fibre volume fraction to a negligible value (e.g. 1.0E-9).
- The Fibre Multi-crack concrete material model (model 119) is used to predict the gains in strength and ductility for varying fibre contents, using the PC material (model 109) as a basis.
- SFRC beams were analysed by using the Fibre Multi-crack concrete material model (model 119), since this model incorporates fibre bridging mechanisms over the underlying Smoothed Multi-crack concrete material model (model 109).

Table 4: Concrete material 1a - Smoothed multi-crack concrete material model (model 109).

Young's modulus	40.0 kN/mm ²	Constant in interlock state function	0.3
Poisson's ratio	0.2	Contact multiplier on ϵ_0	0.5
Mass density	0.0	Final contact multiplier on ϵ_0	5.0
Coefficient of thermal expansion	0.0	Shear intercept to tensile strength	1.25
Mass Rayleigh damping constant	0.0	Slope of friction asymptote for damage	0.8
Stiffness Rayleigh damping constant	0.0	Multiplier on ϵ_0 to define crack fixity strain	0.05
Reference temperature	0.0	Fracture process zone width	60.0 mm
Uniaxial compressive strength	64.0 N/mm ²	Iterations for crack fixity	2.0
Uniaxial tensile strength	4.8 N/mm ²	Maximum iterations for fracture strain update	2.0
Strain at peak uniaxial compression	0.0022	Residual softening factor	0.01
Strain at end of softening curve	0.0	Material constant A_p	0.60
Fracture energy per unit area	0.07 N/mm	Material constant A_n	0.75
Biaxial to uniaxial stress ratio	1.15	Contact sharpness Z1	8.0
Initial relative position of yield surface	0.6	Contact sharpness Z2	8.0
Dilatancy factor	-0.1	Limit of contact transition	3.0

Table 5: Concrete material 1b - Fibre multi-crack concrete material model (model 119).

Young's modulus	40.0 kN/mm ²	Final contact multiplier on ϵ_0	5.0
Poisson's ratio	0.2	Shear intercept to tensile	1.25

		strength	
Mass density	0.0	Limiting friction ratio	0.8
Coefficient of thermal expansion	0.0	Multiplier on ϵ_0 to define crack fixity strain	0.05
Mass Rayleigh damping constant	0.0	Fracture process zone width	60.0 mm
Stiffness Rayleigh damping constant	0.0	Iterations for crack fixity	2.0
Reference temperature	0.0	Maximum iterations for fracture strain update	2.0
Uniaxial compressive strength	64.0 N/mm ²	Residual softening factor	0.01
Uniaxial tensile strength	4.8 N/mm ²	Material constant A_p	0.60
Strain at peak uniaxial compression	0.0022	Material constant A_n	0.75
Strain at end of softening curve	0.0	Contact sharpness Z1	8.0
Fracture energy per unit area	0.07 N/mm	Contact sharpness Z2	8.0
Fibre Young's modulus	210.0 kN/mm ²	Limit of contact transition	3.0
Fibre volume fraction	1.0E-9	Fibre-matrix interface hardening parameter	0.075
Fibre length	50.0 mm	Fibre-matrix interface hardening ratio	0.0
Fibre diameter	0.625 mm	Fibre frictional sliding stress	3.5 N/mm ²
Biaxial to uniaxial stress ratio	1.15	Fibre snubbing parameter	0.9
Initial relative position of yield surface	0.6	Fibre SUR parameter 1	0.1
Dilatancy factor	-0.1	Fibre SUR parameter 2	0.2
Constant interlock state function	0.3	Effective pull-out displacement parameter	0.8
Contact multiplier on ϵ_0	0.5	Limiting COD parameter	0.8

Table 6: Concrete material 2 - Fibre multi-crack concrete material model (model 119).

Young's modulus	40.0 kN/mm ²	Final contact multiplier on e0	5.0
Poisson's ratio	0.2	Shear intercept to tensile strength	1.25
Mass density	0.0	Limiting friction ratio	0.8
Coefficient of thermal expansion	0.0	Multiplier on e0 to define crack fixity strain	0.05
Mass Rayleigh damping constant	0.0	Fracture process zone width	60.0 mm
Stiffness Rayleigh damping constant	0.0	Iterations for crack fixity	2.0
Reference temperature	0.0	Maximum iterations for fracture strain update	2.0
Uniaxial compressive strength	64.0 N/mm ²	Residual softening factor	0.01
Uniaxial tensile strength	4.8 N/mm ²	Material constant Ap	0.60
Strain at peak uniaxial compression	0.0022	Material constant An	0.75
Strain at end of softening curve	0.0	Contact sharpness Z1	8.0
Fracture energy per unit area	0.07 N/mm	Contact sharpness Z2	8.0
Fibre Young's modulus	210.0 kN/mm ²	Limit of contact transition	3.0
Fibre volume fraction	0.01	Fibre-matrix interface hardening parameter	0.075
Fibre length	50.0 mm	Fibre-matrix interface hardening ratio	0.0
Fibre diameter	0.625 mm	Fibre frictional sliding stress	3.5 N/mm ²
Biaxial to uniaxial stress ratio	1.15	Fibre snubbing parameter	0.9
Initial relative position of yield surface	0.6	Fibre SUR parameter 1	0.1

Dilatancy factor	-0.1	Fibre SUR parameter 2	0.2
Constant interlock state function	0.3	Effective pull-out displacement parameter	0.8
Contact multiplier on e0	0.5	Limiting COD parameter	0.8

Table 7: Concrete material 3 - Fibre multi-crack concrete material model (model 119).

Young's modulus	40.0 kN/mm ²	Final contact multiplier on e0	5.0
Poisson's ratio	0.2	Shear intercept to tensile strength	1.25
Mass density	0.0	Limiting friction ratio	0.8
Coefficient of thermal expansion	0.0	Multiplier on e0 to define crack fixity strain	0.05
Mass Rayleigh damping constant	0.0	Fracture process zone width	60.0 mm
Stiffness Rayleigh damping constant	0.0	Iterations for crack fixity	2.0
Reference temperature	0.0	Maximum iterations for fracture strain update	2.0
Uniaxial compressive strength	64.0 N/mm ²	Residual softening factor	0.01
Uniaxial tensile strength	4.8 N/mm ²	Material constant Ap	0.60
Strain at peak uniaxial compression	0.0022	Material constant An	0.75
Strain at end of softening curve	0.0	Contact sharpness Z1	8.0
Fracture energy per unit area	0.07 N/mm	Contact sharpness Z2	8.0
Fibre Young's modulus	210.0 kN/mm ²	Limit of contact transition	3.0
Fibre volume fraction	0.02	Fibre-matrix interface hardening parameter	0.075
Fibre length	50.0 mm	Fibre-matrix interface hardening ratio	0.0

Fibre diameter	0.625 mm	Fibre frictional sliding stress	3.5 N/mm ²
Biaxial to uniaxial stress ratio	1.15	Fibre snubbing parameter	0.6
Initial relative position of yield surface	0.6	Fibre SUR parameter 1	0.1
Dilatancy factor	-0.1	Fibre SUR parameter 2	0.2
Constant interlock state function	0.3	Effective pull-out displacement parameter	0.8
Contact multiplier on e_0	0.5	Limiting COD parameter	0.8

Support Conditions

Node	Support Type	Prescribed Boundary Conditions
1, 37	Roller	FR
241, 574	Restrained horizontally + vertical incremental displacement	RR

Note that any deformation resulting from the self-weight of the beam are considered small compared to that resulting from the applied load by the reaction frame and thus neglected.

Theory

The PC and SFRC beams analysed here formed part of an experimental investigation undertaken by Bencardino et al [1]. Under load the beam exhibits both flexural and shearing deformation and shows progressive crack propagation from the notch to the top face of the specimen mostly in a vertical fashion. The beam has been used as a benchmark test by many research workers in the field of nonlinear concrete analysis [7, 9].

LUSAS results

1. Figure 3 shows contours of the major principal stress at the onset of cracking; and clearly demonstrates the areas of tensile stress around the notch that drive the crack propagation in the PC beam.
2. Figure 4 shows the load-deflection responses obtained from nonlinear analyses of the PC and SFRC beams, which compare well against experimental recordings.
3. Figure 5 shows the experimental evidence of the development of crack faces in PC beams along the vertical plane above the notch location, which compares well with the failure patterns obtained with concrete models 109 and 119.
4. Figures 6 to 8 show the progression of the cracks through the notched section of the PC beam as the deflection over the mid-axis increases.

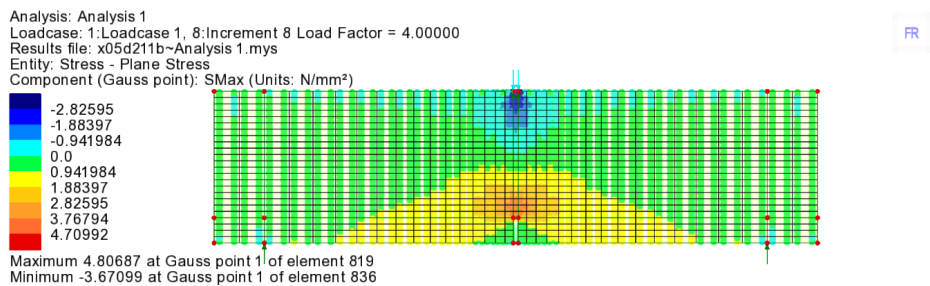


Figure 3: Bencardino's notched beam (PC case). Vertical deflection $\delta = 0.04$ mm. Major principal stress contour from Fibre Multi-crack concrete material model 119.

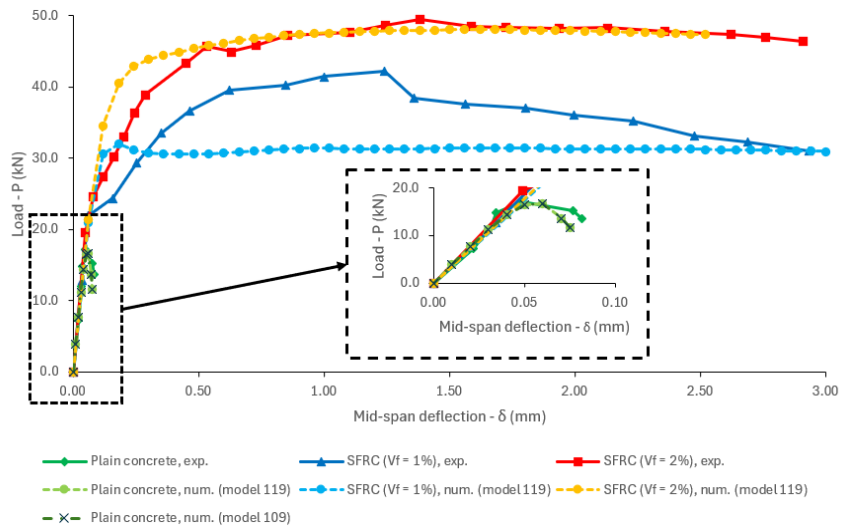


Figure 4: Load (P) vs. Mid-span deflection (δ) curve for Bencardino's FRC notched beam.



Figure 5: Failed specimens (PC) show a localised crack propagated from the notch to the top face mostly following a vertical path. Figure reported in Bencardino et al [1] has been modified to highlight matching cracking faces from each half of the beams.

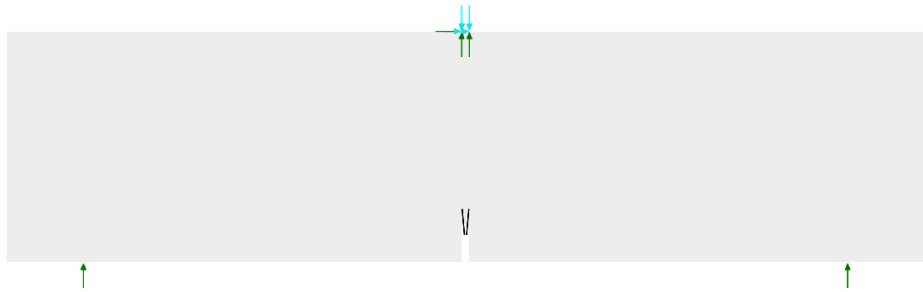


Figure 6: Crack pattern across of notched PC beam. Vertical deflection $\delta = 0.04$ mm. Crack pattern from Fibre Multi-crack concrete material model 119.

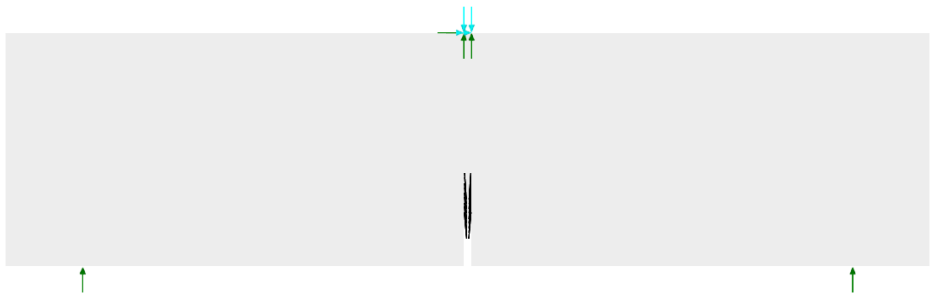


Figure 7: Crack pattern across of notched PC beam. Vertical deflection $\delta = 0.06$ mm. Crack pattern from Fibre Multi-crack concrete material model 119.

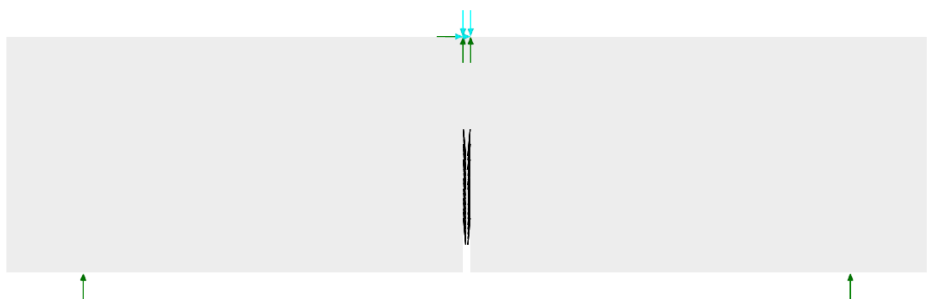


Figure 8: Crack pattern across of notched PC beam. Vertical deflection $\delta = 0.075$ mm. Crack pattern from Fibre Multi-crack concrete material model 119.

References

1. Bencardino, F., Rizzuti, L., Spadea, G., Swamy, R. N., (2010). ‘Experimental evaluation of fiber reinforced concrete fracture properties’, *Composites Part B: Engr.*, 41(1): 17-24.
2. Jefferson A.D. (2003). Craft – a plastic-damage-contact model for concrete. I. Model theory and thermodynamic considerations. *International Journal of Solids and Structures* 40: 5973-5999.
3. Jefferson A.D. (2003). Craft – a plastic-damage-contact model for concrete. II. Model implementation with implicit return-mapping algorithm and consistent tangent matrix. *International Journal of Solids and Structures* 40: 6001-6022.
4. Jefferson A.D. and Mihai I.C. (2015). The simulation of crack opening–closing and aggregate interlock behaviour in finite element concrete models. *International Journal for Numerical Methods in Engineering* 104(1): 48-78.
5. Jefferson A.D., Mihai I.C., Tenchev R., Alnaas W.F., Cole G., Lyons P. (2016). A plastic-damage-contact constitutive model for concrete with smoothed evolution functions. *Computers and Structures* 169: 40-56.
6. LUSAS Internal Report, ‘SDR/LUSAS/484h concrete model, CraftS – Solver’, Finite Element Analysis Ltd. Forge House, 66 High Street, Kingston Upon Thames, London, U.K.
7. Mihai I.C., Jefferson A.D., Lyons P. (2016). A plastic-damage constitutive model for the finite element analysis of fibre reinforced concrete. *Engineering Fracture Mechanics* 159: 35-62.
8. LUSAS Internal Report, ‘SDR/LUSAS/484n Fibre reinforced concrete model, CraftH – Solver’, Finite Element Analysis Ltd. Forge House, 66 High Street, Kingston Upon Thames, London, U.K.
9. Le, L.A, Nguyen G.D., Bui H.H., Sheikh, A.H., Kotousov, A. (2019). Incorporation of micro-cracking and fibre bridging mechanisms in constitutive modelling of fibre reinforced concrete. *J. Mech. Phys. Solids* 133: Article 103732.

Input data

X05D211A.DAT
X05D211B.DAT
X05D211C.DAT
X05D211D.DAT

Example 5.2.12

Uniaxial Tension-Compression Cyclic Response Of Masonry Panel

Keywords

Plane Stress, Masonry, Cyclic, Damage

Description

Determine the uniaxial tension-compression cyclic response of a masonry panel involving damage (Figure 1).

Discretisation

Model the panel by one QPM4 plane stress element.

Geometry

The square masonry panel has side length 1.0m and thickness 0.01m.

Material properties

Properties of the masonry panel

E_x	3.0 GPa
E_y	2.0 GPa
G_{xy}	0.9 GPa
ν_{xy}	0.1
θ	0
f_{11}^t	0.35MPa
f_{22}^t	0.15 MPa
f_{12}^t	0.20MPa
f_{11}^c	7.0MPa

f_{22}^c	3.0 MPa
f_{12}^c	3.0 MPa
κ_{pc}	0.005
α	0.2983
α^p	0.2983
G_{fx}^t	100.0Nm/m ²
G_{fy}^t	13.8Nm/m ²
G_{fx}^c	40000.0Nm/m ²
G_{fy}^c	5510.0Nm/m ²

Loading

Prescribed displacements on the right side (Figure 1) with history shown in Figure 2.

Boundary conditions

Fixed on left side (Figure 1).

Theory

The stress response can be computed from the strain history corresponding to the prescribed displacements using the constitution relationship.

Comparison

Figure 3 shows the computed tension-compression cyclic responses corresponding to the elastic-damage and elasto-plastic-damage laws, agreeing with the theoretical solution.

Input data

X05D212A.DAT

X05D212B.DAT

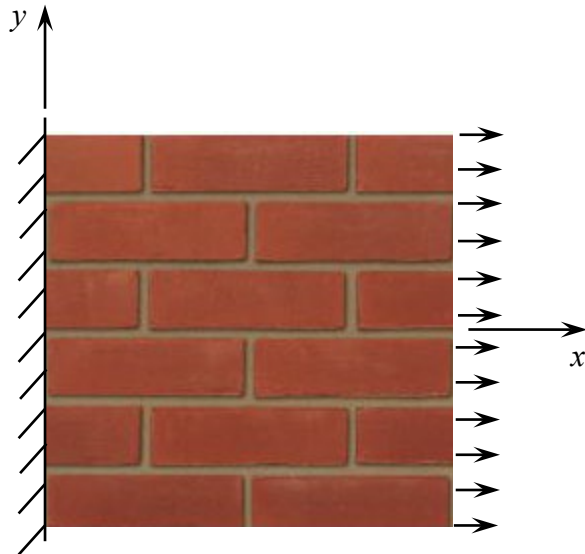


Figure 1: Masonry panel subject to uniaxial loading.

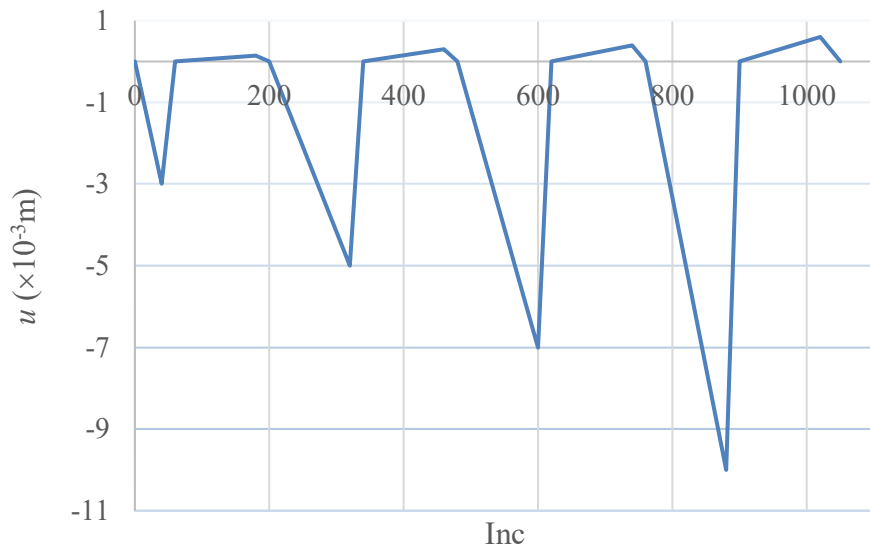


Figure 2: Prescribed displacement history.

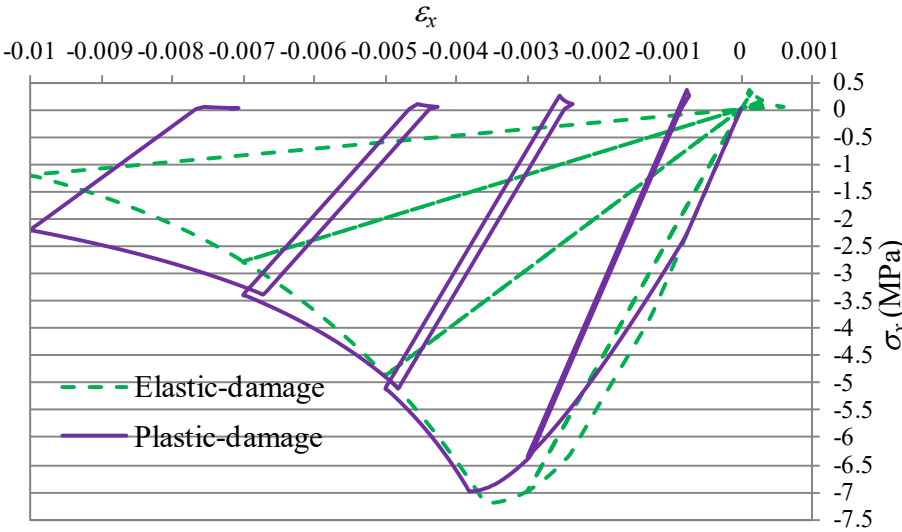


Figure 3: Uniaxial tension-compression cyclic response.

Example 5.2.13

TU Eindhoven Shear-walls

Keywords

Plane Stress, Masonry, Plasticity, Damage, Pushover

Description

Simulate the shear walls J2G and J3G with a central opening tested at TU Eindhoven by Raijmakers and Vermeltoort [2] (Figure 2).

Discretisation

Model the wall using QPM4 plane stress elements with a mesh similar to Lourenço and Rots [1] (Figure 3), or TPM3 elements by dividing each quadrilateral into two triangles.

Geometry

The walls have dimensions of $990 \times 1000 \text{mm}^2$ and are constituted by 18 courses, of which 16 courses are active and 2 courses are clamped in steel beams. The walls are made of wire-cut solid clay bricks with dimensions $210 \times 52 \times 100 \text{mm}^3$ and 10mm thick mortar, prepared with a volumetric cement:lime:sand ratio of 1:2:9.

Material properties

The values of the mechanical parameters used in the numerical analysis to describe the masonry behaviour are [1]

E1	7520MPa	E2	3960MPa
G12	1460MPa	ν_{12}	0.09
f_{11}^+	0.35MPa	f_{11}^-	6.30MPa
f_{22}^+	0.25MPa	f_{22}^-	4.50MPa
f_{12}^+	0.30MPa	f_{12}^-	3.00MPa
κ_p	0.093 [†]		
α	0.5 [†]	α_d	0.0058 [†]
G_{f1}^+	50J/m ²	G_{f1}^-	20000J/m ²
G_{f2}^+	48J/m ²	G_{f2}^-	19400J/m ²

† These parameters are taken after Van Zijl [3]: α corresponds to a friction coefficient of 0.75, or friction angle of 36.9° ; α_d corresponds to a near zero dilatancy angle of 0.5° .

Loading

Vertical pre-compression uniformly distributed forces $p = 0.30\text{N/mm}^2$ are applied to the walls before a horizontal load is monotonically increased under top displacement control in a confined way, i.e. keeping the bottom and top boundaries horizontal and precluding any vertical movement.

Boundary conditions

Fixed the bottom of the wall.

Theory

The experimentally measured horizontal reaction versus displacement curves are shown in Figure 1. The failure patterns of the shear walls after loading are shown in Figure 2. Diagonal cracks appear initially at the two corners of the opening and propagate up to the top and bottom of the wall. Additionally, tensile cracks appear at the vertical external sides of the wall involving the top left pier next to the opening and at the bottom right one, the compressed struts located next to the opening fail at both of their ends.

Although both walls J2G and J3G were tested under the same conditions, the latter one resisted a lower ultimate loading.

Comparison

LUSAS predicts reasonably the reaction–displacement response (Figure 1) and failure patterns (Figure 3).

References

1. Lourenço, P.B. and Rots, J.G. (1997) Multisurface interface model for analysis of masonry structures. *J. Eng. Mech. ASCE* 123(7): 660–668.
2. Raijmakers, T.M.J. and Vermeltoort, A.T.h. (1992) Deformation controlled tests in masonry shear walls. Report B-92-1156, TNO-Bouw, Delft [in Dutch].
3. Van Zijl, G.P.A.G. (2004) Modeling masonry shear-compression: Role of dilatancy highlighted. *J. Eng. Mech. ASCE* 130(11): 1289-1296.

Input data

X05D213A.DAT

X05D213B.DAT

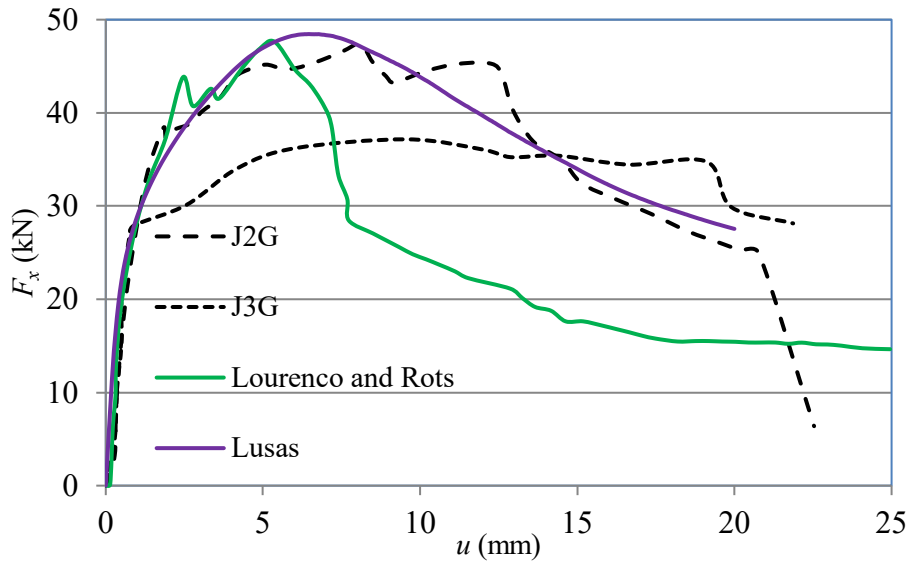


Figure 1: Comparison of the reaction–displacement curves obtained by LUSAS with the simulation of Lourenço and Rots [1] and experiments of Raijmakers and Vermeltfoort [2].

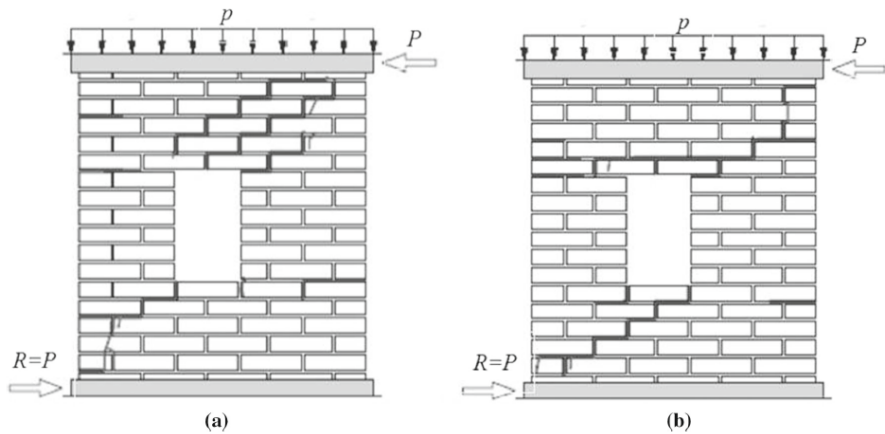


Figure 2: Crack patterns of the walls tested by Raijmakers and Vermeltfoort [2].

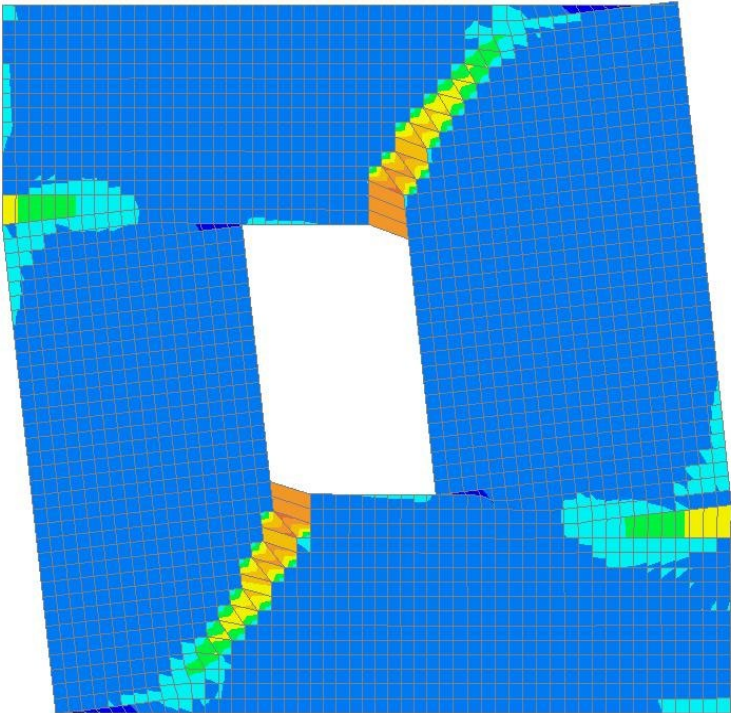


Figure 3: Failure mode and maximum strains by LUSAS corresponding to an imposed horizontal displacement of 20 mm.

Example 5.4.1

Buried Pipe With Soil-Pipe Interface Modelled Using 3d Interface Model

Keywords

Soil Structure Interaction, Interface Model, Elasto-plastic, Friction

Description

This example (figure 1) consists of an elastic pipe buried in a homogeneous and elastic soil. The interface between the pipe and soil is modelled using an elasto-plastic interface material. Three cases of interface friction are considered:-

- (i) frictionless slip ($\mu = 0.001$),
- (ii) stick ($\mu = 2$),
- (iii) frictional slip ($\mu = 0.25$).

Discretisation

The discretisation (figure 2) is similar to that used in [1]. HX20 elements are used to discretise the pipe, soil and interface. The model is totally restrained from moving in the z-direction.

Theory

The interaction between the soil and pipe is governed by a frictional type law i.e. bond between the pipe and soil is maintained by a frictional force and once this is overcome debonding and slip will occur. This friction/slip behaviour is modelled using an elasto-plastic interface model, with yielding (slip) defined using the Mohr-Coulomb criterion [2] defined as

$$\tau = c + \sigma \tan \phi \quad (0.0.111)$$

where τ maximum shear stress,
 σ stress normal to the soil/pipe interface,
 c cohesion,
 ϕ friction angle.

Comparison

Figure 3 is the deformed mesh for the frictionless slip analysis. A significant amount of sliding is visible in the interface. Figure 4 shows the shear stress distribution along the pipe-soil interface.

References

1. DESAI,C.S., ZAMAN,M.M., LIGHTNER,J.G. and SIRIWARDANE,H.J. Thin-layer element for interfaces and joints. Int. J. Num. Anal. Meth. Geomech., Vol.8, 19-43, 1984.
2. OWEN,D.R.J. and HINTON,E. Finite elements in plasticity: theory and practice. Pineridge Press, Swansea, UK, 1980.
3. KATONA,M.G. A simple contact-friction interface element with applications to buried culverts. Int. J. Num. Anal. Meth. Geomech., Vol.7, 371-384, 1983.

Input data

X05D41A.DAT

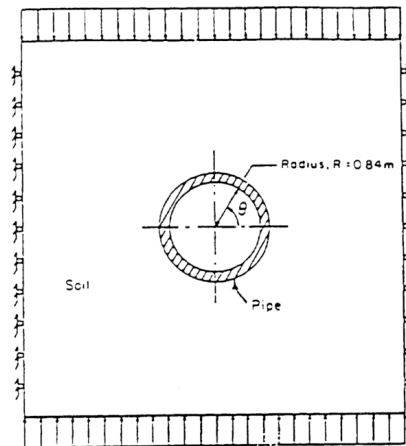


Figure 1 Buried Pipe Example

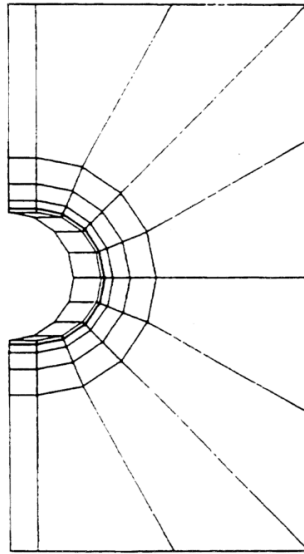


Figure 2 Finite Element Mesh

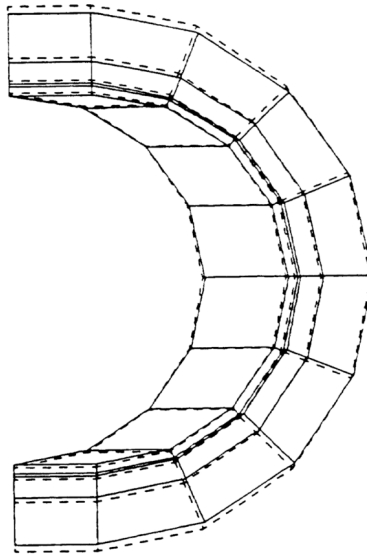
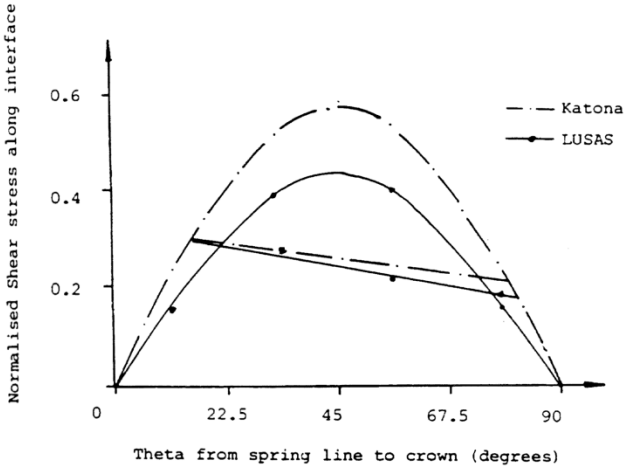


Figure 3 Deformed Mesh Showing Sliding on Interface



Example 5.4.2

Elasto-Plastic Analysis of a Thick Porous Cylinder Under Internal Pressure

Keywords

Cylinder, Drained, Plasticity, Porous, Undrained

Description

An infinitely long thick porous cylinder of internal and external radii 100 mm and 200 mm respectively is subjected to an increasing internal pressure.

Geometry, boundary and loading conditions

The cylinder is idealised into both plane strain and 3D problems. The global Z axis is coincident with the axis of the cylinder. In the 3D analysis, one symmetric quarter of the structure with a length of 80mm is considered, as shown in Figure 1; boundary and loading conditions are also shown in the figure. Symmetric conditions are specified on the straight boundaries; the curved internal surface (which has a pressure loading) and external surface are unrestrained. The plane strain idealisation is a projection of the 3D idealisation in the Z-direction.

Discretisation

The 3D finite element discretisation with 120 hexahedral (HX20P) elements is shown in Figure 2. In the plane strain analysis, 30 quadrilateral (QPN8P) elements are used without discretisation in the Z-direction.

Material properties

The nonlinear material behaviour is modelled using a von Mises yield criterion and a perfectly plastic post-yield response. The material properties are as follows:

Fully drained analysis:

Young's modulus	$E = 21000\text{dN/mm}^2$
Poisson's ratio	$\nu = 0.3$
Yield stress	$\sigma_{ys} = 24\text{dN/mm}^2$

Undrained analysis:

Young's modulus of the soil skeleton	$E' = 17830.2 \text{ dN/mm}^2$
Poisson's ratio of the soil skeleton	$\nu' = 0.1038$
Bulk modulus of the pore fluid	$K_w = 10^4$
Porosity	$\eta = 1$

Theory

Under fully drained conditions, geotechnical elements give identical results to their counterpart continuum elements using drained properties. Furthermore, following the principle of effective stress, if an undrained analysis is performed with soil and pore fluid properties being chosen so as to correspond to the drained material parameters, the obtained displacement and strain results (but not stresses or pore pressures) are comparable to those obtained by the fully drained analysis. Slight difference may occur due to a two-field (displacement and pressure) interpolation employed in the undrained analysis.

With the increase of the applied internal pressure, the cylinder deforms elastically until an internal pressure of approximately 12 dN/mm^2 is reached; beyond this pressure level the cylinder behaves elasto-plastically. The spread of plastic deformation through the thickness of the cylinder can be seen from the distribution of the hoop stress component with increasing load in 5.2.2.

LUSAS Results

For the current materially non-linear, but geometrically linear analysis, the progressive radial displacements of the internal circumference against the internal pressure are:

Internal pressure		8	10	12	14	16	18	
u_r	Target	QPN8	0.0721	0.0901	0.1116	0.1399	0.1823	0.2566
		HX20	0.0726	0.0908	0.1115	0.1398	0.1828	0.2622
	LUSAS fully drained	QPN8P	0.0721	0.0901	0.1116	0.1399	0.1823	0.2566
		KX20P	0.0726	0.0908	0.1115	0.1398	0.1828	0.2622
	LUSAS undrained	QPN8P	0.0721	0.0901	0.1116	0.1399	0.1821	0.2565
		KX20P	0.0726	0.0908	0.1115	0.1398	0.1826	0.2623

From the above table, 3D drained/undrained results agree favourably with 2D analysis. However, the 3D analysis reproduces better axisymmetry of the problem than the plane strain analysis. The following table gives the pore pressure on the inner and outer faces of the cylinder obtained by the 3D undrained analysis:

Internal pressure		8	10	12	14	16	18
Pore pressure	inner	-1.3206	-1.6508	-1.3847	-0.0732	0.9772	2.1293
	outer	-1.3206	-1.6508	-2.0188	-2.4936	-3.1749	-4.3960

As the deformation is small, similar results have been obtained with the consideration of geometric nonlinearity. A difference in pore pressure between the inner and outer surfaces can be seen at an internal pressure of 12 when the material has yielded.

References

1. Owen, D.R.J., Hinton, E. Finite Elements in Plasticity: Theory and Practice Publisher. Pineridge Press Ltd. Swansea, U.K. 1980. ISBN 0-906674-05-2
2. Zienkiewicz, O.C... The Finite Element Method, 3rd Edition. Publisher. McGraw Hill Ltd, London, U.K. 1977. ISBN 0-07-084072-5
3. FEAL internal Report 'Plane Strain', FEAL708, Finite Element Analysis Ltd. Forge House, 66 High Street, Kingston Upon Thames, Surrey KT1 1HN. 1986.
4. Hodge, P.G., White, G.N. A quantitative comparison of flow and deformation theories of plasticity. J. Applied Engineering Mechanics, Vol.17, 180-184, 1950.

Input Data

X05D42A.DAT (Plane strain)

X05D42B.DAT (3D continuum)

Note: The load incrementation may alternatively be defined automatically using NONLINEAR CONTROL INCREMENTATION and TERMINATION cards as in 5.2.2.

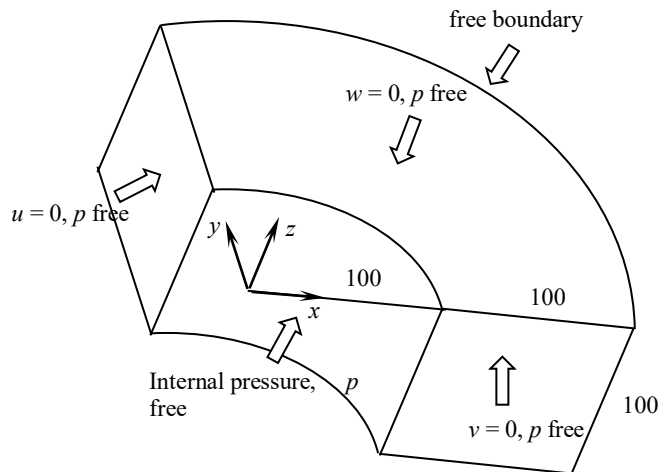


Figure 1

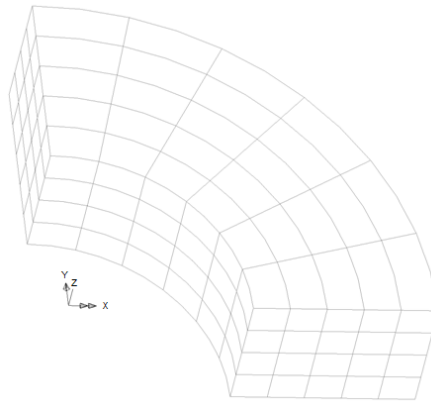


Figure 2

Example 5.5.1

Cylindrical Shell Subject To Self Weight

Keywords

Anisotropic, Elasto-Plastic

Description

This example (figure 1) consists of a cylindrical shell subjected to a uniformly distributed load over the outer surface. The shell has a length of 7.6m, a radius of 7.6m and a thickness of 0.076m. The angle subtended by the arc of the shell at the centre of the circle is 80 degrees.

Discretisation

Because of symmetry conditions only a quarter of the shell is modelled. A 4*4 mesh of QSL8 (Semiloof shell) elements are used to discretise the shell; this is shown in figure 1.

Material properties

This problem is geometrically linear but the non-linear Hill criterion for anisotropic plasticity is used to model the material. The following values are used to describe the yield surface for each of the anisotropic property definitions:

1. Isotropic

$$\bar{\sigma}_{11} = \bar{\sigma}_{22} = \bar{\sigma}_{33} = \bar{\sigma} \quad (0.0.112)$$

$$\bar{\sigma}_{12} = \bar{\sigma}_{23} = \bar{\sigma}_{13} = \frac{1}{\sqrt{3}} \bar{\sigma} \quad (0.0.113)$$

2. Anisotropic

$$\bar{\sigma}_{11} = 2\bar{\sigma} \quad (0.0.114)$$

$$\bar{\sigma}_{22} = \bar{\sigma}_{33} = \bar{\sigma} \quad (0.0.115)$$

$$\bar{\sigma}_{12} = \bar{\sigma}_{23} = \bar{\sigma}_{13} = \frac{1}{\sqrt{3}} \bar{\sigma} \quad (0.0.116)$$

3. Anisotropic

$$\bar{\sigma}_{11} = \bar{\sigma} \quad (0.0.117)$$

$$\bar{\sigma}_{22} = 2\bar{\sigma} \quad (0.0.118)$$

$$\bar{\sigma}_{33} = \bar{\sigma} \quad (0.0.119)$$

$$\bar{\sigma}_{12} = \bar{\sigma}_{23} = \bar{\sigma}_{13} = \frac{1}{\sqrt{3}}\bar{\sigma} \quad (0.0.120)$$

Here $\bar{\sigma}$ is the reference yield stress ($=4200 \text{ kN/m}^2$). Note that even though the shell formulation is based on the plane stress hypothesis, the complete yield surface must be defined for the material. No hardening is present in this problem. The Elastic modulus, $E = 21E6 \text{ kN/m}^2$ and a Poisson's ratio of zero are used to define the elastic behaviour of the material.

Comparison

Figure 2 shows the load-displacement curves at the point A. These results agree exactly with the results in the reference solution [1]. It can be seen that anisotropic properties allow a much higher limiting load to be sustained (an increase of approximately 25%).

References

1. De BORST, R. and FEENSTRA, P.H. Studies in Anisotropic Plasticity with Reference to the Hill Criterion. Int. J. Num. Meth. Eng., v29, pp315-336, 1990.
2. LUSAS Theory Manual. Finite Element Analysis Ltd, Forge House, 66 High Street, Kingston-upon-Thames, Surrey, KT1 1HN.

Input Data

X05D51A.DAT

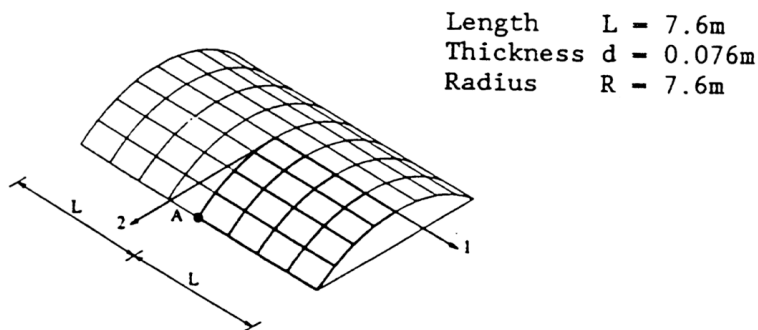


Figure 1 Geometry of cylindrical shell

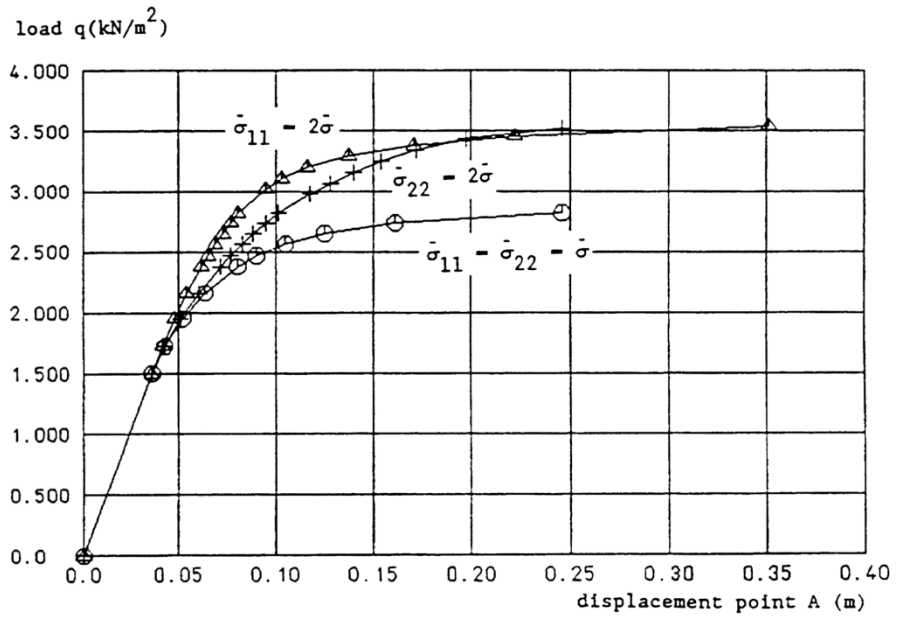


Figure 2 Load-displacement curve at point A of the cylindrical shell for isotropic and anisotropic material properties and using 4*4 Semiloof elements.

Example 5.6.1

Axisymmetric analysis of sand under compression

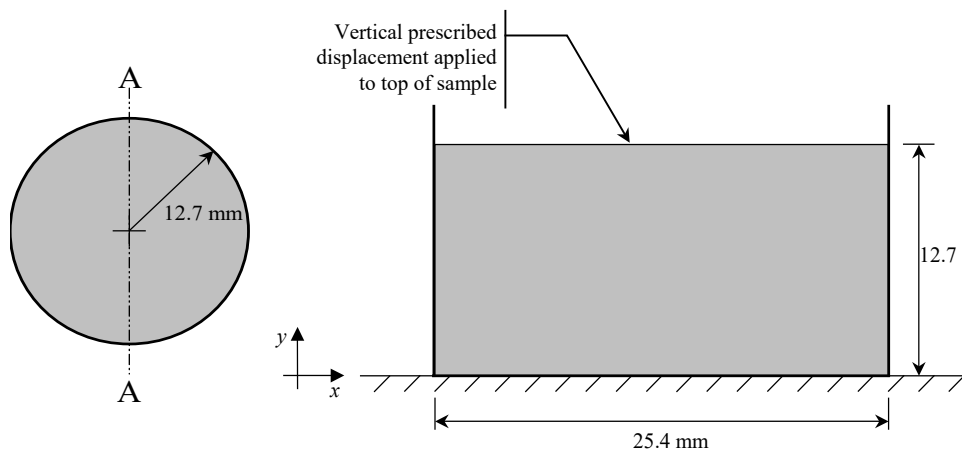
Keywords

Elasto-Plastic, Drucker-Prager, Mohr-Coulomb

Description

This example is a uniaxial strain test of McCormick Ranch sand, details of which can be found in Figure 13. A compressive load is applied to the sand sample and the resulting stress and strain characteristics are compared with experimental and other finite element solutions.

The axisymmetric nature of the model means that the example is analysed as an axisymmetric problem. The line of axisymmetry passes through the centre of the sand sample in the y direction.



Top view of sand sample

Section through A-A

Figure 9: The uniaxial McCormick Ranch sand test. Dimensions are not to scale.

Discretisation

The finite element mesh is shown in Figure 14, where only one half of the cross-section illustrated in Figure 13 has been modelled. The sand is modelled using four linear enhanced strain axisymmetric elements QAX4M.

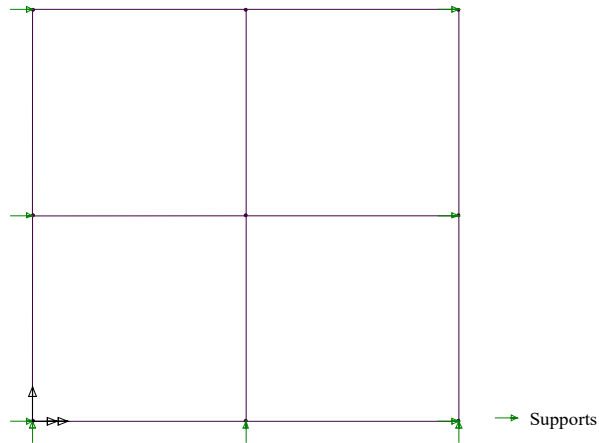


Figure 10: Finite element mesh for the uniaxial McCormick Ranch sand test. A vertical compressive prescribed displacement is applied to the top set of nodes.

Material properties

The Drucker-Prager and Mohr-Coulomb material models are used to define the material properties of the sand. The material properties can be found in Table 5. For the Mohr-Coulomb material model, the dilation angle is set to the angle of friction.

Table 8: Material properties for uniaxial McCormick Ranch sand test.

Young's Modulus, E	Poisson's Ratio, ν	Angle of friction, ϕ	Cohesion, c
689 MPa	0.25	7.15	0.577 MPa

Loading

The top face of the sand sample is loaded by a compressive prescribed displacement in the y direction. The maximum vertical displacement is 0.8382 mm. In the full experimental test, the variation of the prescribed displacement is shown in Figure 15.

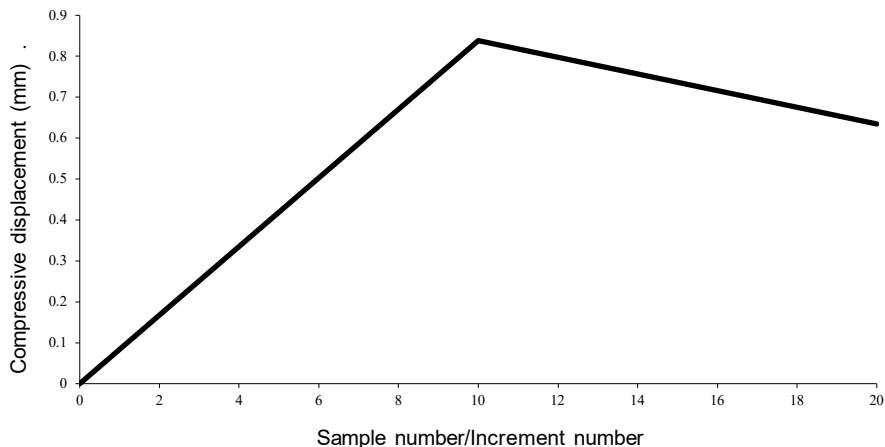


Figure 11: Variation of applied compressive prescribed displacement for the uniaxial McCormick Ranch sand test. The graph shows the full variation used for the experimental results. Only one set of results, from [1], is published for the reduction in displacement between increment numbers 10 and 20, with very specific cap and tension cut off definitions.

LUSAS Results

Results for the test can be found Figure 16, which shows the variation of compressive stress with compressive strain in the direction of the applied displacement. In addition to the results from the LUSAS Drucker-Prager model, the graph also shows experimental results [1,2], results from the LUSAS Mohr-Coulomb model and finite element results from [1]. Results in [1] are from a Drucker-Prager model that has a cap and a tensions cut off.

The graph in Figure 16 shows that the results from LUSAS are in good agreement with experimental results and results from other FE packages when compressing the sand specimen. Both LUSAS Drucker-Prager and Mohr-Coulomb material models produce identical results in this test.

Experimental results have also been generated for the case when the prescribed displacement loading is reversed (see Figure 15 between sample numbers 10 and 20), shown by the reduction in compressive stress after its peak value. Reference [1] has been able to approximate these experimental results with a very specific cap definition and tension cut off.

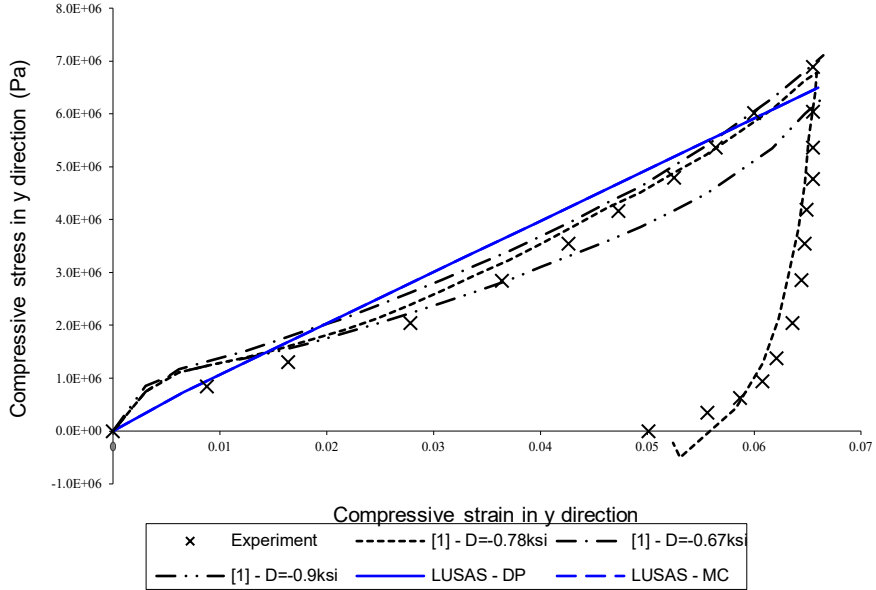


Figure 12: Variation of compressive stress with compressive strain in the direction of the applied displacement. Graphs with D values represent results from Drucker-Prager models that have caps and tension cut offs, where D is used to define the cap. See [1]. MC – LUSAS Mohr-Coulomb material model, DP – LUSAS Drucker-Prager material model.

Input Data

Drucker-Prager : X05D61A.DAT
 Mohr-Coulomb : X05D61B.DAT

References

1. K.-J. Bathe, M.D. Snyder, A.P. Cimento, W.D. Rolph III. 'On some current procedures and difficulties in finite element analysis of elastic-plastic response'. Computers and Structures, Volume 12, pp. 607-624 (1980).
2. F.L. DiMaggio, I.S. Sandler. 'Material model for granular soils'. Journal of the Engineering Mechanics Division ASCE 97, pp. 935-949 (1971).

Example 5.7.1

Single joint test for lateral earth pressure

Keywords

Lateral Earth Pressure, Multi-linear

Description

This example models lateral earth pressures via a single joint. Displacements or forces are applied at one degree of freedom, while other degrees of freedom are fixed. The numerical response can then be compared with hand calculations.

Geometry, Boundary and Loading Conditions

A single joint is defined by 3 or 4 nodes

node	1	2	3	4
Coordinates	2.0, 0.0, 0.0	1.0, 0.0, 0.0	2.0, 1.0, 0.0	2.0, 1.0, -1.0

For 2D joints, the 3rd node is used to define the local x-direction; for 3D joints, the 3rd and 4th nodes are used to define the local x-axis and local xy-plane respectively.

Node 2 is fixed; the prescribed displacement u_x at node 1 in the x-direction varies as

t_i	0.0	1.0	2.0	3.0	10.0	1.50
$f(t_i)$	0.0	0.016	0.1	0.016	-0.16	-0.2

where t_i and $f(t_i)$ are controlling variable time and curve factor, respectively.

Discretisation

The joint is discretised into one 2D or 3D joint element.

Material properties

The properties for active, at rest and passive lateral earth pressures are

$$\delta_a = -0.016, f_a = 66.6, \delta_0 = 0.0, f_0 = 100.0, \delta_p = 0.16, f_p = 600.0$$

in the lateral or horizontal direction; properties in all other directions are zero.

The corresponding properties for multi-linear elastic models with number of segments $n = 1, 2$ and 3 are

n	f_1	δ_1	f_2	δ_2	f_3	δ_3	f_4	δ_4	r
1	-600.0	-0.16	-66.6	0.016					0
2	-600.0	-0.16	-100.0	0.0	-66.6	0.016			0
3	-600.0	-0.16	-350.0	-0.08	-100.0	0.0	-66.6	0.016	0

LUSAS results

For all tests the obtained relationship between lateral earth pressure and relative joint deformation, as shown in Figure 1, was confirmed by hand calculations.

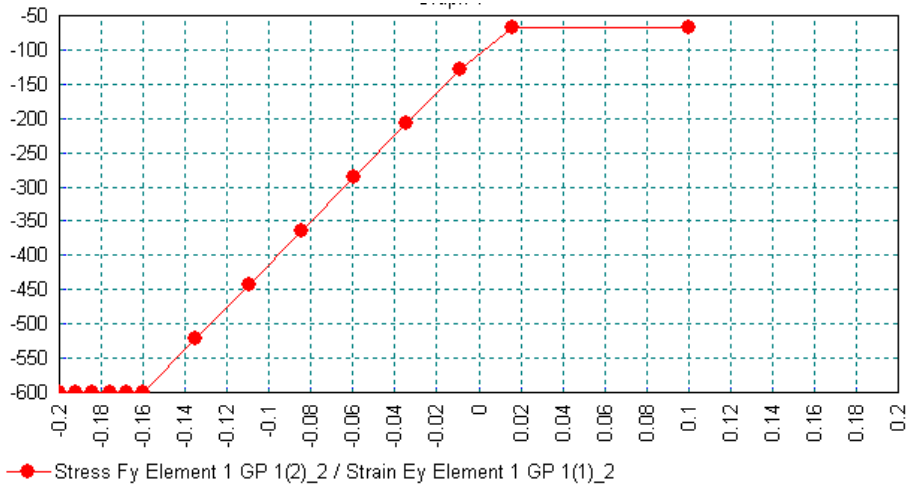


Figure 1

Input data

- x05d71a** (JNT3, coupled, $n = 3$)
- x05d71b** (JNT3, uncoupled, $n = 2$)
- x05d71c** (JNT3, coupled (USER), $n = 2$)
- x05d71d** (JNT3, uncoupled (USER), $n = 2$)
- x05d71e** (JNT4, coupled, $n = 2$)
- x05d71f** (JPH3, coupled, $n = 2$)
- x05d71g** (JAX3, coupled $n = 2$)
- x05d71h** (JF3, coupled, $n = 2$)
- x05d71i** (JXS3, coupled, $n = 2$)

x05d71j (JL43, coupled, $n = 2$)
x05d71k (JSH4, coupled, $n = 2$)
x05d71l (JL46, coupled, $n = 2$)
x05d71m (JSL4, coupled, $n = 2$)

Example 5.7.2

Plastic hinge with axial force dependent moment-curvature relation

Keywords

Multi-linear, Plastic Hinge, Pushover

Description

This example models a plastic hinge with axial force dependent moment-curvature relationship, which is widely used in pushover analysis. Rotations or moments are applied at one degree of freedom, while other degrees of freedom are fixed. The numerical response can then be compared with hand calculations.

Geometry, Boundary and Loading Conditions

A single joint is defined by 3 or 4 nodes

node	1	2	3	4
Coordinates	2.0, 0.0, 0.0	1.0, 0.0, 0.0	2.0, 1.0, 0.0	2.0, 1.0, -1.0

For 2D joints, the 3rd node is used to define the local x-direction; for 3D joints, the 3rd and 4th nodes are used to define the local x-axis and local xy-plane respectively.

Node 2 is fixed; for the JPH3 element the prescribed rotation θ_z at node 1 in the z-direction varies as:

step	θ_z
0	0.
1	-0.1
2	-5.0
3	-5.1
4	-10.
5	-10.1

For the JSH4 element, the same θ_z is applied at node 1 but in the positive direction.

Discretisation

The joint is discretised into one 2D or 3D joint element.

Material properties

The following multi-linear moment-curvature relationship is defined in the local direction, which corresponds to the global z-direction

(0.0, 0.0), (0.0, 0.1), (10.0, 5.0), (0.0, 5.1), (5.0, 10.0), (0.0, 10.1), $r = 0$. at $F_{ax} = -10.0$

(0.0, 0.0), (20.0, 0.1), (20.0, 5.0), (10.0, 5.1), (5.0, 10.0), (0.0, 10.1), $r = 0$. at $F_{ax} = 10.0$

Properties in all other directions are zero.

LUSAS results

The variation of joint moment with curvature is shown in Figure 1, which is in agreement with the prescribed moment-curvature relation at $F_{ax} = 0$.

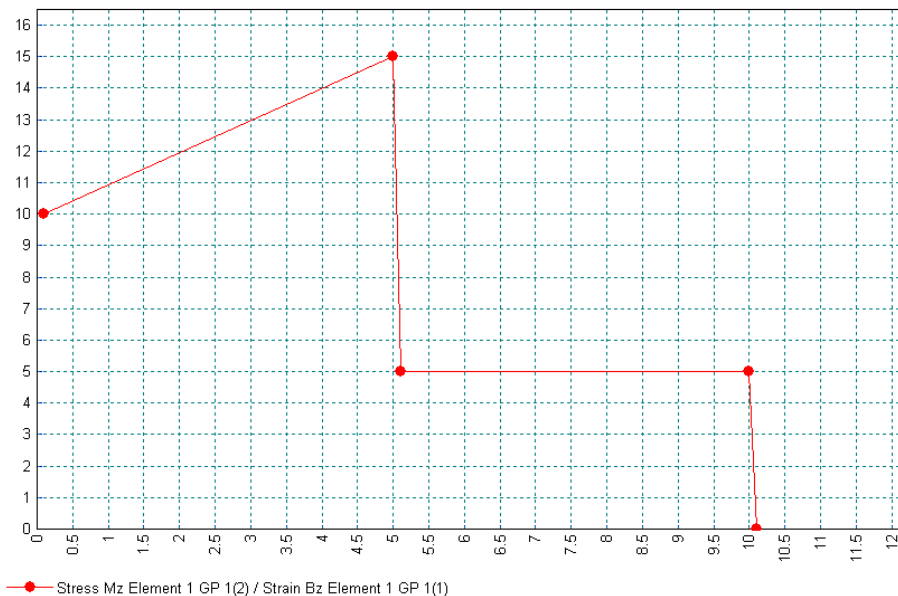


Figure 1

Input data

x05d72a (JPH3)

x05d72b (JSH4)

Example 5.8.1

Definition of soil-structure interface material parameters from experimental data

Keywords

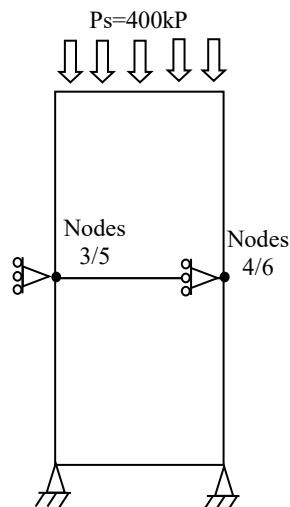
Interface, friction, dilation

Description

This example shows how experimental data from a direct shear test may be input into the interface element material properties and how by including a variation of cohesion with tangential displacement the range of applicability of the interface under different normal stress may be extended. Experimental data is taken from tests by Hu and Pu [1].

Geometry, Boundary and Loading Conditions

Two square plane strain QPN4 elements of unit dimension are connected by the interface element IPN4. A face load of 400kPa is applied to the upper surface and the blocks are then sheared by applying a horizontal displacement to the lower face of the upper block.



Material properties

Block		Interface	
E	1×10^6 kPa	K_n	2×10^6 kPa
ν	0.0	P_s	400 kPa
		C	0 kPa
		t	1.0 m

The variation of shear force and dilation with tangential displacement along interface under a normal pressure of 400 kPa is given in the table

Tangential Displacement (mm)	Shear force (kPa)	Dilation (mm)
0.0	0	0
0.1	150	.*-
0.25	225	.*-
0.5	289	0
0.75	330	.*-
1.0	352	0.12
1.25	365	.*-
1.5	370	0.25
2.0	367	0.38
2.5	352	0.51
3.0	337	0.61
3.5	319	0.69
4.0	301	0.76
4.5	285	0.8
5.0	272	0.84
5.5	260	0.85
6.0	254	0.86

6.5	252	0.87
10.0	252	0.87

A unit thickness of t is used so that the displacements input in the shear stress and dilation curves are equal to the physical displacements measured in the shear test.

Discretisation

2 QPN4 elements with 1 IPN4 interface element at their junction.

Experimental Results

Data from experiments of H_u and P_u showing the shear stress and normal displacement with respect to relative tangential displacement are shown in figure 1.

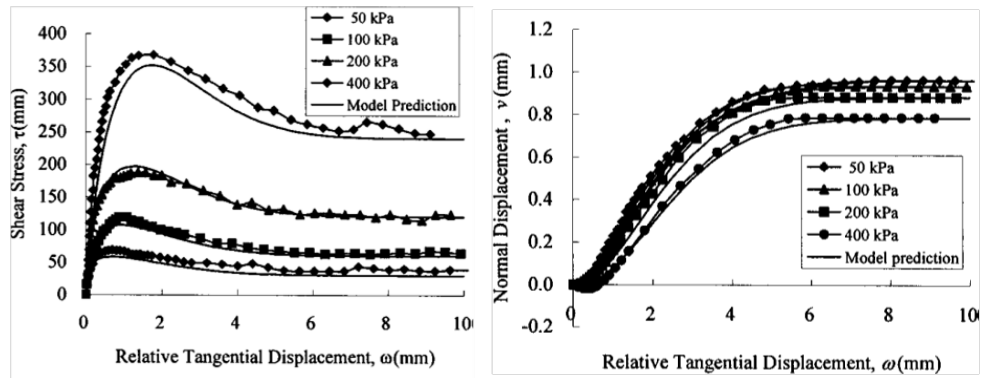


Figure 1. Experimental results of direct shear test of H_u and P_u [1]

LUSAS results

Four runs are made with normal stresses of 50, 100, 200 and 400kPa. Results for each run are compared to the experimental data in figure 2. The data for the normal stress of 400kPa exactly reproduces the input curve. Peak shear stresses at the lower values of normal stress are not so well predicted.

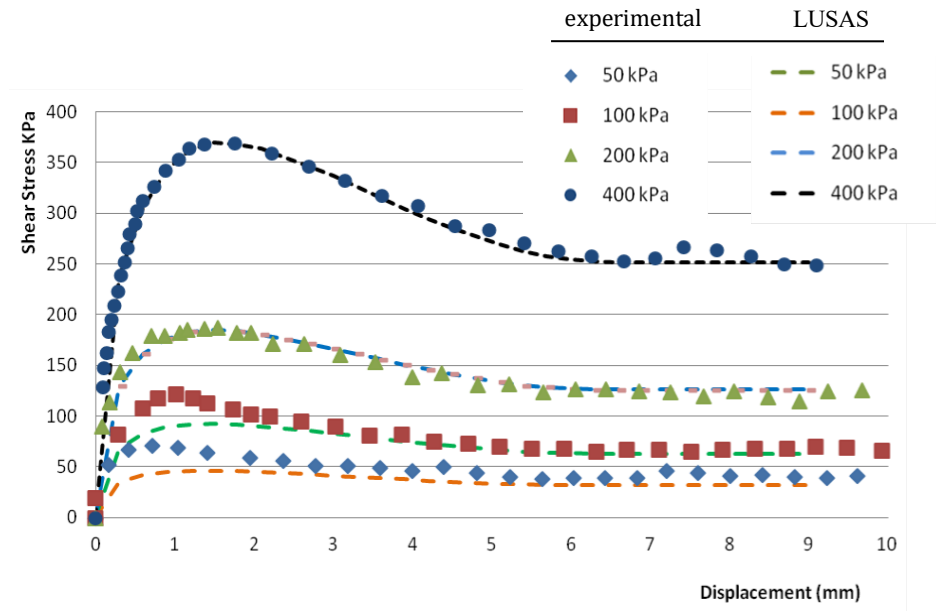


Figure 2. Shear stresses at different normal stresses compared with experimental data

We now modify the original solution data by including cohesion. At lower values of normal stress the effect of cohesion will have a greater effect on the results than at higher stress so we can improve the numerical model by adding a contribution from cohesion. To do this we plot the displacement and experimental results for the 100kPa normal pressure at a larger scale as shown in figure 3. We then attribute the difference between the experimental data and the numerical solution to cohesion which allows us to define a function to represent the variation of cohesion with tangential displacement.

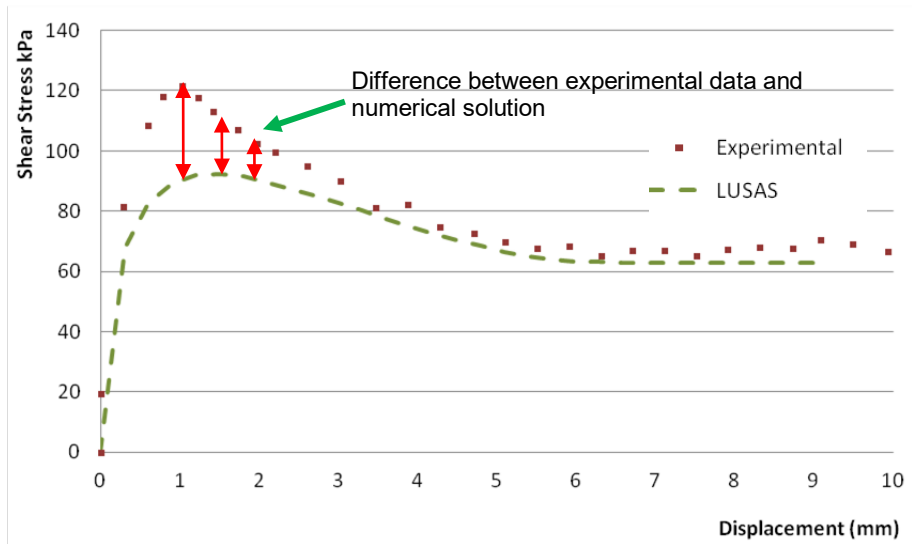


Figure 3. Evaluation of cohesion function from difference in numerical solution and experimental data

The resulting function defining the cohesion is shown in figure 4. It is assumed that the cohesion is constant until the peak stress is reached at which point it declines rapidly as the displacement increases.

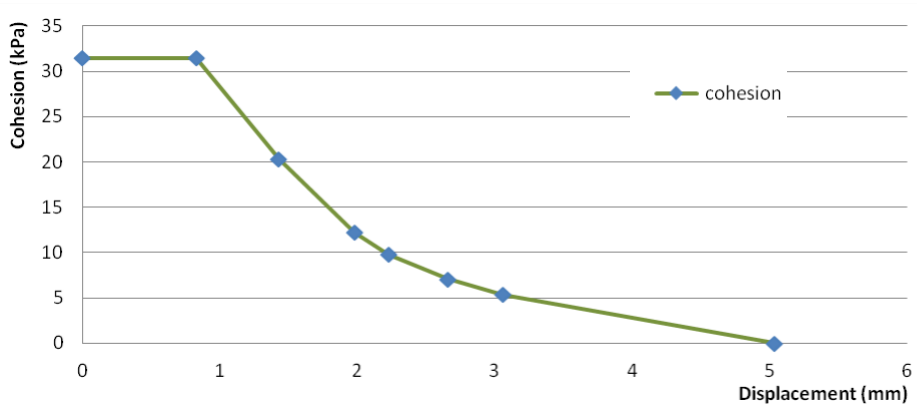


Figure 4. Variation of cohesion with tangential displacement

The numerical data are given in the following table.

Displacement (mm)	Cohesion (kPa)	Displacement (mm)	Cohesion (kPa)
0.0	31.42	2.66	7.08
0.83	31.42	3.06	5.33
1.43	20.25	3.47	4.1
1.98	12.22	5.04	0
2.23	9.82	10.0	0

The shear tests are re-run with the new cohesion data. This time there is much better agreement at the lower normal pressures as shown in figure 5.

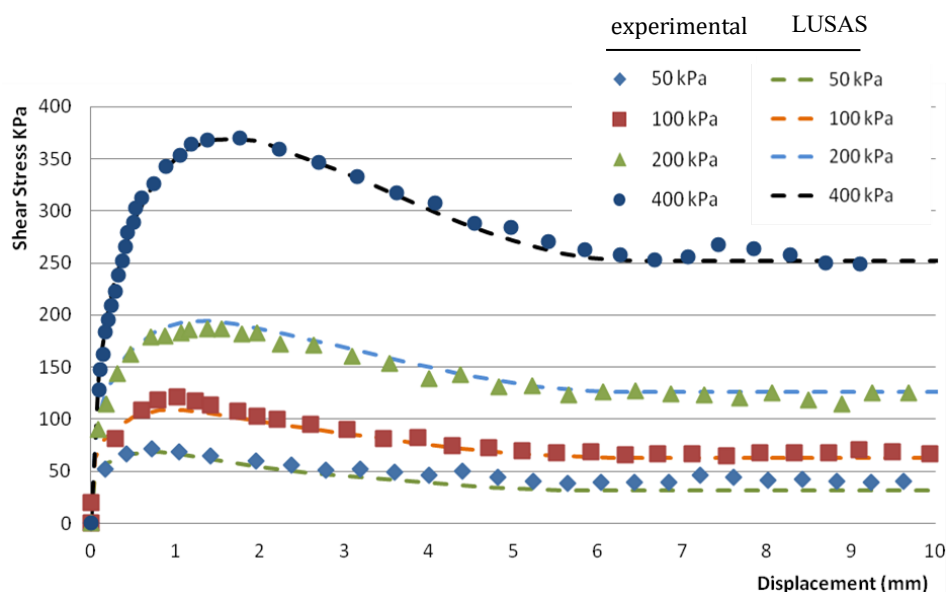


Figure 5. Shear stresses at different normal stresses compared with experimental data using improved material data

The dilation is not substantially affected by the normal pressure so the solution for only one normal pressure is shown below.

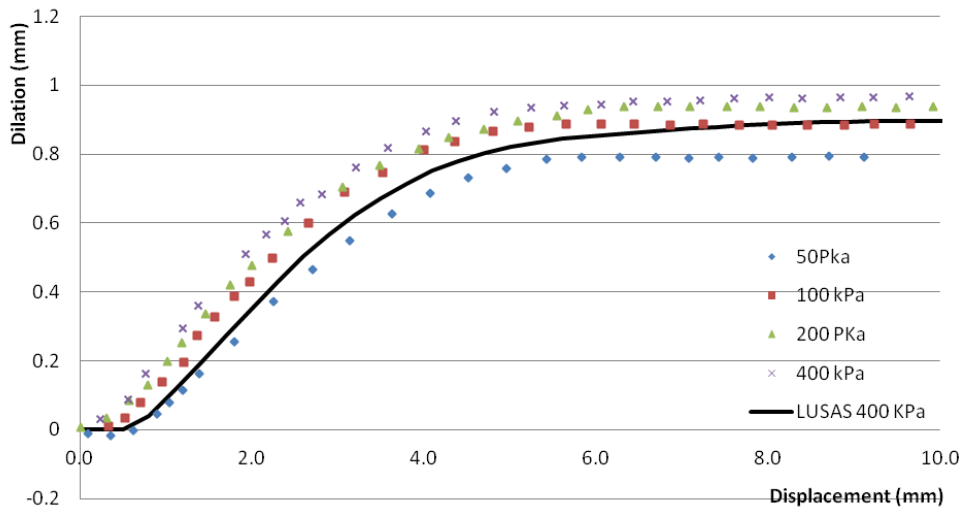


Figure 6. Variation of dilation at different normal stresses

References

3. Hu L. and Pu J., 'Testing and modeling of soil-structure interface', J.Geotech.Geoenv.Eng., ASCE, 851-860, (2004)

Input data

X05D81.DAT

Example 6.3.1

Materially And Geometrically Nonlinear Encastre Beam

Keywords

Nonlinear, Plasticity, Updated Lagrangian Description

Description

An encastre beam of length 495mm, width 7.78mm, and depth 7.72mm is subjected to a central transverse concentrated load. The loading is applied in increments of 100N. Figure 1 shows the dimensions of the beam, the boundary conditions and the position of the load.

Discretisation

Due to its symmetrical nature only a half of the beam is discretised using six curved beam elements (BSX4). The nodal positions and element numbers are shown in figure 2. Symmetrical and fully restrained boundary conditions are imposed on the central and encastre ends of the mesh respectively.

Modelling

The geometric nonlinearity is modelled using an updated Lagrangian description. The material nonlinear behaviour is modelled using a Von-Mises elasto-plastic model with the following material properties:

Young's modulus	$197.3 \times 10^3 \text{ N/mm}^2$
Poisson's ratio	0.3
Yield stress	248.0 N/mm^2

Comparison

The LUSAS results are presented in the table below, and are compared to the experimental data [1] in the following load deflection graph.

Applied Load, N	Central Deflection BSX4
100	1.059
200	2.044
300	2.921
400	3.758
500	4.609

Applied Load, N	Central Deflection BSX4
600	5.956

References

1. Campbell, T.I. Charlton, T.M. 'Finite defrmatio of a fully fixed beam comprised of a nonlinear material'. Int.Jou.Mechanical Science, Vol.15, No.5, 415-428.

Input data

X06D31A.DAT

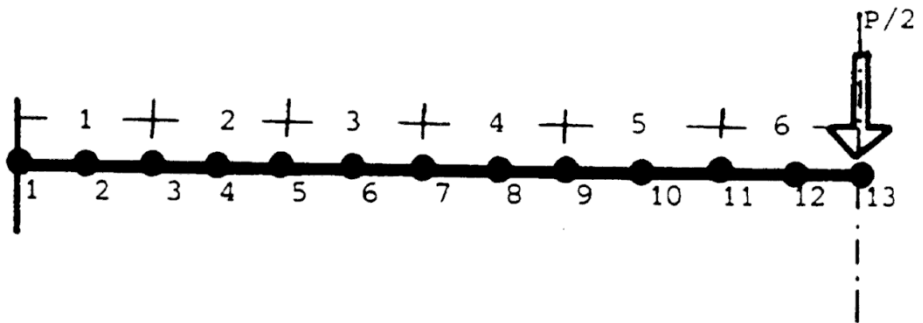
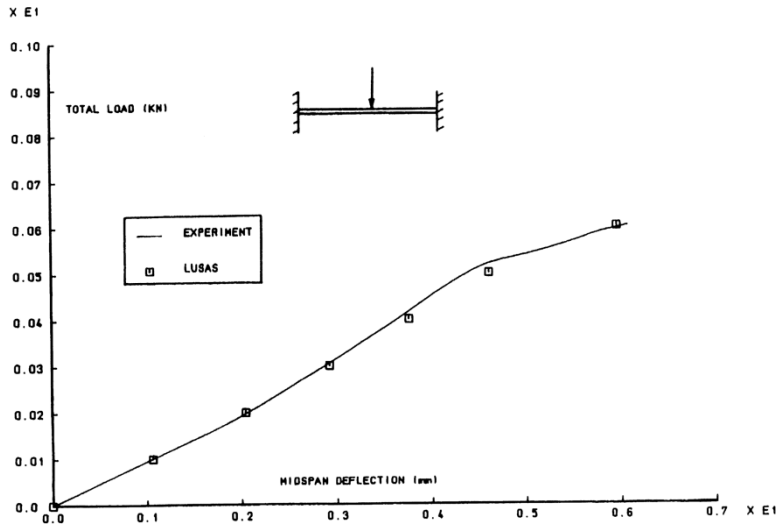


Figure 1.

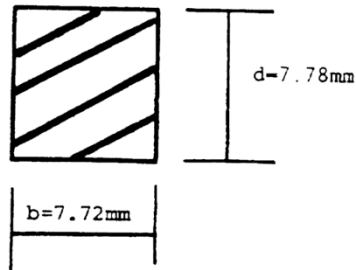
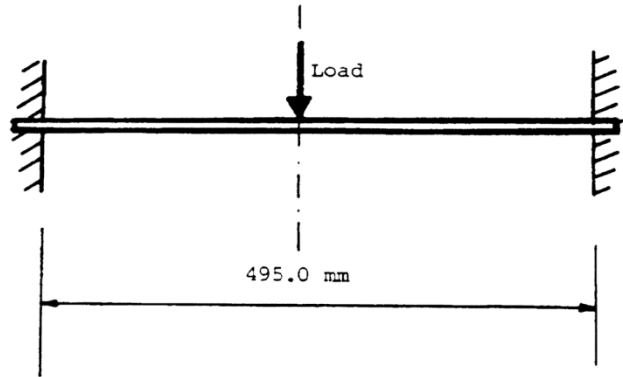


Figure 2.

Example 6.5.1

Elasto-Plastic Buckling Analysis Of A An Imperfect Rectangular Panel

Keywords

Buckling, Plasticity, Total Lagrangian, Nonlinear, Rectangular Panel

Description

Determine the buckling behaviour of an imperfect rectangular panel subject to an in-plane compressive loading.

The dimensions of the panel are as follows:

side length	$a = 875$ mm
side length	$b = 1000$ mm
thickness	$t = 25$ mm
side length ratio	$a/b = 0.875$
aspect ratio	$b/t = 40$

In order to initiate a buckling mode of failure the panel is given an out of plane initial imperfection in the form of half of a sine wave. The semi sine wave imperfection acts over the entire plate surface and has a maximum amplitude of $0.001 * b$ at the centre of the plate.

$$z = d_0 \sin\left(\frac{\pi x}{a}\right) \sin\left(\frac{\pi y}{b}\right) \quad (0.0.121)$$

where d_0 is the maximum amplitude.

The panel is subjected to an in-plane compressive loading acting along its long edges.

Discretisation

A symmetric quarter of the panel is discretised using a uniform mesh of sixteen Semiloof shell (QSL8) elements. The nodal coordinates of the mesh are calculated so as to give an initial sine wave imperfection as described by (0.0.121).

The external edges of the panel are assumed to be simply supported and the internal edges are subject to symmetry enforcing boundary conditions.

The geometrically nonlinear behaviour of the panel is recorded using a total Lagrangian approach.

The material is assumed to behave in an elasto-plastic manner according to a Von Mises yield criterion. The assumed material properties of the panel are as follows:

Young's modulus	207.0x10 ³ N/mm ²
Poisson's ratio	0.3
Yield stress	247.0 N/mm ²

The in-plane compressive loading is applied via prescribed displacements along the long edges of the panel. The results quoted were obtained by using the standard frontal equation solver.

Theory

The behaviour of the panel is represented in the form of a load versus shortening curve. Previous studies [1-2] have established that the lowest critical buckling strength occurs at a side length ratio of approximately 0.875.

The squash load is calculated from the yield stress as

$$P_0 = \sigma_y A = \sigma_y \left(\frac{b}{2} \right) t = 247 * 500 * 25 = 3087.5 \text{ kN}$$

Similarly the strain at the squash load may be calculated as

$$\epsilon_0 = \frac{\sigma_y}{E} = \frac{247.0}{207 \times 10^3} = 0.001932$$

Solution Comparison

The results obtained from the nonlinear LUSAS analysis are compared to the linear solution and to the nonlinear solutions of [1].

Increment	Displacement in X direction along line Y=0	Average membrane strain in X direction (x10 ³)	Strain/squash strain (ε ₀)	Load in X direction	Load/squash load (P ₀)
1	0.261021	0.5966	0.5	1538.96	0.49891
2	0.417633	0.9548	0.8	2458.54	0.79628
3	0.469837	1.0739	0.9	2763.93	0.89519
4	0.522041	1.1932	1.0	3020.4	0.97826
5	0.574245	1.3124	1.1	3052.56	0.98868
6	0.626449	1.4317	1.2	3039.9	0.98458
7	0.678653	1.5512	1.3	3022.94	0.97908

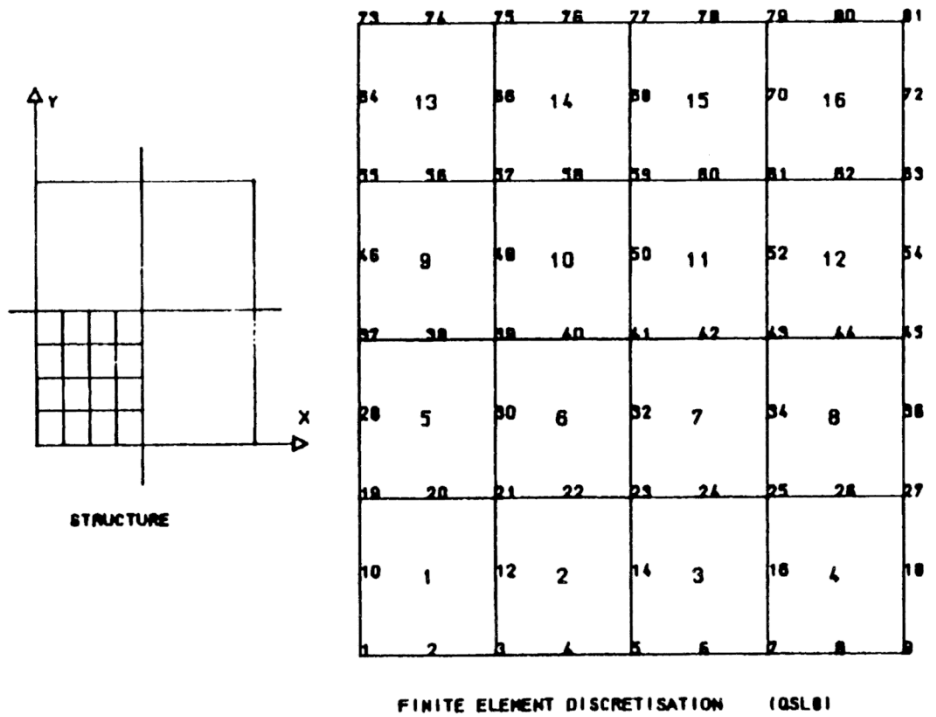
Increment	Displacement in X direction along line Y=0	Average membrane strain in X direction ($\times 10^3$)	Strain/squash strain (ϵ_0)	Load in X direction	Load/squash load (P_0)
8	0.730857	1.6706	1.4	3000.57	0.97184
9	0.783062	1.7898	1.5	2972.4	0.96272
10	0.835266	1.9092	1.6	2938.48	0.95173
11	0.887470	2.0285	1.7	2899.49	0.93911
12	0.939674	2.1411	1.8	2856.62	0.92522

References

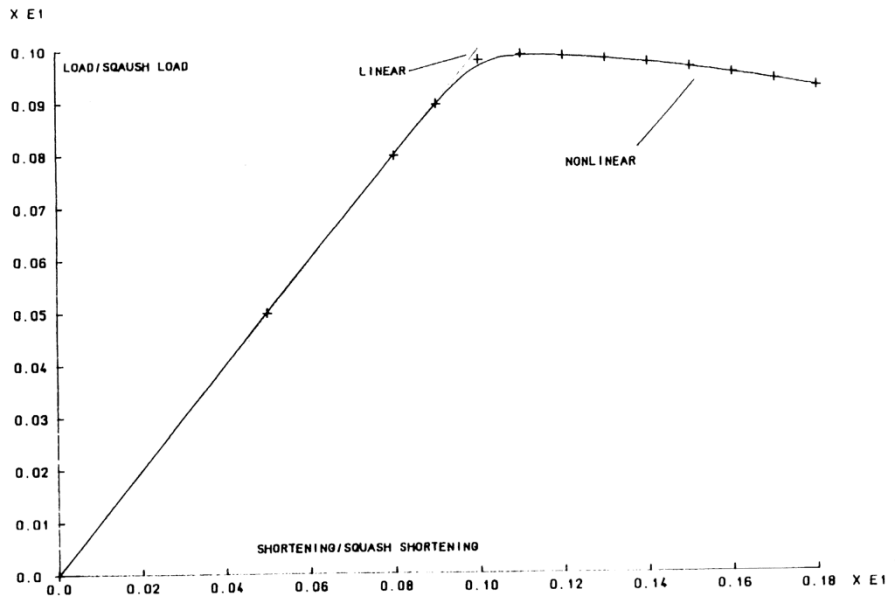
1. Crisfield, M.A. 'Full range analyses of steel plates and stiffened plating under uniaxial compression'. Proc.Inst.Civil Engineers, Part 2, Volume 59, 595-624, (1975)
2. Irving,D.J. 'Large deformation elasto-plastic finite element analysis of plates, shells and tubular joints using Semiloof shell elements', Ph.D. Thesis, Kingston Polytechnic, London, U.K. (1982).

Input data

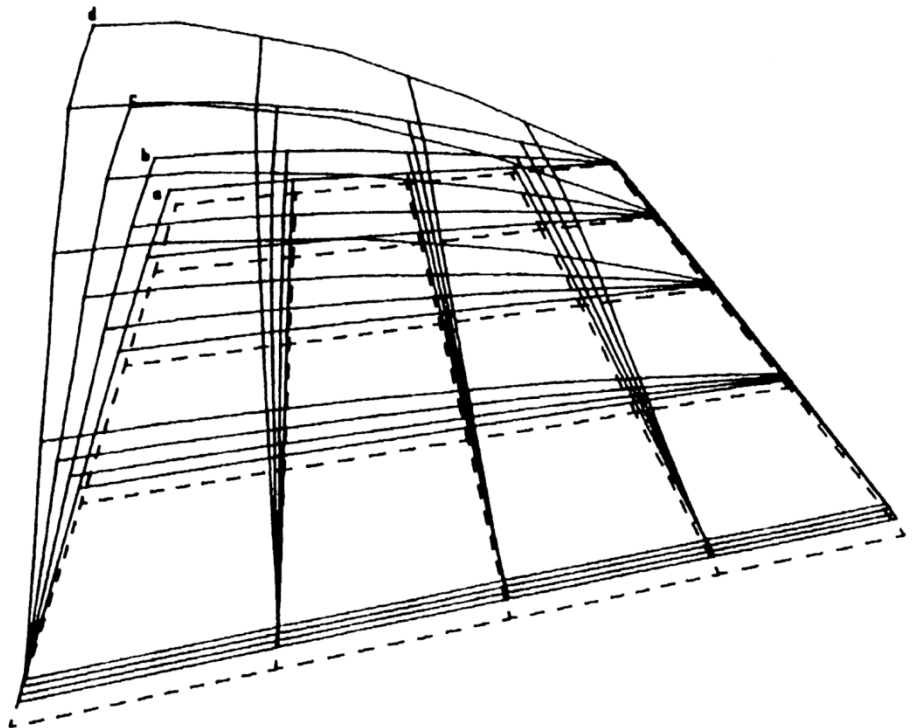
X06D51A.DAT



Imperfect rectangular panel subject to in-plane compressive load



Nonlinear buckling analysis of imperfect rectangular panel (QSL8 elements)



**BUCKLED IMPERFECT RECTANGULAR PANEL
DEFORMED CONFIGURATIONS**

INITIAL CONFIGURATION
a INCREMENT 3
b INCREMENT 6
c INCREMENT 9
d INCREMENT 12

Example 6.5.2

Elasto-Plastic Analysis Of A Clamped Spherical Cap

Keywords

Spherical Shell, Total Lagrangian, Nonlinearity, Elasto-Plastic,

Description

Determine the load-deflection response of an elasto-plastic spherical shell cap. The geometry of the shell is formed from a truncated sphere of radius 4.758 inches. The cap has a base radius of 0.9 inches, a central height of 0.085895 inches, and a thickness of 0.01576 inches. The shell is fully restrained at its base and is subject to an increasing concentrated transverse load at its apex.

Discretisation

Due to its doubly symmetric nature only a quarter of the structure is considered in the finite element model. The shell is discretised using 32 Semiloof shell (QSL8 and TSL6) elements. The initial geometry of the shell is formed using the LUSAS arc facility to generate the truncated portion of the sphere. Symmetric boundary conditions (restraint of the loof rotations and the appropriate lateral translations) are imposed on the internal boundaries of the mesh, and the nodes at the base of the structure are restrained against translation and rotation. The nonlinear material behaviour is modelled by a Von-Mises elasto-plastic model with the following material properties:

Young's modulus	10.0x10 ⁶ psi.
Poisson's ratio	0.3
Yield stress	50.0x10 ³ psi.

Theory

The maximum (apex) deflection for a fully restrained partial sphere is given by the expression [1]

$$y = \frac{-A_2}{16} \frac{PR^2}{\pi D} \quad (0.0.122)$$

Where

$$D = \frac{Et^3}{12(1-\nu)^2} \quad (0.0.123)$$

and in which A_2 is tabulated according to the parameter α , where

$$\alpha = 2 \frac{\left(3(1-\nu^2)h^2\right)^{1/4}}{t^2} \quad (0.0.124)$$

For the current sphere geometry the following values apply:

$$\alpha = 6.00 \quad A = 0.161 \quad D = 3.584$$

Hence for a total load of 50 lbs the maximum deflection is

$$y = - 0.036189 \text{ inches}$$

Comparison

The results obtained from the LUSAS analysis are compared to the linear solution [1] and the axisymmetric nonlinear analysis of Wood [2,3].

Increment Number	Displacement at Apex (ins)	Total Force (lb) (Elastic)	Total Force (lb) (Elastoplastic)
1	0.01	9.50	9.40
2	0.02	14.15	13.17
3	0.03	16.94	15.07
4	0.04	19.38	17.20
5	0.05	21.98	19.70
6	0.06	24.84	22.46
7	0.07	27.90	25.26
8	0.08	31.04	28.00
9	0.09	34.09	30.60
10	0.1	36.86	32.98
11	0.11	39.18	35.18
12	0.12	41.06	37.19
13	0.13	42.86	38.77
14	0.14	45.80	40.50

References

1. Roark, R.J. Young, W.C. 'Formulas for stress and strain : Fifth edition', McGraw-Hill Publishing Co. (1975)

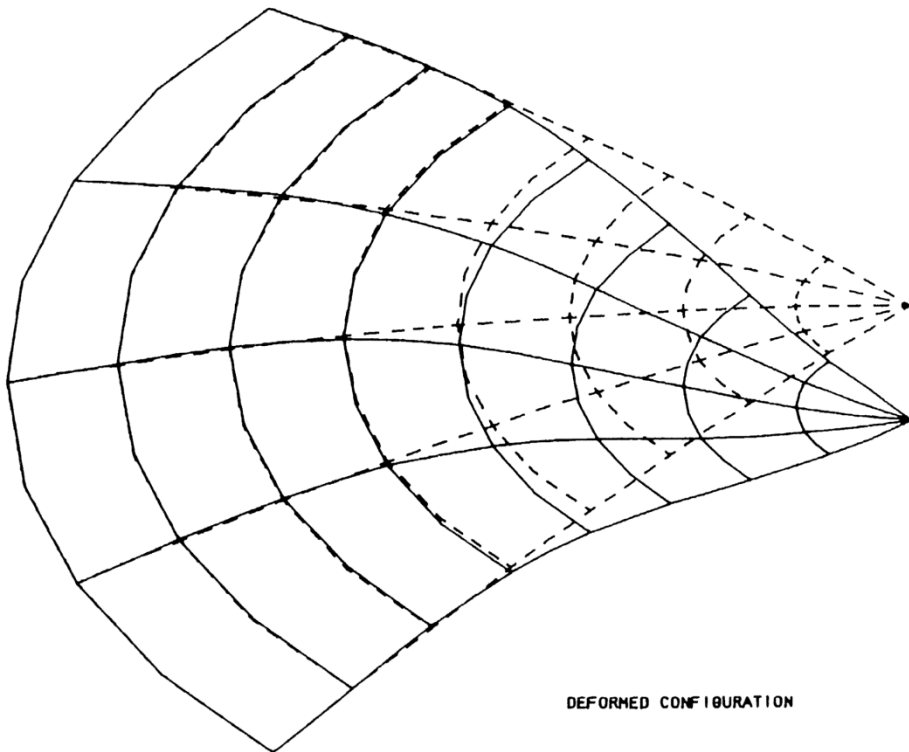
2. Oliver, J. Onate, E. A total Lagrangian formulation for the geometrically nonlinear analysis of structures using finite elements: Part 1: Two dimensional problems: Plate and shell structures'. Int. Journ. Num. Mthds. in Eng. Vol.20. 2253-2281, (1981).
3. Wood,R.D. 'The application of finite element methods to geometrically nonlinear structural analysis'. PhD.Thesis C/Ph/20/73, University of Wales, Swansea, U.K.

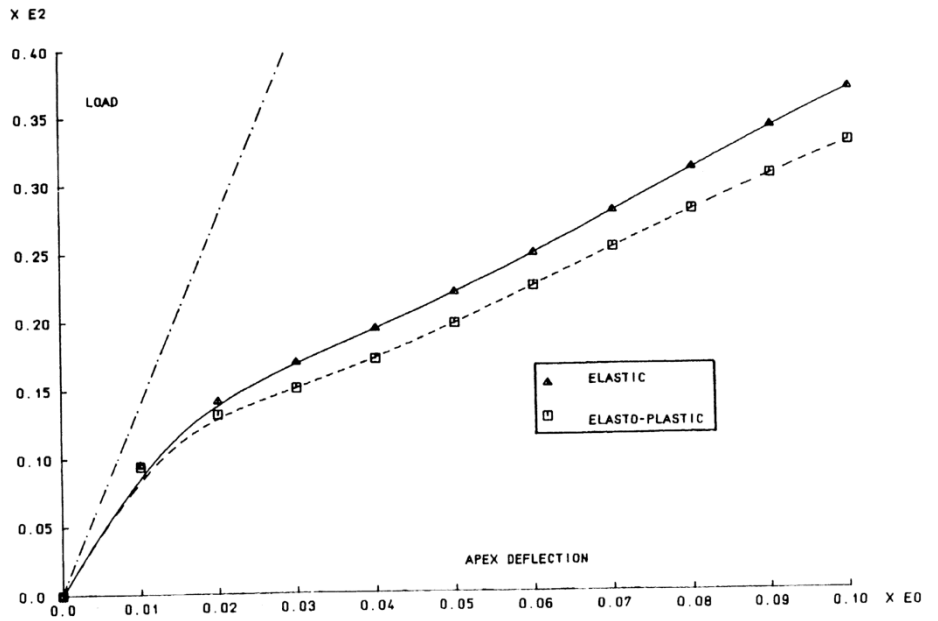
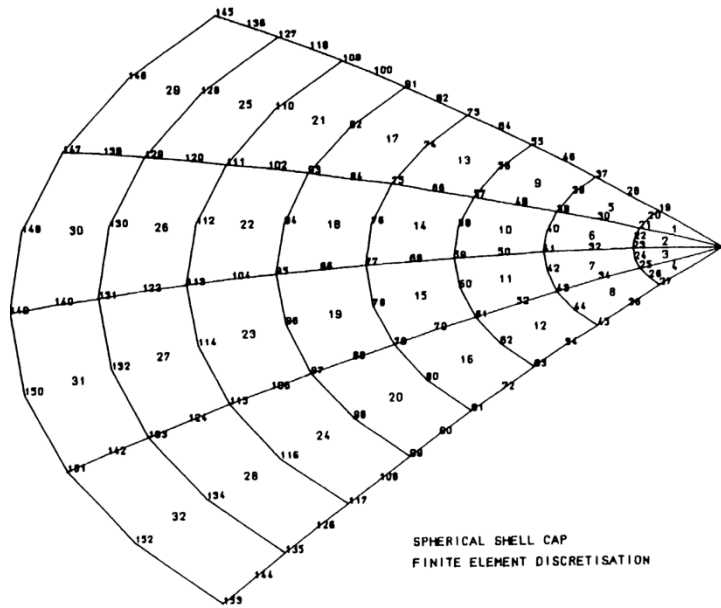
Input Data

Note: Load incrementation may alternatively be defined using the nonlinear control INCREMENTATION and TERMINATION control cards.

X06D52A.DAT

X06D52B.DAT





Load-deflection response for spherical shell under apex point load

Example 6.5.3

Nonlinear Analysis Of A CHS Welded Tubular Joint

Keywords

Tubular Joint, Elasto-Plastic, Total Lagrangian Nonlinearity, Semiloof Shell, Three Dimensional Solid

Description

Determine the relationship between the applied axial load and the penetration for the welded tubular joint.

The X-joint is formed by the right angled intersection of two circular section hollow tubes. The intersection is secured by a fillet weld. The vertical tube is subjected to an axial load such that the horizontal tube is progressively penetrated.

Discretisation

Owing to the symmetrical nature of the problem only one half and one quarter of the vertical and horizontal tubes are modelled respectively.

The hollow tubes are represented using 8 and 6 noded Semiloof shell (QSL8 and TSL6) elements, and the fillet weld by 15 noded solid wedge (PN15) elements.

The vertical tube is axially compressed by means of prescribed displacement of its top edge.

The nonlinear behaviour is modelled using a nonlinear Von-Mises elasto-plastic material model, and a total Lagrangian geometric description.

Modelling Hints

The solid wedge elements are numerically integrated using three pairs of two Gauss points located on the quadrilateral faces of the element. The Semiloof shell elements are integrated in plane using a 5 point integration rule, and through the thickness by a five point mid-ordinate rule.

The configuration of the loof node rotations [1] allows the Semiloof shell element to model branched or intersecting shell geometries. In this case the intersection of the shell and three dimensional elements is achieved by coupling the global translational degrees of freedom of the two element types. The loof rotations however are unrestrained. Although theoretically this permits a rotation at the tube-weld interface, in practice the small size of the weld and the relative stiffness of the connection prevents the occurrence of any serious discretisation error.

Theory

The welded tubular structure has been investigated experimentally and numerically by several authors [2-4].

The response of the structure is represented by a graph of applied axial load against the branch penetration (the branch penetration of the vertical tube is defined as the applied axial displacement minus any elastic compressional deformation). Although somewhat inconclusive, the experimental results clearly show a limit point in this response at a load level of approximately 90 kN.

Comparison

The solution obtained from the LUSAS analysis (tabulated below) is compared to the experimental results [2].

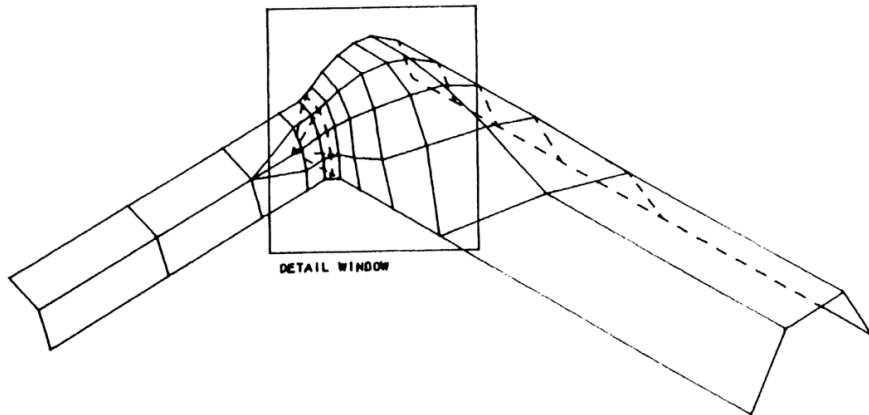
Increment Number	Prescribed Displacement	Branch Penetration	Axial Load (kN)
1	-1	-0.9491	-54.326
2	-2	-1.9086	-91.984
3	-3	-2.8934	-101.263
4	-4	-3.8908	-100.564
5	-5	-4.8972	-97.096
6	-6	-5.8944	-93.02
7	-7	-6.8987	-89.329
8	-8	-7.9019	-85.844
9	-9	-8.9053	-82.676
10	-10	-9.9084	-80.267
11	-11	-10.911	-78.134
12	-12	-11.9131	-76.631

References

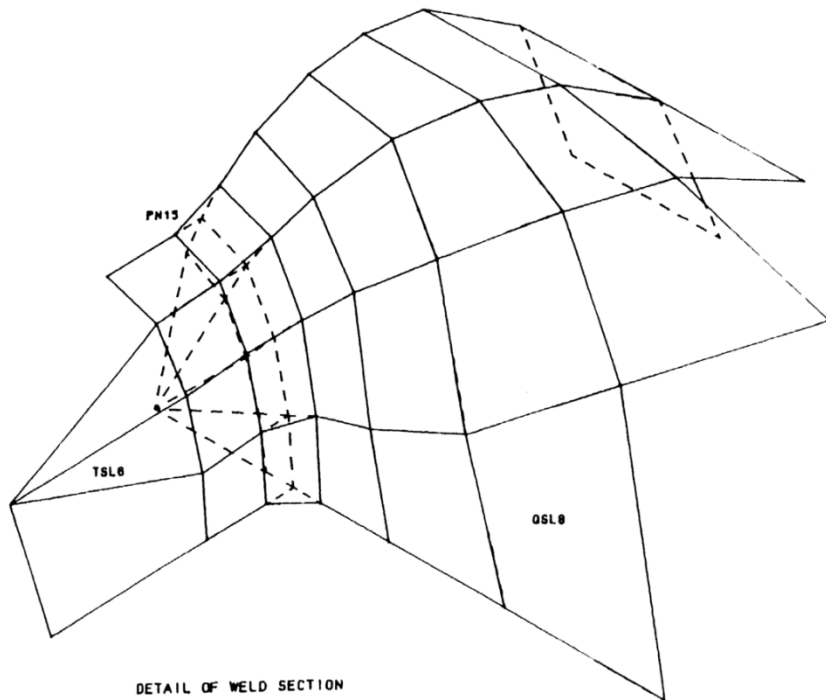
1. Irons, B.M. 'The Semiloof shell element', Finite Elements for thin shells and curved members, Eds. Ashwell and Gallagher, Wiley (1976).
2. Sparrow, K.D. 'Ultimate strength of welded joints in tubular steel structures', Ph.D. Thesis, Kingston Polytechnic, London (1979).
3. Hoadley, P.W. Yura, J.A. 'Ultimate strength of tubular joints subjected to combined loads', Department of Civil Engineering, University of Texas at Austin, U.S.A. (1982).
4. Holsgrove, S.C. Lyons, L.P.R. 'Nonlinear FEM analysis of CHS T/X joints under axial load, in plane bending, and out of plane bending', Safety Criterion in the Design of Tubular Structures, (1987).

Input data

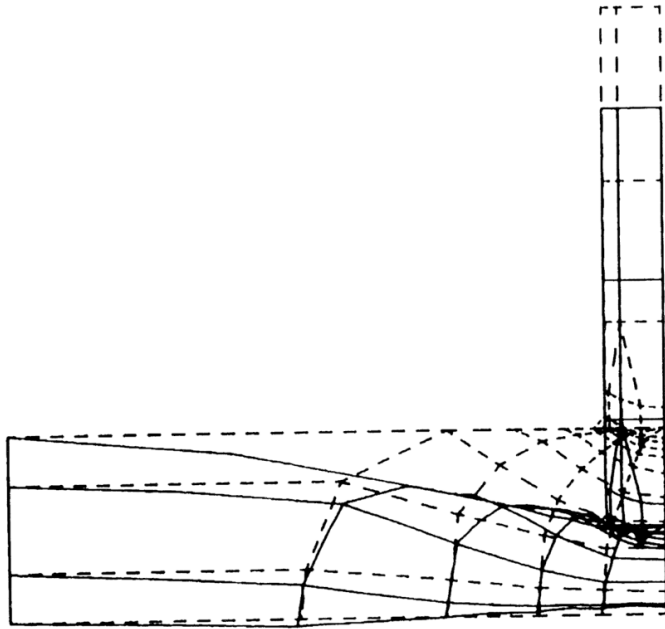
X06D53A.DAT



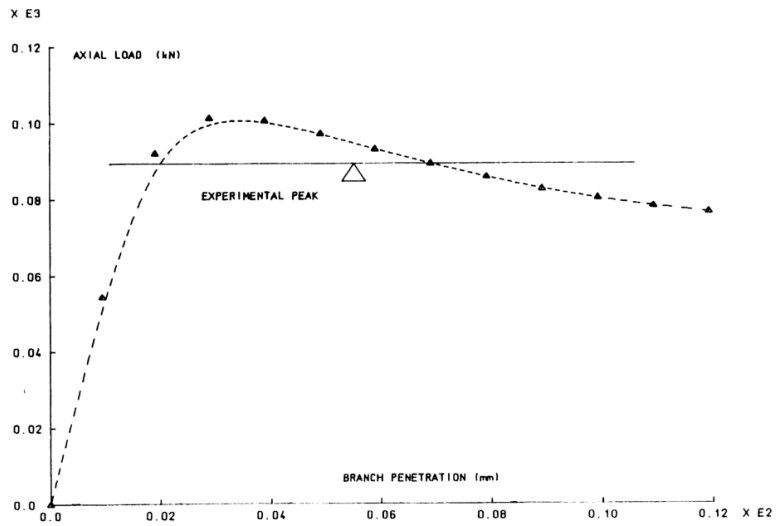
Circular hollow section welded tubular joint finite element discretisation



Detail of weld section



Deformed configuration (increment 3) magnification 20



Load-penetration response for welded circular tube joint

Example 6.5.4

Large Deflection Of Orthotropic Spherical Cap

Keywords

Total Lagrangian, Large Displacement, Hill Yield Criterion

Description

A material which has yield stresses in the principle directions of 200, 200 and 100 is applied with the weak direction of the material aligning with the hoop, meridional and through thickness directions in turn. The orientation of the yield surface produces different responses as the cap snaps through under a point load applied at its vertex.

Finite Element Model

The cap is restrained to deform axisymmetrically and is modelled by a mesh of 8*1 axisymmetric shell elements.

Geometry

Radius of sphere = 4.758

Angle subtended = 21.8 degrees

Shell thickness = 0.01576



Material properties

Young's modulus in X direction = 1×10^5

Young's modulus in Y direction = 1×10^5

Poisson's ratio = 0.3

Case 1

Yield stress in meridional direction = 200

Yield stress in hoop direction = 100

Yield stress in through-thickness direction = 200

Shear yield stress (not used) = 1

Case 2

Yield stress in meridional direction = 100

Yield stress in hoop direction = 200

Yield stress in through-thickness direction = 200

Shear yield stress (not used) = 1

Case 3

Yield stress in meridional direction = 200

Yield stress in hoop direction = 200

Yield stress in through-thickness direction = 100

Shear yield stress (not used) = 1

Boundary Conditions

Symmetry conditions are applied to the apex. The shell is hinged but fixed against translational motion.

Solution Comparison

Figure 1 illustrates the loading paths for the various material orientations. After buckling, three distinctly different responses occur. The apex displacement is detailed in figures 2 to 4, and figures 5 to 7 plot the development of the snap through for each case.

The material is considered to be in a state of plane stress. However, the through thickness yield stress is significant and does effect the results as the out-of-plane plastic strain is related to the inplane plastic strains, by the constraint that there must be no change of volume following inelastic straining.

It is important when considering orthotropic yield that all three yield stresses in the principle directions are known. On the other hand, the shear stresses are de-coupled, both from themselves and the direct stresses so only the relevant values need be input.

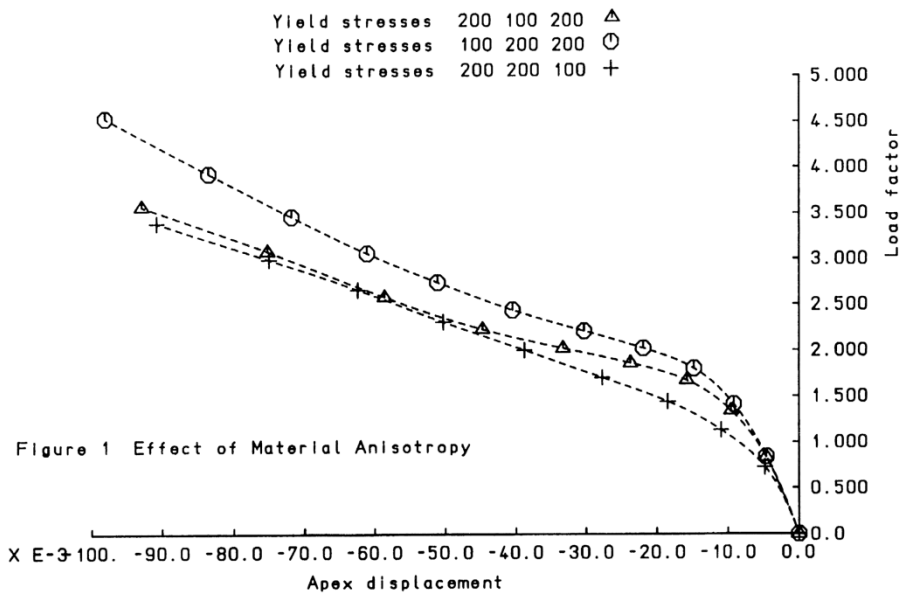
Input Data

X06D54A.DAT

X06D54B.DAT

X06D54C.DAT

The data files for cases 2 and 3 are obtained by changing the yield values on the STRESS POTENTIAL data command.



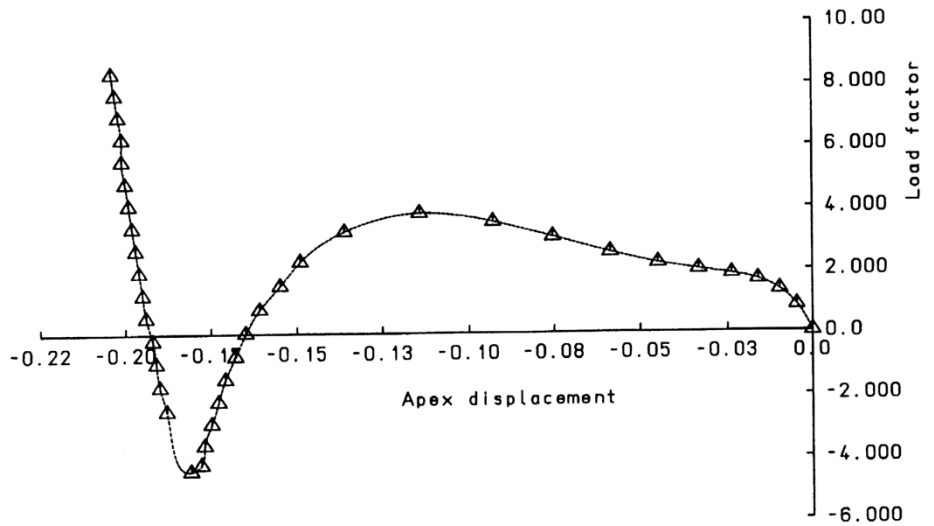


Figure 2 Yield stresses in Principle Directions 200 100 200

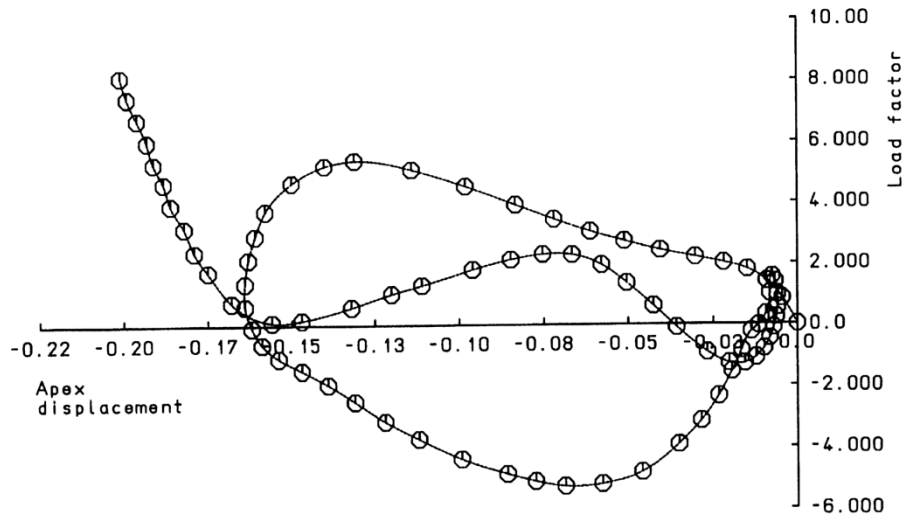


Figure 3 Yield stresses in Principle Directions 100 200 300

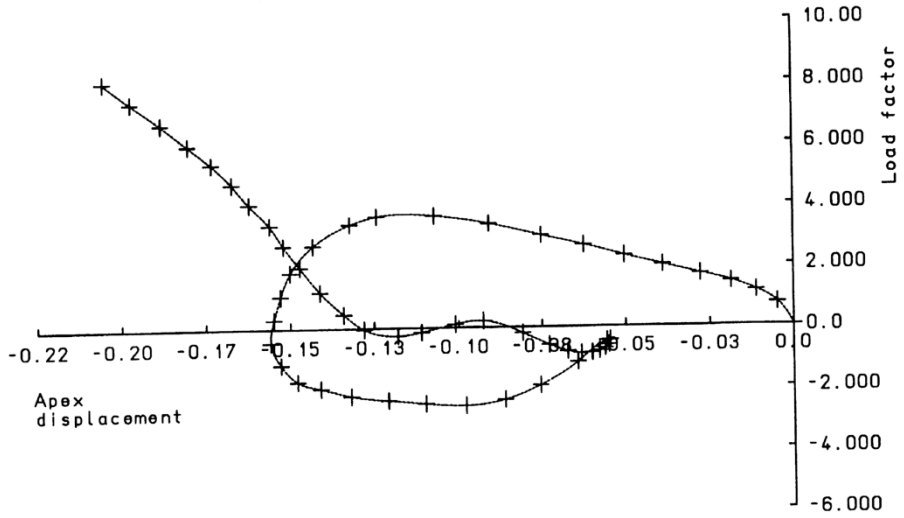


Figure 4 Yield stresses in Principle Directions 200 200 100

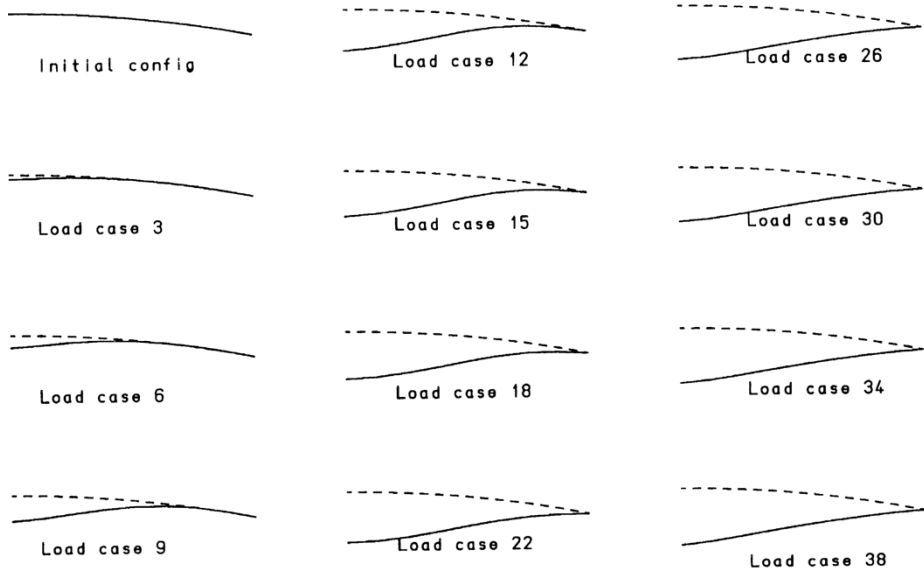


Figure 5 Deformation for yield stresses 200 100 200

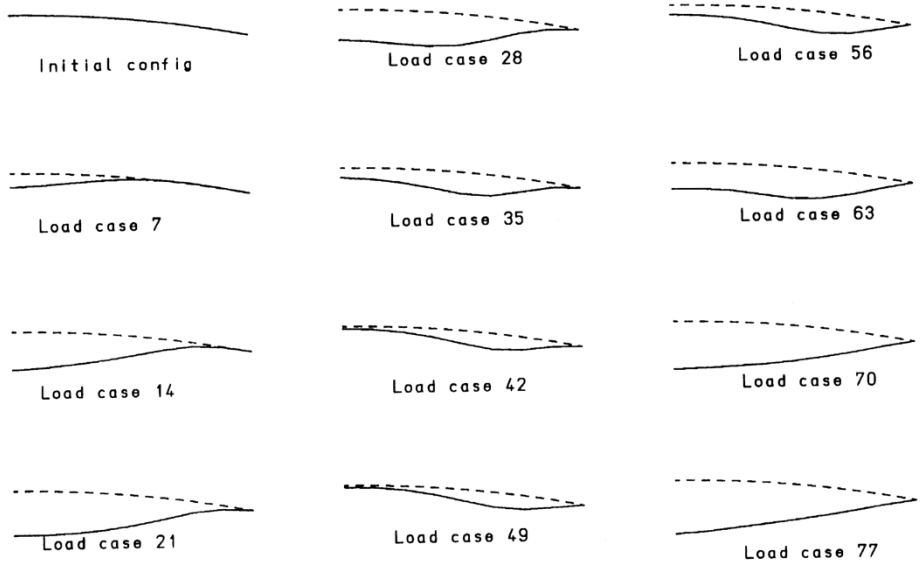


Figure 6 Deformation for yield stresses 100 200 200

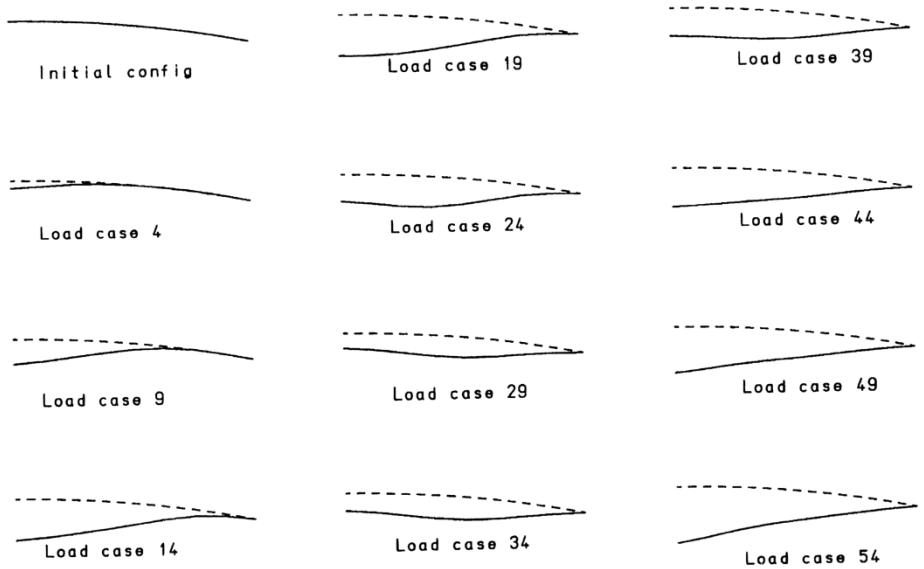


Figure 7 Deformation for yield stresses 200 200 100

Example 7.1.1

Transient Analysis With Radiation And Convection

Keywords

Radiation, Convection, Transient Analysis

Description

This problem involves an infinite slab subjected to combined radiation and convection and constitutes a two dimensional nonlinear transient analysis. The analysis involves computing temperature at the centre (T_c) and surface (T_s) of the slab as a function of time (t). This problem was chosen to demonstrate the iterative procedures available in LUSAS for solving problems involving nonlinear radiation and convection boundary conditions.

Discretisation

The analysis is performed using 20 QFD8 elements to model half the slab, figure 3.

Geometry

Infinite slab

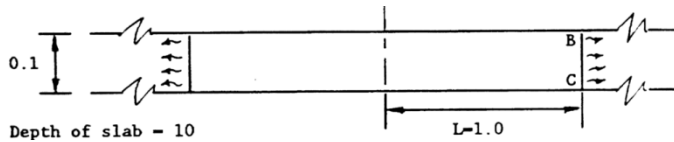


Figure 1

Material properties

Thermal conductivity $K=0.01$ Btu/ F.hr.in.

Specific heat $c=0.01$ Btu/ F.in³

Convective heat transfer coefficient $h_c =0.04$

Emissivity $\epsilon=1.0$

Stefan-Boltzmann's constant $\sigma=0.118958E-10$ Btu/in² .hr.R⁴

Boundary conditions

Initial temperature field $T_i = 1498.1505$ F

Radiation to environment at $T = 0$ F at points B and C

Convection to environment at $T = 0$ F at points B and C

Lusas results

	$t=0.04$ hr	$t=0.66$ hr	$t=3.66$ hr
T_s	681.448	191.611	1.899
T_c	1497.62	636.820	6.300

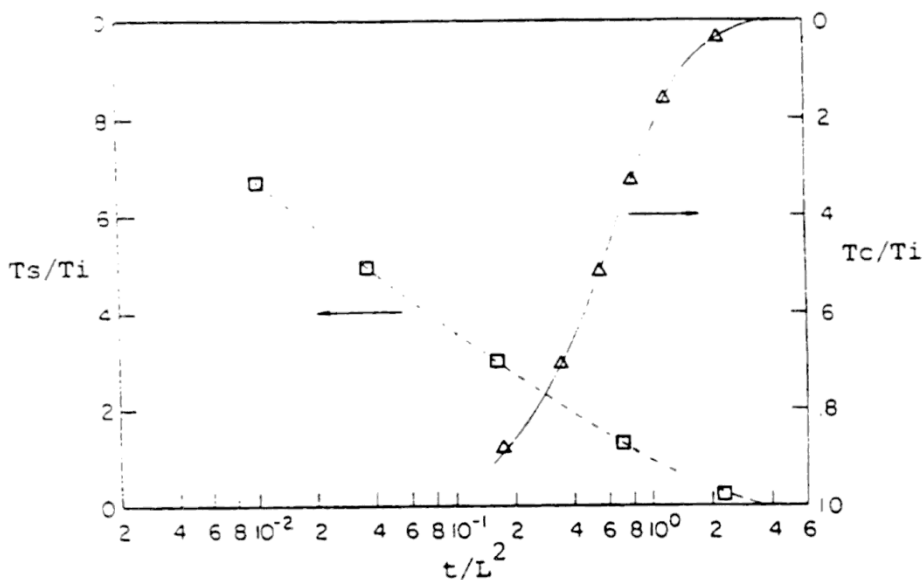


Figure 2

References

1. BATHE, K.J. KHOSHGOFTAAR, M.R. Finite Element Formulation and Solution of Nonlinear Heat Transfer J. Nuclear Engineering and Design, Vol. 51, 389-901
2. Haji-Sheikh, A. and Sparrow, E.M., The Solution of Heat Conduction Problems by Probability Methods, Trans. ASME, J. Heat Transfer, Vol. 39, pp. 121-131, 1967

Input data

X07D11A.DAT

81	82	83	84	85	86	87	88	89	90	91	92	93	94	95	96	97	98	99	100	101	102	103	104	105	106	107	108	109	110	111	112	113	114	115	116	117	118	119	120	121	122	123						
82	81	84	82	85	83	88	84	90	85	92	86	94	87	96	89	98	90	100	101	102	103	104	105	106	107	108	109	110	111	112	113	114	115	116	117	118	119	120	121	122	82							
83	83	83	83	83	83	83	83	83	83	83	83	83	83	83	83	83	83	83	83	83	83	83	83	83	83	83	83	83	83	83	83	83	83	83	83	83	83	83	83	83	83	83	83	83	83	83	83	83

Figure 3

Example 7.2.1

Transient Field Analysis Of Heat Conduction Problem

Keywords

Transient Field Analysis, Heat, Conduction

Description

Determine the temperature distribution with time along an insulated bar, initially at zero degrees C, due to a unit temperature rise at one end (see Figure 1).

Discretisation

Model the bar using eight QFD4 plane field elements (see Figure 1).

Geometry

The geometry of the bar is shown in Figure 1.

Material properties

Coefficient of thermal conductivity = 1.0 J/sec.m. C

Coefficient of specific heat = 1.0 J/m³ . C

This value is computed from the product of the specific heat and the density which are

Specific heat = 1.0 J/kg. C

Density = 1.0 kg/m³

Coefficient of convection heat transfer = 0.0 J/m² .sec. C

Boundary conditions

The left-hand end of the bar, nodes 1 and 10, are restrained to remain at unit temperature. The top, bottom and right-hand surfaces are insulated.

Theory

The exact solution for a uniform initial temperature of zero is given in [1] as

$$\phi = 1 - \sum_{k=1}^{\infty} \frac{4}{(2k-1)\pi} \exp\left\{-\left[\frac{(2k-1)\pi}{8}\right]^2 t\right\} \sin\left[\frac{(2k-1)\pi x}{8}\right] \quad (0.0.125)$$

The exponential factor decreases rapidly so that for practical purposes only the first few terms of the expansion need be considered.

Comparison

A comparison of the LUSAS results with the theoretical solution is presented in graphical form in Figure 2.

References

1. W. L. Wood and R. W. Lewis, "A Comparison of Time Marching Schemes for the Transient Heat Conduction Equations", Int. Jnl for Num. Methods in Eng., Vol 9, 1975, p679

Input Data

X07D21A.BAT

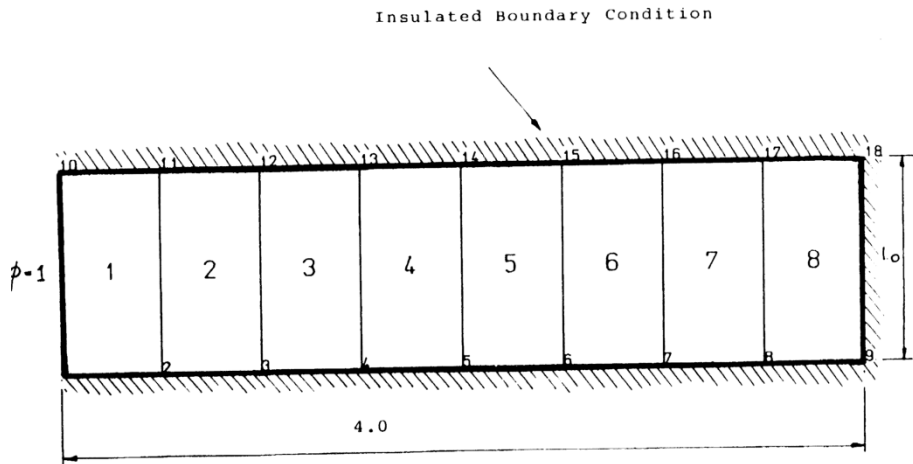


Figure 1 Finite element mesh for heat conduction problem.

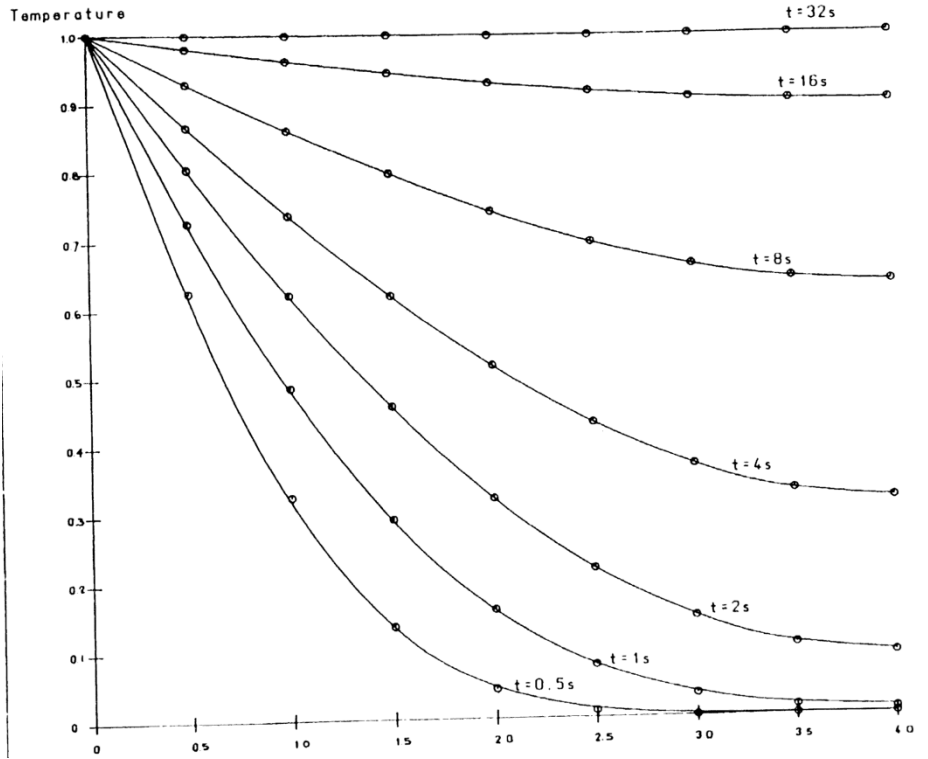


Figure 2 Temperature distribution in bar at times $t=0.5\text{s}$ to 32s

Example 7.2.2

2-D Solidification Of A Corner Region

Keywords

Transient, Nonlinear, Phase Change, Enthalpy

Description

This problem involves a transient nonlinear analysis with phase changes. A corner region, which is initially in a temperature field, has prescribed temperatures imposed along two of its boundaries. The temperatures at selected points in the region are computed as a function of time. This problem demonstrates facilities available in LUSAS for solving problems involving phase changes with the use of enthalpy averaging methods. The problem is solved for three different phase change intervals using a time step of $\Delta t = 0.05$ sec.

Discretisation

The analysis is performed using 81 QFD4 elements. The element mesh is gradually refined towards the two sides of the corner where boundary temperatures are prescribed, Figure 2.

Geometry

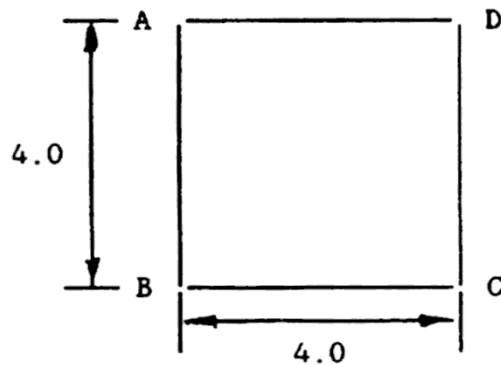


Figure 1

Material properties

$$K = 1.08; \quad \rho C = 1.0; \quad \rho L = 70.26$$

Phase change temperature = -0.15

where:

K = Thermal conductivity

ρ = Density

C = Specific heat

L = Latent heat

The analytical solution is evaluated for a pure substance i.e. it is assumed that the phase change occurs instantaneously at $T = -0.15$. With the enthalpy formulation a phase change zone must be defined. LUSAS analyses were carried out using three different phase change zones:

1. Phase Change Zone = 0.5 C

Temperature	Conductivity	Specific Heat	Change of Total Enthalpy
-45.0	1.08	1.0	0.0
-0.40	1.08	1.0	44.6
0.10	1.08	1.0	115.36
10.1	1.08	1.0	125.36

2. Phase Change Zone = 1.0 C

Temperature	Conductivity	Specific Heat	Change of Total Enthalpy
-45.0	1.08	1.0	0.0
-0.65	1.08	1.0	44.35
0.35	1.08	1.0	115.61
10.35	1.08	1.0	125.61

3. Phase Change Zone = 1.5 C

Temperature	Conductivity	Specific Heat	Change of Total Enthalpy
-45.0	1.08	1.0	0.0
-0.90	1.08	1.0	44.10
0.60	1.08	1.0	115.86
10.60	1.08	1.0	125.86

Boundary conditions

Initial Temperature field $T = 0RF$

Prescribed temperature $T = -45RF$ along AB and BC

AD and CD insulated

Theory

The transformation of a material between phases is accompanied by either liberation or absorption of latent heat in the phase transition zone, i.e. the enthalpy gradient is discontinuous. The most suitable methods for incorporation in standard finite element codes are the enthalpy or specific heat formulations (see [1]).

Reference

1. Morgan, K., Lewis, R.W., Zienkiewicz, O.C., An Improved Algorithm for Heat Conduction Problems with Phase Change, Int. J. Num. Meth. Eng., Vol.12, 1191-1195, 1978

LUSAS results

Comparison between LUSAS results and those in [1] are shown for the time variation of the point $x=1m, y=1m$ (node 45).

Input data

X07D22A.DAT

1	2	3	4	5	6	7	8	9	10
11	12	13	14	15	16	17	18	19	20
21	22	23	24	25	26	27	28	29	30
31	32	33	34	35	36	37	38	39	40
41	42	43	44	45	46	47	48	49	50
51	52	53	54	55	56	57	58	59	60
61	62	63	64	65	66	67	68	69	70
71	72	73	74	75	76	77	78	79	80
81	82	83	84	85	86	87	88	89	90
91	92	93	94	95	96	97	98	99	100

Figure 2

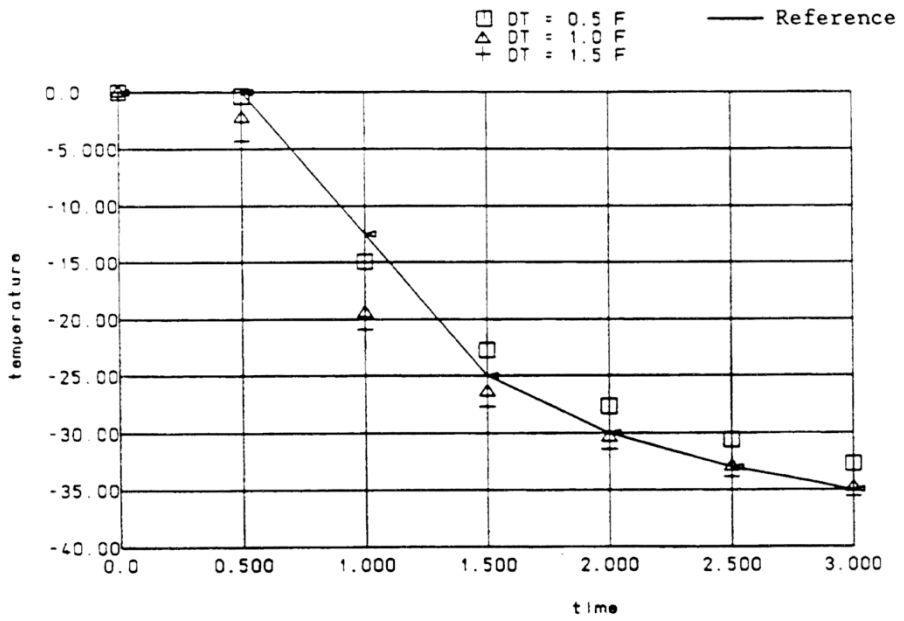


Figure 3 - Temperature at coordinates (1,1) Vs Time for phase change zones 0.5, 1.0 and 1.5

Example 7.2.3

Heat Conducting Plate With Sudden Cooling

Keywords

Transient, Heat, Conduction

Description

This example shows the LUSAS solution for heat transfer between two contacting surfaces of a structure. The problem is a nonlinear transient analysis with temperature dependant convective heat transfer coefficients. The problem is solved for $\Delta t=0.35$ hr using 20 steps.

Discretisation

Two analyses are performed using 10 QFD8 and 20 PF6 field elements respectively, figures 2 and 3.

Geometry

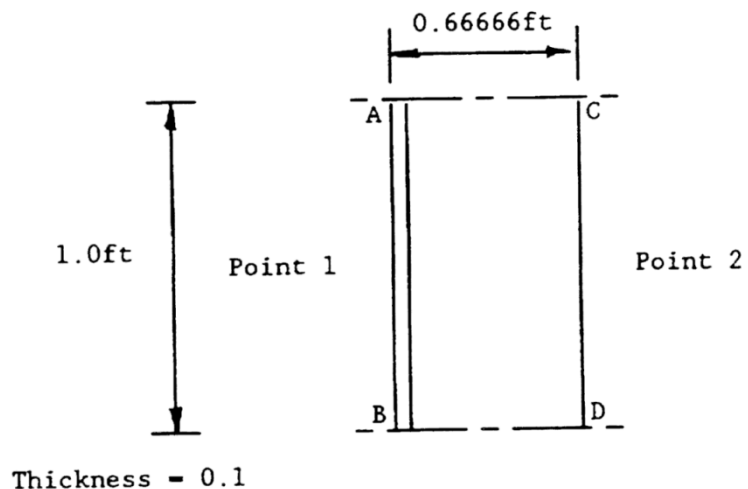


Figure 1

Note that the QFD8 element mesh forms an x-y plane between points 1 and 2, figure 2.

Material properties

Density, ρ	800 lb/ft ³
Specific heat, C	0.83333 BTU/lb F
Thermal conductivity, K	2.0 BTU/hr.ft F
Convective heat transfer coefficient, h	$0.04(T_{AB} + 100)/2 - 2.0$ BTU/hr.ft ² F

Boundary conditions

- (i) Initial temperature along the surface AB is $T=500$ F and along CD is $T=100$ F.
- (ii) Step change in environmental temperature on AB to $T=100$ F.

Reference

1. Kreith, F., Principles of heat transfer, International Textbook Co., Scranton, Pennsylvania, USA, 2nd Printing, 1959.

Lusas results

	Point 1	Point 2
Reference	285.0	100.00
QFD8	287.679	100.00
*PF6	286.243	100.00

* results for convection through triangular faces

LUSAS results for change in temperature at point 1 with respect to time are plotted in figure 4.

Input data

X07D23A.DAT

LUSAS results for temperature at point 1 Vs time.

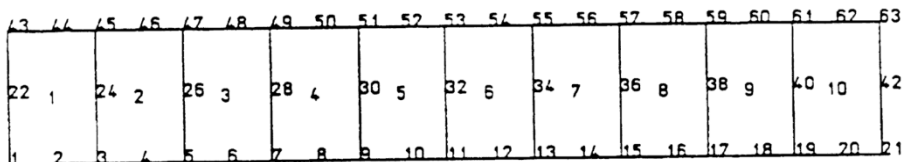


Figure 2

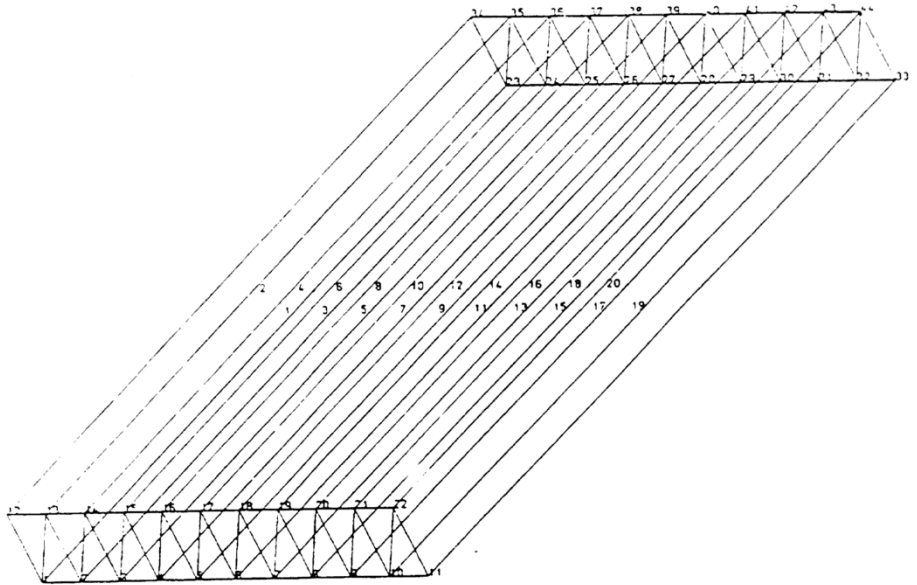


Figure 3

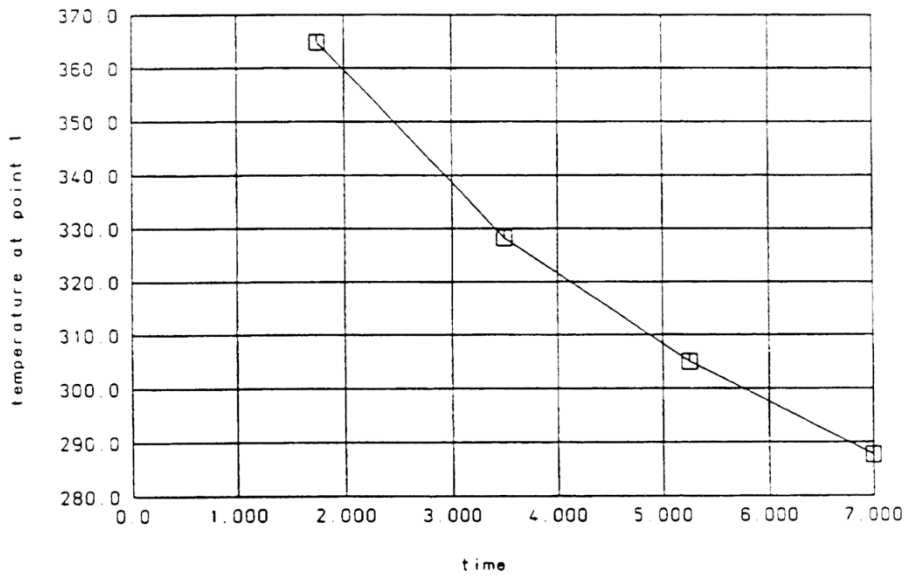


Figure 4 - LUSAS results for temperature at point 1 Vs time.

Example 8.1.1

Spectral Response Analysis Of A 2-D Frame Structure

This example has now been retired.

Example 8.1.2

Linear Dynamic Analysis Of A Spring/Mass/ Damping System

Keywords

Linear Dynamics, Damping

Problem Description

Determine the damped natural period (Td) and the ratio (R) between any two successive amplitudes of a freely vibrating spring/mass/damping system. The mass is initially displaced and subsequently allowed to vibrate freely.

Discretisation

The spring/mass/damping system is modelled using a single joint (JNT3) element. The material properties are as follows:

$$K_1 = 30 \text{ lb/in} \quad M_1 = 0.0259 \text{ lb sec}^2/\text{in} \quad C_1 = 0.12 \text{ lb sec}^2/\text{in}$$

The system is fully restrained at node 1 and restrained in the Y direction at node 2, resulting in a single degree of freedom problem. An initial load of 30 lb is applied to the structure.

Theory

The undamped natural frequency of the system in radians per second is

$$w_n = \sqrt{\frac{K}{M}} \quad (0.0.126)$$

$$\text{so that } w_n = \sqrt{\frac{30}{0.0259}} = 34.033 \text{ rads / sec} \quad (0.0.127)$$

The critical damping coefficient and damping factor are

$$c_c = 2 M w_n = 1.7629 \text{ lb / in / sec} \quad (0.0.128)$$

$$T = \frac{c}{c_c} = \frac{0.12}{1.7629} = 0.06807 \quad (0.0.129)$$

The logarithmic decrement is

$$d = \frac{2T}{\sqrt{1-T^2}} = 0.4286 \quad (0.0.130)$$

The amplitude ratio for any two consecutive cycles is

$$\frac{x_1}{x_2} = e^d = 1.535 \quad (0.0.131)$$

The damped period is

$$T_d = \frac{d}{T_{W_n}} = 0.185 \text{secs} \quad (0.0.132)$$

Comparison

The LUSAS results are compared to the theoretical solution.

Peak	1	2	3	4
Maximum amplitude (in)	1.000	0.650	0.423	0.275
Time (secs)	0.000	0.186	0.372	0.558

Ratio	R(1-2)	R(2-3)	R(3-4)
Theory	1.535	1.535	1.535
LUSAS	1.538	1.538	1.538
Difference (percent)	0.195	0.195	0.195

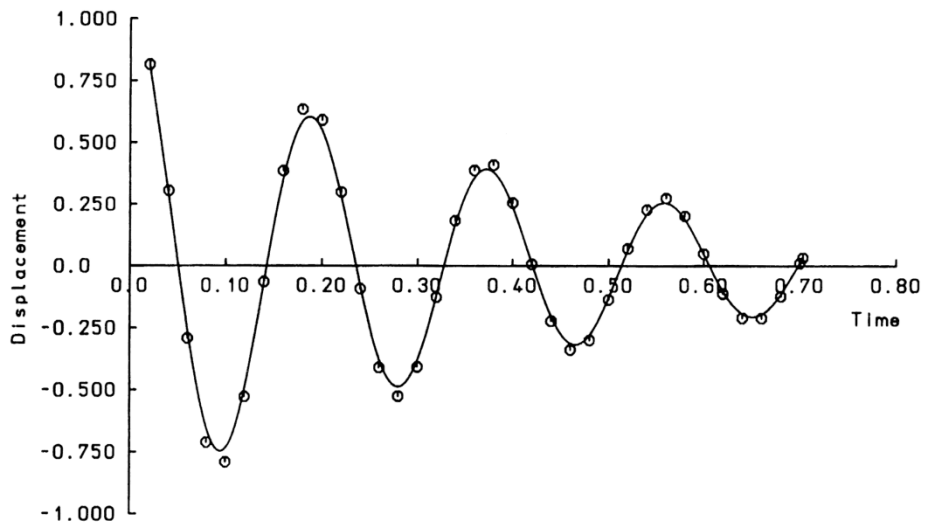
Damped natural Period	Td(1-2)	Td(2-3)	Td(3-4)
Theory	0.185	0.185	0.185
LUSAS	0.186	0.186	0.186
Difference (percent)	0.54	0.54	0.54

References

1. Thomson, W.T. 'Theory of vibration with applications', 2nd Edition, George Allen of Unwin.

Input data

X08D12A.DAT



Time v Displacement for damped spring mass system

Example 8.1.3

Beam Subject To A Harmonic, Periodic And Step Load

Keyword

Linear Elastic, Periodic, Harmonic

Description

The response of a deep, simply supported beam to a harmonic, periodic and direct uniformly distributed load is presented in this example. The objectives are to establish the displacement and stress amplitudes at the midpoint of the beam. An initial eigenvalue analysis of the system is also performed.

Discretisation

The beam is modelled using 10 equal, two noded beam elements (BMS3). Boundary conditions are applied in the global X,Y,Z and jx directions at one of the beam extremities. The other extremity has Y and Z supports only.

Geometry

Consider a beam (see figure 1) of length 10m, square cross-section (b) of 2m and aligned with the global X-axis, for which the following sectional values are used:

$$I_{yy} = I_{zz} = (b^4)/12$$

$$K_t = 0.1406(b^4)$$

$$A_{sy} = A_{sz} = gA$$

where:

$$g = (10+10\nu)/(12+11 \nu) \quad (\nu \text{ is Poisson's ratio})$$

Material properties

Young's modulus	200x10 ⁹ N/m ²
Poisson's ratio	0.3
Density	8000 Kg/m ³

Loading

The forcing function for the steady state harmonic loading is:

$$F = 1E6 \sin(Wt) \quad \text{Nm}^{-1}$$

where:

$$\Omega = 2\pi f \quad (0 < f < 70 \text{ Hz})$$

Viscous damping of 0.02 is used with no structural damping. The first 16 modes are used to form the modal domain. This test is repeated with distributed viscous damping of approximately 0.02 for mode 8 and viscous damping of 0.02 for all other modes and no structural damping.

2. The forcing function for the steady state periodic loading is:

$$F = 1E6 (\sin(\Omega t) - \sin(3\Omega t)) \quad \text{Nm}^{-1}$$

where:

$$\Omega = 2\pi f$$

Rayleigh damping is used with: $\alpha = 5.36$, and $\beta = 7.46E-5$

3. The forcing function for the direct loading is:

$$F = 1E6 \quad \text{Nm}^{-1}$$

Rayleigh damping is used with: $a = 5.36$, and $b = 7.46E-5$

LUSAS results

Eigenvalue Analysis

Figure 2 shows vibration modes 1, 6 and 9, whilst the table below gives the values obtained using Lusas:

Mode	Frequency	
	Lusas	Reference*
1	42.5363	42.65
2	42.5363	42.65
3	71.2751	71.20
4	125.129	125.0
5	144.220	148.15
6	144.220	148.15
7	215.587	213.61
8	260.624	283.47
9	260.624	283.47

* : A closed form solution

Harmonic Loading Response

Figure 3 shows the response of the beam in the frequency domain, whilst the table below compares the values obtained at the beam midpoint for both the peak displacement and the peak stress.

	Lusas	Target*	Reference#
Frequency (Hz)	42.54	42.60	42.65
Peak displacement at beam midpoint	12.48	13.44	13.45
Peak stress at beam midpoint (Pa)	243.8E8	240.3E6	241.9E6

: Closed form analytical solution

* : Value for engineer's beam (ignoring shear and rotary inertia)

Periodic Loading Response

Figure 4 shows the response of the beam in the time domain as the transient components die out, whilst the table below compares the values obtained at the beam midpoint for both the peak displacement and the peak stress.

	Lusas	Target*	Reference#
Peak displacement (mm)	0.944	0.953	0.951
Peak stress (Pa)	17.19E6	17.33E6	17.1E6

: Closed form analytical solution

* : Value for engineer's beam (ignoring shear and rotary inertia)

Direct Loading response

Figure 4 shows the response of the beam in the time domain, whilst the table below compares the values obtained at the beam midpoint for both the peak displacement and the peak stress. Note that the peak occurs at $t=0.0117$ for both the Lusas and reference solutions.

	Lusas	Target*	Reference#
Peak displacement (mm)	1.044	1.057	1.043
Peak stress (Pa)	18.64E6	18.77E6	18.76E6
Time (s)	0.0117	0.0117	0.0117

: Closed form analytical solution

* : Average of two codes:-

(i) Value for engineer's beam (ignoring shear and rotary inertia)

(ii) Timoshenko beam (with shear and rotary inertia)

Reference

1. NAFEMS Report Number E1261/R002

Input Data

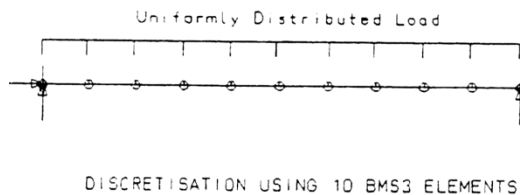
X08D13A.DAT

X08D13B.DAT

X08D13C.DAT

X08D13D.DAT

X08D13E.DAT



STEADY STATE HARMONIC

$F = F_0 \sin \omega t$
 $F_0 = 1E6 \text{ N/m}$
 $\omega = 0 \text{ to } 60 \text{ Hz}$
 Damping 2% (every mode)

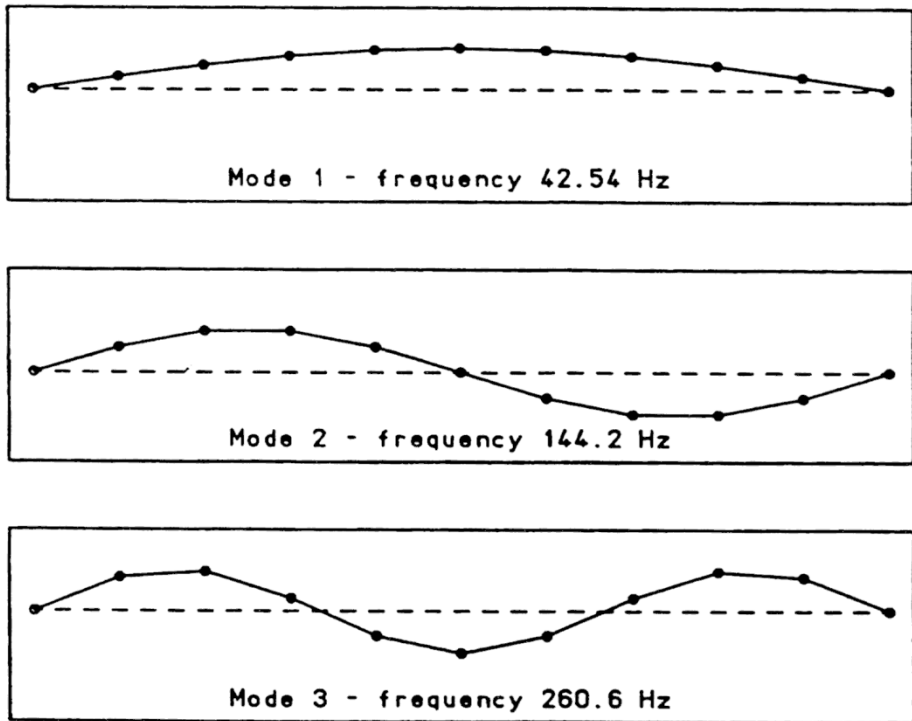
PERIODIC LOADING

$F = F_0(\sin \omega t - \sin 3\omega t)$
 $F_0 = 1E6 \text{ N/m}$
 $\omega t = 20 \text{ Hz}$
 Damping
 $A_r = 5.36 \text{ Br} = 7.46E-5$

TRANSIENT STEP LOADING

$F_0 = 1E6 \text{ N/m}$
 Damping
 $A_r = 5.36 \text{ Br} = 7.46E-5$

Figure 1



FLEXURAL MODE SHAPES AND FREQUENCIES

Figure 2

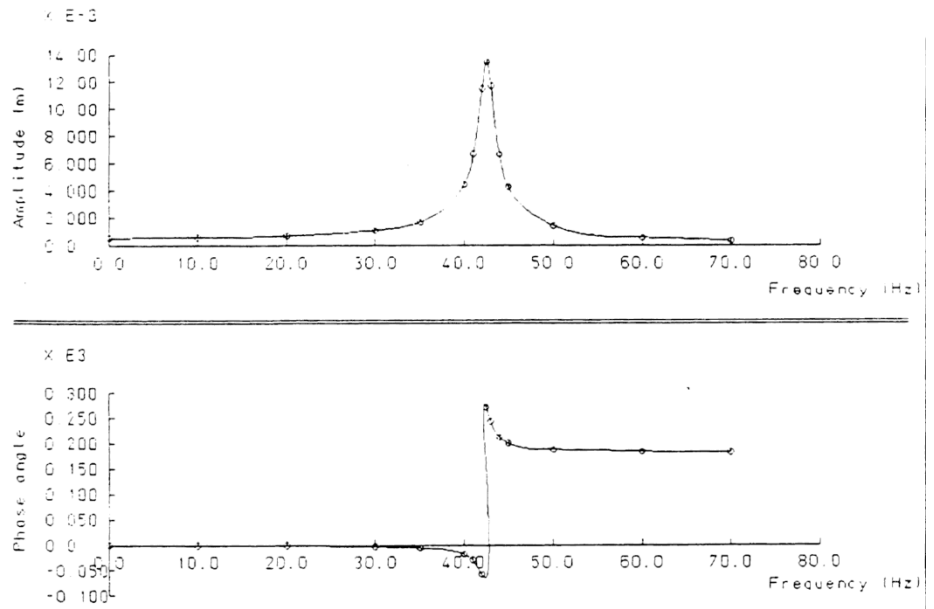


Figure 3

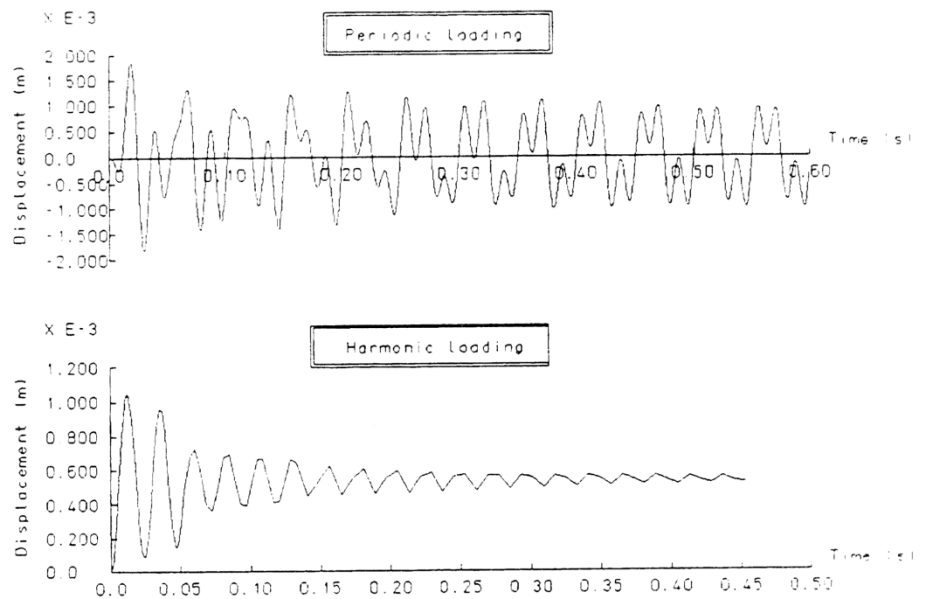


Figure 4

Example 8.1.4

Large Deformation Dynamics of Stiff and Elastic Pendulum

Keyword

Large Deformation, Step-By-Step Dynamics

Description

The rotation of a pendulum is simulated by the generalized α -method together with a co-rotational formulation for large deformation. The pendulum can be stiff, undergoing approximate rigid-body rotation, or flexible, undergoing coupled rotation and axial vibration with medium strains.

Stiff pendulum

The geometry and material properties, boundary and initial conditions of the pendulum presented in Kuhl and Crisfield [2] and adopted by Bathe [1] are given in Figure 1. The pendulum is powered by the initial tangential velocity $\dot{u}_0 = 7.72\text{m/s}$. In order to obtain an equilibrium state at the initial time $t_0 = 0$ the initial radial acceleration is calculated to $\ddot{u}_0 = 19.6\text{m/s}^2$.

Elastic pendulum

Following Kuhl and Crisfield [2] and Bathe [1], the stiffness of the truss element is reduced from $EA_0 = 10^{10}\text{ N}$ to $EA_0 = 10^4\text{ N}$, hence the element is now flexible and shows an axial vibration. Also, we now use the initial radial acceleration $\ddot{u}_0 = 0.0\text{ m/s}^2$.

Discretisation

The pendulum is modelled by one two-node bar or truss BAR2 or BRS2 element with a consistent mass matrix. The time step $\Delta t = 0.01\text{ s}$.

Theory

Stiff pendulum

As a result of the large stiffness EA_0 the motion of the truss is (approximately) a rigid-body rotation with the angular velocity $\dot{\phi} = 0.4036\text{ 1/s}$ (Figure 1). The analytical rotational period is 2.4777 s [1].

Elastic pendulum

The period of axial vibration is 0.28 s [1].

Comparison

Stiff pendulum

Kuhl and Crisfield [2] already report that the trapezoidal rule is unstable; the generalized α -method can be used to solve the problem with integration constant $\alpha = -0.4/1.6$. The obtained time history of displacement, velocity and acceleration shown in Figure 2 agree with the theoretical solution, and are very close to the results given by Bathe [1].

Elastic pendulum

The time step employed corresponds to 28 steps per cycle of the axial vibration, which is a reasonable time step size to capture this vibration. The obtained time history of displacement, velocity, acceleration and strain from BAR2 and BRS2 are the same (Figure 3), and close to the results given by Bathe [1]. The pendulum undergoes medium strains, which reach its maximum 2.56% at $t = 0.14$ s.

References

1. Bathe, K. J. ‘Conserving energy and momentum in nonlinear dynamics: A simple implicit time integration scheme’. *Comput. Struct.* **85**: 437–445 (2007).
2. Kuhl, D., Crisfield, M. A. ‘Energy-conserving and Decaying Algorithms in Non-linear Structural Dynamics’. *Int. J. Numer. Meth. Engng.* **45**: 569-599 (1999).

Input data

x08d14a

x08d14b

x08d14c

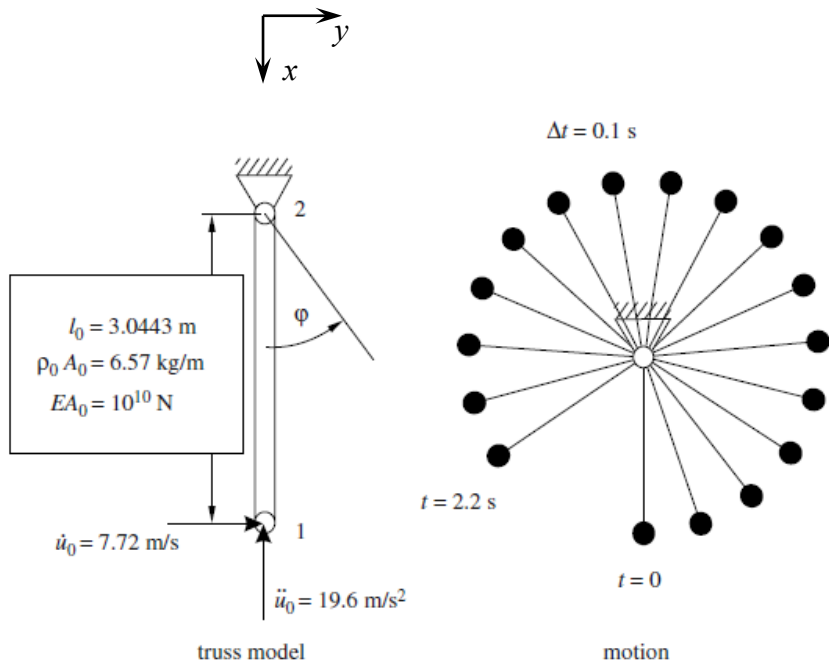
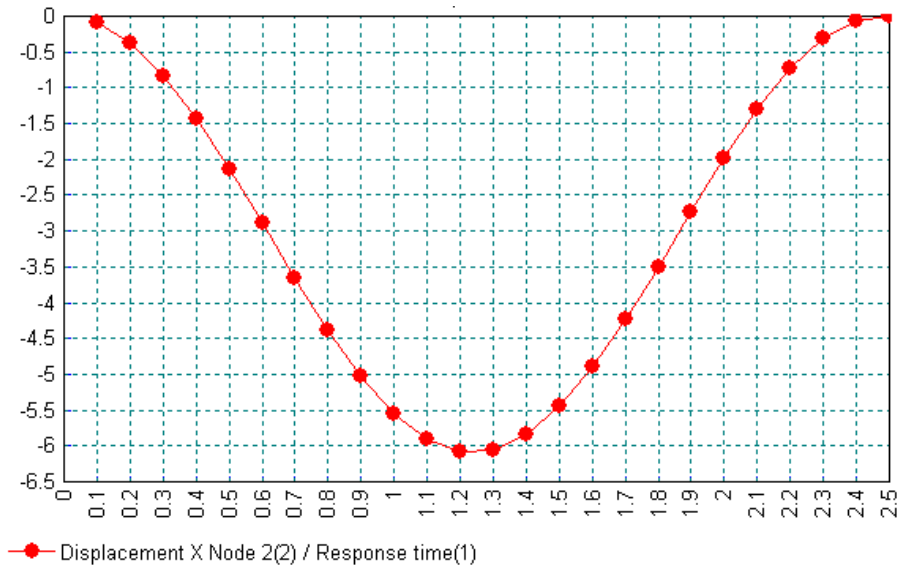
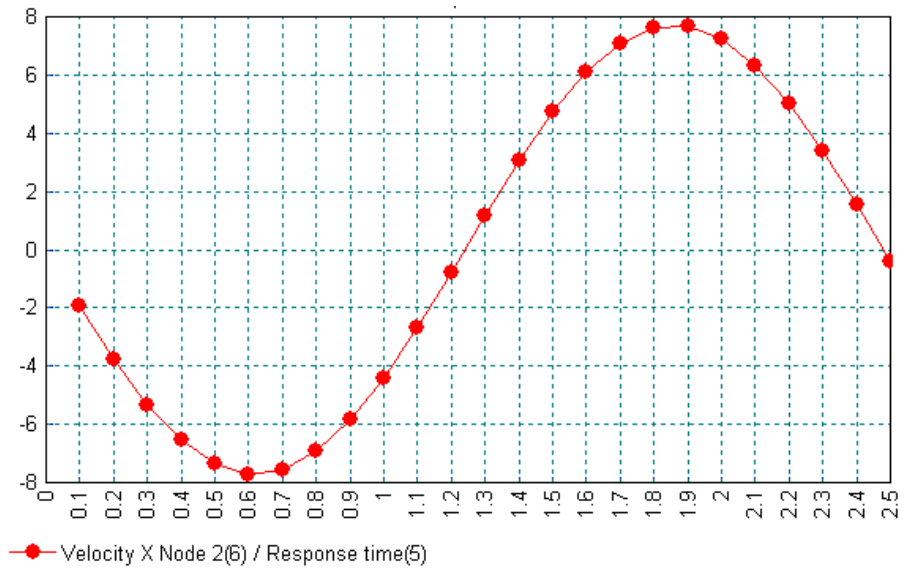
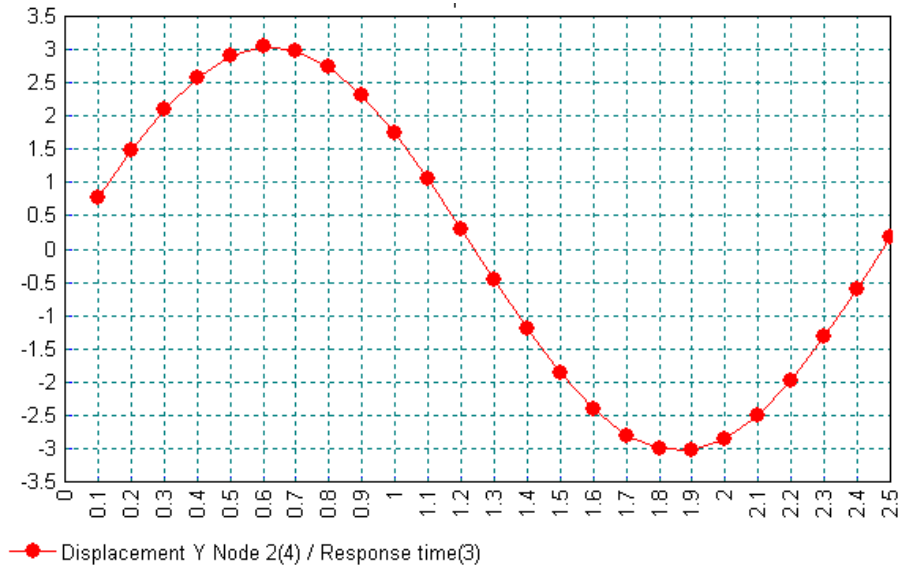
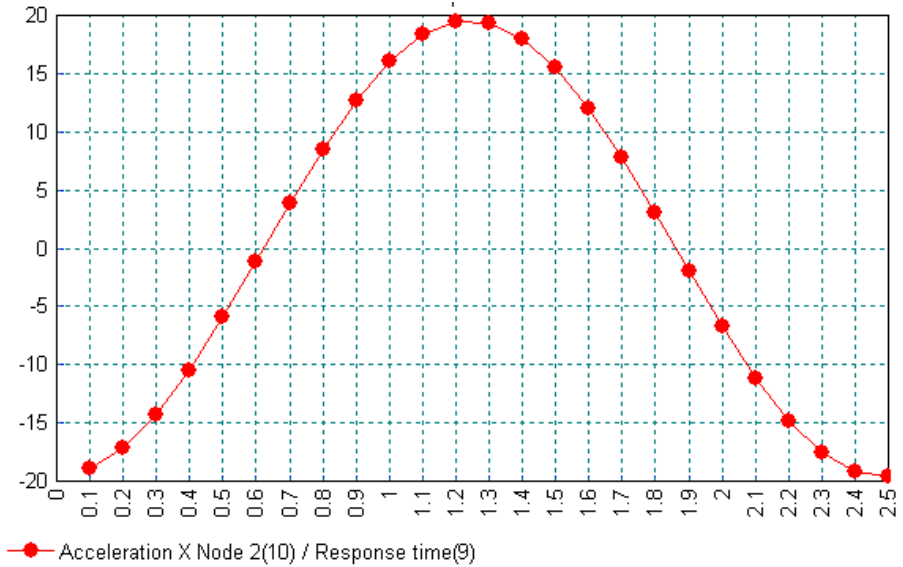
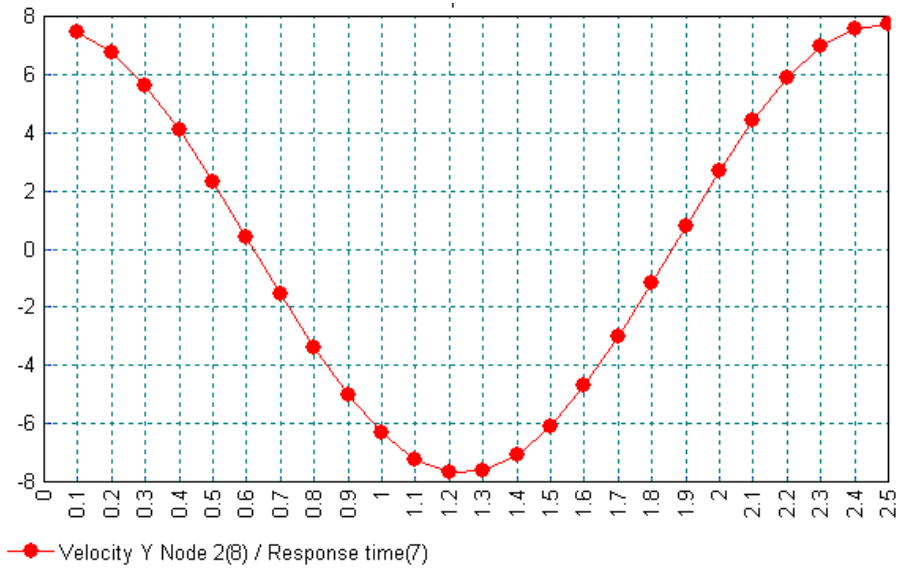


Figure 1. Simple pendulum with boundary and initial conditions.







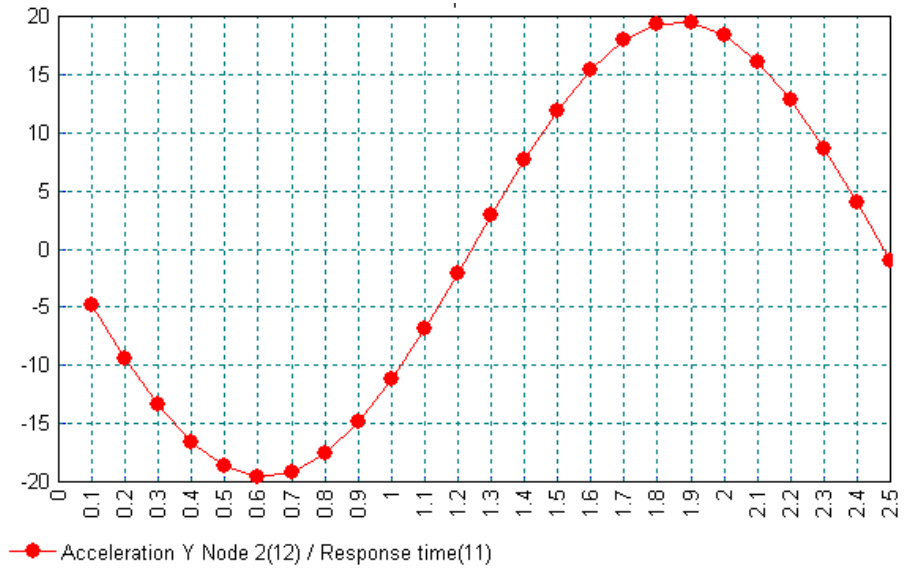
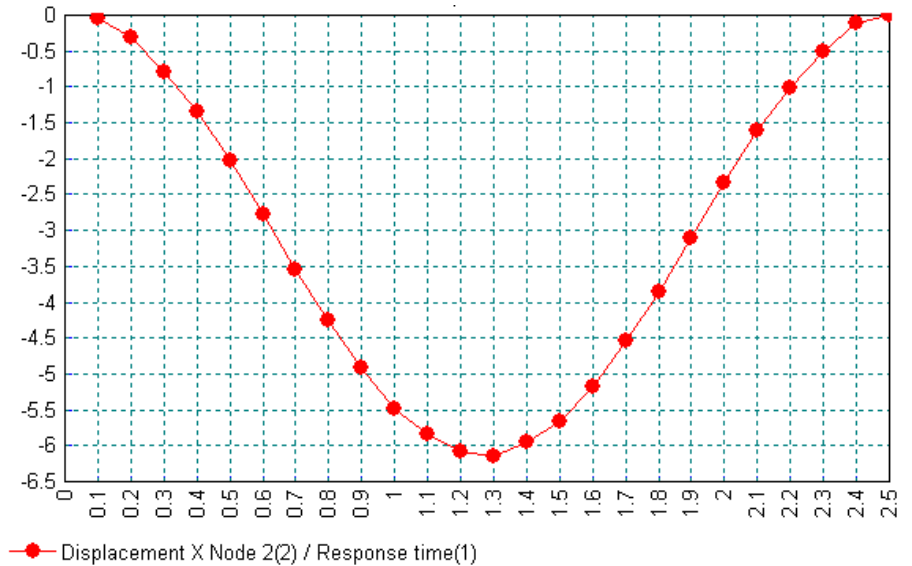
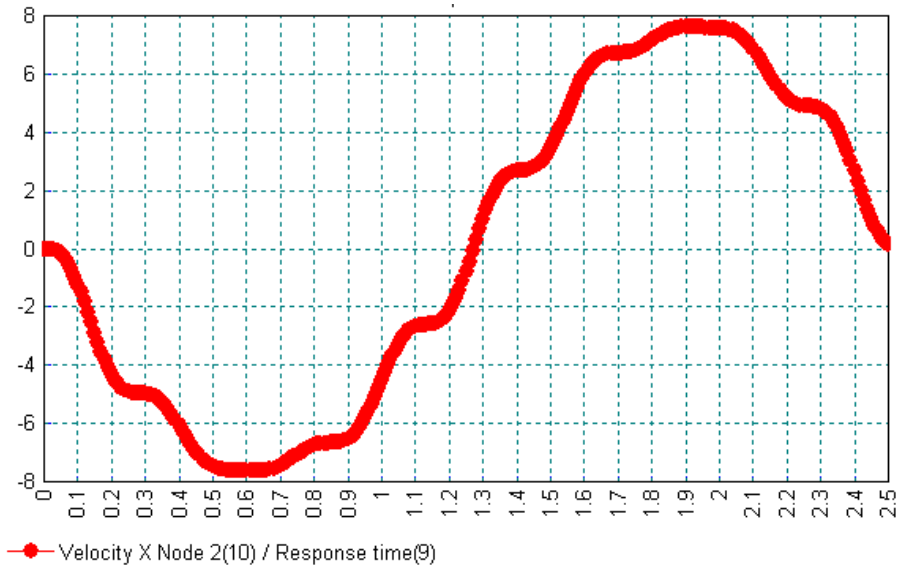
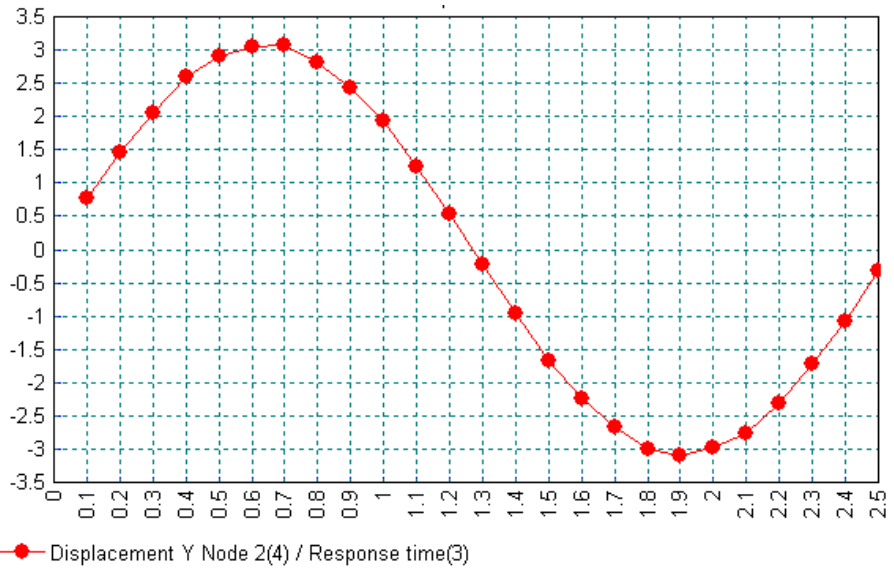
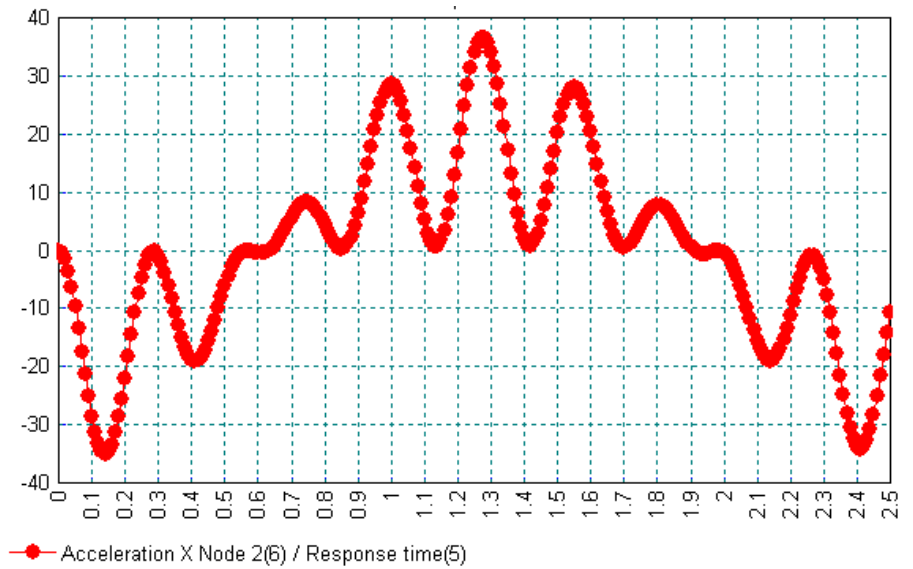
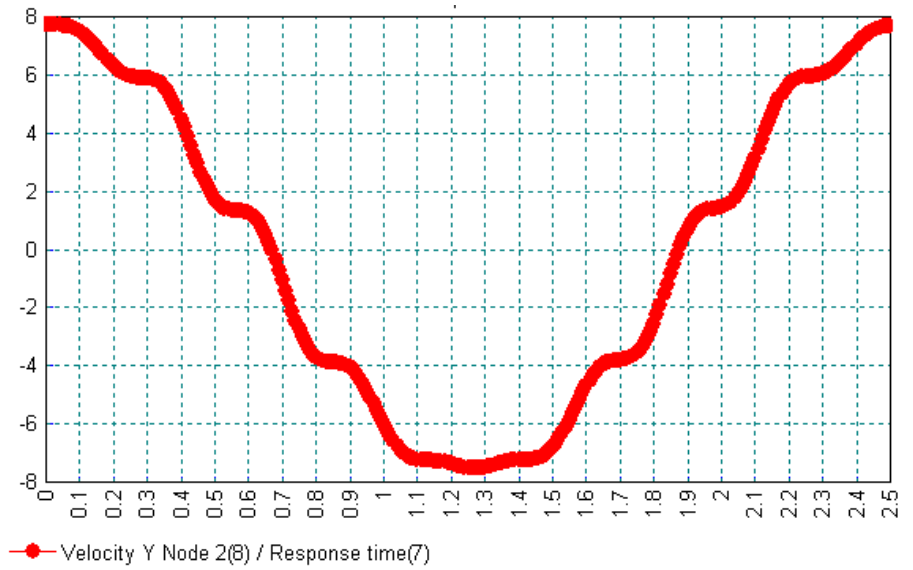


Figure 2. Variation of displacement, velocity and acceleration of the stiff pendulum in 1st cycle.







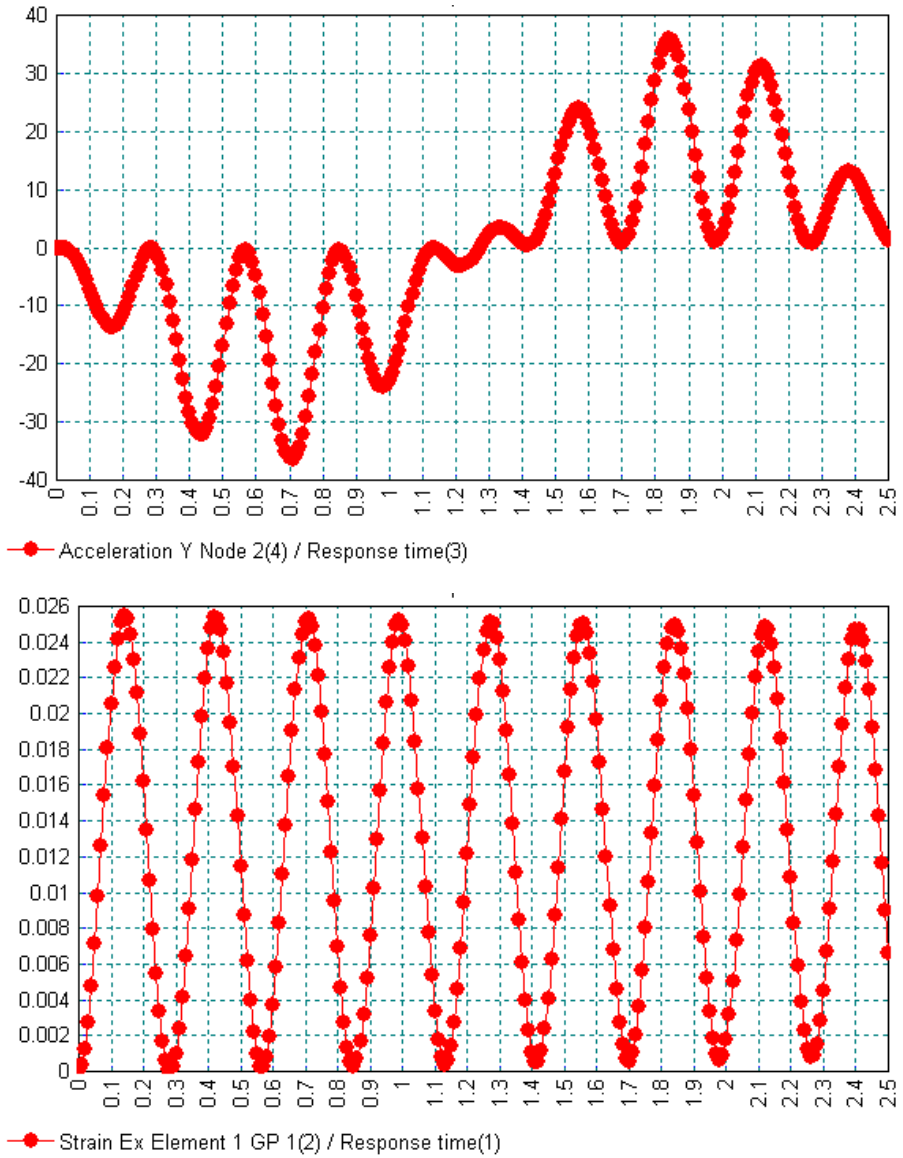


Figure 3. Variation of displacement, velocity, acceleration and strain of the elastic pendulum in 1st cycle.

Example 8.1.5

Free-Free Nearly Rigid Beam Undergoing Large Overall Motion

Keywords

Large Deformation, Step-By-Step Dynamics

Description

The free flight of a beam, which is affected by very small strains so that the motion is similar to a rigid body motion, is simulated by the generalized α -method together with a co-rotational formulation for large deformation. The geometry, initial conditions and material properties, given in Figure 1, are the same as Crisfield et al. [1]. The principle axes of inertia of the cross-section are initially aligned with global coordinate axes X and Z .

Discretisation

The beam is divided into 4 linear BMI21 or quadratic BMI31 elements with a consistent mass matrix. The initial time step size is $\Delta t = 0.2$ s.

Comparison

The integration constant $\alpha = 0$ is adopted by the generalized α -method. The displacements of the lower end B in the first revolution are given in Figure 2. BMI21 and BMI31 elements give results identical to the BMS3R element of Crisfield et al. [1].

References

1. Crisfield, M. A., Galvanetto, U. and Jelenić, G., ‘Dynamics of 3-D co-rotational beams’. *Comput Mech* **20**: 507-519 (1997).

Input data

x08d15a

x08d15b

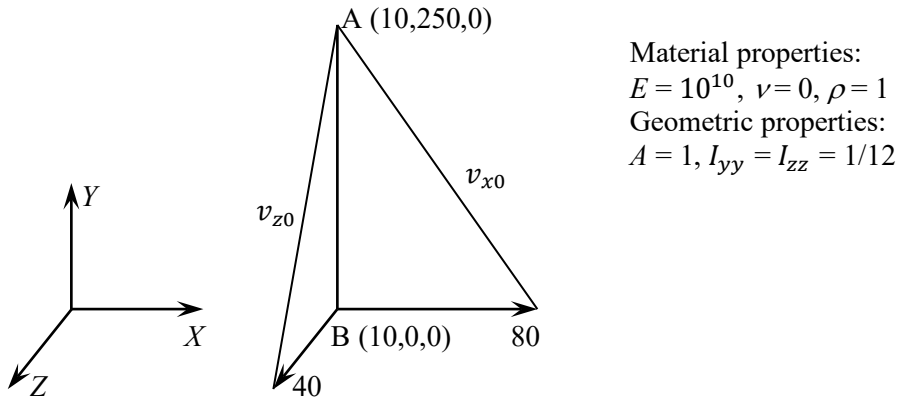
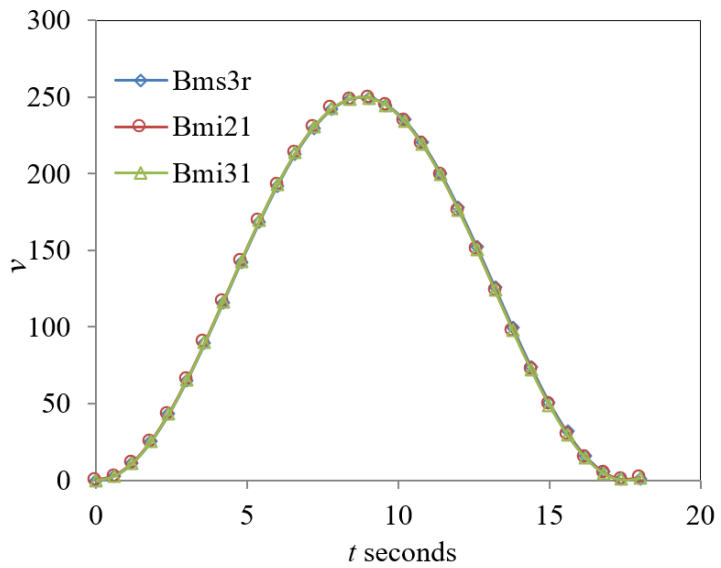
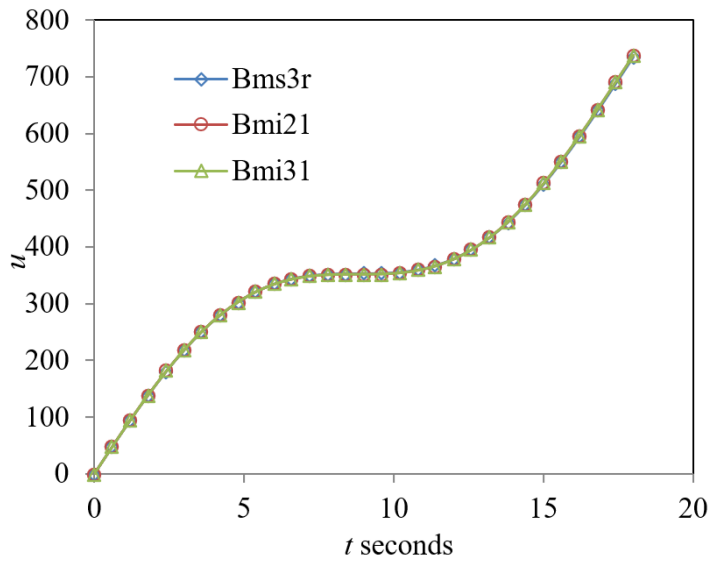


Figure 1. Free flight beam.



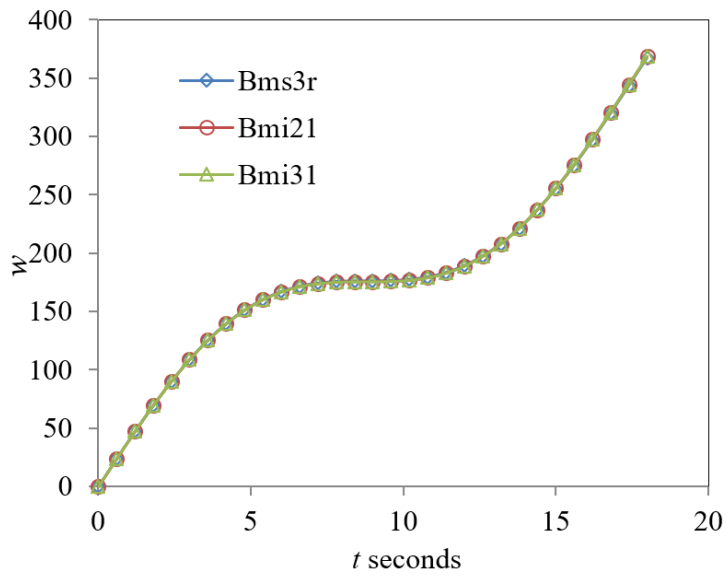


Figure 2. Time history of the displacements at the lower end B.

Example 8.1.6

Static And Dynamic Responses Of Prestressed Cable Under Uniform Loading

Keywords

Bar, Cable, Dynamics, Large Deformation

Description

Determine the static and dynamic responses of an initially stressed cable subjected to uniform transverse load as shown in Figure 1. The horizontal line joining the supports is used as the starting geometry.

Discretisation

In the static analysis, the cable is discretised into two equal length CTNS2 catenary cable elements, or 40 BRS2 bar elements, or 20 BRS3 curved bar elements; in the dynamic analysis, the cable is discretised into 40 equal length CTNS2 catenary cable elements, or 40 BRS2 bar elements, or 20 BRS3 curved bar elements.

Geometry

See Figure 1.

Material properties

See Figure 1.

Loading

For static analysis, initial stress $\sigma_0 = 20 \times 10^3 \text{ lb/in}^2$ (unstressed length = 9990.00999 in, Figure 1), maximum uniform load = 0.18 lb/in.

For dynamic analysis, initial stress $\sigma_0 = 20 \times 10^3 \text{ lb/in}^2$ (unstressed length = 9990.00999 in) and $\sigma_0 = 160 \times 10^3 \text{ lb/in}^2$ (unstressed length = 9920.6349206 in) are considered; a uniform load of 0.2 lb/in is suddenly applied to the static equilibrium configuration obtained for a dead load of 0.02 lb/in.

Boundary conditions

Fixed at both ends (Figure 1).

Theory

For the static case, Jayaraman and Knudson [1] had presented exact vertical displacements at the centre of the span with the use of 2 catenary elements (1 element/half span), which are given in Table 1.

For the dynamic problem, Jayaraman and Knudson [1] had obtained the response curve using 20 catenary elements per half span (Figure 2); they used lumped mass matrices. They also gave the first peak displacements for the two different prestress values (Table 2).

Comparison

The vertical displacements at the centre under static loading obtained by LUSAS are given in Table 1 and compared well with Jayaraman and Knudson [1].

The dynamic responses predicted by LUSAS are plotted in Figure 2 and agree well with those of Jayaraman and Knudson [1]. The displacements at the first peak are given in Table 2 and compare reasonably well with Jayaraman and Knudson [1]. The minor difference with Jayaraman and Knudson [1] seems because they used a slightly less accurate unstressed length, e.g. $L = 9990.0099$ in for $\sigma_0 = 20 \times 10^3$ lb/in². For the displacements at the first peak, we may not pick the exact values as we output the results every 20 steps.

Table1: Vertical displacement at midspan (in)

Load parameter	Jayaraman and Knudson [1]	LUSAS		
		CTN2/CTNS2	BAR2/BRS2	BAR3/BRS3
1 ($w_D = 0.02$ lb/in)	-131.63	-131.492	-131.533	-131.474
3	-234.19	-234.204	-234.308	-234.065
5	-292.79	-292.786	-292.924	-292.495
7	-336.03	-336.041	-336.206	-335.588
9	-371.13	-371.137	-371.322	-370.516

Table 2: First peak displacement at center (in)

Prestress (psi)	Jayaraman and Knudson [1]	LUSAS		
		CTN2/CTNS2	BAR2/BRS2	BAR3/BRS3
20×10^3	-633.10	633.121	631.108	629.488
160×10^3	-398.79	397.011	399.739	398.981

References

1. Jayaraman, H.B., Knudson, W.C. (1981) A curved element for the analysis of cable structures. Computers and Structures 14: 325-333.

Input data

X08D16A.DAT

X08D16B.DAT

X08D16C.DAT

X08D16D.DAT

X08D16E.DAT

X08D16F.DAT

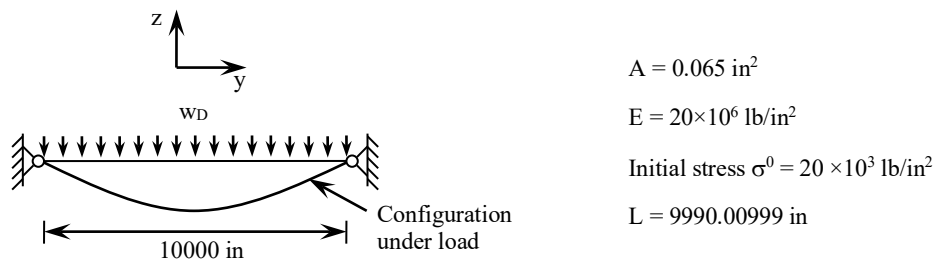


Figure 1: Prestressed cable under dead load.

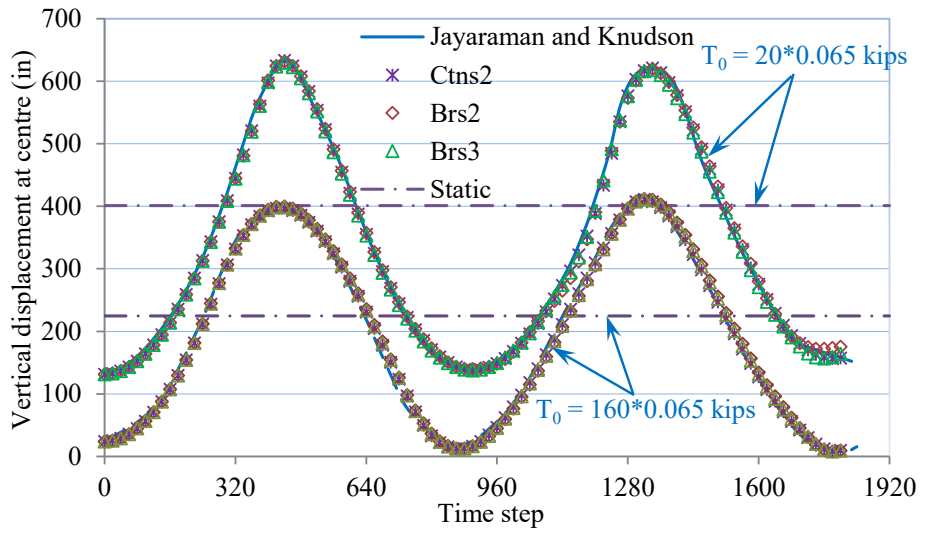


Figure 2: Dynamic response of catenary cable under uniformly distributed suddenly applied load.

Example 8.2.1

Linear Dynamic Analysis Of A Beam With Pressure Loading

Keywords

Step-By-Step Dynamics

Description

Determine the dynamic response of a cantilevered beam subject to a suddenly applied uniformly distributed load (see Figure 1).

Discretisation

Model the two-dimensional cantilevered structure using 8 QPM8 plane membrane elements (see Figure 1).

Geometry

The cantilevered structure has unit depth and breadth and is ten inches in length (see Figure 1).

Material properties

Young's modulus	12000 lb/in ²
Poisson's ratio	0.3
Density	10x10 ⁻⁶ lb.sec ² /in ²

Boundary conditions

The structure is fully restrained at nodes 1,18 and 35 forming a cantilevered condition. The pressure load is applied according to the load/time history graph in Figure 2. To allow for a zero initial displacement condition the structure is fully restrained at every node for the first load case and then freed accordingly for subsequent loads.

LUSAS Results

From the results of an eigenvalue extraction of this structure the following parameters were determined:

$$\text{Fundamental eigenvalue} = 0.1235E6 \text{ 1/sec}^2$$

Natural frequency = 55.93 Hz

Period of response, T = 0.01788 sec

Increment of time for step-by-step, T/30 = 0.0006 sec

The time-displacement response curve derived from the dynamic analysis results is shown in figure 3.

References

1. K.-J. BATHE, E. RAMM and E. L. WILSON, "Finite Element Formulations for Large Deformation Dynamic Analysis", Int. Jnl. Num. Mthd. Eng., VOL 9, pp 353-386, 1975.

Input Data

X08D21A.DAT

X08D21B.DAT

1.425 lb/in applied to the top and bottom faces

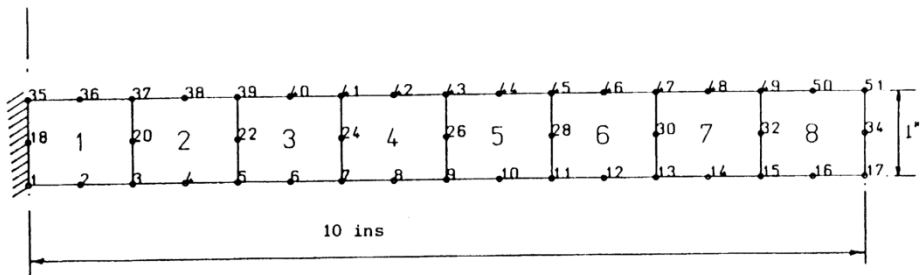


Figure 1 Linear dynamic analysis of cantilevered beam.

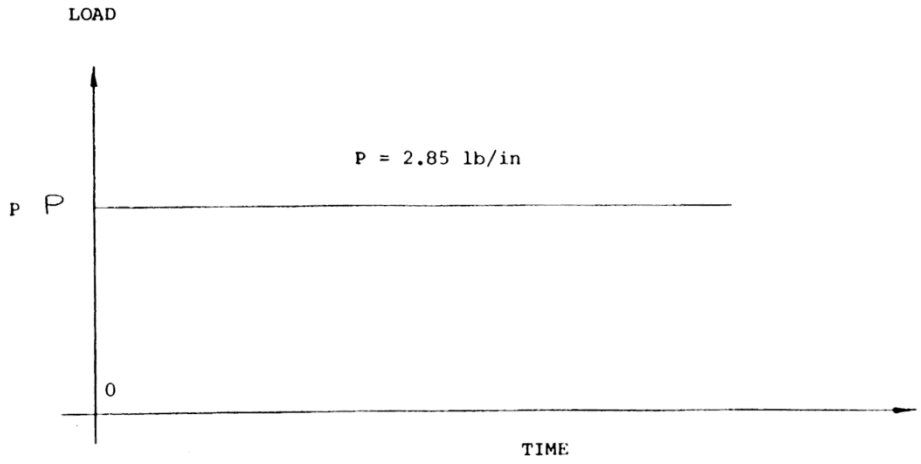


Figure 2 Load/time history graph for cantilevered beam.

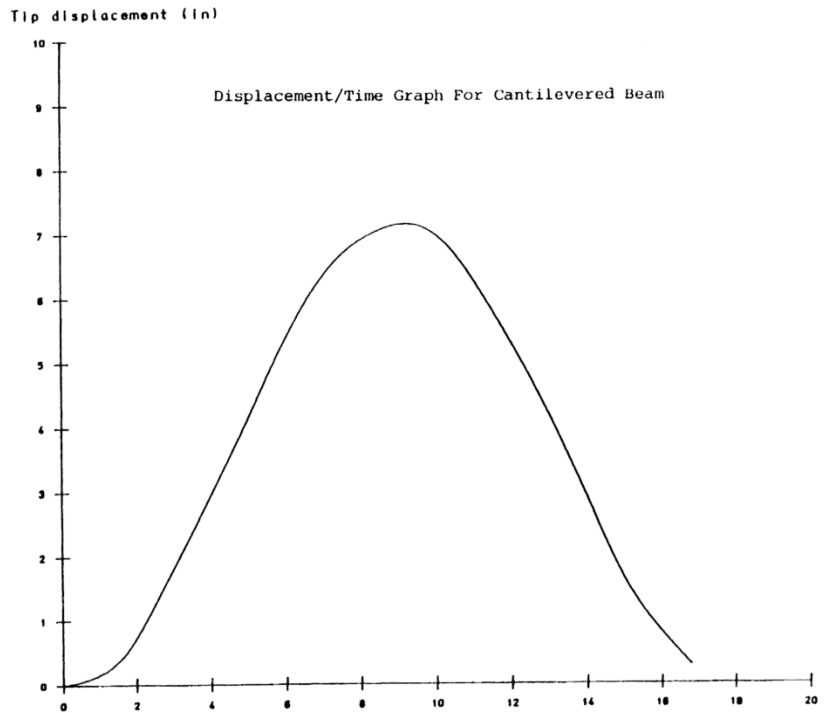


Figure 3 Displacement time graph for cantilevered beam.

Example 8.6.1

Nonlinear Dynamic Analysis Of A Clamped Spherical Shell

Keywords

Nonlinear Dynamics, Elasto-Plastic, Natural Frequency, Spherical Shell

Description

Determine the natural frequency and dynamic behaviour of a clamped spherical cap subject to a uniform lateral pressure over its outer surface. The shell geometry is in the form of a truncated sphere with a radius of 22.27 inches. The truncated spherical cap subtends a semi angle of 26.67 degrees at the centre of the sphere, and has a thickness of 0.41 inches. The shell is fully clamped around its periphery, and is subject to a uniform external pressure. The geometry and loading of the shell are shown in figure 1.

The finite element analysis is performed in four stages:

- Stage 1 Eigenvalue extraction for natural frequency analysis
- Stage 2 Linear elastic step-by-step dynamic stress analysis
- Stage 3 Elasto-plastic step-by-step dynamic stress analysis
- Stage 4 Geometrically nonlinear elasto-plastic step-by-step dynamic stress analysis

Discretisation

The shell structure is modelled using five curved axisymmetric shell elements (BXS3). The shell is assumed to be fully clamped at its supported base. The material properties used in the above analyses are as follows:

- i) Eigenvalue extraction, and linear analysis

$$\text{Young's modulus} = 10.5E6 \text{ lb/in}^2$$

$$\text{Poisson's ratio} = 0.3$$

$$\text{Mass density} = 2.45E-4 \text{ lbsec}^2/\text{in}^4$$

- ii) Elasto-plastic analyses: Von-Mises elasto-plastic model

$$\text{Young's modulus} = 10.5E6 \text{ lb/in}^2$$

$$\text{Poisson's ratio} = 0.3$$

Mass density	= 2.45E-4 lbsec ² /in ⁴
Yield stress	= 0.024E6 lb/in ²
Hardening modulus	= 2.142E5 lb/in ²

The shell is assumed to be axisymmetric about its centre line and fully restrained against deflection and rotation at the nodes representing its clamped base. Geometrically nonlinear effects are modelled using a total Lagrangian description.

The dynamic analyses were performed using a time step of 0.000025 seconds.

Results Comparison

Stage 1: Eigenvalue analysis for Natural Frequency

The natural frequency obtained from the LUSAS eigenvalue extraction analysis compares well with that obtained by Bathe and Ozdenir in [1].

Lowest eigenvalue = 0.132202

Natural Frequency = 1829.95 Hz

Stages 2-4: Step-by-step Dynamic Analyses

Figure 2 presents results of the LUSAS step-by-step dynamic analyses of the pressure loaded shell and compares each of the following cases :

- LE - Linear elastic step-by-step analysis
- MNL - Materially nonlinear analysis (elastoplastic)
- GMNL - Geometrically and materially nonlinear analysis

References

1. Bathe, K.J. and Ozdemir, H. 'Elasto-plastic large deformation static and dynamic analyses', Computers and Structures, Volume 6, 81-92, 1976
2. FEAL Internal Report FEAL503 'Axisymmetric thin shell element', Finite Element Analysis Ltd. Kingston upon Thames, (1985).

Input data

Total Lagrangian geometric nonlinearity is invoked by including OPTION 87.

X08D61A.DAT

X08D61B.DAT

X08D61C.DAT

X08D61D.DAT

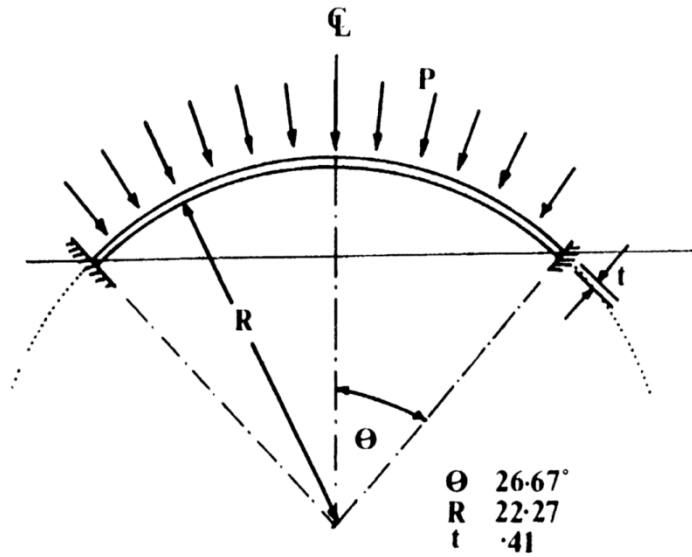


Figure 1

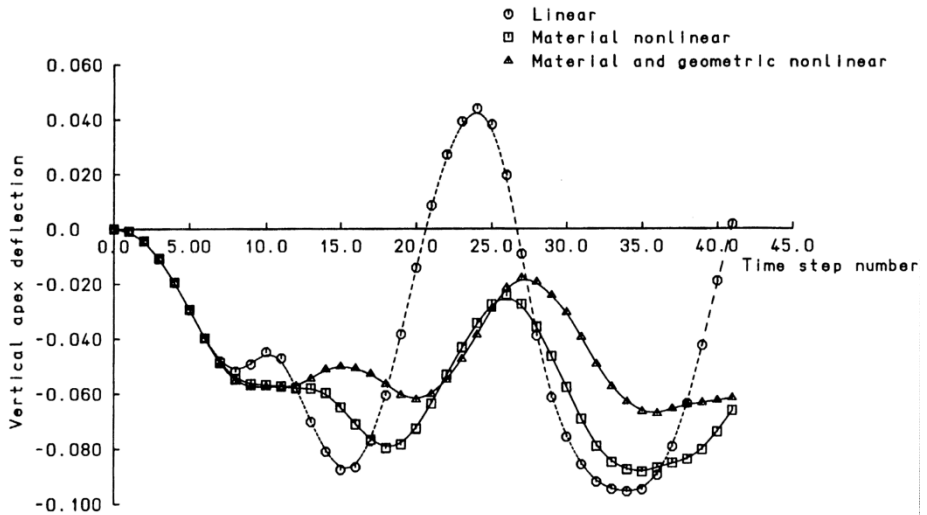


Figure 2 Clamped Spherical Cap

Example 9.1.1

Quenching Of An Infinite Plate

Keywords

Coupled Analysis, Thermal Stress

Description

This example is an illustration of semi-coupled heat transfer and subsequent thermal stress analysis. Because a semi-analytic solution is available for the case (see [1]), the problem provides verification of this type of analysis. The purpose of the analysis is to predict the residual stresses caused by the quenching of a large, homogeneous plate in regions away from the edges of the plate. In this manner it can be treated as a plate of infinite extent in all but the thickness direction. The plate is made of an elastic, perfectly plastic material, with a yield stress that drops linearly with temperature above 121 C (250 F). Because the plate is assumed to be of infinite extent the problem is one-dimensional and the only gradient occurs through the thickness of the plate. The plate is initially at a uniform temperature near its melting point (when its yield stress is small). It is assumed to be stress free in this condition. The surface is then quenched by convective cooling to a medium at room temperature. Cooling is allowed to continue until all of the plate reaches room temperature. The analysis consists of a transient heat transfer analysis followed by a thermal stress analysis. During the heat transfer analysis the temperature-time history is used as input to the thermal stress analysis. The transient stresses are large enough to cause significant plastic flow, so that residual stresses will remain after the plate reaches room temperature.

Discretisation

Ten elements are used through the half thickness of the plate. The heat transfer mesh uses QXF8 elements and the stress analysis QAX8 elements.

Geometry

The plate is 914.4mm (36in) thick.

Material properties

Young's modulus	206.8 GPa (30.0E6 lb/in ²)
Poisson's ratio	0.3
Yield stress	248.2 MPa for $j < 121$ C (36000 lb/in $j < 250$ F)

	$248.2(1-(j-121)/1111.1)$ MPa, $j > 121$ C
	$(36000(1-(j-250)/2000))$ lb/in ² , $j > 250$ F
Density	7832 kg/m ³ (0.283 lb/in ³)
Specific heat	0.6 kJ/kg C (0.1431 BThu/lb F)
Thermal conductivity	58.8 W/m C (7.872E-4 BThu/in sec F)

The film coefficient on the surface of the plate is 193.1 W/m. C (6.559E-5 BThu/in.sec F)

Theory

Equations for the determination of transient and residual stresses in plates subject to transient temperature distributions, based on the assumption of a viscoelastic, perfectly plastic material obeying a von Mises temperature-dependent yield condition are given in [1]. The analytical values for residual stress for this problem are given in [1] and are compared with LUSAS values in figure 2.

Reference

1. Landau, H.G., J.H. Weiner, E.E Zwicky, Jr., "Thermal Stress in a Viscoelastic-Plastic Plate with Temperature Dependent Yield Stress", Journal of Applied Mechanics, Vol.27, pp.297-302 (1960).

Input Data

- X09D11A.DAT
- X09D11B.DAT
- X09D11C.DAT
- X09D11D.DAT

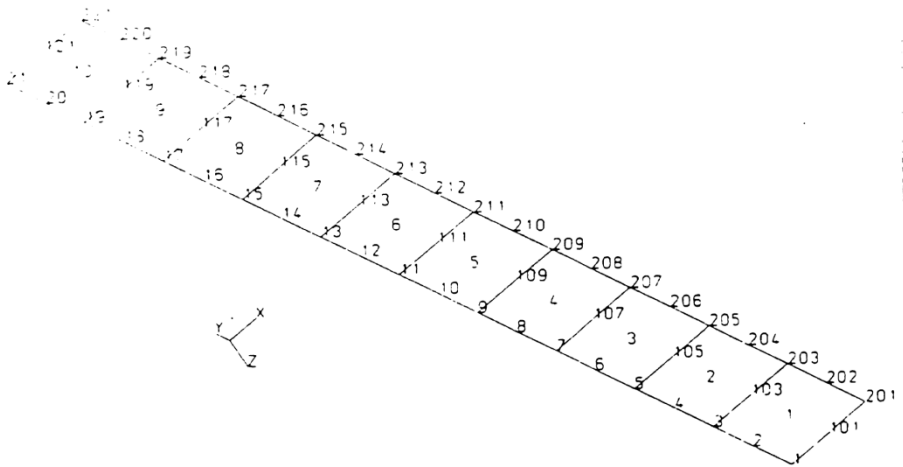


Figure 1

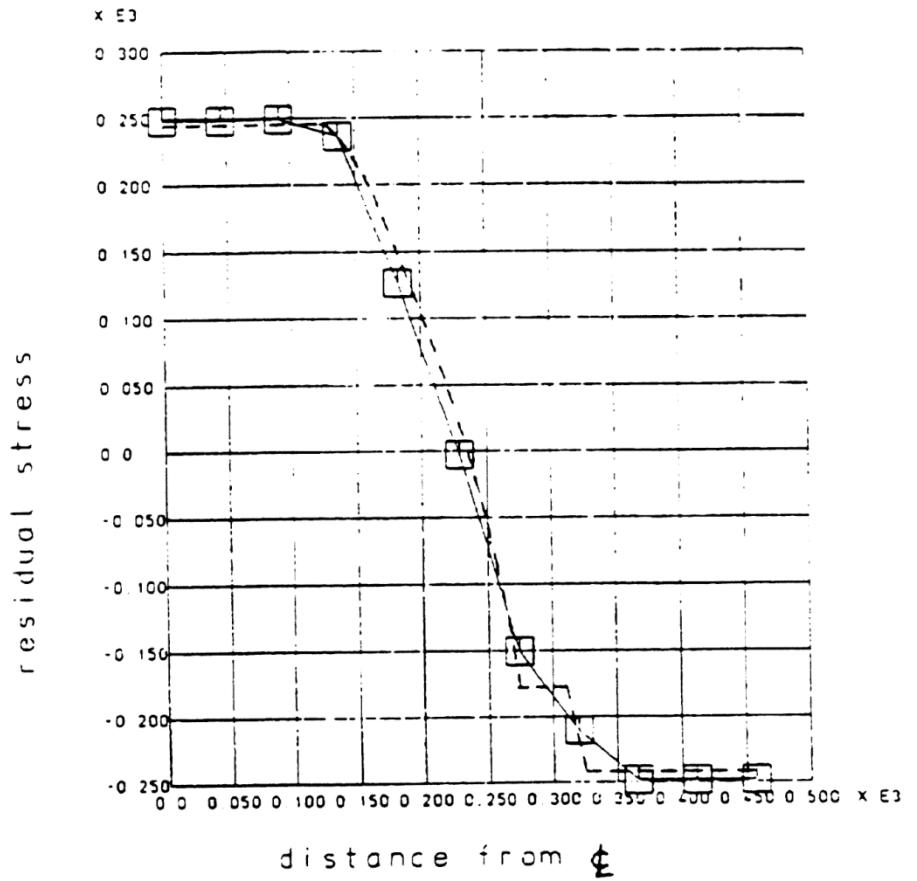


Figure 2 - Residual stresses in plate at room temperature. '—' LUSAS results, '—' Reference.

Example 9.1.2

Coupled Temperature Displacement Analysis

Keywords

Coupled Analysis

Description

This example is an elementary nonlinear case of one dimensional, fully coupled, heat transfer and stress analysis. The model is shown in figure 1. A conductive rod is fixed at one end, A, and free at the other end B. Between the free end and an adjacent body, C, there is a gap, across which heat will be conducted. The heat transfer coefficient for the gap drops linearly as the clearance increases. The fixed end of the rod, A, and the wall, C, (which is also fixed in position) are both held at fixed temperatures, ϕ_A and ϕ_C .

The objective is to predict the displacement, u_B , and temperature, ϕ_B , of the free end of the rod. For simplicity, all temperatures and displacements are measured from a standard, constant temperature position in which the gap distance is d_0 . It is assumed that the strains are small and the behaviour of the rod is linear elastic with constant modulus and thermal expansion coefficient. We also assume that the gap never closes, so that the rod is always stress free.

Discretisation

The following element types are used:

- (i) Structural - 1 HX8 element and 4 JNT4 elements.
- (ii) Thermal - 1 HF8 element.
- (iii) 4 LFS2 link elements.

Geometry

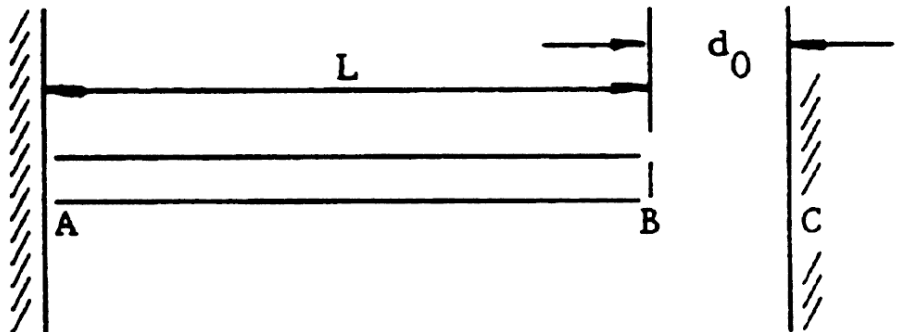


Figure 1

Material properties

All specifications in consistent units

$$E = \text{Young's modulus} = 3.0E6$$

$$\nu = \text{Poisson's ratio} = 0.0$$

$$\alpha = \text{expansion coefficient} = 1.0E-5$$

$$c = \text{rod conductivity} = 1.0$$

Boundary conditions

(i) Structural

at (a) restrained, at (b) free

(ii) Field

at (a) temperature $\phi_A = 400$, at (c) temperature $\phi_C = 200$

Theory

The exact solution to the problem is developed using the equilibrium and compatibility equations with the appropriate boundary conditions. Heat conduction in the rod is assumed to be governed by Fourier's Law:

$$q = K_r \frac{d\phi}{ds} \quad (0.0.133)$$

where K_r is the thermal conductivity of the rod and distance s is measured from A.

Heat conduction across the gap is given by:

$$q = K_g (\phi_B - \phi_C) \quad (0.0.134)$$

and the thermal conductivity of the gap, K_g , decreases linearly as the clearance increases:

$$K_g = K_0 \left[1 + \frac{U_B}{d_1 - d_0} \right] \quad (0.0.135)$$

where K_0 and d_1 are constants and U_B the displacement of B.

For this problem the following values have been chosen:

$$K_r = K_0 - 1$$

$$K_g = 2.0 \text{ when } U_B = 0.0$$

$$K_g = 0.0 \text{ when } U_B = 0.02$$

$$\therefore d_1 - d_0 = 0.01$$

For thermal equilibrium:

$$\frac{dq}{ds} = 0 \quad (0.0.136)$$

Therefore, from (0.0.133) $d\phi/ds$ is constant in the rod, so that (0.0.133) may be expressed as:

$$q = K_r (\phi_A - \phi_B) \quad (0.0.137)$$

The thermal expansion of the rod is given by:

$$U_B = \frac{\alpha L}{2} (\phi_A + \phi_B) \quad (0.0.138)$$

For thermal equilibrium:

$$K_r (\phi_A - \phi_B) = K_g (\phi_B - \phi_C) \quad (0.0.139)$$

Substituting (0.0.135) and (0.0.138) in (0.0.139) yields a quadratic equation for ϕ_B . The boundary values and chosen constants can be used in this equation to solve for ϕ_B , where only one admissible positive root is obtained. Substitution of ϕ_B in (0.0.139) gives U_B

$$\phi_B = 285.4 \quad U_B = 3.427E-3$$

Results

Two approaches are implemented to allow a solution of this example. Firstly, if two analyses can be run concurrently, an iterative solution of the problem is possible. Secondly, if only one module can be run at once, a solution is obtained by the use of restart files. The temperature and displacement at point b computed by the two approaches are:

	Iteration 0		Iteration 1		Iteration 2		Itn. 3
	Temp	Disp	Temp	Disp	Temp	Disp	Temp
Method 1							
Thermal	300.0	3.5×10^{-3}	285.084	3.425×10^{-3}	285.206	3.426×10^{-3}	285.208
Structural							
Method 2							
Thermal	300.0	3.5×10^{-3}	284.936	3.425×10^{-3}	285.213	3.426×10^{-3}	
Structural							

The slight differences with theoretical values are due to the use of a constant value for L in the manual calculations.

Input Data

X09D11c.DAT

X09D11d.DAT

Note that restart file X09D12C.RST is renamed to Z09D12C.RST

Note that restart file X09D12D.RST is renamed to Z09D12D.RST

Example 9.2.1

Compression Of An Angle Into A Corner

Keywords

Thermal Surfaces, Coupled Analysis, Nonlinear

Description

A poorly formed angle bracket, subtending an angle greater than 90 degrees, is pushed against a second right angle bracket, figure 1. Contact along the faces is progressive as the angles deform. A semi-coupled static structural/thermal analysis is carried out using thermal surfaces. The temperature at the interface between the angles is a function of the pressure at the contact point.

Discretisation

Each angle is meshed using the following two dimensional elements:

Structural analysis - 36 QPM4 plane stress continuum elements.

Thermal analysis - 36 QF4 plane field elements.

The mesh at the initial configuration is shown in figure 2.

Geometry

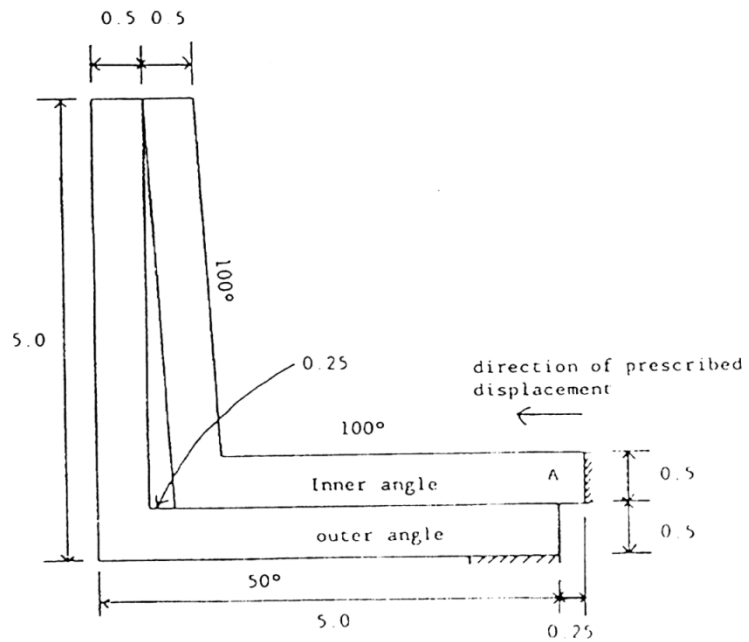


Figure 1 - Initial geometry

Boundary conditions

Thermal:

Prescribed temperature

outer angle - outer surface temperature of 50

inner angle - outer surface temperature of 100

Structural:

Total prescribed displacements applied to end A

step 1 -0.12

step 2 -0.24

step 3 -0.25

step 4 -0.26

step 5 -0.27

Material properties

Thermal:

solid conductance = 101

thermal contact properties:

gap conductance contact pressure

0 0

1000 0.03

Structural:

E = 100

Poisson's ratio = 0.0

Master surface stiffness = 0.1

Slave surface stiffness = 0.1

Loading

Structural:

Total prescribed displacements applied to end A

step 1 -0.12

step 2 -0.24

step 3 -0.25

step 4 -0.26

step 5 -0.27

LUSAS results

The results should show a uniform progression of contact with the hottest point indicating the point of greatest contact pressure. If the surfaces are in contact, but there is no contact pressure, heat will not flow between the surfaces. Figure 3 details the progression of contact as the end displacement of the inner angle is increased. Initial contact is at the top of the angles as shown in load case 1. A second contact point is predicted at the point of prescribed displacement as the outer angle bends to accommodate the inner angle. The largest stresses arise from bending. As loading is increased, load cases 2 to 4, the point of contact moves down the angles. Above the point of contact the angles are stress free. Finally, in load case 5, the inner angle is in a state of almost pure compression and the outer angle is restraining this load by a combination of bending and tension. Figure 4 mirrors the progression of contact with the heat flowing across the contact as expected.

Input data

X09D21A.DAT

X09D21B.DAT

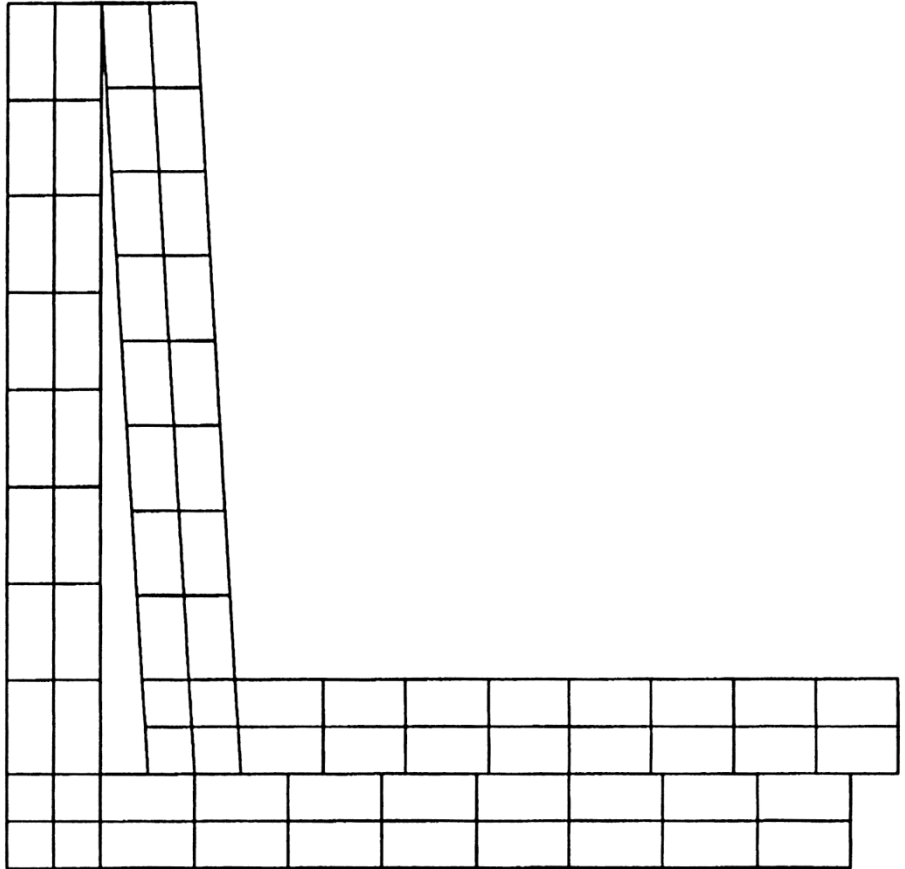


Figure 2 Mesh in initial configuration

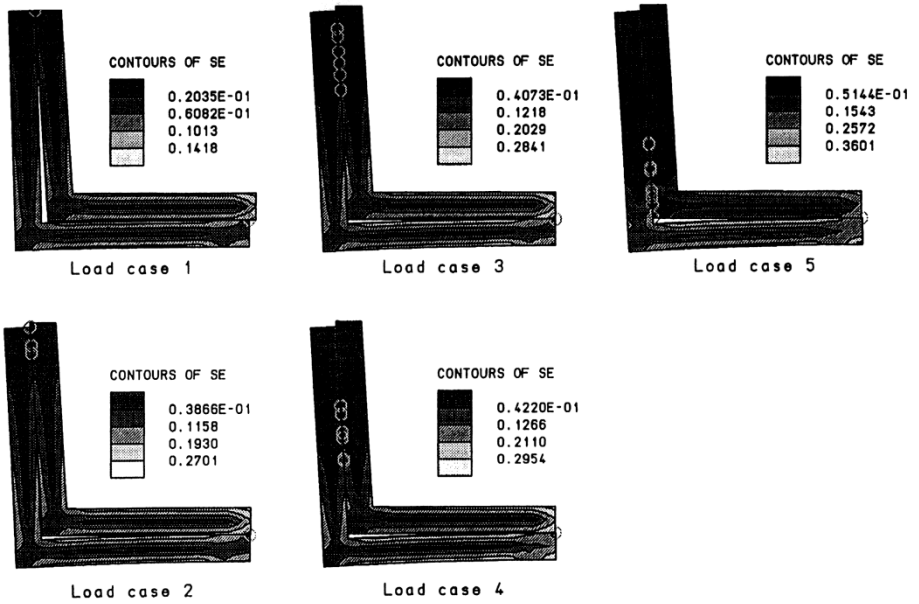


Figure 3 Stress contours and contact points (circled)

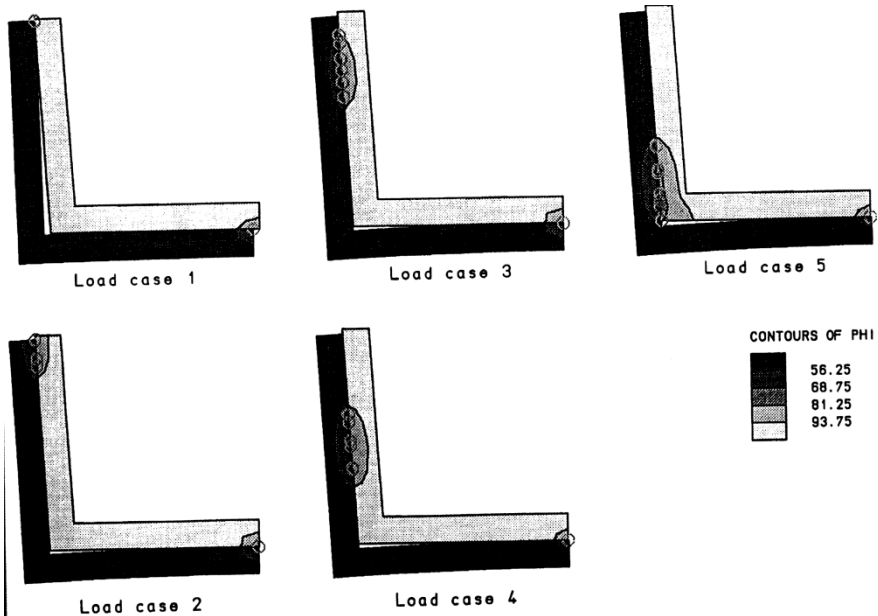


Figure 4 Temperature contours and contact points (circled)

Example 9.2.2

Upsetting Of A Cylindrical Billet

Keywords

Plasticity, Coupled Analysis, Plastic Work

Description

A cylindrical billet is compressed between two plattens so that its length is reduced by 52%. The rate at which the billet is compressed dictates the amount of heat developed as a result of plastic work done. This example compares the temperature distributions for a fast and slow rate of compression.

The billet is 30mm long and of 10mm radius with all surfaces fully insulated. The initial and final configurations of the billet are shown in Figure 1. Symmetry of the problem allows an axisymmetric analysis to be performed. Elasto-plastic material properties are assumed for this metal forming example. The effects of applying the prescribed displacement loading at a rate of 0.09 mm/sec and 90 mm/sec are compared. Note that inertia effects have been ignored and the time-step used in the thermal analysis dictates the rate at which the heat is developed. Data transfers are performed in parallel during the execution of this thermo- mechanical coupled analysis.

Discretisation

A mesh of 119 axisymmetric solid elements (QAX4) was used in the structural analysis, while the same number of QXF4 elements was used in the thermal analysis. The initial mesh is shown in Figure 1.

Material properties

Young's modulus = $2E11 \text{ N/m}^2$

Poisson's ratio = 0.3

Thermal expansion coefficient = $1.2E-5 \text{ per } ^\circ\text{C}$

Initial yield stress = $7E8 \text{ N/m}^2$

Work hardening rate = $3E8 \text{ N/m}^2$

Specific heat = $586\text{J}/(\text{Kg } ^\circ\text{C})$

Density = 7833 Kg/m^3

Conductivity = 52J/(m-s- °C)

Heat fraction $h_r = 0.9$

Boundary conditions

Structural:

Symmetry conditions are applied along the axis and over the middle surface of the billet so that only half an axisymmetric segment is modelled. Nodes along the axis of symmetry are restrained horizontally but are free to move in the vertical direction. To simulate the loading platten, the nodes along the top surface are free to move in the horizontal direction but are restrained vertically solely to apply the prescribed displacements. Symmetry conditions for nodes on the middle surface require restraint in the vertical direction and freedom horizontally.

Thermal

All external surfaces are insulated. This is achieved by initialising the environmental temperature at the boundary to zero and defining a very low convective heat transfer coefficient at the external surface of the billet. An initial environmental load is applied to all element faces along the boundary to model this condition.

Solution comparison

The general response observed for both the rapidly loaded test and the slower case agrees with what would be expected for such analyses. The slow loading test shows that the temperatures have time to diffuse leading to a uniform temperature distribution throughout the billet, Figure 3; the temperatures in this case range between 121 and 122.8 degrees. The opposite is true for the faster loading case where higher temperatures are computed with a large temperature gradient occurring across the billet. The highest temperatures are located at the point where most plastic deformation occurs. Results for each case are compared in Figures 2 and 3.

Input Data

X09D22A.DAT

X09D22B.DAT

X09D22C.DAT

X09D22D.DAT

Note:

This data file can be used for both the fast and slow cases. However, different data transfer file names should be used to avoid confusion.

Note:

For the slow rate of loading, the incrementation line in TRANSIENT CONTROL must be changed from 0.01/9 to 10/9. The data transfer file should also be renamed to avoid confusion.

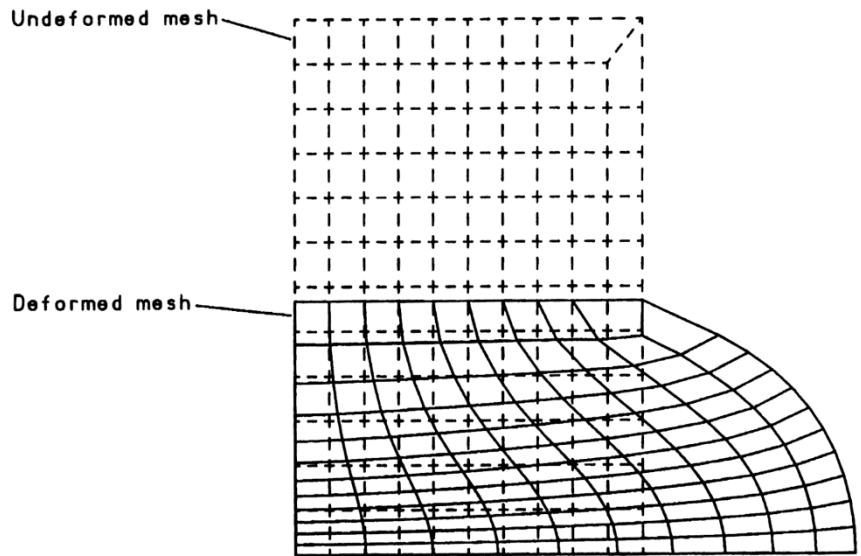


Figure 1. Deformed mesh plot at 52% upsetting

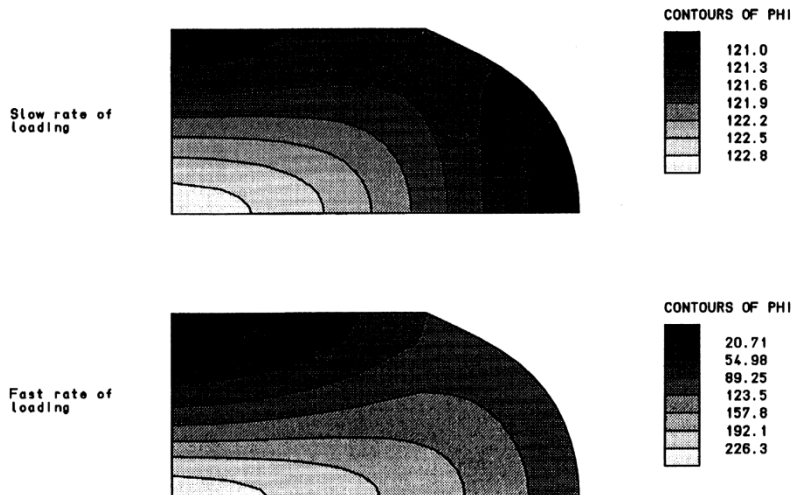


Figure 2. Temperature distributions for slow and fast rates of loading at 52% upsetting.

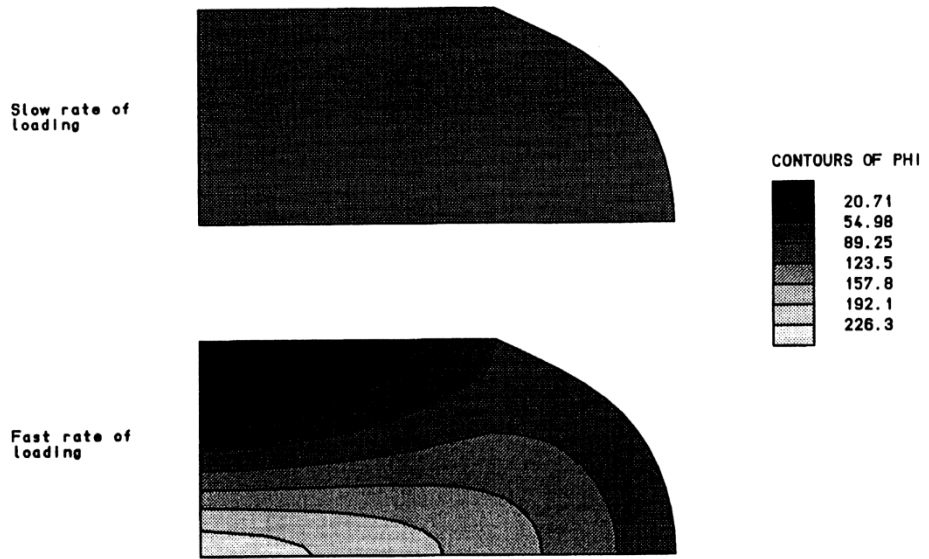


Figure 3. Comparison of temperature distribution for slow and fast rates of loading at 52% upsetting

Example 10.1.1

Plastic Bar Impact Against A Rigid Wall.

Keywords

Impact, Slideline, Plastic Flow

Description

This example consists of a cylindrical steel projectile striking perpendicular to a rigid boundary. Upon impact, the stress in the projectile at the impact point exceeds the elastic limit of the material, and a plastic front moves back through the projectile. Within the plastic zone the material flows radially and results in a shortening of the projectile.

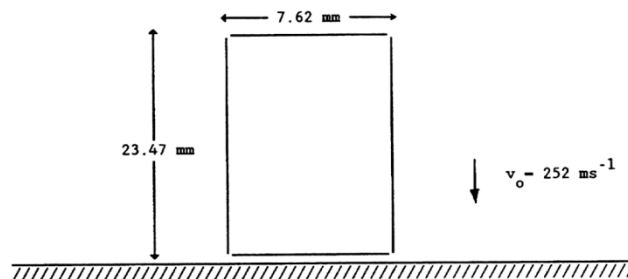
Wilkins [1] performed a series of experiments which illustrated that the final cylinder length is very sensitive to the yield strength of the material. Consequently, as the projectile undergoes finite strains, this example furnishes a worthwhile test for both elastoplastic algorithms and finite strain procedures in explicit dynamic analysis.

Figures 1 and 2 illustrate the final configuration of the bar for an initial velocity of 252 m/s. The accuracy of the bar shortening predicted in the analysis is compared with the shortening observed experimentally [1].

Discretisation

The projectile is modelled using 5x21 4-noded one point quadrature axisymmetric elements (QAX4E), figure 1. The boundary between the projectile and the rigid wall is represented using a penalty based slideline procedure [2].

Geometry



Material properties

Young's modulus, E	211.0x10 ⁹ Pa
Poisson's ratio, ν	0.3
Density, ρ	7840.0 kg/m ³
Initial yield stress, σ_0	1.2x10 ⁹ Pa
Isotropic hardening parameter, H_{II}	1.0x10 ⁶ Pa

Default values for the hourglass viscosity and for the artificial viscosity coefficients are to be used.

LUSAS results

(i) The final length of the bar can be approximated as 19.87mm by considering the net displacement of the top and bottom surfaces; this is in good agreement with the experimental value of 19.76mm given in [1], figure 1. The configuration at the point of maximum deformation is given in figure 2.

References

1. WILKINS, M. L., GUINAN, M. W. Impact of Cylinders on a Rigid Boundary. J. Appl. Phys., Vol. 44, No. 3, pp1200-1207, March 1973.
2. GOUDREAU, G. L., HALLQUIST, J. O. Recent Developments in Large-Scale Finite Element Lagrangian Hydrocode Technology. Comp. Meth. in Appl. Mech. and Eng., 33, pp725-757, 1982.

Input data

X10D11A.DAT

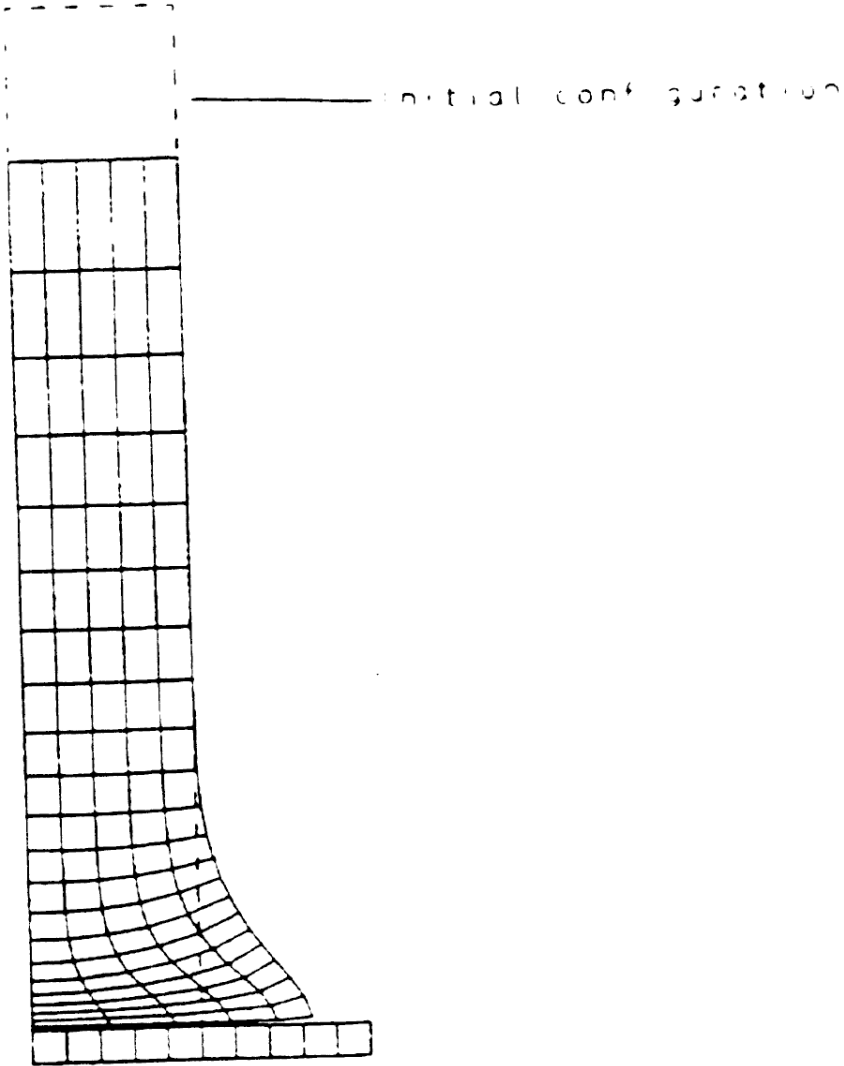


Figure 1

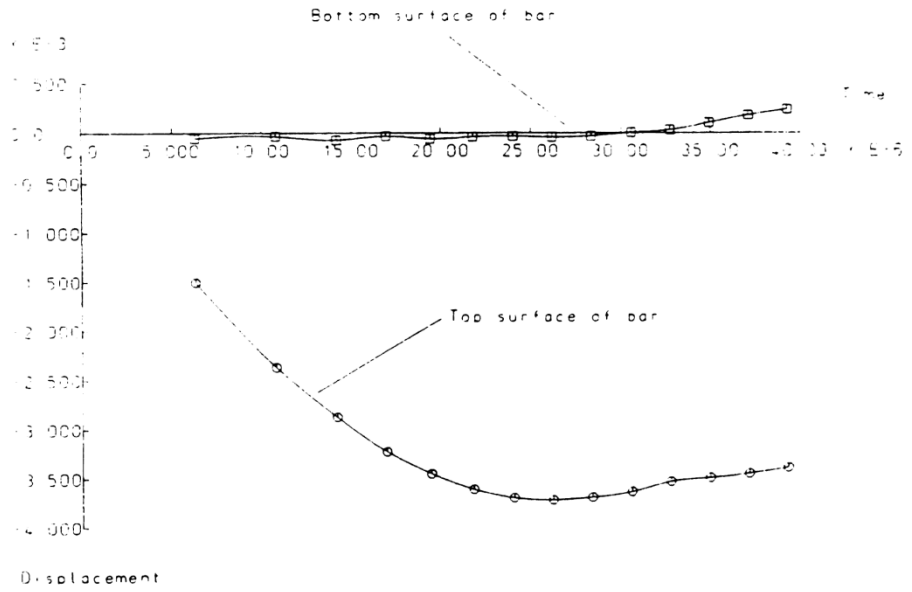


Figure 2

Example 10.1.2

Cantilever Subject To Dynamic Loading.

Keywords

Impact, Tied Slideline

Description

This example consists of an elastic cantilever which is subjected to an instantaneously applied uniformly distributed load. A single tied slideline is used to enable refinement of the mesh near the fixed end. The free end displacements computed by the dynamic finite element analysis are compared with those given by static linear and nonlinear analyses.

The free end displacements calculated by static analysis are:

Linear solution $= 0.36$

Geometrically nonlinear solution $= 0.33$

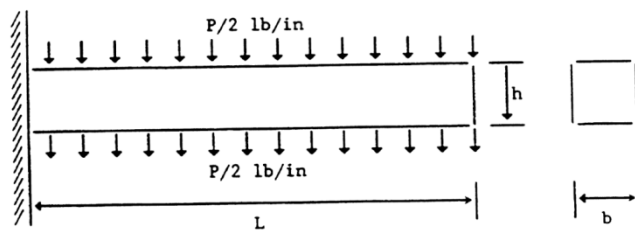
Discretisation

The beam is modelled with 36 HX8E elements, figure 3, arranged in the following manner:

6 x 4 element mesh near the support

4 x 3 element mesh for remainder

Geometry



$$L = 10 \text{ in.} \quad h = 1 \text{ in.} \quad b = 1 \text{ in.}$$

Figure 1

Material properties

Young's modulus, E	12.0 x10 ³ lb/in ²
Poisson's ratio, ν	0.20
Density, ρ	1.0x10 ⁻⁶ lb sec ² /in ⁴

Default values for the hourglass viscosity and for the artificial bulk viscosity coefficients are to be used.

Reference

- BATHE, K-J., RAMM, E., WILSON, E. L. Finite Element Formulations for Large Deformation Dynamic Analysis. Int. J. Num. Meth. Eng., Vol. 9, pp353-386, 1975.

Lusas results

Figure 2 shows the peak deflection computed by LUSAS compared with that given in [1]. The differences observed can be attributed to the use of different strain measures. In [1] a Total Lagrangian approach is used whereas the LUSAS solution is based on the Green-Naghdi stress rate and velocity strain.

Taking further time steps confirms oscillation about the nonlinear static solution. The deformed mesh at peak deflection is shown in figure 3.

Input data

X10D12A.DAT

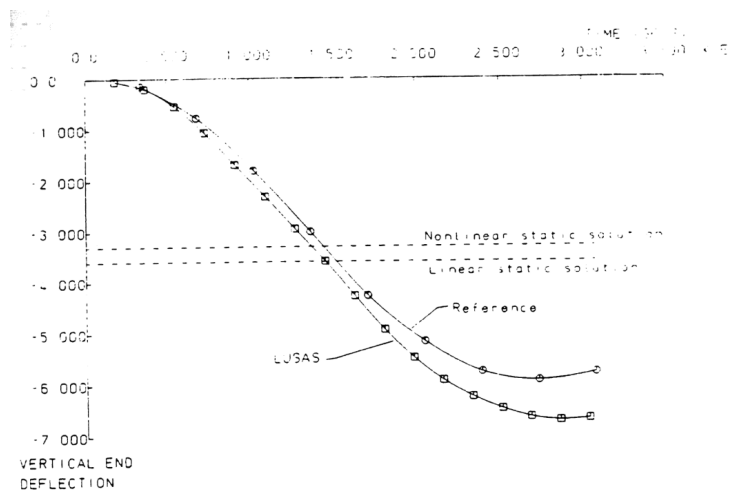


Figure 2

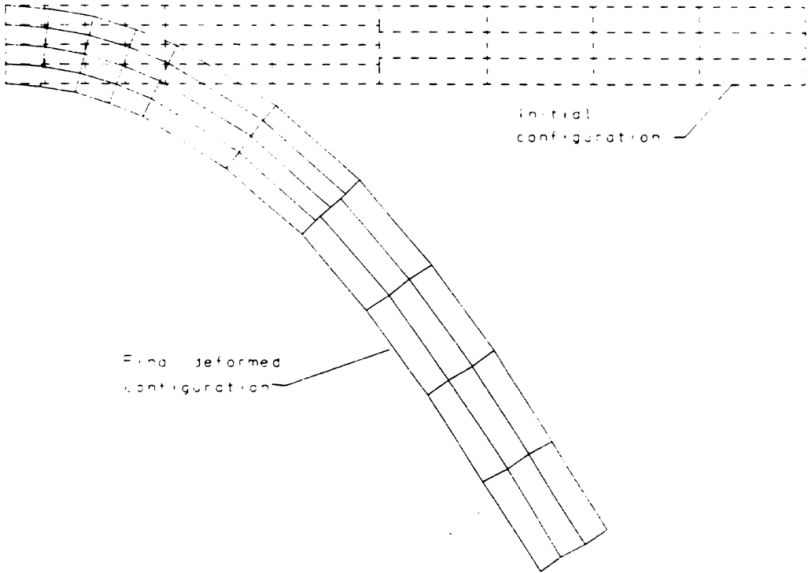


Figure 3

Example 10.1.3

Interference Fit Test

Keywords

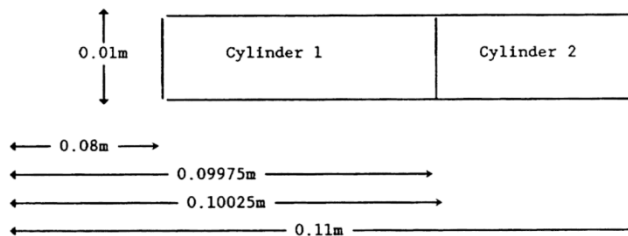
Axisymmetric Solid, Elastic, Slideline, Implicit

Description

One range of problems which is of considerable interest to the Engineer is the assembly of components using interference fit techniques.

This example consists of two cylinders of length 0.01m and outer and inner diameters of (0.10025, 0.08m) and (0.11, 0.09975m) respectively. An initial interference of 0.0005m is thus considered between the cylinders. The geometry of the initial configuration of the cylinders is shown below. The first phase of the analysis is a linear elastic solution to obtain the initial configuration as a result of the interference fit. The response of the structure to subsequent loading on the innermost diameter corresponding to a suddenly applied constant radial load is also investigated. 2% damping of the two lowest modes is applied to the structure for this secondary phase utilising the Rayleigh damping facility. The cylinders are modelled using a 10x2 element mesh (see figure 1) with 4 noded axisymmetric solid elements (QAX4).

Geometry



Boundary conditions

Top and bottom surfaces fully restrained in global Y only

Material properties

	Cylinder 1	Cylinder 2
Young's modulus, E	150 x10 ⁹ kN/m ²	207 x10 ⁹ kN/m ²
Poisson's ratio, ν	0.25	0.3
Density, ρ	7470 Kg/m ³	7470 Kg/m ³

2% critical damping of the lowest two vibration modes is also required. This will give the Rayleigh damping factors as (according to the primary eigen-frequencies of 8213 and 8383 Hz obtained from an initial eigenvalue analysis on the structure):-

Rayleigh damping factor α	104265
Rayleigh damping factor β	3.83598x10 ⁻⁷

Loading

A compressive radial loading is applied over the inner diameter of the inner cylinder as a concentrated step load of magnitude 2.5 GPa.

Slideline Properties

Stiffness scale factor, master surface	Stiffness scale factor, slave surface	Zonal contact detection parameter	Slideline extension
1.0	1.0	100.0	1.0

Theory

The Rayleigh damping factors may be computed from the following equation:-

$$2\zeta = \frac{\alpha}{\omega} + \beta\omega \quad (0.0.140)$$

where z is the known modal damping factor, a and b are the Rayleigh damping factors and w is the circular frequency at which the modal damping factor is operative. The Rayleigh damping factors are thus computed as:

$$\alpha = \frac{2\zeta(1/\omega_2 - \omega_1)}{(1/\omega_2^2 - 1/\omega_1^2)} = 104265 \quad (0.0.141)$$

And

$$\beta = \frac{2\zeta(\omega_2 - \omega_1)}{(\omega_2^2 - \omega_1^2)} = 3.83598 \times 10^{-7} \quad (0.0.142)$$

The approximate analytical solution for the interface pressure (P) due to an initial interference fit and an internal pressure (P_i) acting on the inside surface of the inner cylinder is given by the following:

$$P_i = \frac{\frac{\gamma}{b} + \frac{2Pa^2}{E_1(b^2 - a^2)}}{\frac{1}{E_1} \left[\frac{a^2 + b^2}{b^2 - a^2} - \nu_1 \right] + \frac{1}{E_2} \left[\frac{b^2 + c^2}{c^2 - b^2} \right] + \nu_2} \quad (0.0.143)$$

where:

γ is the initial interference

a is the inner diameter of the inner cylinder (0.08)

b is the diameter of the interference fit (0.10)

c is the outer diameter of the outer cylinder (0.11)

For the initial interference configuration without internal pressure loading, the analytical solution yields:-

$$P = 61.7 \text{ MPa}$$

whilst for the secondary case of superimposed internal loading of 2.5 GPa, the interface pressure is given as:-

$$P = 793.4 \text{ MPa}$$

Lusas Results

The initial radial stress distribution over the cylinder cross-section is shown in Figure 3, from which the normal interface pressure obtained is 62.8 MPa. The effect of damping on the normal interface displacement for node 111, subsequent to the application of the internal pressure may be seen in Figure 2.

The final radial stress distribution over the cylinder cross-sections for the damped response is shown in Figure 4. It may be seen that the final value for the interface pressure of 818 MPa represents a difference of 3% when compared with the approximate analytical solution of 793.4 MPa. This analysis was also carried out using a statically applied load, figure 6, where the final interface pressure was found to be 820 MPa. A comparison of radial stresses at each side of the interface for the damped system is given in figure 5. This figure shows that as the analysis progresses a state is reached where the effects of loading the structure dynamically have effectively been damped. This leads to a final stress distribution very similar to that for the static analysis.

Reference

1. Reismann,H.,Pawlik,P., Elasticity: Theory and Applications, J.Wiley and Sons, 1980

Input Data

- X10D13A.DAT
- X10D13B.DAT
- X10D13C.DAT

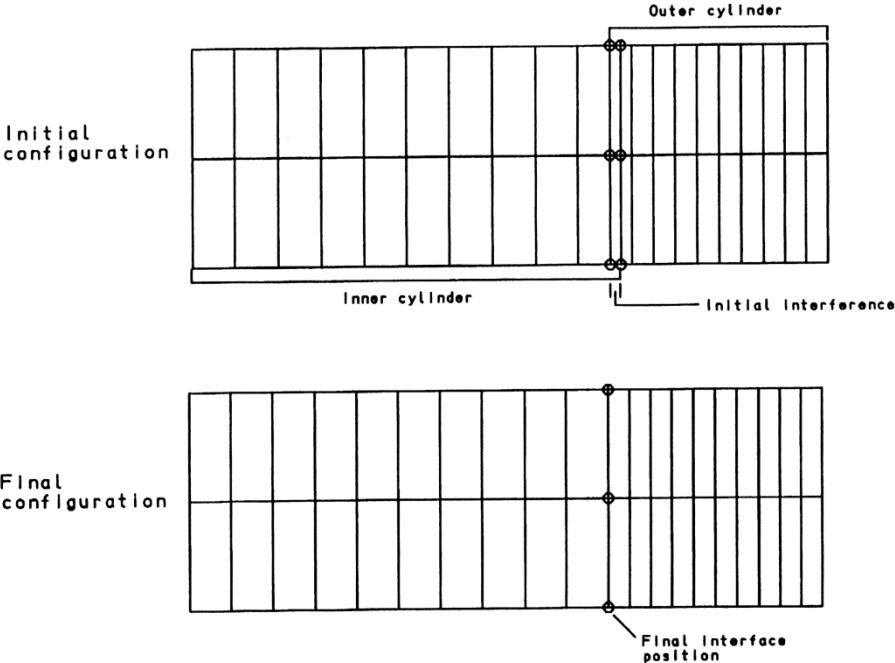


Figure 1 Initial and final configuration of cylinders

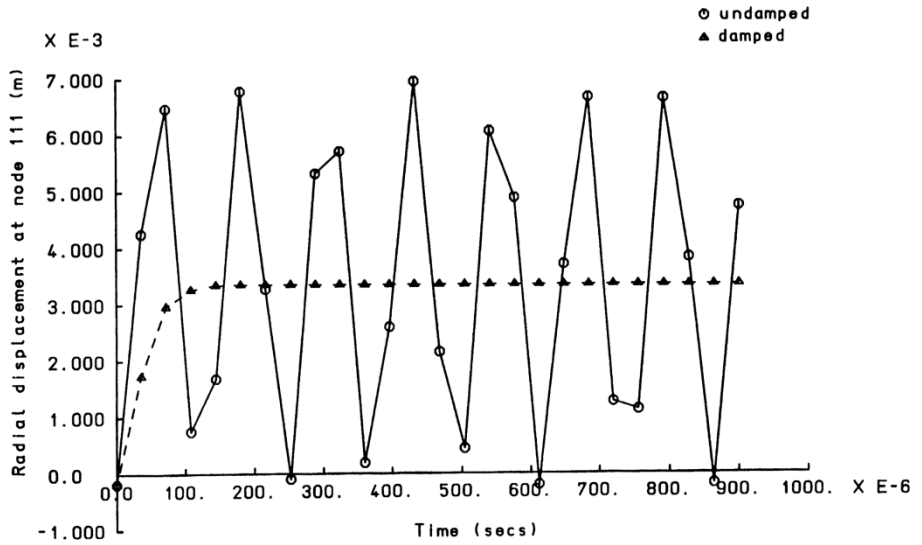


Figure 2 Comparison of damped and undamped response for Interface node 111

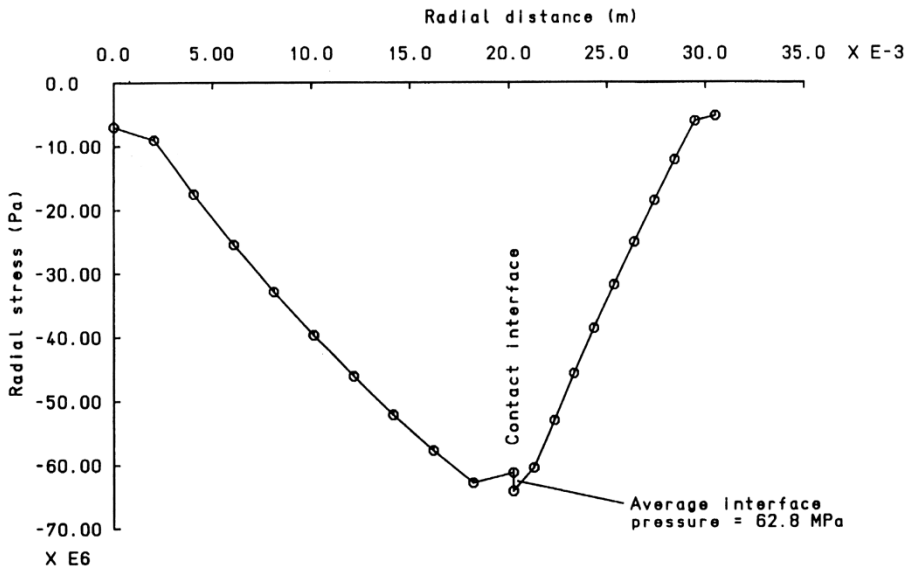


Figure 3 Initial radial stress distribution for cylinders.

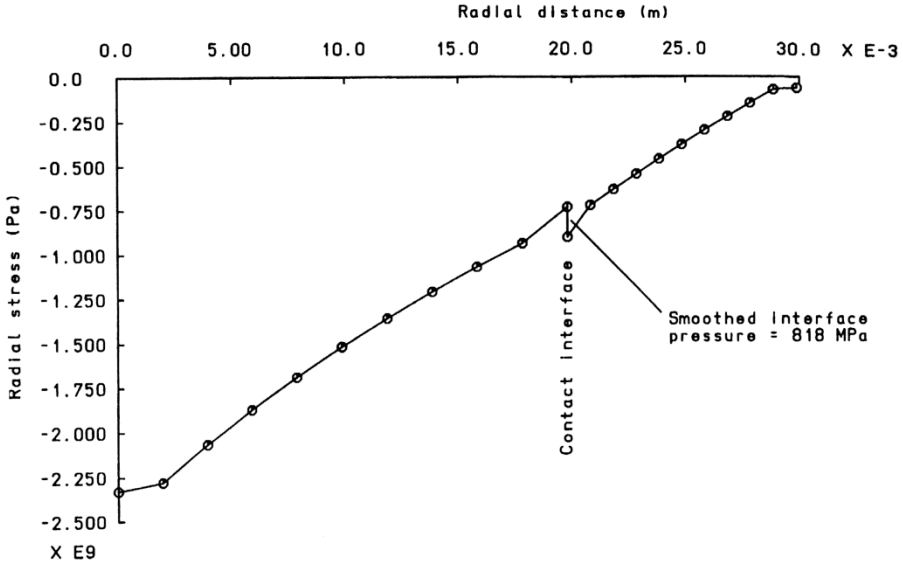


Figure 4 Final radial stress distribution for cylinders.

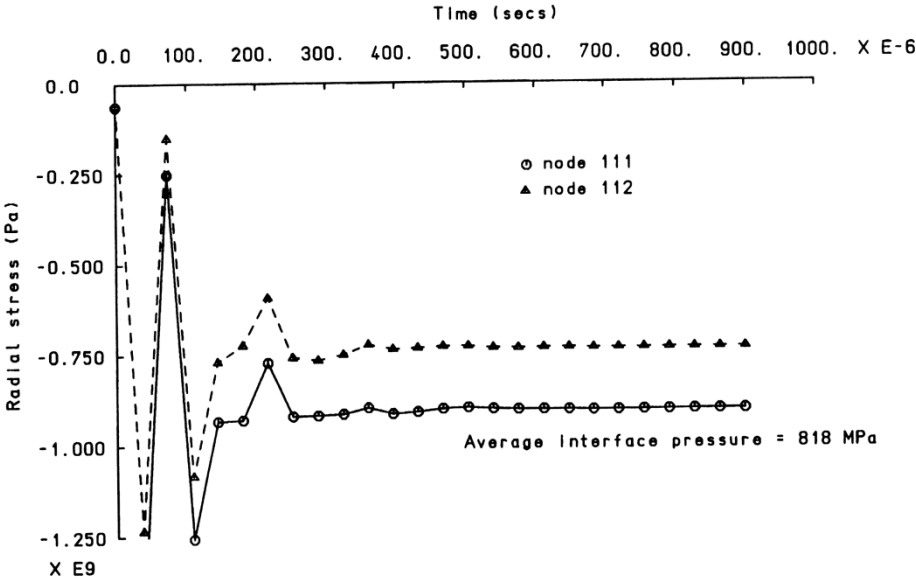


Figure 5 Radial stresses on each side of interface.

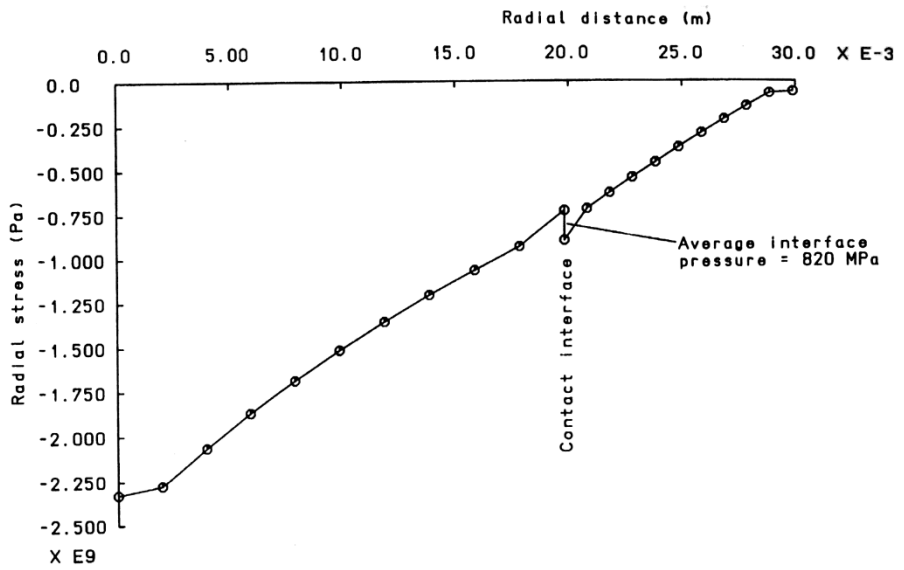


Figure 6 Final radial stress distribution - static analysis

Example 10.1.4

Cylinder Compression Between Platens

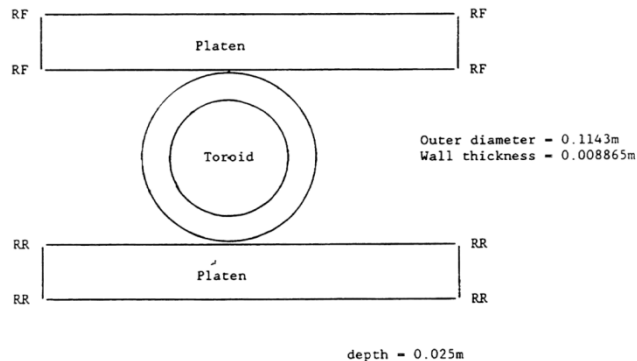
Keyword

Nonlinear, Contact, Implicit, Static, Slidelines

Description

The crushing of a long, straight pipe between two flat, frictionless anvils is presented in this example. The objectives are to establish the load deflection response of the pipe and to describe the overall deformation of the section. The example is a simple test for modelling contact problems involving deformable bodies and rigid, impenetrable surfaces.

Geometry



Discretisation

The cylinder is modelled using 8x4x2 eight noded solid elements (HX8), whilst the platen utilises an 8x1x2 element mesh (Figure 1). The boundary between the outer cylinder surface and the platen face is represented using the frictionless slideline option (type 1). The boundary conditions are depicted in the preceding diagram and loading is applied over 36 increments to the upper platen via a prescribed displacement to give a total relative displacement of -0.0315m. Note that there are two symmetry planes in this problem.

Material properties

Young's modulus, E	30 x10 ⁶ kN/m ²
Poisson's ratio, ν	0.3
Density, ρ	7800 Kg/m ³
Yield stress, σ_0	241 N/m ²

where σ_0 is the von Mises initial yield stress. The hardening curve is as follows:-

Hardness, C_i (N/m ²)	Plastic strain, ϵ
9.850x10 ⁹	0.0035
5.386x10 ⁹	0.0083
3.447x10 ⁹	0.0133
1.741x10 ⁹	0.0281
1.144x10 ⁹	1.0000

Slideline Properties

Default values are specified for all slideline properties, except for the slideline extension where a value of 0.1 is used.

Lusas results

The undeformed mesh is shown in Figure 1, together with the deformed mesh at load increment 36. Figure 2 shows the deformation history. The force displacement variation of total normal interface force corresponds well with the experimental curve given in [1]. Note that the relative displacement is plotted, i.e. twice the applied displacement.

Reference

1. Taylor,L.M., "A finite Element Analysis for Large Deformation Metal Forming Problems Involving Contact and Friction" TICOM report number 81-15, 1981

Input Data

X10D14A.DAT

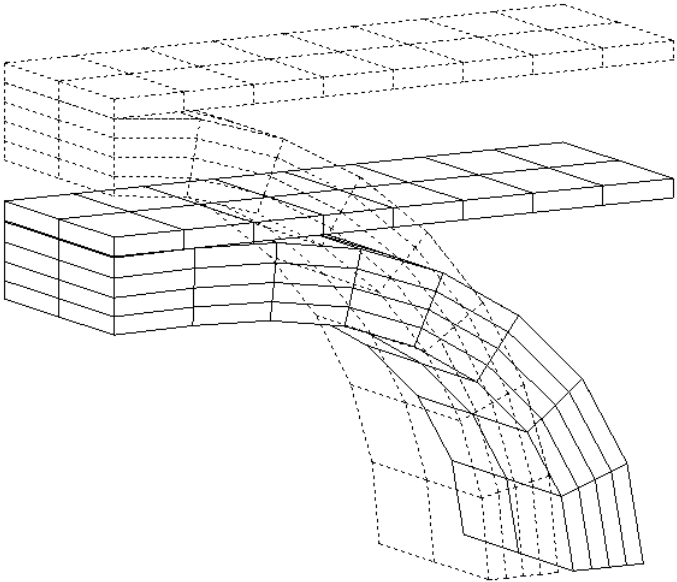


Figure 1: Deformation of cylinder at increment 36

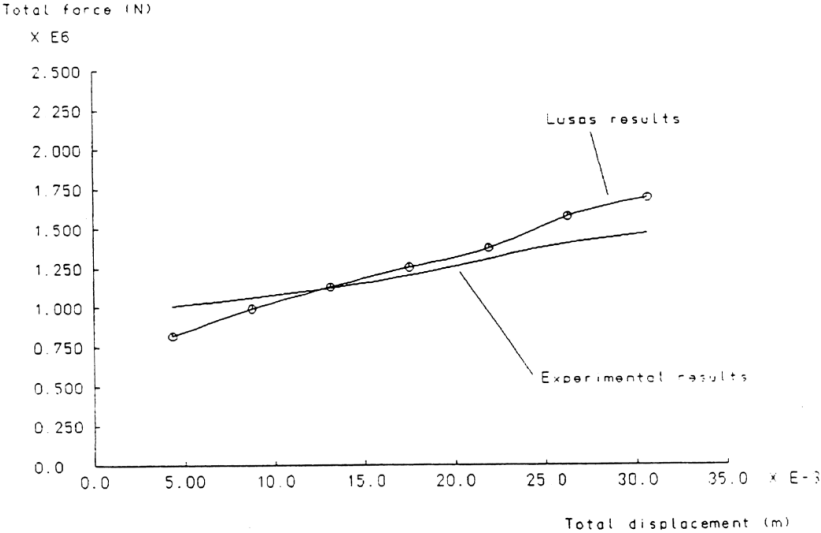


Figure 2: Variation of normal interface force with total platen displacement (3D)

Example 10.2.1

Propped Cantilever With Joint Elements And Contact/Gap Model

Keywords

Cantilever, Contact, Gap, Joint

Description

Determine the end deflection and reactions of point loaded cantilever beam fully restrained at one end and supported at its mid length by a sunken support.

Discretisation

The cantilever is modelled using two BS4 element. The prop is modelled using one JSH4 element and the nonlinear contact/gap model.

Three support conditions are considered:

1. Free cantilever
Since the contact stiffness is only invoked by a downward (negative) deflection of the cantilever, a positive end load results in a free cantilever condition.
2. Propped cantilever
The propped cantilever condition is modelled using an initial gap of 0 mm and a large contact stiffness (10E16). The end load is applied in the negative Z direction.
3. Cantilever with sunken prop
The sunken propped cantilever is modelled using an initial gap of 1 mm and a large contact stiffness (10E16). The end load is applied in the negative Z direction.

Geometry

The dimensions and geometry of the cantilever are shown in figure 1.

Length, L	40 mm
Distance to prop, l	20 mm
Second moment of area, I	833.3 mm ⁴

Material properties

Young's modulus, E	2.0×10^6
--------------------	-------------------

Loading

The cantilever is subjected to a concentrated end load ($P = 390609.3$ N) designed to produce a free cantilever end deflection of 5 mm. The total load is applied in five equal increments:

Increment	Case 1	Case 2	Case 3
1	0.2P	-0.2P	-0.2P
2	0.4P	-0.4P	-0.4P
3	0.6P	-0.6P	-0.6P
4	0.8P	-0.8P	-0.8P
5	1.0P	-1.0P	-1.0P

Theory

Case 1. Free cantilever condition (Figure 2)

The end deflection of a free cantilever subject to a transverse end load is given by the expression [1]

$$d_{\max} = \frac{Pa^3}{3EI} \left(1 + \frac{3b}{2a} \right) \quad (0.0.144)$$

Hence, since ($a=L$) and ($b=0$)

$$d_{\max} = \frac{PL^3}{3EI} \quad (0.0.145)$$

Case 2. Propped cantilever condition (Figure 3)

The end deflection of a propped cantilever is given by the expression

$$d_D = \frac{P1^3}{12EI} (4p^2 + 6pq + 3p + 3q) \quad (0.0.146)$$

and the reactions by the expressions

$$R_A = \frac{3Pp}{2} \quad \text{and} \quad R_B = -P \left(1 + \frac{3p}{2} \right) \quad (0.0.147)$$

where

$$p = \frac{a}{l} \quad \text{and} \quad q = \frac{b}{l} \quad (0.0.148)$$

Hence, since (a=l) and (b=0), therefore (p=1) and (q=0), and

$$D = \frac{Pl^3}{12EI}(4+3) = \frac{7Pl^3}{12EI} \quad (0.0.149)$$

and

$$R_A = \frac{3P}{2} \quad \text{and} \quad R_B = -P\left(\frac{5}{2}\right) \quad (0.0.150)$$

Case 3. Propped cantilever with sunken support

The propped cantilever with the sunken mid support behaves as the free cantilever until the initial gap of 1 mm is closed. Following this deflection the stiff contact spring is invoked, the end deflection restricted, and the reaction at the prop progressively increased.

$$fP = K_1 R_A + K_2 R_B \quad (0.0.151)$$

where

f is the load factor (Total Load level = fP)

K_1 , K_2 are the support reaction scaling factors

Comparison

The LUSAS results for the end deflection and the support reactions are compared to the theoretical solutions.

Case 1. Free Cantilever.

Increment	Load Level	End Displacement	
		Theory	LUSAS
1	0.2P	1.000	0.9999
2	0.4P	2.000	1.9999
3	0.6P	3.000	2.9988
4	0.8P	4.000	3.9988
5	1.0P	5.000	4.9988

Case 2. Propped Cantilever

Inc.	Load	End Displacement		End Reaction R _A		Prop Reaction R _B	
		Theory	Lusas	Theory	Lusas	Theory	Lusas
1	-0.2P	-0.2187	-0.2187	-117182	-117183	195304	195305
2	-0.4P	-0.4374	-0.4375	-234365	-234366	390609	390609
3	-0.6P	-0.6562	-0.6562	-351548	-351548	585914	585914
4	-0.8P	-0.8749	-0.8749	-468730	-468731	781217	781219
5	-1.0P	-1.0937	-1.0937	-585913	-585913	976523	976523

Case 3. Cantilever with sunken prop.

Inc.	Load	End Displacement		End Reaction R _A		Prop Reaction R _B		K ₁	K ₂
		Theory	Lusas	Theory	Lusas	Theory	Lusas		
1	-0.2P	-0.2187	-0.2187	-117182	-117183	195304	195305	1.0	0.0
2	-0.4P	-0.4374	-0.4375	-234365	-234366	390609	390609	1.0	0.0
3	-0.6P	-0.6562	-0.6562	-351548	-351548	585914	585914	1.0	0.0
4	-0.8P	-0.8749	-0.8749	-468730	-468731	781217	781219	0.5	0.5
5	-1.0P	-1.0937	-1.0937	-585913	-585913	976523	976523	0.1	0.9

References

1. C.S.Gray et al. 'Steel Designers Manual : Second Edition', Crosby-Lockwood and Sons Publishers Ltd. (1960)

Input Data

X10D21A.DAT

X10D21B.DAT

X10D21C.DAT

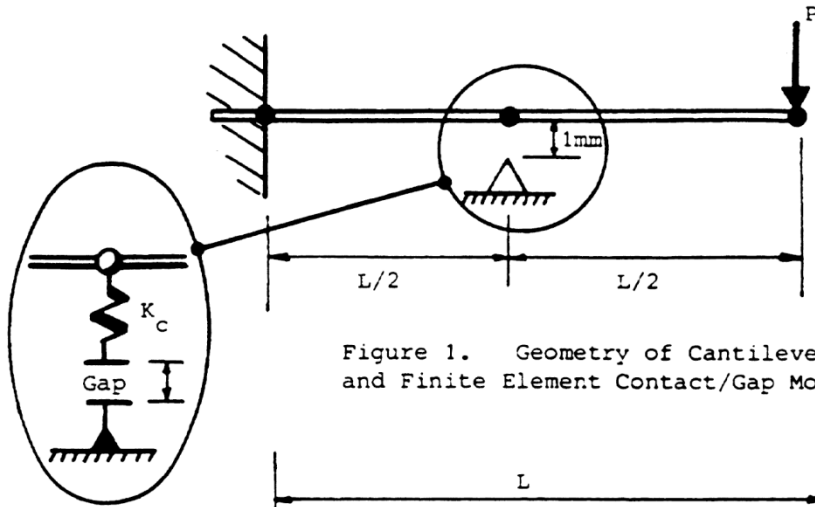


Figure 1. Geometry of Cantilever and Finite Element Contact/Gap Model

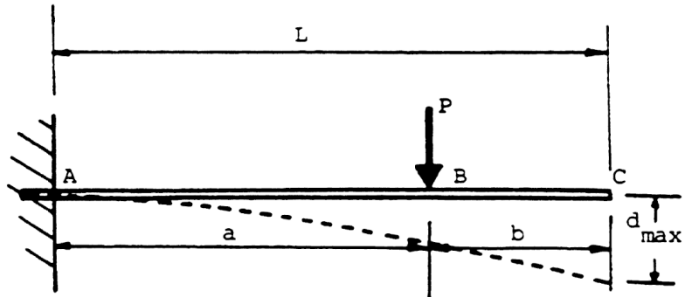


Figure 2. Theory of Free Cantilever

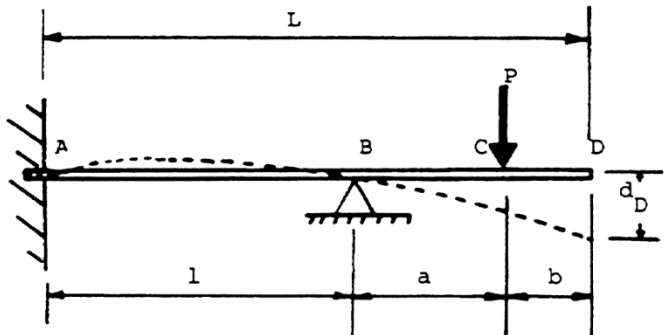


Figure 3. Theory of Propped Cantilever.

Example 11.1.1

Eigenvalue Analysis Of Pinned Double Cross

Keywords

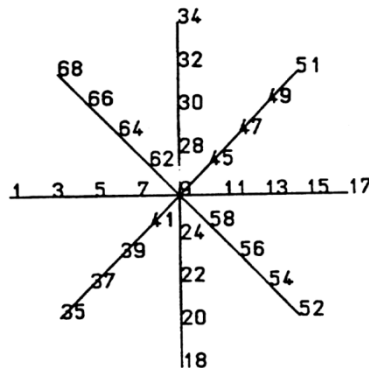
Superelements, Eigenvalue Analysis, Generalised Coordinates

Description

The eigenvalues of a pinned double cross are calculated using a full mesh. The structure is then partitioned into three superelements and the same analysis is repeated. Generalised coordinates are used to improve the solution.

Finite Element Model

Superelement 1 is defined by arms with node numbers 68-9, 1-9, and 35-9, superelement 2 by 34-9 and 18-9 and superelement 3 by 51-9, 17-9, and 52-9. The master freedoms are those of node 9.



Geometry

Length of arms	5 m
Arm cross-sectional area	0.125 m ²

Material properties

Young's modulus	200.0 x10 ⁹
Density	8x10 ³ kg/m ³

Boundary Conditions

Pinned at each support.

Solution Comparison

The lowest 16 eigenvalues of the full mesh compared to [1] are:

Eigenvalue (Hz)		
Modes	Reference	Full mesh
1	11.336	11.336
2-3	17.687	17.687
4-8	17.715	17.715
9	45.477	45.477
10-11	57.364	57.364
12-16	57.683	57.683

The problem has multiple and close eigenvalues for which the corresponding eigenvectors are detailed in Figure 1. Surprisingly, there is no symmetry associated with the multiple vectors at the higher modes. The structure is split into superelements which are connected at node 9. There are only three eigenvalues associated with the reduced structure.

Eigenvalue (Hz)		
Modes	Full mesh	Reduced mesh (master freedoms only)
1	11.336	14.411
2-3	17.687	175.866

The eigenvalues of the reduced structure do not adequately describe the behaviour of the complete structure since only three degrees of freedom are used to simulate the complete structure. To improve the estimate, additional freedoms called generalised coordinates are introduced. Generalised coordinates are fictitious freedoms that are used to enhance the reduced stiffness and mass of the individual superelements by using the modes of vibration of the individual superelements.

Figure 2 details the three lowest modes of each of the superelements. In their calculation, node 9 was fully restrained; therefore they correspond to the first mode of a beam which is simply supported at one end and encastre at the other. Superelement 2 has only two arms, thus the third mode corresponds to the next highest mode for the beam. Including generalised coordinates into the computations the lowest 9 modes are:

Modes	Eigenvalue (Hz)	
	Full mesh	Reduced mesh (master freedoms + 3 generalised coordinates)
1	11.336	11.343
2-3	17.687	17.687
3		17.687
4-8	17.715	17.715
9	45.477	53.404

There is a large improvement in the accuracy of the analysis. The best results are obtained for modes 4-8. In this instance node 9 is stationary and the generalised coordinates exactly represent the full eigenvectors.

Superelement Analysis Sequence

- a) Solve with Master freedoms only
 - (i) Generate superelements 1, 2, 3
 - (ii) Combine superelements and solve eigen problem
- b) Solve with Master freedoms + Generalised coordinates
 - (i) Generate superelements with modal freedoms defined
 - (ii) Combine superelements and solve eigen problem

References

1. Test No FV2, The Standard NAFEMS benchmarks, NAFEMS.

Input Data

- X11D11A.DAT
- X11D11B.DAT
- X11D11C.DAT
- X11D11D.DAT
- X11D11E.DAT
- X11D11F.DAT

X11D11G.DAT

X11D11H.DAT

X11D11I.DAT

a) Solve complete structure

b) Use superelements with master freedoms only

(i) Create superelement 1

(ii) Create superelement 2

(iii) Create superelement 3

(iv) Solve eigenvalue analysis

c) Use superelements with master freedoms and generalised coordinates

(i) Create superelement 1

Note for other superelements 2 and 3 include GENERALISED COORDINATES command

(ii) solve for eigenvalues of combined structure

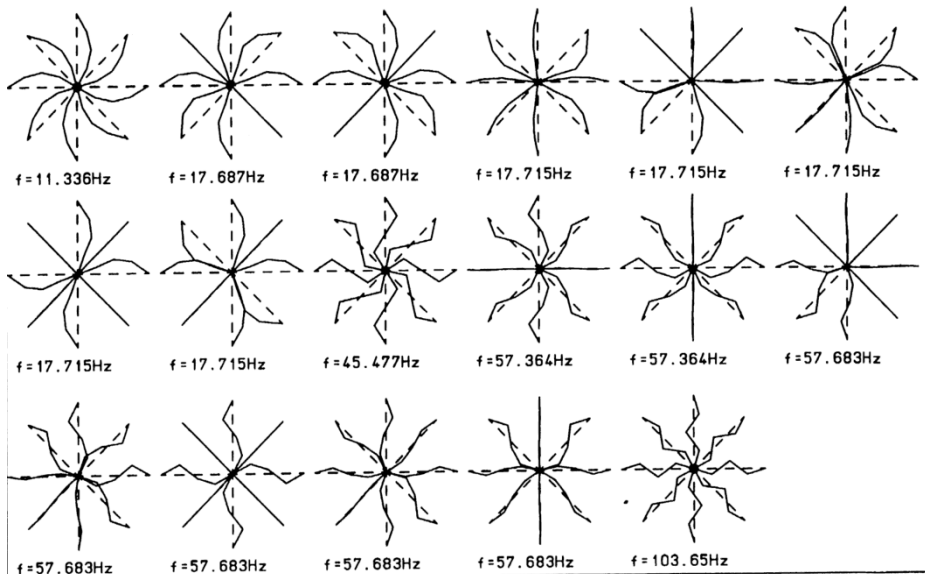


Figure 1 Eigenvectors of Pin-Ended Double Cross.

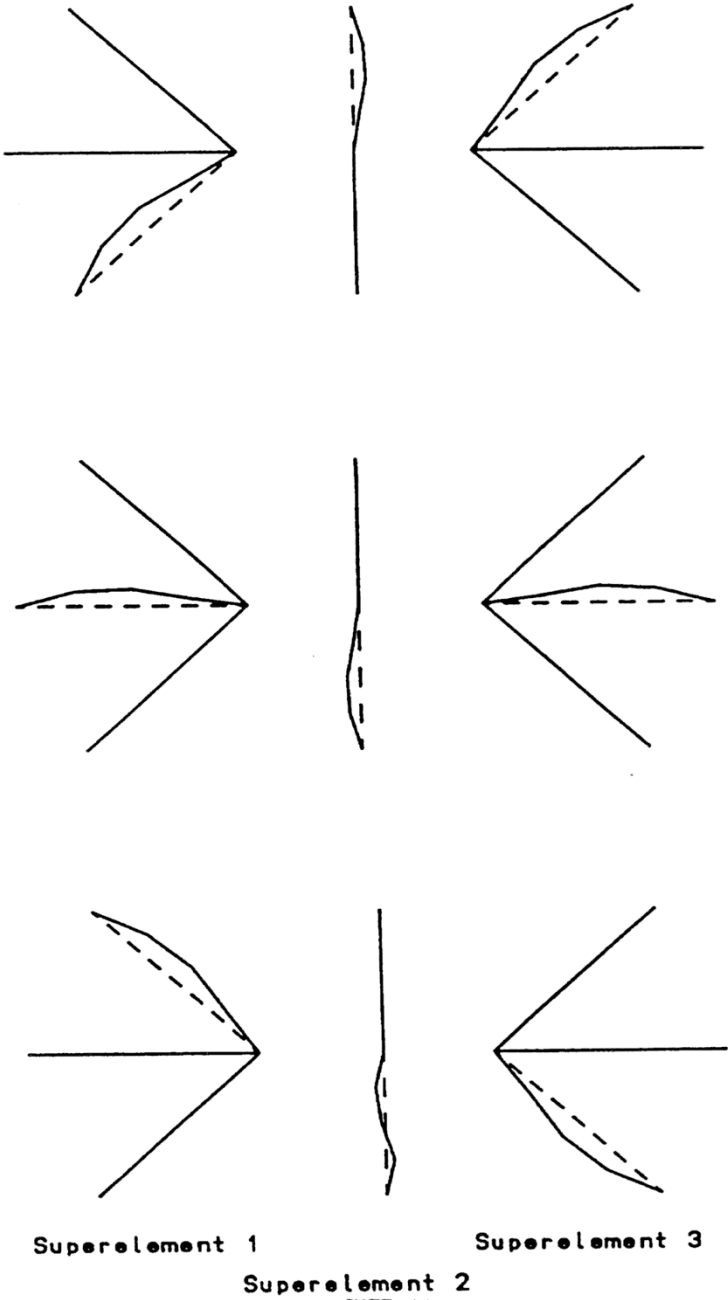


Figure 2 Generalised Coordinates.

Example 11.5.1

Tip Loaded Cantilever Analysed Using Superelements

Keywords

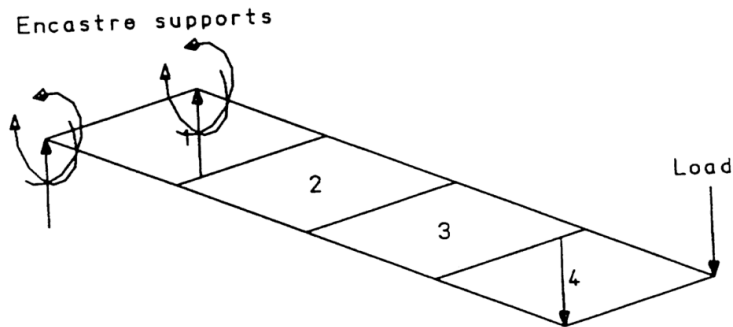
Superelements, Static Analysis

Description

A cantilever is divided into two superelements, one modelling the root, the other the free end. The superelements are assembled and load is applied. Displacement and stresses of the superelements are then recovered using the restart file for the root and by re-defining the superelement data for the tip.

Finite Element Model

Elements 1 and 2 form the root superelement, whilst 3 and 4 constitute the tip superelement.



Geometry

Length	4
Width	1
Thickness	0.05

Material properties

Young's modulus	200.0×10^{11}
Poisson's ratio	0.3

Load

Concentrated load of -1 applied at cantilever tip (total load=-2)

Boundary Conditions

Encastre at fixed end

Solution Comparison

Moment at restrained nodes = $4x-2/2 = -4$

Shear force = $2/2 = 1$

Analysis Sequence

- (i) Generate root superelement - use RESTART WRITE to save superelement data
- (ii) Generate tip superelement - RESTART WRITE is not used so a full solution is required to recover superelement data
- (iii) Solve superelement with applied concentrated loads
- (iv) Recover root data using RESTART READ
- (v) Recover tip data using full re-definition of problem

Both superelements are stored in the same external file

CANTLVR.SDA

If a restart file is not saved, then data defining the elements comprising the superelement must be input in the data file.

Input Data

X11D51A.DAT

- (i) Create root superelement
- (ii) Create tip superelement
- (iii) Assemble root and tip superelement into cantilever and apply load
- (iv) Recover root stresses and displacements using restart file to define superelement
- (v) Recover tip stresses by re-defining superelement data input

Example 12.1.1

1-D Soil Consolidation

Keywords

Consolidation, Linear, Nonlinear, Transient

Description

A soil column fixed along its base and subjected to uniform vertical load applied along its upper face is analysed by plane strain and 3D two phase elements. In order to establish 1D soil consolidation, proper horizontal constraints are applied to the column.

Geometry, Boundary and Loading Conditions

distributed load $q = 100$, undrained conditions (p free) applied at time 0; drainage ($p = 0$) is provided in the subsequent time steps

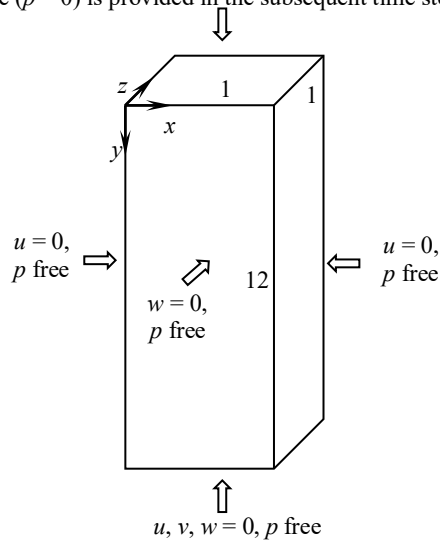


Figure 1

The 3D model of the column is shown in Figure 1, together with boundary and loading conditions. In the plane strain analysis, only one xy section (projection of the 3D model in z -direction) is considered.

Discretisation

In the 3D analysis, the column is discretised by 96 hexahedral (HX20P) elements (four columns of 24 elements as shown in Figure 2); in the plane strain analysis, it is discretised by 48 quadrilateral (QPN8P) elements (two columns of 24 elements) (without discretisation in the Z-direction).

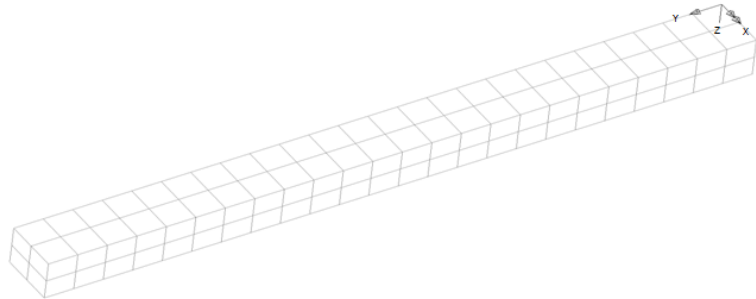


Figure 2

Material properties

Linear material properties:

Effective Young's modulus of the soil $E' = 6.0 \times 10^3$

Poisson's ratio $\nu = 0.0$ (1D deformation)

Consolidation data:

Bulk modulus of pore fluid $K_w = 2.2 \times 10^{15}$

Soil permeability factor $\kappa_x = \kappa_y = \kappa_z = 0.02$

Porosity $\eta = 1$

Unit weight of water $\gamma_w = \rho g = 10$

Mohr-Coulomb material properties:

Cohesion of the soil skeleton $c = 20$

Angle of friction $\phi = \pi/6$

Theory

Firstly, a linear analysis is carried out, then, the same linear problem is solved using non-linear solution facilities. The target results for these two cases are the Terzaghi 1D consolidation analytical solution. The results for the displacement at the top and the pore pressure at the bottom at specific times are (Craig, 1974):

Time (t)	0.0	0.1	0.5	1.0	1.999
$v(0, t)$	0.0	0.02061	0.04607	0.06515	0.09208
$p(12, t)$	100.0	100.0	99.8936	97.1388	83.3619

Finally, the problem is solved using the non-linear Mohr-Coulomb material model; the final displacements, stresses and plastic strains should be the same as those obtained by their counterpart continuum elements using drained properties.

All analyses are run for a total time of 2 units using a constant time step of length $\Delta t = 0.1$ units after the initial conditions have been established at time $t = 0.001$ units.

Reference

1. Craig, R.F. Soil Mechanics. Van Nostrand Reinhold Ltd., U.K., 1974.
2. Norris, V.A. The elasto-plastic analysis of soil consolidation with special reference to kinematic hardening. Ph.D. Thesis, Department of Civil Engineering, University College of Swansea, 1980.

LUSAS results

Displacements and pore pressures from QPN8P and HX20P elements for the linear problem using linear (L) and nonlinear (NL) facilities (QPN8P gives identical results for the two cases)

Time (t)		0.001	0.101	0.501	1.001	2.000
$v(0, t)$	QPN8P	0.0	0.01842	0.04497	0.06437	0.09149
	HX20P(L)	0.0	0.01841	0.04493	0.06422	0.09097
	HX20P(NL)	0.0	0.01842	0.04497	0.06437	0.09149
$p(12, t)$	QPN8P	100.0	99.9968	99.5893	96.5290	83.3734
	HX20P(L)	99.9984	99.8649	99.0530	95.6493	82.1417
	HX20P(NL)	100.000	99.9968	99.5893	96.5290	83.3734

The above linear consolidation solutions by elements QPN8P and HX20P are satisfactory considering the coarse mesh adopted. A finer mesh at the permeable boundary and a smaller time step can further improve the accuracy of the solution.

In 3D linear consolidation analysis, slight out-of-balance may occur, i.e. the reaction force becomes slightly different from the applied load. This effect becomes more serious with softer soils and when increasing the number of elements. This is because of the ill conditioning of the stiffness matrix due to the big difference in the amplitude of displacements and pressures, as also noticed by Norris (1980). This problem disappears when we solve the linear transient problem using nonlinear control.

The results from QPN8P and KHX20P elements using a Mohr-Coulomb plasticity model are:

Time (t)		0.001	0.101	0.501	1.001	2.000
$v(0, t)$	QPN8P	0.0	0.01862	0.04556	0.06523	0.09273
	HX20P	0.0	0.01862	0.04556	0.06523	0.09273
$p(12, t)$	QPN8P	100.0	99.9968	99.5902	96.5392	83.4284
	HX20P	100.0	99.9968	99.5902	96.5392	83.4284

They are close to the above linear solution; when using a non-linear material model, the final displacements are somewhat larger than the linear material model due to the onset of yielding. The final displacements, stresses and plastic strains agree well when compared with their counterpart continuum elements.

Input data

- x12d11a.dat** (Plane strain, linear analysis)
- x12d11b.dat** (Plane strain, linear problem with nonlinear control)
- x12d11c.dat** (Plane strain, nonlinear material)
- x12d11d.dat** (3D, linear analysis)
- x12d11e.dat** (3D, linear problem with nonlinear control)
- x12d11f.dat** (3D, nonlinear material)

Example 12.1.2

Isothermal Drainage of Water from a Sand Column

Keywords

Consolidation, Geostatic, Nonlinear, Transient, Unsaturated

Description

This example simulates the experiment performed by Liakopoulos [1] on desaturation of a column of very fine Del Monte sand due to gravitational effects. Before the start of the experiment, water was continuously added from the top and allowed to drain freely at the bottom through a filter, until uniform flow (i.e. fully saturated) conditions were established. At the start of the experiment, the water supply ceased and water flows out from the bottom due to the desaturation process, and also to the squeezing effect of soil deformation.

Geometry, Boundary and Loading Conditions

In accordance with [2, 3], a column of soil with height 1m and width 0.1m is analysed. The boundary conditions are

lateral surface	$q^w = 0, u = 0$ (impervious and constrained)
top surface	$q^w = 0, t > 0$
bottom surface	$p^c = 0$ (free water outflow) for $t > 0, u = v = 0$

The initial conditions are: at $t = 0, p^c = 0$ at all nodes (i.e. full saturation with water), which corresponds to a steady flow of water through the sand column. Furthermore, a state of mechanical equilibrium is assumed for $t = 0$. All the displacements are related to these initial displacements which correspond to the equilibrium state.

Only gravity of soil and water is considered.

Discretisation

The column is discretised into 10 uniform 2D QPN8P or 3D HX20P (with thickness of 0.1m) elements along the height.

Material properties

Deformable linear elastic soil and isotropic permeability are assumed. The porosity and hydraulic properties of Del Monte sand were measured by Liakopoulos [1] in an independent set of experiments.

Young's modulus*	$E = 1.3 \text{ MPa}$
Poisson's ratio*	$\nu = 0.4$
Solid grain density	$\rho^s = 2000 \text{ kg m}^{-3}$
Liquid density	$\rho^w = 1000 \text{ kg m}^{-3}$
Porosity	$n = 0.2975$
Intrinsic permeability	$\kappa = 4.5 \times 10^{-13} \text{ m}^2$
Water viscosity	$\mu^w = 1 \times 10^{-3} \text{ Pa s}$
Air viscosity	$\mu^g = 1.8 \times 10^{-5} \text{ Pa s}$
Gravitational acceleration	$g = 9.80665 \text{ m s}^{-2}$
Atmospheric pressure (T = 293.15K)	$p_{atm} = 101 \text{ 325 Pa}$
Biot's constant*	$\alpha_b = 1$
Bulk modulus of solid grains*	$K_s = 1.0 \times 10^6 \text{ MPa}$
Bulk modulus of water*	$K_w = 2.0 \times 10^3 \text{ MPa}$

(* These mechanical parameters adopted by Lewis and Schrefler [2] were not measured by Liakopoulos [1])

Liakopoulos [1] used the following saturation-capillary pressure and relative permeability-saturation relationships in isothermal conditions, valid for water saturation $S_w \geq 0.91$

$$S_w = 1 - 1.9722 \times 10^{-11} p_c^{2.4279}$$

$$\kappa^{rw} = 1 - 2.207(1 - S_w)^{1.0121}$$

which can be fitted by the relationships of Valiantzas [4] with $n = 3.207$, $w = 0.522$ and $h_c = -1.654$; the maximum errors in S_w and κ^{rw} are 5.4% and -3.2%, respectively.

Reference

1. Liakopoulos, A.C. Transient flow through unsaturated porous media. PhD thesis, University of California, Berkeley (CA), USA, 1965.
2. Lewis, R.W. and Schrefler, B.A. The finite element method in the static and dynamic deformation and consolidation of porous media. John Wiley & Sons Ltd, Chichester, 1998.
3. Kolditz, O. and Shao, H. (Eds) OpenGeoSys developer-benchmark-book. OGS-DBB 5.04, UFZ Publisher, 2010.

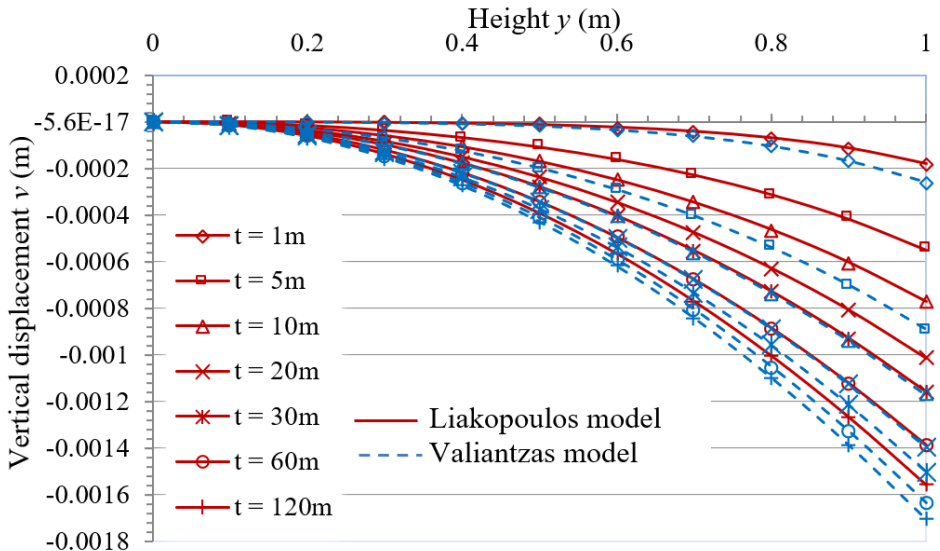
4. Valiantzas, J.D. Combined Brooks-Corey/Burdine and van Genuchten/Mualem closed-form model for improving prediction of unsaturated conductivity. *J. Irrig. Drain Eng.* 137: 223-233, 2011.

LUSAS results

We first carry out an initial ($t = 0$) nonlinear static (or Geostatic) analysis to the column under gravity with the given displacement condition and $p^w = 0$ at all nodes to ensure an equilibrium geostatic stress field. The obtained effective stresses are transformed into initial stresses for the subsequent transient coupled pore diffusion/stress analysis from $t > 0$.

The timestep size is controlled by the target change in water pressure and the target change in saturation. Up until 8 seconds the change in water pressure is critical afterwards the timestep is controlled by the change in saturation. The target change of pressure is set to 1Pa and the target change in saturation to 0.001. 3×3 full Gauss integration was adopted.

Figure 1 shows the vertical displacement and water pore pressure versus height at different times obtained by QPN8P. The results from HX20P are identical to those from QPN8P. When the $S_w - p^c$ and $\kappa^{rw} - S_w$ relationships of Liakopoulos are adopted (input in tabular form), the obtained results (solid lines in Figure 1) are the same as in the literature [2, 3]. If the deformability of the solid grains is considered, i.e. $K_s = 10^6$ MPa is used instead of an infinite value, the change in the results is negligible. However, when the fitted Valiantzas relationships [4] with $n = 3.207$, $w = 0.522$ and $h_c = -1.654$ are used, evident differences are noticed in the results (dash lines in Figure 1), especially at intermediate stages, e.g. $t = 5, 10$ and 20 m.



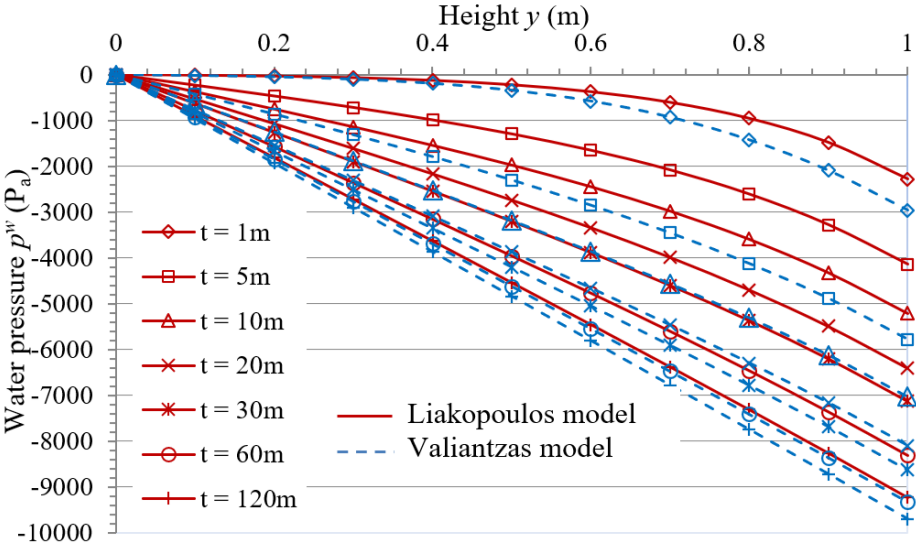


Figure 1

Input data

- x12d12a.dat (Plane strain QPN8P element)
- x12d12b.dat (3D HX20P element)

Example 12.1.3

Volumetric deformation of unsaturated soils

Keywords

Nonlinear, Unsaturated, Barcelona Basic Model

Description

Selected triaxial stress paths involving wetting, drying and increasing confining stress are modelled to demonstrate the capabilities of the Barcelona Basic Model (BBM) and agreement with the results originally presented in [1].

Geometry, Boundary and Loading Conditions

A unit cube is restrained on three faces and loaded with face loads in each of the other faces to impose a uniform pressure. Pore water pressure is prescribed at all of the nodes with a pore water pressure degree of freedom. The face load and pore water pressure are then changed through the use of load curves to give different combinations of changes in suction and pressure.

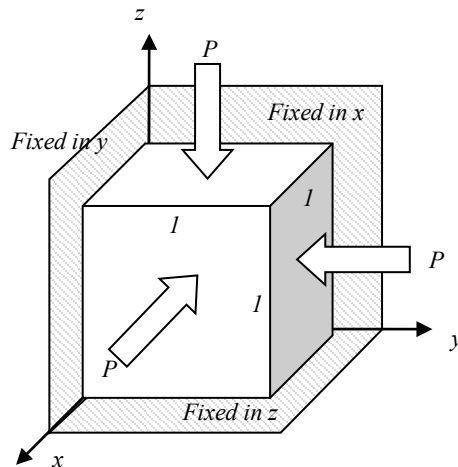


Figure 1

The 3D hexahedral element (HX20P) is shown in Figure 1, together with boundary and loading conditions. In the plane strain analysis, only one xz section (projection of the 3D model in y -direction) is considered using a quadrilateral (QPN8P) element.

The pressure applied through face loads (P) and the suction (equal to the negative pore water pressure) (u) are varied using load curves as follows:

Path	u (MPa)	P (MPa)	u (MPa)	P (MPa)	u (MPa)	P (MPa)	u (MPa)	P (MPa)
Wetting 1	0.2	0.15	0.2	0.6	0.1	0.6	0.0	0.6
Wetting 2	0.2	0.15	0.1	0.15	0.1	0.6	0.0	0.6
Wetting 3	0.2	0.15	0.1	0.15	0.0	0.15	0.0	0.6
Drying 1	0.0	0.15	0.0	0.6	0.1	0.6	0.2	0.6
Drying 2	0.0	0.15	0.1	0.15	0.1	0.6	0.2	0.6
Drying 3	0.0	0.15	0.1	0.15	0.2	0.15	0.2	0.6

The wetting tests here begin at a net pressure (input as a residual stress) of 0.15MPa and a suction of 0.2MPa and are subsequently loaded and wetted through different paths until a final net pressure of 0.6MPa and a suction of 0MPa are reached. The drying tests also begin at 0.15MPa but in a fully saturated and are dried and loaded until a final net pressure of 0.6MPa and a suction of 0.2MPa are reached.

Material properties

The following parameters are given in [1]

M	G	λ_0	κ	r	κ_s	p_{c0}	p_{ref}	β
1	10MPa	0.2	0.02	0.75	0.008	0.1MPa	0.1MPa	12.5MPa ⁻¹

These have been adjusted to allow for use of Poisson’s ratio instead of shear modulus (although due to the applied boundary conditions this does not have any effect here). Additionally, to account for the bi-logarithmic definition of λ and κ they have been modified to the following. To exactly replicate the existing behaviour the semi-log parameters would be divided by the specific volume to get the bi-log parameters. As the void ratio changes, an average value which fits the data has been chosen. It can be seen in the following examples that this approach gives a good overall fit to the response.

M	ν	λ_0	κ	r	κ_s	p_{c0}	p_{ref}	β
1	0.3	0.111	0.0111	0.75	0.00421	0.1MPa	0.1MPa	12.5MPa ⁻¹

The initial yield surface position at zero suction is set at 0.2MPa and the movement of the LC curve can be seen as plastic yielding causes this to increase to 0.6MPa. The specific volume is set initially to 1.9.

The tests are undertaken without any two phase material definition so that an effective stress is not calculated in order to replicate the behaviour seen in [1] which uses net stress.

Reference

1. Alonso, E. E., Gens, A. & Josa, A. A constitutive model for partially saturated soils Géotechnique 40, No. 3, 405-430 (1990).

LUSAS results

The stress paths described above are plotted along with the development of the LC curve. The volumetric response is plotted on top of the behaviour in [1], it can be seen that excellent agreement is observed for all stress paths.

Wetting and loading:

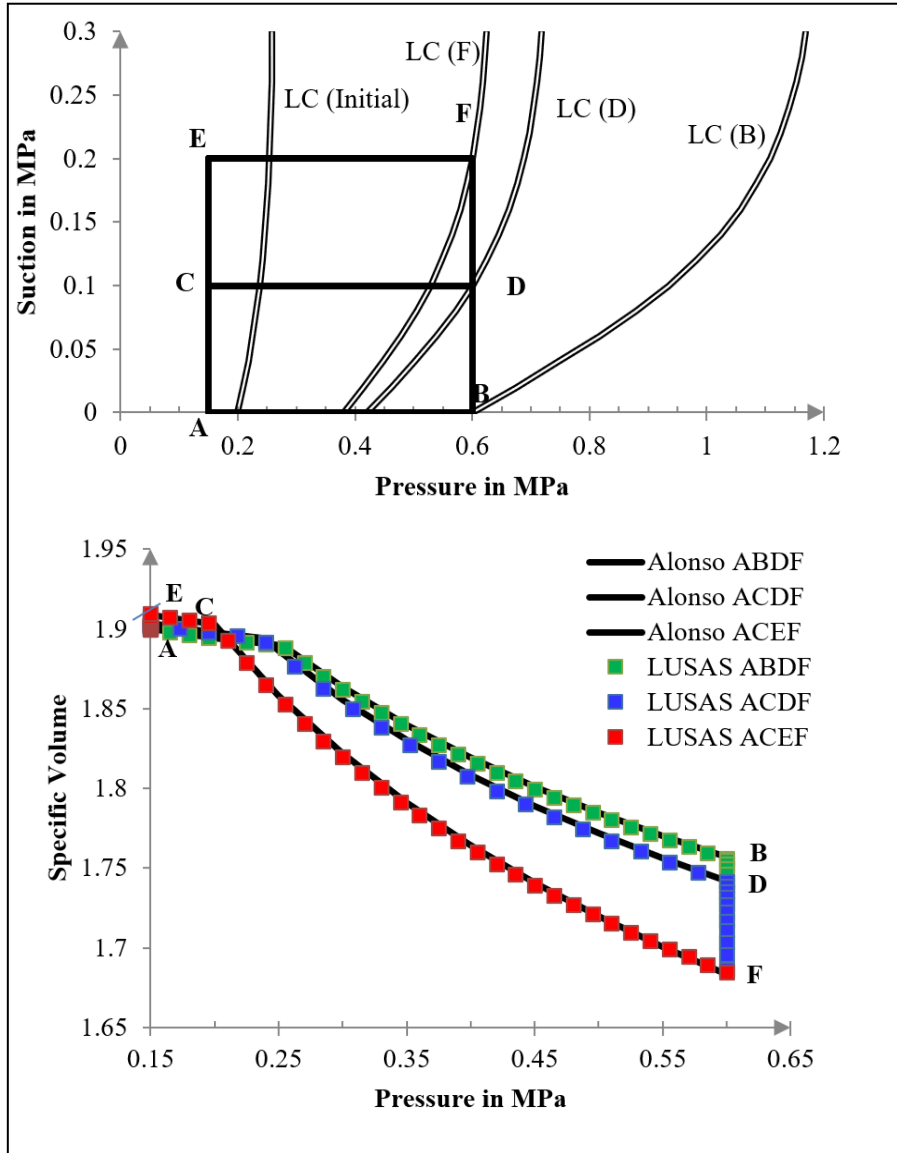


Figure 2

Drying and loading:

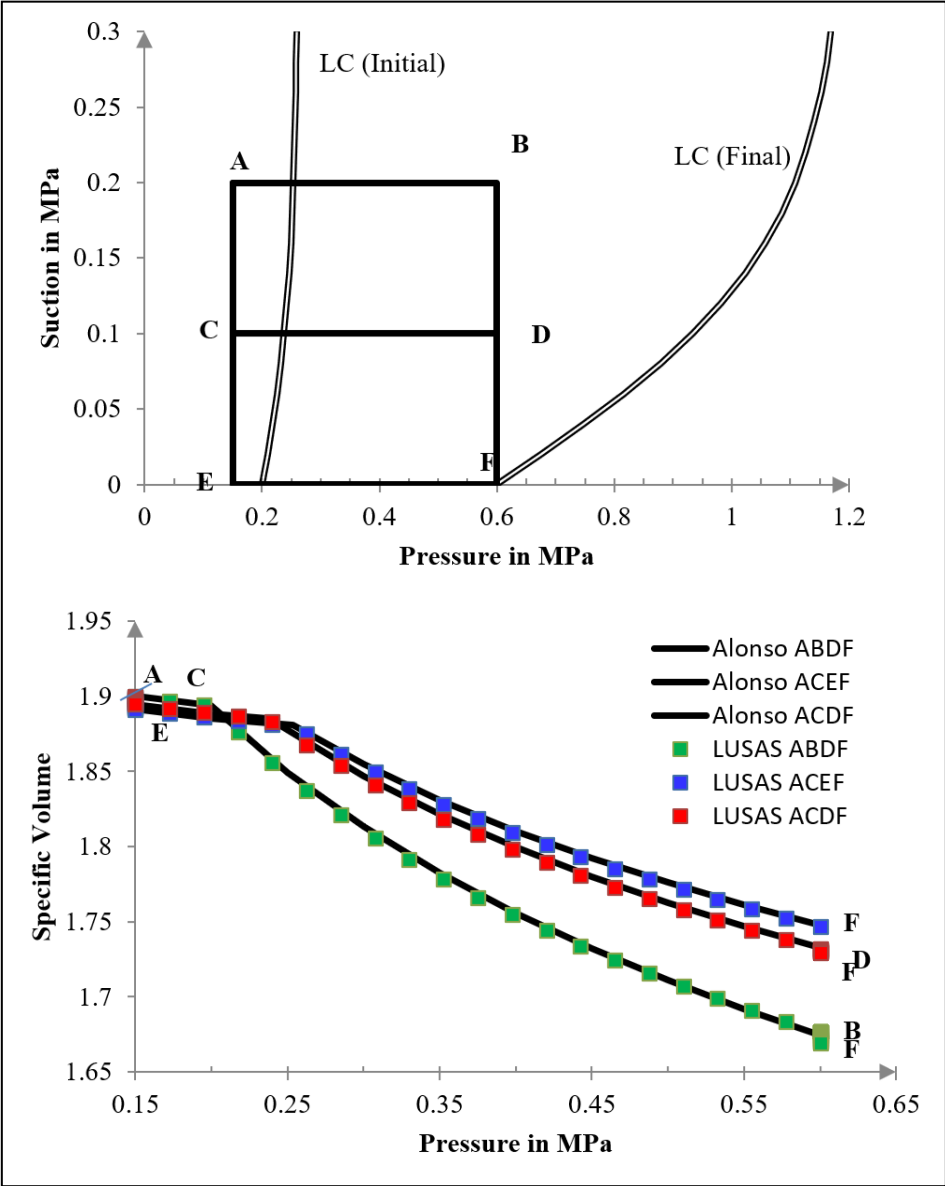


Figure 3

The 2D and 3D elements yielded identical results so only one set of graphs are shown.

Input data

E02N96.dat	(2D wetting then loading of soil at $u=0$ MPa)
E02N102.dat	(2D wetting, loading of soil at $u=0.1$ MPa and further wetting)
E02N98.dat	(2D loading of soil at $u=0.2$ MPa and then wetting)
E02N104.dat	(2D drying and then loading of soil at $u=0.2$ MPa)
E02N105.dat	(2D drying, loading of soil at $u=0.1$ MPa and further drying)
E02N106.dat	(2D loading of soil at $u=0$ MPa and then drying)
E18N46.dat	(3D wetting then loading of soil at $u=0$ MPa)
E18N52.dat	(3D wetting, loading of soil at $u=0.1$ MPa and further wetting)
E18N48.dat	(3D loading of soil at $u=0.2$ MPa and then wetting)
E18N54.dat	(3D drying and then loading of soil at $u=0.2$ MPa)
E18N55.dat	(3D drying, loading of soil at $u=0.1$ MPa and further drying)
E18N56.dat	(3D loading of soil at $u=0$ MPa and then drying)

Example 13.1.1

Coupled Hygro-Thermal-Mechanical Analysis

Keywords

Coupled Hygro-Thermal-Mechanical Analysis

Description

This example is a concrete reinforced beam under a constant sustained service load for a period in excess of 400 days, experimentally tested by Gilbert, [1, 2]. The model is shown in Fig 1. Dimensions are in [mm].

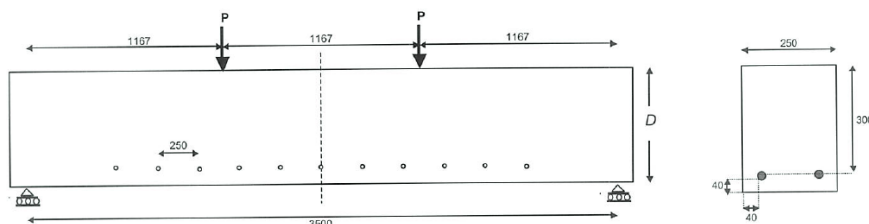


Fig. 1

Load and dimension of beam tested by Gilbert [1, 2]. $D=348\text{mm}$; bar diameter $\phi=16\text{ mm}$;
 Case B1-a: $P=18.6\text{ kN}$, (50% of ultimate load)
 Case B1-b: $P=11.8\text{ kN}$, (30% of ultimate load)

The properties of concrete at various ages after casting were measured from companion cylinders and prisms using standard test procedures and are give in Table 1.

Material Property (in MPa)	Age (days)			
	7	14	21	28
Compressive strength	12.9	18.3	23.1	24.8
Flexural tensile strength (mod. of rupture)	3.0	3.7	4.3	5.6
Indirect tensile strength (split cylinder)		2.0	2.6	2.8
Modulus of elasticity ()	21090	22820	23990	24950

Table 1. Concrete properties

The creep coefficient φ_{cc} for concrete first loaded at age 14 days and the shrinkage strain ε_{sh} were measured on 300mm diameter cylinders and slab specimens 160 mm thick, respectively, and the values at various concrete ages are given in Table 2. At present, this data is not used in the analysis.

Age (days)	14	16	21	27	53	96	136	200	242	332	394
φ_{cc}	0	0.14	0.36	0.48	0.92	1.15	1.29	1.40	1.50	1.64	1.71
ε_{sh}	0	-14	-109	-179	-403	-591	-731	-772	-784	-816	-825

Table 2. Creep coefficient and shrinkage strain ($\times 10^{-6}$)

The specimens were undisturbed in their moulds for 3 days. After the 3rd day the specimens were removed from the moulds and kept continuously moist by a thick and complete covering of wet hessian to minimise the loss of moisture from the specimens. After 14 days the covers and wet Hessian were removed, the demec strain targets were glued to the concrete surface and initial measurements were recorded. Beam specimens were subjected to two concentrated loads located at the third of the span and applied via steel channel beams.

Discretisation

A quarter of the beam is modelled by 2208 8-node solid elements HX8/HHT8 and 46 2-node bar elements BRS2/BFS2, Fig. 2.

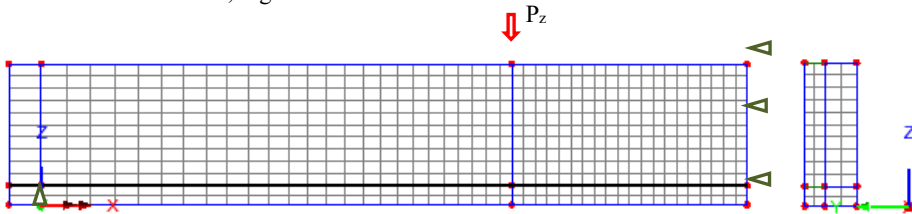


Fig. 2. Model discretization

Material properties

Concrete hygro-thermal - main

k_{T0}	Thermal conductivity [W/m.K]	= 2.0	(*)
C_{s0}	Specific heat capacity of dry concrete [J/kg.K]	= 900	(*)
ρ_{s0}	Density of dry concrete [kg/m ³]	= 2400	(*)
K_{I0}	Permeability (intrinsic) [m ²]	= 0.1E-18	(*)
V_{ea}	Entrapped air volume ratio [-]	= 0.023	(*)

Concrete hygro-thermal - advanced

f_s	Tortuosity coefficient [-]	= 0.01	(*)
H_v	Latent heat of evaporation [J/kg]	= 0.0	
k_{T1}	Change of thermal conductivity with temperature [-]	= -0.01	(*)
C_{s1}	Change of specific heat capacity with temperature [-]	= 0.0	(*)
ρ_{s1}	Change of density with temperature [-]	= 0.0	(*)
f_k	Check box 'Thermal conductivity depends on water saturation' = 0 or 1		

Properties that change with temperature are computed from:

$$\rho_s(T) = \rho_{s0} + \rho_{s1}(T - T_{\text{ref}})$$

$$C_s(T) = C_{s0} + C_{s1}(T - T_{\text{ref}})$$

$$k_T(T, S_w) = [k_{T0} + k_{T1}(T - T_{\text{ref}})] [1 + f_k \Phi(S_w)]$$

where:

T_{ref} Built-in reference temperature = 20 °C or 293.14 K, based on model units.

$\Phi(S_w)$ Built-in function of the water saturation S_w

Concrete hygro-thermal – Heat of Hydration

<i>Cement type</i>		Type I (*)
w_{cem}	Mass of cement per unit volume [kg/m ³]	= 350
w_c	Water/Cementitious mass ratio [-]	= 0.45
w_{slg}	Mass of slag per unit volume [kg/m ³]	= 0.0 (*)
w_{pfa}	Mass of fly ash per unit volume [kg/m ³]	= 0.0 (*)
CaO_{pfa}	CaO content of fly ash [%]	= 0.0 (*)
<i>delay</i>	Delay of heat of hydration	= 0.0 (*)

Steel bars thermal

k_T	Thermal conductivity [W/m.K]	= 45.0
ρ_s	Density [kg/m ³]	= 7800
C_s	Specific heat capacity [J/kg.K]	= 450

Note: Since the concrete and steel bars share the same volume it would be more accurate for the bars to have equivalent properties that are computed by subtracting the value of the concrete property from the corresponding steel property. Thus:

$$\begin{aligned}
 k_T^* & \text{ Equivalent bar thermal conductivity [W/m.K]} = 45 - 2 = 43 \\
 \rho_s^* & \text{ Equivalent bar density [kg/m}^3\text{]} = 7800 - 2400 = 5400 \\
 C_s^* & \text{ Equivalent bar specific heat capacity [J/kg.K]} = \frac{7800 \times 450 - 2400 \times 900}{5400} = 250
 \end{aligned}$$

Concrete mechanical - main

E	Young's modulus [N/m ²]	= 25.0E9
ν	Poisson's ratio	= 0.2
ρ	Mass density [kg/m ³]	= 2400
α	Expansion coefficient	= 1.0E-5
f_c	Compressive strength [N/m ²]	= 25.0E6
f_t	Tensile strength [N/m ²]	= 2.24E6
ϵ_c	Strain at peak uniaxial compression	= 2.2E-3 (*)
G_f	Fracture energy per unit area [N/m]	= 130 (*)
β_{ds}	Coefficient of dry shrinkage	= 0.9E-3 (*)
β_{cs}	Coefficient of chemical shrinkage	= 0.1E-3 (*)

Concrete mechanical - advanced

β_r	Biaxial to uniaxial stress ratio	= 1.15 (*)
Z_o	Initial relative position of yield surface	= 0.6 (*)
ψ	Dilatancy factor	= -0.1 (*)
m_g	Constant in interlock state function	= 0.3 (*)
m_{hi}	Contact multiplier on ϵ_o	= 0.5 (*)
m_{ful}	Final contact multiplier on ϵ_o	= 5.0 (*)

r_{σ}	Shear intercept to tensile strength	=1.25	(*)
μ	Slope of friction asymptote for damage	=0.8	(*)
m_{cf}	Multiplier on ϵ_0 to define crack fixity strain	=0.5	(*)
f_{pz}	Fracture process zone width [m]	= 0.06	(*)
it_{fx}	No. of iterations after which cracks are fixed	= 2	(*)
it_{mx}	Max. iterations for fracture strain update	= 2	(*)
R_s	Residual softening factor	= 0.001	(*)
A_p	Material constant A_p	= 0.6	(*)
A_n	Material constant A_n	= 0.75	(*)
Z_1	Contact sharpness Z_1	= 8.0	(*)
Z_2	Contact sharpness Z_2	= 8.0	(*)
C_{LM}	Limit of contact tension	= 3.0	(*)
fm_r	Multiplier on relaxation times	= 1.0	(*)
fm_c	Creep factor multiplier	= 1.0	(*)
fm_p	Pickett factor multiplier	= 1.0	(*)
$\Gamma_{r,min}$	Degree of hydration percolation	= 0.05	(*)
$\Gamma_{r,l}$	Degree of hydration at 1st cure	= 0.5	(*)
m_p	Moisture rate Pickett factor effect [sec^{-1}]	=10.0E-12	(*)
S_{wd}	Saturation start Pickett effect	= 0.85	(*)
τ_{sh}	Short relaxation time [days or its equivalent]	= 10	(*)
τ_{L1}	1 st long relaxation time [days or its equivalent]	= 150	(*)
τ_{L2}	2 nd long relaxation time [days or its equivalent]	= 1100	(*)
c_E	Logistic model coefficient for E	= 12.5	(*)
c_{fc}	Power model coefficient for f_c	= 3.0	(*)
c_{fi}	Power model coefficient for f_i	= 3.0	
T_{40}	Temperature when degradation starts [°C]	= 40	(*)
T_{80}	Temperature when degradation stops [°C]	= 80	(*)
C_{rE}	Finishing degradation coefficient for E	= 0.9	(*)
C_{rc}	Finishing degradation coefficient for f_c	= 0.8	(*)
C_{ri}	Finishing degradation coefficient for f_i	= 0.9	(*)

(*) Default property value

Note:

The true tensile strength f_i is about 80% of the cylinder splitting strength [3]. Thus

$$f_i(t=25days) = 0.8 * 2.8 = 2.24 \text{ MPa}$$

$$f_i(t=14days) = 0.8 * 2.0 = 1.60 \text{ MPa}$$

To achieve $f_i(t=14days)=1.60\text{MPa}$, c_{fi} (default = 1) is set to 3.0

Steel bars mechanical

E	Young's modulus [N/m ²]	= 200.0E9
ν	Poisson's ratio [-]	= 0.3
ρ	Mass density [kg/m ³]	= 7800
α	Expansion coefficient [-]	= 11.0E-6

Note: Since the concrete and steel bars share the same volume it would be more accurate the bars to have an equivalent properties that are computed by subtracting the value of concrete property from the corresponding steel property. Thus:

E	Equivalent bar Young's modulus [N/m ²]	= 175.0E9
ρ	Equivalent bar mass density [kg/m ³]	= 5400

Boundary conditions

(i) Hygro-thermal

Time 0.0 to time 14.0 days (wet Hessian cover) on all external surfaces:

ENVT load: $T_{env} = 20$ °C; $\alpha_T = 5.0$ W/m²K

TPDSP load: RH=1, contact with water.

Time 40.0 to time 400 days. All external surfaces exposed to air.

ENVT load: $T_{env} = 20$ °C; $\alpha_T = 5.0$ W/m²K; RH=0.5; $\alpha_T = -1$

where:

T_{env} Environmental temperature

α_T Convective heat transfer coefficient

RH Relative humidity

α_V Vapour mass transfer coefficient (negative - invokes Chiltern-Colburn analogy)

(ii) Structural

Support Z=0 along Y axis; Support X=0 on plane of symmetry.

Global distributed load along the half-width: $P_z = -P/(\sqrt{0.125})$

Case B1-a (P=18.6/ kN): $P_z = 18.6/(\sqrt{0.125}) = -74.4$ N/m

Case B1-b (P=11.8 kN) $P_z = 11.8/(\sqrt{0.125}) = -47.2$ N/m

Time steps

Hygro-thermal analysis

A reduction of the time step at time 14 days is required when Hygro TPDSP is removed and replaced by ENVT. Time step of 1 day is used until the end of the simulation. Fig 3a

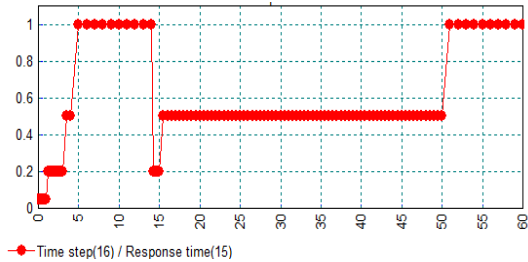


Fig 3a. Hygro-thermal analysis

Variation of Time step [days] vs Response time [days]

Structural analysis

The beam tests start at age 14 days. In the LUSAS analysis the self weight is applied at this age. After that, the sustained load is applied in 200 short time steps. After that, the load remains constant for 400 days. The time steps used up to day 60 are plotted in Fig. 3b. A constant time step of 3 days is used until the end of the simulation (Time=400 days).

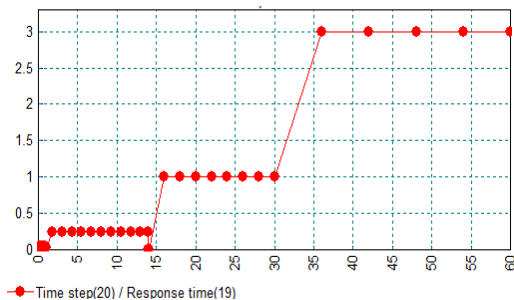


Fig 3b. Structural analysis

Variation of Time step [days] vs Response time [days]

Theory

LUSAS results are compared to experimental results [1, 2], wherever available.

Reference

1. Gilbert, R. I., Nejadi, S., (2004). An Experimental Study of Flexural Cracking in R.C. Members under Sustained Loads, UNICIV Report R-435, School of Civil & Env. Eng., University of New South Wales, Sydney, Australia, (http://www.civeng.unsw.edu.au/staff/ian_gilbert/).
2. Gilbert, R. I. (2013). Time-Dependent Stiffness of Cracked Reinforced and Composite Concrete Slabs, *Procedia Engineering* 57, 19 – 34.
3. Neville, A.M. (2013) *Properties of Concrete*, 5th ed., Pearson Education.

Input Data

X13D11a.DAT

X13D11b.DAT

LUSAS Results

The computed maximum net deflection (i.e. the deflection due to self weight is subtracted) is compared to the experimentally measured one in Fig 4. When the load level is 30% of the ultimate load, test B1-b, LUSAS results agree very well with the experimental results. When the load level is 50% of the ultimate load, test B1-a, there is an 11% underestimation of the final deflection.

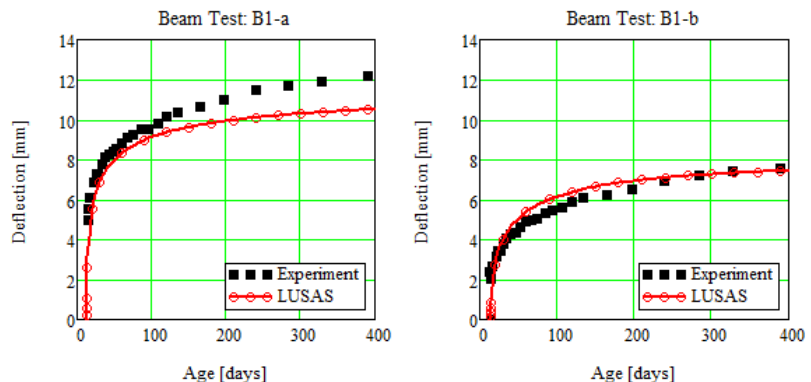


Fig. 4. Creep deflection.

Temperature, degree of hydration and relative humidity distributions are shown in Figs. 5a, 5b and 5c, resp.

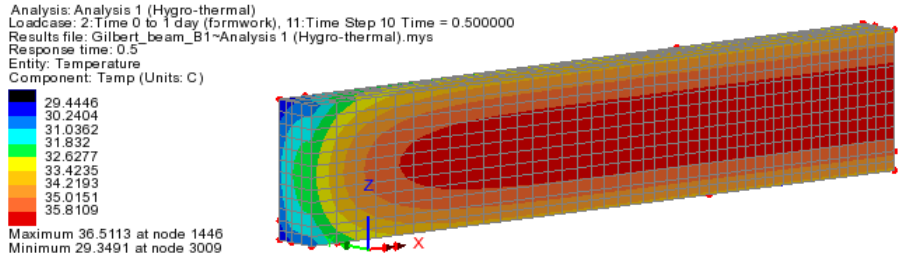


Figure 5a. Temperature distribution at time 0.5 days

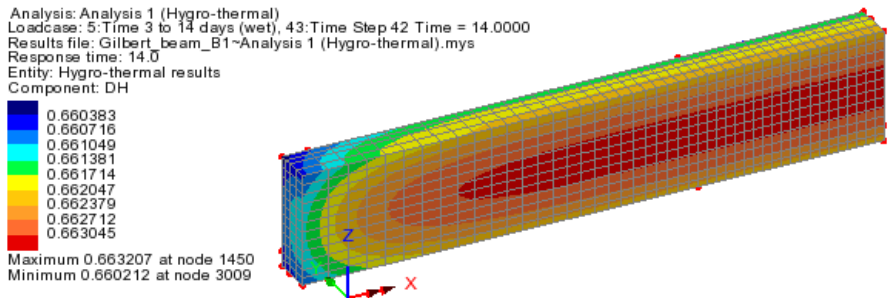


Figure 5.9b. Degree of hydration at time 14.0 days

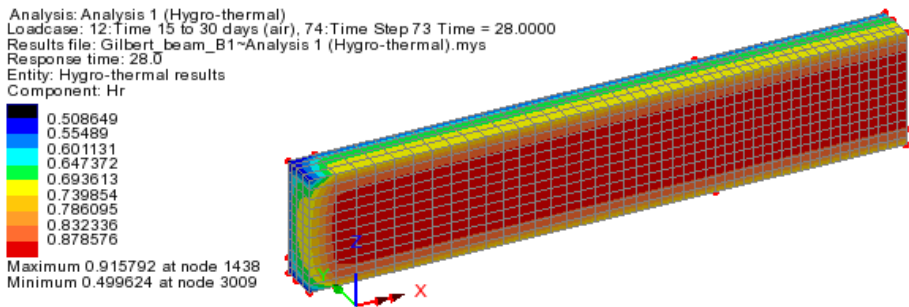


Figure 5.9b. Relative humidity at time 28.0 days

LUSAS time history hygro-thermal results at the beam centre are given in Fig. 6.

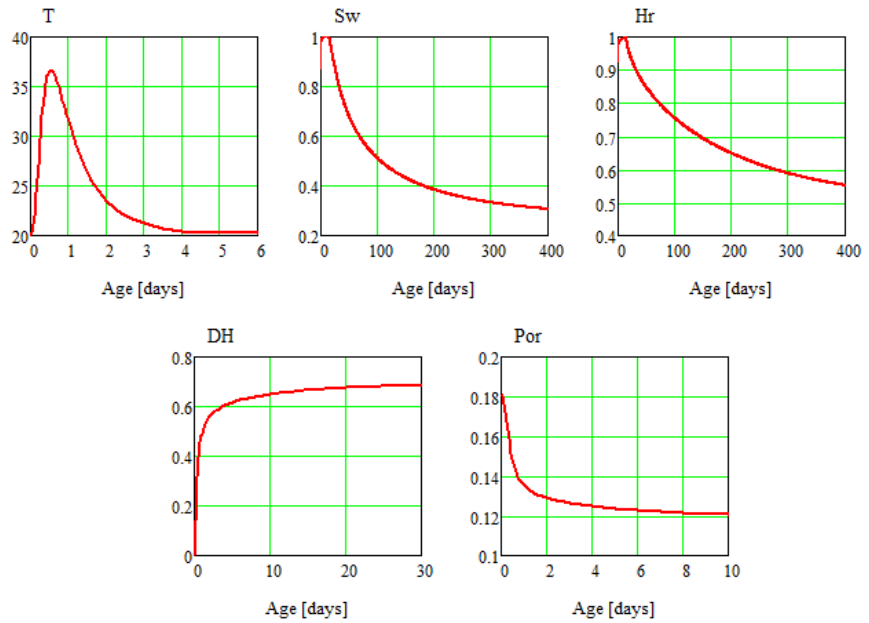


Fig. 6. Hygro-thermal results at beam centre

- T – temperature
- Sw – water saturation
- Hr – relative humidity
- DH – degree of hydration
- Por – porosity

There are no experimental hygro-thermal results to compare with.

The experimental data for the crack widths in beams B1-a and B1-b is given in Gilbert’s Table 7, shown below:

Table 7 Initial and final crack widths for beams containing 2 N16 bars.

Beam or slab	Cover (mm)	Crack width (mm) At first loading			Crack width (mm) After 400 days		
		Avg	Min	Max	Avg	Min	Max
		W_{avg}	W_{min}	W_{max}	W_{avg}	W_{min}	W_{max}
B1-a	40	0.11	0.06	0.13	0.28	0.10	0.38
B1-b	40	0.04	0.02	0.05	0.13	0.10	0.18

LUSAS crack distribution and crack width, CWmax, contour plot for test B1-a at Time=14 days (i.e. just after loading) and Time=400 days, are presented in Figs 7a and 7b, resp.

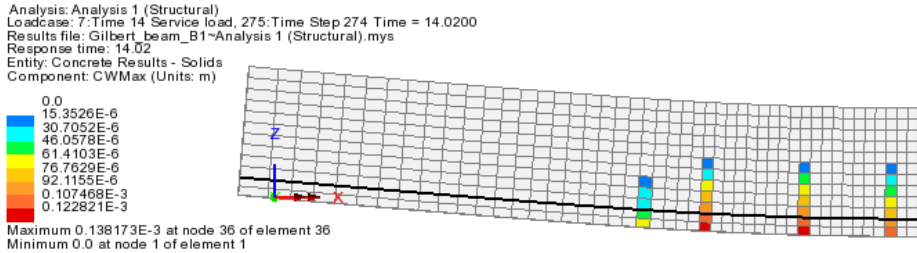


Fig. 7a

Test B1-a: Crack distribution and crack widths at time 14 days, i.e. at first loading
 A – LUSAS: CWmax=0.14 mm
 B – Experiment: CWmax=0.13mm

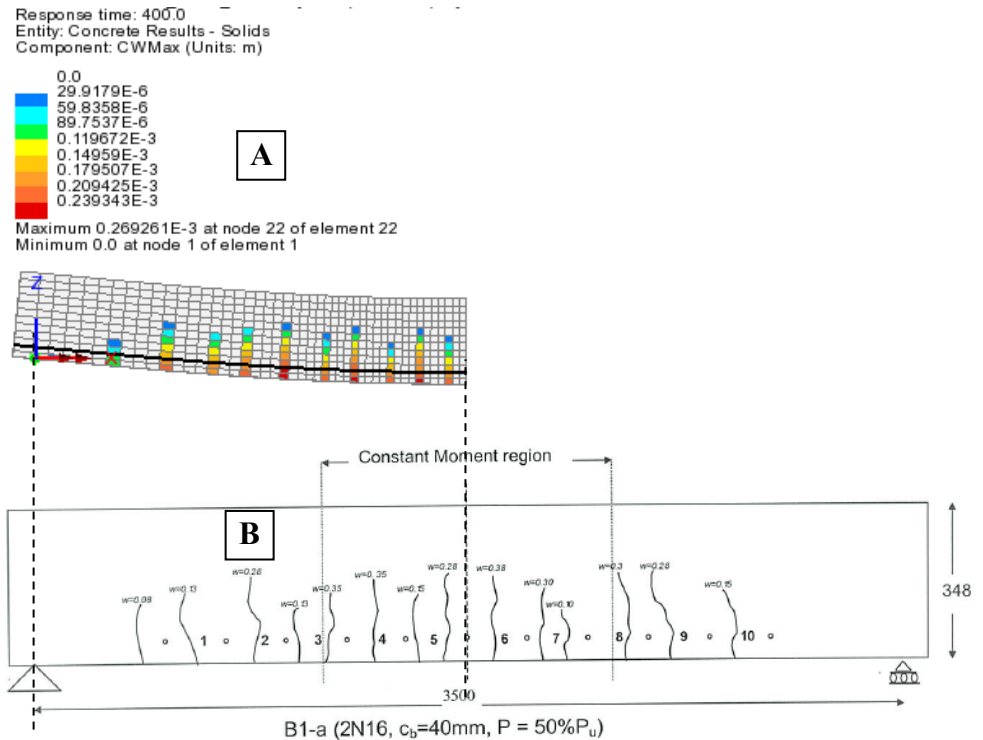


Fig. 7b

Test B1-a: Crack distribution and crack widths at time 400 days:
 A – LUSAS: CWmax=0.27 mm. Number of cracks along half length – 10.
 B – Experiment: CWmax=0.38mm. Number of cracks along full length – 14

LUSAS crack distribution and crack width, CWmax, contour plot for test B1-b at Time=14 days (i.e. just after loading) and Time=400 days, are presented in Figs 8a and 8b, resp.

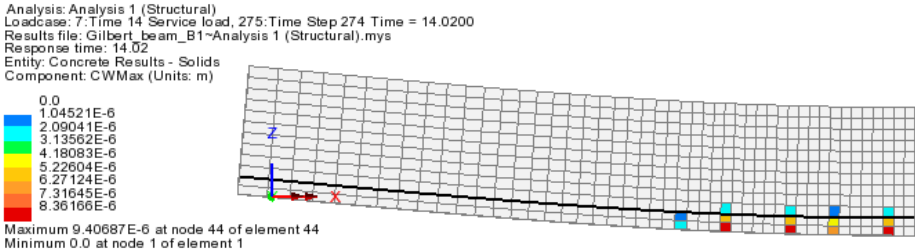


Fig. 7b

Test B1-b: Crack distribution and crack widths at time 14 days, i.e. at first loading
 A – LUSAS: CWmax=0.01 mm
 B – Experiment: CWmax=0.05mm

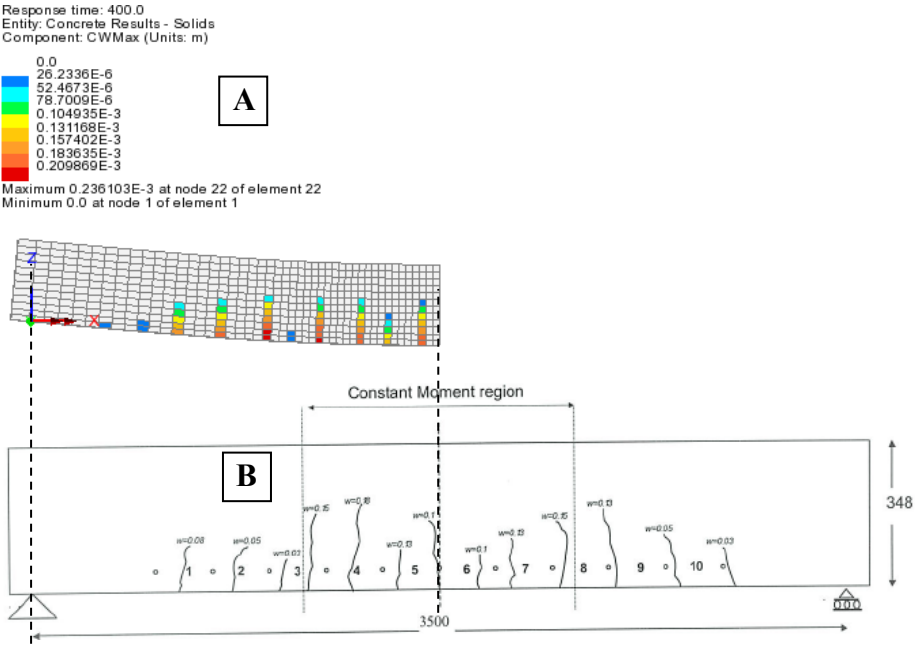


Fig. 8b

Test B1-b: Crack distribution and crack widths at time 400 days:
 A – LUSAS: CWmax=0.236 mm. No of cracks along half length – 7.
 B – Experiment: CWmax=0.18mm (at crack 4). No of cracks along full length – 13

Index

A

ANISOTROPIC, 37, 254
AXISYMMETRIC SHEET, 67, 70
AXISYMMETRIC SHELL, 70, 147
AXISYMMETRIC SOLID, 67, 70, 147,
366

B

BAR, 131
BEAM 3D, 12
BIFURCATION, 131
BOX BEAM, 55
BUCKLING, 121, 276

C

CANTILEVER, 376
CARTESIAN SET CYLINDRICAL, 75
CENTRIPETAL STIFFENING, 137
CIRCULAR PLATE, 67
COFFERDAM, 79
COMPACT TENSION SPECIMEN, 51
COMPOSITE ANALYSIS, 63
CONCRETE, 184, 226
CONDUCTANCE, 91
CONDUCTION, 299, 307
CONDUCTIVITY, 96
CONSTANT STRAIN, 12
CONTACT, 373, 376
CONVECTION, 296
CO-ROTATIONAL, 141
COUPLED ANALYSIS, 343, 346, 350,
355
COUPLED HYGRO-THERMAL-
MECHANICAL ANALYSIS, 401
CREEP, 198, 201
CURVE ASSIGNMENT, 75
CURVE DEFINITIONS, 75
CURVED BEAM, 1, 4

CURVILINEAR COORDINATES, 23
CYCLIC LOADING, 171, 175, 194

D

DAMAGE, 171, 194
DAMPING, 311
DRUCKER-PRAGER, 209, 257

E

ECCENTRIC, 45
EIGENVALUE, 99, 101, 109, 118, 121,
124
EIGENVALUE ANALYSIS, 381
EIGENVECTORS OF STIFFNESS
MATRIX, 115
ELASTIC, 366
ELASTO-PLASTIC, 178, 181, 209, 217,
246, 254, 257, 282, 286, 340
ELASTOPLASTICITY, 163
ENTHALPY, 302
ENVIRONMENTAL NODES, 91

F

FACE LOADING, 75
FIELD, 83, 91
FOURIER, 75, 124
FRACTURE, 15
FRICTION, 178, 246

G

GAP, 376
GENERALISED COORDINATES, 381
GEOMETRIC NONLINEARITY, 128,
137, 144
GROUNDWATER, 79
GUYAN REDUCTION, 109

H

HARMONIC, 314
HEAT, 299, 307
HILL YIELD CRITERION, 290

I

IMPACT, 359, 363
IMPLICIT, 198, 201, 366, 373
INCOMPATIBLE ELEMENTS, 205
INCOMPATIBLE MODELS, 23
INTERFACE MODEL, 246

J

JOINT, 376

L

LAMINATED PLATE, 63
LARGE DISPLACEMENT, 290
LARGE ROTATION, 115
LARGE ROTATION,, 151
LINEAR, 41, 45
LINEAR BUCKLING, 103
LINEAR DYNAMICS, 311
LINEAR ELASTIC, 314
LOAD CYCLING, 163
LOADING, 47

M

MODIFIED VON MISES, 166
MOHR-COULOMB, 209, 217, 257

N

NATURAL FREQUENCY, 118, 340
NONLINEAR, 141, 273, 276, 302, 350,
373
NONLINEAR DYNAMICS, 340
NONLINEARITY, 282

O

ORTHOTROPIC, 37

P

PERIODIC, 314
PHASE CHANGE, 302
PLANE FRAME, 7
PLANE STRESS, 32, 184, 226, 238, 242
PLASTIC, 201
PLASTIC FLOW, 359
PLASTIC WORK, 355
PLASTICITY, 194, 205, 273, 276, 355
PLATE, 37, 41, 45
PRESSURE, 181
PRESSURE VESSEL, 70

R

RADIATION, 296
RECTANGULAR PANEL, 276
REINFORCEMENT, 184, 226
ROTATING MACHINERY, 137

S

SEEPAGE, 79
SEMILOOF, 121
SEMILOOF SHELL, 75, 124, 286
SHAPE FUNCTIONS, 23
SLIDELINE, 359, 366
SLIDELINES, 373
SNAP THROUGH, 144
SOIL STRUCTURE INTERACTION, 246
SOLID, 51
SPHERICAL SHELL, 282, 340
SPRING, 131
STATIC, 373
STATIC ANALYSIS, 386
STEADY STATE, 83, 96
STEP-BY-STEP DYNAMICS, 337
STRESS CONCENTRATION FACTOR,
32
STRESS INTENSITY, 15
SUPERELEMENTS, 381, 386

T

TEMPERATURE DEPENDENT
PROPERTIES, 12
THERMAL CONDUCTION, 83
THERMAL STRESS, 343
THERMAL SURFACES, 91, 350

THREE DIMENSIONAL BEAM, 47
THREE DIMENSIONAL CONTINUUM,
51
THREE DIMENSIONAL SOLID, 286
TIED SLIDELINE, 363
TOTAL AND UPDATED
LAGRANGIAN, 147
TOTAL LAGRANGIAN, 115, 137, 141,
144, 151, 155, 160, 276, 282, 290
TOTAL LAGRANGIAN
NONLINEARITY, 286
TRAIN HARDENING, 163
TRANSIENT, 302, 307
TRANSIENT ANALYSIS, 296
TRANSIENT FIELD ANALYSIS, 299
TUBULAR JOINT, 286
TUNNEL, 83

U

UPDATED LAGRANGIAN, 128
UPDATED LAGRANGIAN
DESCRIPTION, 273

V

VISCOUS, 198, 201
VOLUMETRIC CRUSHING, 209

W

WARPED ELEMENTS, 151
WIND LOADING, 75



LUSAS

LUSAS, Forge House, 66 High Street, Kingston upon Thames, Surrey, KT1 1HN, UK
Tel: +44 (0)20 8541 1999 | Fax: +44 (0)20 8549 9399 | info@lusas.com | www.lusas.com